

70-12,961

ROSSETTI, Salyatore J., 1941-  
EXPERIMENTAL DETERMINATION OF PRESSURE DROP  
AND FLOW CHARACTERISTICS OF DILUTE GAS-SOLID  
SUSPENSIONS.

The City University of New York, Ph.D., 1969  
Engineering, chemical

University Microfilms, A XEROX Company, Ann Arbor, Michigan

EXPERIMENTAL DETERMINATION OF PRESSURE DROP  
AND FLOW CHARACTERISTICS OF DILUTE GAS-SOLID  
SUSPENSIONS

by

Salvatore J. Rossetti

A dissertation submitted to the  
Graduate Faculty in Engineering in partial  
fulfillment of the requirements for the  
degree of Doctor of Philosophy,  
The City University of New York.

1969

This manuscript has been read and accepted for the Graduate Faculty in Engineering in satisfaction of the dissertation requirement for the degree of Doctor of Philosophy.

Aug 20, 1969  
date

Robert Pfeffer  
Chairman of Examining Committee

Sept 5, 1969  
date

Leon Brewer  
Executive Officer

Clarence B. Anderson

Latif M. Jiji

Harvey L. List

Robert Pfeffer, Chairman

Supervisory Committee

THE CITY UNIVERSITY OF NEW YORK

PLEASE NOTE:

Not original copy. Some  
pages have indistinct print.  
Filmed as received.

UNIVERSITY MICROFILMS

## ACKNOWLEDGEMENTS

The author would like to acknowledge with gratitude the assistance given him in the preparation of this dissertation by his mentor Professor Robert Pfeffer without whom this work would not have been initiated. The author also would like to express his thanks to Professor Alois X. Schmidt and Dean Egon Brenner for their active support and encouragement. Gratitude is also expressed for helpful discussions with Professor Harvey List and the cooperation and help of Professors Clarence B. Anderson, Latif M. Jiji and Robert A. Graff.

The author is especially indebted to Mr. John Bodnaruk of the chemical engineering shop who guided him through a maze of mechanical and instrumentation problems, Mr. George Di Iorio who took such care in the construction of the experimental loop, Mr. Robert Sperle whose practical knowledge solved some difficult problems and Mr. Dave Marden, Mr. Dick Pratt and Mr. John Spencer of the chemical engineering shop, all of whom lent assistance during some phase of the investigation.

Special thanks are expressed to Chuck Rosenecker and the people at the Bureau of Mines in Morgantown, West Virginia for the donation of the gas-solids circulator and loan of the two phase flow meter as well as their helpful advice. Howard Turner, Ed Sakata and the E.I. Du Pont de Nemours Company also deserve special thanks for the very useful particle size analyses which they generously performed for this investigation. The author is also grateful to

Ron Humphrey and the DISA S & B Corporation for their cooperation and advice during the course of the study.

The author also would like to acknowledge Henry A. Putré of NASA for his meaningful contributions to the study as well as NASA itself for supporting the investigation under Grant #NGR 33-013-029. The author also received financial support from an NDEA Title IV fellowship and a City University research assistantship.

Most importantly, the author is forever grateful for the encouragement and active help received from his wife, sister and parents.

TABLE OF CONTENTS

	Page
ABSTRACT.....	i
LIST OF TABLES .....	iii
LIST OF FIGURES.....	iv
I. INTRODUCTION .....	1
II. LITERATURE SURVEY .....	4
BACKGROUND MATERIAL.....	4
Drag Coefficient Model .....	5
Equivalent Friction Factor Model .....	8
PREVIOUS EXPERIMENTAL STUDIES .....	9
Large Particle Studies .....	9
Vogt and White .....	9
Belden and Kassel .....	10
Wen and Simons .....	11
Dogin and Lebedev .....	11
Doig and Roper .....	13
Other work .....	15
Small Particle Studies .....	18
Horizontal test section studies .....	18
Farbar.....	18
Mehta, Smith and Comings .....	19
Schluderberg et. al .....	22
Peskin .....	23
Soo .....	26
McCarthy and Olson .....	29
Bureau of Mines .....	31
Vertical test section studies.....	33
Depew .....	33
Tien and Quan .....	35
Boothroyd .....	36
ANALYTICAL STUDIES .....	39
Tien .....	39
Soo .....	41
Sproull .....	45
Saffman .....	46
Julian and Dukler .....	49
Pfeffer, Rossetti and Lieblein .....	51
DRAG REDUCTION WITH LIQUIDS .....	52
III. DISCRIPTION OF APPARATUS, MATERIALS AND EXPERIMENTAL PROCEDURES .....	54
Apparatus .....	54
Gas-solids circulator .....	54
Closed experimental loop .....	61
Anemometry.....	67
Mass-flow meter .....	70
Open calibration loop .....	72
Materials .....	76
Experimental Procedures .....	77
Pure air runs .....	77

	Page
Open loop calibration runs .....	87
Closed-loop experiments .....	89
IV. EXPERIMENTAL RESULTS AND DISCUSSION .....	92
Pure Gas results .....	92
Velocity profiles .....	92
Friction factors .....	94
Anemometer Calibrations .....	99
Orifice Calibration .....	101
Open-loop Calibration Results .....	101
Closed Loop Results .....	111
Mass flow ratios .....	111
Friction factors .....	128
Orifice Coefficient .....	166
Turbulence measurements .....	168
Gross flow photography .....	181
Particle size analysis .....	188
V. CONCLUSIONS .....	198
VI. RECOMMENDATIONS FOR FUTURE WORK .....	203
VII. LITERATURE CITED .....	205
VIII. LIST OF SYMBOLS .....	209
IX. APPENDIX A .....	213
X. APPENDIX B .....	230
XI. VITA .....	235

## ABSTRACT

### EXPERIMENTAL DETERMINATION OF PRESSURE DROP AND FLOW CHARACTERISTICS OF DILUTE GAS-SOLID SUSPENSIONS

by

Salvatore J. Rossetti

Adviser: Professor Robert Pfeffer

A closed loop experimental setup was assembled for the purpose of making pressure drop and turbulence measurements for dilute gas-solid suspensions flowing in a tube. The apparatus included a two phase flow meter for solids concentration determination and solid state anemometry for velocity and turbulence measurements.

Five different sizes of glass beads ranging from a nominal diameter of 10 to 59 microns were circulated at loading ratios up to 2.5. Three different Reynolds number ranges from 12,000 to 25,000 were investigated in both a vertical and horizontal test section.

The results of the investigation showed that for the vertical test section less pressure drop was found for all of the dilute gas solid suspensions studied than was observed for a pure gas at the same gas Reynolds number. For the horizontal test section pressure drop increases above the pure gas values were found for the two largest sized particles but decreases were also observed with the smaller particles.

The vertical test section results may be explained in terms of the interaction of the particles and the fluid energy in the vicinity of the wall, especially in view of the fact that an optimum particle size of  $30\mu$  was found to yield the greatest reduction in frictional pressure loss. The results of the horizontal test section could not be wholly explained on this bases due to the "segregated" and "bouncing" flow phenomena observed with the larger particles.

Turbulence measurements made in a vertical section show an increase in the centerline intensity of turbulence when drag reduction was observed. This might indicate that a buildup of the laminar sublayer is caused by the particle extracting energy from the fluid near the wall. Similar trends have been reported in cases of drag reduction with liquids.

LIST OF TABLES

Table	Title	Page
I	Summary of operating conditions employed in large particle research.	16,17
II	Summary of operating conditions for small particle research with horizontal test sections.	32
III	Summary of operating conditions for small particle research with vertical test sections.	40
IV	Particle sizes.	78
V	Variation of ratio of average to centerline gas velocity with gas Reynolds number.	95

## LIST OF FIGURES

Figure	Title	Page
1	View of centrifugal impeller and housing volute.	56
2	Impeller and nose cone assembly.	57
3	Exploded view of circulator assembly.	58
4	Preliminary assembly of circulator.	59
5a	25 hp Motor-Generator.	60
5b	Slave motor coupled to gas-solids circulator.	60
6	Schematic Diagram of the Closed Loop.	63
7	Close up of Thermistor Probe.	68a
8	Front panels of four Anemometer Modules.	68a
9	Two phase Flowmeter.	71
10	Schematic Diagram of the Open Loop.	73
11	Particle Collector.	75
12	Photographs of 50 $\mu$ Glass beads a) Before recirculation. b) After recirculation.	79
13	Photographs of 30 $\mu$ Glass beads a) Before recirculation. b) After recirculation.	80
14	Photographs of #279 Glass beads a) Before recirculation. b) After recirculation.	81
15	Photographs of #981 Glass beads a) Before recirculation. b) After recirculation.	82

Figure	Title	Page
16	Photographs of #980 Glass beads a) Before recirculation. b) After recirculation.	83
17	Gas Velocity Profile.	93
18	Variation of Friction Factor with gas Reynolds number.	97
19	Variation of Friction Factor with gas Reynolds number.	98
20	Typical anemometer probe calibration.	100
21	Variation of Orifice Coefficient with gas Reynolds number.	102
22	Strain gage readout for pure gas, $V_{STO}$ , as a function of centerline mass flow rate.	106
23	Variation of Pure Gas Strain gage reading with centerline mass velocity.	107
24	Typical pure gas recorder output a) High Reynolds Number. b) Moderate Reynolds Number.	108
25	$V_{ST} - V_{STO}$ as a function of centerline mass velocity with particle flow rate as a parameter.	109
26	Variation of $\frac{V_{ST} - V_{STO}}{\rho V^c}$ with particle flow rate.	110
27	Open loop strain gage output for high and low feed rates a) High particle feeding rate. b) Very low particle feed rate.	112
28	Typical closed loop flow meter output for 30 $\mu$ Glass beads.	113

Figure	Title	Page
29	Loading ratio as a function of weight added to the closed loop system - 50 $\mu$ Glass beads. a) $(Re)_g = 25225$ b) $(Re)_g^g = 18700$	115
30	Loading ratio as a function of weight added to the closed loop system - 30 $\mu$ Glass beads at $(Re)_g = 25250$ .	116
31	Loading ratio as a function of weight added to the closed loop system - 30 $\mu$ Glass beads. a) $(Re)_g = 17550$ b) $(Re)_g^g = 13750$	117
32	Loading ratio as a function of weight added to the closed loop system for #279 Glass beads at $(Re)_g = 25900$ .	118
33	Loading ratio as a function of weight added to the closed loop system - #279 Glass beads. a) $(Re)_g = 18650$ b) $(Re)_g^g = 14400$	119
34	Loading ratio as a function of weight added to the closed loop system - #981 Glass beads at $(Re)_g = 25925$ .	120
35	Loading ratio as a function of weight added to the closed loop system - #981 Glass beads a) $(Re)_g = 19100$ b) $(Re)_g^g = 15000$ .	121
36	Loading ratio as a function of weight added to the closed loop system - #980 Glass beads at $(Re)_g = 27675$	122
37	Loading ratio as a function of weight added to the closed loop system - #980 Glass beads a) $(Re)_g = 20650$ b) $(Re)_g^g = 16200$	
38	Variation of Horizontal section static pressure with centerline mass velocity for the closed loop system.	130

Figure	Title	Page
39	Variation of Vertical section static pressure with centerline mass velocity for the closed loop system.	132
40	Friction factor ratio as a function of loading ratio for 50 $\mu$ Glass beads in Horizontal test section at $(Re)_g = 25225$ .	133
41	Friction factor ratio as a function of loading ratio for 50 $\mu$ Glass beads in Horizontal test section a) $(Re)_g = 18700$ . b) $(Re)_g = 14300$ .	134
42	Friction factor ratio as a function of loading ratio for 50 $\mu$ Glass beads in Vertical test section at $(Re)_g = 22375$ .	135
43	Friction factor ratio as a function of loading ratio for 50 $\mu$ Glass beads in Vertical test section a) $(Re)_g = 16400$ . b) $(Re)_g = 12500$ .	136
44	Friction factor ratio as a function of loading ratio with Reynolds number as a parameter for 50 $\mu$ particles. a) Horizontal test section. b) Vertical test section.	137
45	Friction factor as a function of loading ratio for 30 $\mu$ Glass beads in Horizontal test section a) $(Re)_g = 25250$ . b) $(Re)_g = 17550$ .	138
46	Friction factor ratio as a function of loading ratio for 30 $\mu$ Glass beads in Horizontal test section at $(Re)_g = 13750$ .	139
47	Friction factor ratio as a function of loading ratio for 30 $\mu$ Glass beads in Vertical test section at $(Re)_g = 22300$ .	140

Figure	Title	Page
48	Friction factor ratio as a function of loading ratio for 30 $\mu$ Glass beads in Vertical test section a) $(Re)_g = 15375$ b) $(Re)_g = 11990$ .	141
49	Friction factor ratio as a function of loading ratio with Reynolds number as a parameter for 30 $\mu$ particles. a) Horizontal test section. b) Vertical test section.	143
50	Friction factor ratio as a function of loading ratio for #279 Glass beads in Horizontal test section at $(Re)_g = 25900$ .	145
51	Friction factor ratio as a function of loading ratio for #279 Glass beads in Horizontal test section. a) $(Re)_g = 18650$ b) $(Re)_g = 14400$	146
52	Friction factor ratio as a function of loading ratio for #279 Glass beads in Vertical test section at $(Re)_g = 22800$ .	147
53	Friction factor ratio as a function of loading ratio for #279 Glass beads in Vertical test section a) $(Re)_g = 16750$ b) $(Re)_g = 13000$ .	148
54	Friction factor ratio as a function of loading ratio with Reynolds number as a parameter for #279 Glass beads a) Horizontal test section b) Vertical test section.	149
55	Friction factor ratio as a function of loading ratio for #981 Glass beads in Horizontal test section at $(Re)_g = 25925$ .	150
56	Friction factor as a function of loading ratio for #981 Glass beads in Horizontal test section. a) $(Re)_g = 19100$ b) $(Re)_g = 15000$ .	151

Figure	Title	Page
57	Friction factor ratio as a function of loading ratio for #981 Glass beads in Vertical test section at $(Re)_g = 22750$ .	152
58	Friction factor ratio as a function of loading ratio for #981 Glass beads in Vertical test section. a) $(Re)_g = 16700$ b) $(Re)_g = 13150$ .	153
59	Friction factor ratio as a function of loading ratio with Reynolds number as a parameter for #981 Glass beads a) Horizontal test section. b) Vertical test section.	155
60	Friction factor ratio as a function of loading ratio for #980 Glass beads in Horizontal test section at $(Re)_g = 27675$ .	156
61	Friction factor ratio as a function of loading ratio for #980 Glass beads in Horizontal test section a) $(Re)_g = 20650$ b) $(Re)_g = 16200$	157
62	Friction factor ratio as a function of loading ratio for #980 Glass beads in Vertical test section at $(Re)_g = 24300$ .	158
63	Friction factor as a function of loading ratio for #980 Glass beads in Vertical test section a) $(Re)_g = 18075$ b) $(Re)_g = 14225$ .	159
64	Friction factor ratio as a function of loading ratio at high Reynolds number for #980 Glass beads.	160
65	Variation of friction factor ratio with loading ratio at high Reynolds number for the five particle sizes considered in the Horizontal section.	161

Figure	Title	Page
66	Variation of friction factor ratio with loading ratio at high Reynolds number for the five particle sizes considered in the Vertical test section.	162
67	Orifice coefficient $C_V$ as a function of the orifice Reynolds number for all particle sizes at all concentrations at all Reynolds numbers.	167
68	Variation of percent turbulence with Reynolds number for the pure gas.	171
69	Variation of intensity of turbulence ratio with the loading ratio for 50 $\mu$ Glass beads at all Reynolds numbers.	173
70	Variation of intensity of turbulence ratio with the loading ratio for 30 $\mu$ Glass beads at all Reynolds numbers.	174
71	Variation of intensity of turbulence ratio with the loading ratio for the #279 Glass beads at all Reynolds numbers.	175
72	Variation of intensity of turbulence ratio with the loading ratio for the #981 Glass beads at all Reynolds numbers.	176
73	Variation of intensity of turbulence ratio with the loading ratio for the #980 Glass beads at all Reynolds numbers.	177
74	Relative turbulence intensity ratio as a function of loading ratio for the five different size glass beads.	179
75	Gross flow photographs of 50 $\mu$ particles.	182
76	Gross flow photographs of 30 $\mu$ particles.	183

Figure	Title	Page
77	Gross flow photographs of #279 Glass beads.	184
78	Gross flow photographs of #981 Glass beads.	185
79	Gross flow photographs of #980 Glass beads.	186
80	Particle size distribution before and after closed loop recirculation for the 50 $\mu$ Glass beads.	189
81	Particle size distribution before and after closed loop recirculation for the 30 $\mu$ particles.	190
82	Particle size distribution before and after closed loop recirculation for the #279 Glass beads.	191
83	Particle size distribution before and after closed loop recirculation for the #981 Glass beads.	192
84	Particle size distribution before and after closed loop recirculation for the #980 Glass beads.	193
A-1	Variation of the product $vr$ with radial distance $r$ for a typical run.	217
A-2	Typical anemometer calibration curve- Probe #5.	219
A-3	Variation of $\log (V^2 - V_o^2)$ with $\log v_c$ .	220

## I. INTRODUCTION

Historically, the first use of gas-solids suspensions occurred in the conveying of food and materials. When the unique contracting properties of suspensions of finely divided materials in a gas became evident, however, their application was no longer limited to conveying mediums, but spread to include many physical operations as well. Gas-solid suspensions are now being considered as nuclear reactor coolants and as working fluids in conventional gas power cycles for space power generators.

The advantages of using such suspensions include ease of handling, provision of large surface areas for mass and heat transfer, and under certain conditions a higher convective heat transfer coefficient than that of pure gas. One of the most important drawbacks to the use of these suspensions, however, is the dearth of knowledge concerning their flow properties. Even though gas-solid suspensions find such widespread applications, the prediction of pressure losses associated with their flow is still mostly an empirical art.

One would expect that as the suspensions become less and less concentrated the flow properties would be more readily characterized and more easily understood - approaching those of the gas. However, the opposite is true. The flow of dilute gas-solid suspensions is even less predictable than that of concentrated suspensions.

Some investigators have found that the addition of small amounts of solids to a turbulently flowing gas have increased

the frictional resistance to flow; whereas others have reported a phenomenon which could be interpreted as drag reduction. For the purposes of this investigation, drag reduction will be said to occur when, upon the addition of a second phase to a flowing fluid, a decrease in frictional resistance below that obtained with the pure fluid under the same flow conditions is observed.

Drag reduction with liquids has been widely reported and is an established fact. Drag reduction with gas-solid suspensions is a dubious phenomena with only meager evidence supporting it.

One of the purposes of this investigation was to design and develop a closed loop experimental system for the determination of suspension pressure drops as a function of concentration of solids, particle diameter, and gas Reynolds number. The investigation concentrates on dilute gas-solid suspensions in turbulent flow, so as to ascertain the reality of drag reduction. Since little information was available on the effect of particle size on turbulent flow characteristics of a suspension, various particle sizes are studied in the investigation. All particle sizes are 50-microns or less in diameter, since previous analytical and experimental results indicated that drag reduction will not occur with larger sizes. The experimental system includes both vertical and horizontal test sections and both glass and metal sections.

The experimental set-up also includes provisions for

turbulence and gas velocity profile measurements. With the experimental results obtained during this investigation, an attempt is made to clarify the drag reduction phenomena and other aspects of dilute gas-solid flow.

## II. LITERATURE SURVEY

In the following pages some of the more significant and recent literature relating to the flow characteristics of gas-solid suspensions will be summarized. This literature survey will be presented in three parts: the first part will review experimental studies of gas-solid suspension flow, the second part will deal with some of the theoretical analyses and turbulence studies in gas-solid suspension flow, and the third part will be a brief discussion on drag reduction reported with liquid-polymer systems. In order to further understanding and simplify reading of the following text, however, a brief background section describing some of the more frequently used terms, definitions, and concepts found in this work will be presented prior to the summary of the literature.

### BACKGROUND MATERIAL

The two concepts most commonly used to describe the pressure loss of gas-solid suspensions are the drag coefficient and equivalent friction factor models. Both models are based on the assumption that the mixture flows at a velocity greater than either the saltation velocity in horizontal tubes (the lowest possible velocity required to keep a specific particle in suspension) or the choking velocity in vertical tubes (the minimum velocity required to prevent the suspension from being transported up the tube in slug flow). Under these conditions the pressure drop for the general flow of gas-solid suspensions through tubes is considered to be composed of the following



where  $\rho_p'$  the bulk density of solid =  $\rho_s - \rho_g$ , lb solid/ft<sup>3</sup> mixture, and  $f_p'$  is the particle friction factor based on particle velocity and particle density in the mixture.

For a horizontal tube of constant diameter that is of sufficient length so that acceleration forces can be neglected (particles and fluid having reached their respective equilibrium velocities), this equation reduces to

$$\Delta P_s = \frac{2f_g \rho_g v_g^2 L}{g_c D} + \frac{2f_p' \rho_p' v_p^2 L}{g_c D} \quad (2)$$

By use of the Fanning equation

$$\Delta P_g = 2f_g \frac{L}{D} \rho_g \frac{v_g^2}{g_c} \quad (3)$$

dividing  $\Delta P_s$  by  $\Delta P_g$ , the following relation is obtained

$$\frac{\Delta P_s}{\Delta P_g} = 1 + \frac{f_p' \rho_p' v_p^2}{f_g \rho_g v_g^2} \quad (4)$$

Defining the ratio of the mass flow rate of particles to the mass flow rate of pure gas as the loading ratio,  $\eta$

$$\eta = \frac{W_p}{W_g} = \frac{\rho_p' v_p}{\rho_g v_g} \quad (5)$$

then

$$\frac{\Delta P_s}{\Delta P_g} = 1 + \frac{f_p' v_p}{f_g v_g} \eta \quad (6)$$

Before equation (2) can be used to determine  $\Delta P_s$ , however, a means of obtaining both  $f_p'$  and  $v_p$  is necessary.

For particle sizes showing a significant velocity lag or

slip between the particles and the transporting fluid, Hinkle (ref. 2) assumed the pressure drop due to the presence of the particles to be caused entirely by the drag of the fluid on the particles. In this case, the particle-to-wall friction can be neglected in comparison with the drag. Based on this assumption, the pressure drop due to the particle drag is

$$\frac{2f_p' \rho_p' v_p^2 L}{g_c D} = \frac{n C_D \rho_g (v_g - v_p)^2 \pi D_p^2 L}{8 g_c} \quad (7)$$

or

$$f_p' = \frac{n C_D \rho_g (v_g - v_p)^2 \pi D_p^2 D}{16 \rho_p' v_p^2} \quad (8)$$

where  $n$  is the number of particles per cubic foot of mixture and  $C_D$  is the standard drag coefficient for spherical particles defined by

$$C_D = \frac{8 F_D g_c}{\pi D_p^2 \rho_g (v_g - v_p)^2} \quad (9)$$

where  $F_D$  is the drag force and  $v_g - v_p$  is the relative velocity between the gas and particles. Since

$$n = \frac{6 \rho_p'}{\pi \rho_p D_p^3} \quad (10)$$

then

$$f_p' = \frac{3 C_D \rho_g (v_g - v_p)^2 D}{8 \rho_p' v_p^2 D_p} \quad (11)$$

In order to employ this model the particle velocity must be known. If experimental values of  $v_p$  are not available, the particle velocity can be crudely estimated by assuming  $v_p$  to be equal to  $v_g - v_{ps}$  where the terminal settling velocity

$v_{ps}$  can be obtained from the standard drag coefficient-Reynolds number correlation (ref. 1). However, the attendant difficulty of obtaining an accurate particle velocity makes this model difficult to apply in obtaining the particle friction factor. In addition, the effect of particle-to-wall friction has been entirely omitted. For example, for particles small enough to show no slip ( $v_g = v_p$ ), the model would predict no additional pressure drop due to the particles.

#### Equivalent Friction Factor Model

The inherent disadvantages of the previous model indicate the desirability of having a simpler model to predict suspension pressure drops. The equivalent friction factor model simply defines the pressure drop of the suspension as

$$\Delta P_s = 2f_s' \rho_g \frac{L}{D} \frac{v_g^2}{g_c} \quad (12)$$

where  $f_s'$  is an equivalent friction factor and  $\rho_g$  is the density of the gas in the suspension. If this equation is divided by the Fanning equation for the same gas conditions in the tube, then

$$\frac{\Delta P_s}{\Delta P_g} = \frac{f_s'}{f_g} \quad (13)$$

An alternative definition of the equivalent friction factor based on suspension density is given by

$$\Delta P_s = 2f_s \rho_s \frac{L}{D} \frac{v_s^2}{g_c} \quad (14)$$

Thus  $f_s'$  is related to  $f_s$ , assuming negligible slip between the particles and the gas, by the relation

$$f_s' = f_s \frac{\rho_s}{\rho_g} = f_s(1+\gamma) \quad (15)$$

In both cases,  $f_s/f_g$  as well as  $f_s'/f_g$  are presumably functions of loading ratio, gas Reynolds number, particle diameter, and other properties of the suspension that must be determined experimentally.

#### PREVIOUS EXPERIMENTAL STUDIES

A summary of the more important experimental research that has been done in the field will now be presented. Since the present study does not deal with large particles (particle diameters above 100 microns), only a brief description will be made of work in this area. A more comprehensive survey will be presented for previous studies involving small particles.

#### Large Particle Studies

A brief review of the literature available from studies dealing primarily with large particles is presented in the following sections, and a summary of the operating conditions and the physical properties of gases and solids used in each experiment is presented in Table I. The experiments were conducted at room temperature with pressure levels ranging from 1 to 3 atmospheres within the various studies.

Vogt and White. - In an early paper by Vogt and White (ref. 3), the pressure differential required to produce steady flow of suspensions of sand ( $D_p = 200, 330, 440, 730 \mu$ ), clover seed ( $D_p = 1150 \mu$ ) and wheat ( $D_p = 4000 \mu$ ) in air through vertical and horizontal  $\frac{1}{2}$ -inch-diameter pipes was presented. In their work the loading ratio was varied between 0.6 and 41.6 and the gas Reynolds number ranged from 9000 - 39000.

Vogt and White correlated their data by using a form similar to that presented by Gasterstadt (ref. 4) in 1920. Gasterstadt's relation may be written as

$$\frac{\Delta P_s}{\Delta P_g} = 1 + F \eta \quad (16)$$

where F is not a constant but a complicated function of gas Reynolds number, particle size, etc. Vogt and White's correlation was presented as

$$\frac{\Delta P_s}{\Delta P_g} = 1 + B_v \left( \left( \frac{D}{D_p} \right)^2 \left[ \frac{\rho_g \eta}{\rho_p (Re)_g} \right]^1 \right) \quad (17)$$

where  $B_v$  and 1 are functions of the dimensionless group  $Re_p (C_D)^{\frac{1}{2}}$ . However, Vogt and White's correlation and also all of their runs with sand are highly questionable due to the influence of high electrostatic charges which could have been responsible for the high pressure drops reported for these particles.

Belden and Kassel. - Belden and Kassel (ref. 5) presented data on pressure drop required for the vertical transport of spherical catalyst approximately 1015 and 2030  $\mu$  in diameter through two transfer lines with inside diameters of 0.473 and 1.023 inches. In their work the loading ratio was varied between 0.4 and 14.0 and the gas Reynolds number ranged from 3,000 - 24,000. Belden and Kassel expressed total pressure drop as the sum of the static and friction terms which had previously been combined into one term by Vogt and White.

Their findings indicated that the pressure drop is nearly independent of tube-diameter-particle-diameter ratio. Their results are very questionable, however, due to inaccuracies caused by entrance and exit losses in the transfer line and the "somewhat speculative" manner in which particle acceleration effects were accounted for in their data.

Wen and Simons. - The flow characteristics of dense gas-solid mixtures transported through horizontal pipes were studied by Wen and Simons (ref. 6) using glass beads ( $D_p = 70\mu$ ,  $145\mu$  and  $275\mu$ ) and coal powders ( $D_p = 110\mu$ ,  $500\mu$  and  $740\mu$ ) in  $\frac{1}{2}$ ,  $\frac{3}{4}$  and 1 inch glass pipes and a  $\frac{1}{4}$  inch steel pipe. The solid loading ratios used in their work ranged between 80 and 750 and were considerably higher than those used in conventional pneumatic transport. The Reynolds numbers range in this work was between 500 and 9000, so that their system approximated a moving fluidized bed. Wen and Simons observed a large amount of slippage between gas and solids. They found that the solid particle velocities and solid loadings in the pipe line were the primary factors affecting pressure drops while particle size and shape exerted a very slight effect on pressure drops. Wen and Simons felt that this was due to the fact that in their loading ratio range the solids move predominantly in the bottom of the pipe as agglomerated masses rather than individually suspended particles.

Dogin and Lebedev. - In the work of Dogin and Lebedev (ref. 7), an attempt was made to determine the dependence of the friction factor  $f_s'$  of gas-solid suspensions on the

loading ratio, flow velocity, specific weight, and dimensions of the particles being conveyed. The materials conveyed by air in a 5-inch-diameter horizontal pipe were millet ( $D_p = 1900\mu$ ), peas ( $D_p = 5760\mu$ ), turnip seeds ( $D_p = 1280\mu$ ), wheat ( $D_p = 4000\mu$ ), pine kernels ( $D_p = 8400\mu$ ), and sunflower seeds ( $D_p = 5850\mu$ ). The loading ratio was varied between 0 and 15, and the gas Reynolds numbers ranged from 110,000 to 321,000.

Dogin and Lebedev correlated their data by using the form presented by Gasterstadt. They observed that  $\Delta P_s / \Delta P_g$  decreased as the flow velocity of the gas increased and found that  $(\Delta P_s / \Delta P_g) - 1$  was proportional to the ratio of the particle diameter to the pipe diameter taken to the 0.1 power and to the ratio of the densities of particle and gas  $\rho_p / \rho_g$ . The results of their investigations were summarized in their final correlation which was given as

$$f_s' = f_g + \frac{A \left(\frac{D_p}{D}\right)^{0.1} (Re)_g^{0.4} \rho_p}{(Fr_g)^{0.5} \rho_g} \eta \quad (18)$$

where  $Fr_g$  is the gas Froude number equal to  $v_g^2/gD$  and  $A$  is a parameter that varied, depending on pipe roughness; between  $1 \times 10^{-6}$  and  $2.2 \times 10^{-6}$  in the experiments of Dogin and Lebedev.

Assuming that the relationship for the gas friction factor

$$f_g = .046 (Re)_g^{-0.2} \quad (19)$$

can be applied, and dividing equation (18) by equation (19) the resulting relationship for a given gas, particle density, and tube diameter becomes

$$\frac{f_s'}{f_g} = 1 + c (D_p)^{0.1} (v_g)^{-0.4} \eta \quad (20)$$

where  $c$  is a constant depending on the system. Equation (20) shows that  $(f_s'/f_g) - 1$  should increase slightly with particle diameter and increase with decreasing gas velocity. These trends are in good agreement with most of the literature.

Doig and Roper. - Doig and Roper (ref. 8) measured air velocity profiles in a 1.7 inch diameter vertical riser in the presence of suspensions of 304 and 756 micron glass beads in air. The velocity measurements were made with a cylindrical transversely oriented Pitot tube which had been developed and calibrated previously (ref. 9). The loading ratio was varied between 0 and 6, and the gas Reynolds numbers ranged from 12,400 to 44,200. The authors presented their results by means of a series of plots of distribution parameter ratios as a function of loading ratio with Reynolds-Froude numbers and particle to conduit size ratios as parameters. The distribution parameter ratios plotted were as follows:

a) The suspension to pure gas ratio of the reciprocal of the power law index for the gas phase.

b) The suspension to pure gas ratio of the relative distance where the point velocity equals the average velocity for the gas phase.

c) The suspension to pure gas ratio of the ratio of centerline to average velocity for the gas.

d) The suspension to pure gas ratio of the core region slope for the gas.

One of the results of these plots was a rapid decrease of the power law index ratio with increase of the mass flow ratio. The authors indicated that this denoted a decrease in the air velocities near the wall and explains the initial decrease of heat transfer coefficient with loading ratio observed by other investigators. The authors also infer that since corresponding values of this power law index rates for the 300-micron particles are less than half of those for the 756-micron particles the air velocities near the wall will be closer to those of the corresponding particle-free air.

The decrease in the velocity gradient predicted by their plots for the 304-micron particles was less than that predicted for the 756 micron particles under corresponding conditions. The authors considered, therefore, that wakes would form downstream of the particles which would provide local increases in momentum transfer. At low mass flow ratios, the density of these local increases at the wall would be small and probably insignificant, particularly for the larger particles. At higher mass flow ratios it was felt that they may be the cause of previously observed increase in momentum transfer and the gas velocity gradient at the walls may be less important to mass and energy transfer to the walls than eddies produced by particle wakes.

The authors suggest that the main reason for finding reduced air velocities near the wall at low loading ratio was the higher particle concentration at the walls occurring at these low mass flow ratios.

Another interesting result of this study was that the plot of axial velocity ratios indicated a similar degree of flattening of the velocity profile at the higher mass flow ratios for both particles. A flattening of the velocity profile in the core region suggest an increase in the eddy momentum diffusivity, which indicates that momentum transfer is occurring and might signify a decrease of the eddy scale of turbulence approaching the particle dimension and an increase in the wave number in the core region.

Through photographic measurement of particle velocities, it was also found that the particle velocity distributions for the 304-micron glass beads tended to be closer to the air velocity distributions than those obtained for the 756 micron particles under corresponding conditions.

Other work. - Other important experimental studies involving pressure drop of gas-solid suspensions using large particles include the work of Hariu and Molstad (ref. 10); Clark, Charles, Richardson, and Newitt (ref. 11); and the theses of Hinkle (ref. 2); Helander (ref. 12); and Mitlin (ref. 13). The experimental data from these works were thoroughly analyzed by Julian (ref. 14) in order to verify his eddy viscosity model. Therefore, a description of these works will not be repeated herein; however, a summary of the range

Particle	Gas	Particle Diameter, $D_p$ (Microns)	Inside Tube Diameter, $D$ (Inches)	Gas Reynolds Number, $(Re)_g$	Loading Ratio, $\eta$	Horizontal or Vertical Test Section	Source
Sand, Clover Seed, Wheat	Air	200, 730, 330, 1150, 440, 4000	.5	9000-39,000	.6-41.6	Horizontal and Vertical	Vogt & White (ref. 3)
Spherical Catalyst	Air, $CO_2$	1015, 2030	.473 1.023	3000-24,000	.4-14.	Vertical	Belden & Kassel (ref. 5)
Glass, Coal	Air	70, 145, 275, 110, 500, 740	.364, .50, .75, 1.0	500-9500	30.-750.	Horizontal	Wen & Simons (Ref. 6)
Millet, Peas, Turnip Seeds, Pine Kernels and Sunflower Seeds	Air	1280, 5760, 1900, 5850, 4000, 8400	5.0	110,000 - 321,000	.5-15.	Horizontal	Dogin & Lebedev (ref. 7)
Sand, Cracking Catalyst	Air, $CO_2$	200-510	.25, .50	8700-11,000	.5-36	Vertical	Hariu & Molstad (ref. 10)
Cress Seed	Air	1000	1.0	39,000-75,000	2.2-7.4	Horizontal	Clark, et al, (ref. 11)

TABLE I. - SUMMARY OF OPERATING CONDITIONS EMPLOYED IN LARGE PARTICLE RESEARCH

Particle	Gas	Particle Diameter, $D_p$ (Microns)	Inside Tube Diameter, $D$ (Inches)	Gas Reynolds Number, (Re) <sub>g</sub>	Loading Ratio, $n$	Horizontal or Vertical Test Section	Source
Tenite, Polystyrene, Aluminum	Air	2290-6360	2.0, 3.0	178,000	.5-4.5	Horizontal	Hinkle (ref. 2)
Sand, Glass, Polystyrene	Air	435-940	1.5, 2.0	33,000 - 59,000	.4-12.1	Vertical	Helander (ref. 12)
Glass, Fertilizer, Cress, Brass, Aluminum	Air	125-1525	1.0	43,700 - 78,000	1.6-16.5	Horizontal	Mitlin (ref. 13)
Glass	Air	304, 756	1.7	12,400- 44,200	0-6	Vertical	Doig & Roper (ref. 8)

TABLE I. (cont.)

of the operating variables involved appears in Table I.

#### Small Particle Studies

Due to the fact that the experimental work in this study deals with small particles, a comprehensive review of gas-solid suspension research primarily interested in particle sizes of 100 microns or less will be presented in the following pages. In order to clarify some of the apparent inconsistencies in the reported data, studies using horizontal and those employing vertical test sections will be separately described.

#### Horizontal test section studies.

Most small particle research reported in the literature has been performed in experimental loops utilizing a horizontal test section. A review of this work appears on the following pages, and a summary of the operating conditions and the physical properties of gases and solids used in each experiment is presented in Table II.

Farbar. - Farbar (ref. 15) measured the flow characteristics of solid-gas mixtures in both a horizontal and a vertical pipe 0.69 inch in diameter using a mixture consisting of silica-alumina catalyst and air. The loading ratio was varied between 0 and 16, and the particles had a size distribution varying from less than 10 microns to greater than 220 microns with an average diameter of 50 microns. The gas Reynolds number was varied between 17,000 and 50,000.

As a result of his studies, Farbar was able to report that  $\Delta P_s / \Delta P_g = f_s' / f_g$  appeared to decrease when the gas

flow rate or  $(Re)_g$  was increased. Farbar also reported that  $\Delta P_s / \Delta P_g$  increased as  $\eta$  was increased up to  $\eta = 10$ . Although his data above  $\eta = 10$  were inadequate to establish a definite variation, he proposed that above this value the loading ratio no longer has an effect on the pressure drop of the suspension. It should be noted, however, that Farbar presents no correlation for his data and that the data as given in his paper for vertical transport are inconveniently presented because the author neglected to subtract the gravity head (the pressure drop caused by supporting a vertical column of the suspension) from the total pressure drop to obtain the pressure drop caused by friction alone. Although Farbar chose to draw a single line through all of his horizontal section data, several lines could have been drawn for different values of  $(Re)_g$ .

In his conclusions, Farbar also indicated that the results obtained using a wide particle size spectrum such as was used in his work would differ considerably from those obtained using flow mixtures containing particles of fixed size.

Mehta, Smith and Comings. - In the work of Mehta, Smith, and Comings (ref. 16) 36- and 97-micron - diameter glass beads were each suspended in air flowing through both horizontal and vertical  $\frac{1}{2}$  inch-diameter pipe test sections. The gas Reynolds number was varied between 10,000 and 60,000 and the loading ratio was varied between 0.7 and 4.7 for the 36-micron particles and between .7 and 7.0 for the 97 micron

particles. As a result of their study, the authors concluded that the pressure drop in air solid transport systems is dependent upon the type of particle flow. They postulated that the 97-micron solids were primarily in "bouncing" flow, where the particles are in unsteady motion and frequently collide with the wall of the pipe. The 36-micron particles were assumed to be in suspension flow, where the particles flow in a suspended condition that is maintained by the finite slip velocity between the particles and the gas.

The authors attempted to correlate their data by using the drag coefficient model with no success. They finally proposed a correlation based on a so-called mixture friction factor defined by

$$\Delta P_s = \frac{f_m \frac{L}{D} v_g^2 \rho_g}{2g_c} \left[ 1 + \left( \frac{v_p}{v_g} \eta \right)^{a'} \right] \quad (21)$$

where  $a'$  is a constant chosen by the authors as 0.3 for the 36 micron particles and 1.0 for the 97-micron particles. Upon plotting  $f_m$  from their pressure drop data against gas Reynolds number, they found  $f_m$  roughly constant, or independent of solid flow rates, for both particles sizes at Reynolds numbers greater than 30,000. The average values of  $f_m$  were 0.016 for the 36-micron particles and 0.035 for 97-micron particles. At gas Reynolds numbers less than 30,000 these values increased as  $(Re)_g$  was decreased.

In Mehta's experiments,  $v_p/v_g$  for the 36-micron particles remained relatively constant at about 0.7, whereas for the

97-micron particles,  $v_p/v_g$  varied considerably (from about .22 to .67).

If the relationship defining  $f_s'$

$$\Delta P_s = 2 f_s' \rho_g \frac{L}{D} \frac{v_s^2}{g_c} \quad (12)$$

is substituted for  $\Delta P_s$  in equation (21) and the resulting equation is rearranged. The following relation between  $f_s'$  and  $f_m$  is obtained:

$$f_s' = \frac{f_m}{4} \left[ 1 + \left( \frac{v_p}{v_g} \eta \right)^{a'} \right] \quad (22)$$

Substituting the constant values for  $f_m$  suggested by the authors for each particle size gives

$$f_s' = 0.004 + .004 \left( \frac{v_p}{v_g} \eta \right)^3 \quad \text{for the 36-micron particles} \quad (23)$$

and

$$f_s' = 0.0088 + 0.0088 \frac{v_p}{v_g} \eta \quad \text{for the 97-micron particles} \quad (24)$$

The correlation given by equation (23) and (24) are difficult to apply, however, inasmuch as they depend on the magnitude of the particle velocity, which is a difficult quantity to determine. In addition, the correlation is only applicable for  $(Re)_g > 30,000$  since at lower gas Reynolds numbers,  $f_m$  was not found by the authors to remain constant.

Pfeffer, Rossetti, and Lieblein (ref. 17) prepared a plot of  $f_s'$  against  $\eta$  for several values of  $(Re)_g$  calculated from Mehta, Smith, and Comings original horizontal flow data (for  $\eta > 1$ ). This plot showed a greater dependence of  $f_s'$  on  $\eta$  than indicated by equations (23) and (24). The plot also showed that  $f_s'$  decreased with increasing gas

Reynolds number.

Schluderberg, Whitelaw and Carlson. - In an effort to study the properties of gaseous suspensions as reactor coolants, an extensive research program was conducted that is fully described by a series of reports (refs. 18 and 19) and is summarized in a paper by Schluderberg, Whitelaw, and Carlson (ref. 20). Although the primary purpose of this research was the study of heat transfer properties, pressure drops of suspensions of 1- to 5-micron graphite particles in carbon dioxide, helium, nitrogen, and carbon tetrafluoride were also measured at gas pressures between 30 and 130 pounds per square inch gage, gas temperatures between 90 and 1100<sup>o</sup>F and suspension densities of up to 8 pounds per cubic foot ( $\eta$  up to 90).

The authors calculated the friction factor by using a compressible-flow equation derived by assuming a constant average fluid temperature. They studied frictional pressure loss for the following cases:

- a) Flow in a special, isothermal "hairpin" loop located in the experimental loop following coolers,
- b) Flow in tubular heaters with turbulence promoters, and
- c) Flow in annular heaters.

Their data for circular channels without a turbulence promoter showed general agreement with the Moody-friction factor curves for smooth tubes at the lower Reynolds numbers, but dropped below this curve at higher Reynolds numbers.

The authors postulated that the lower values arose from the suppression of flow turbulence by the suspended particles.

The Franklin Institute (ref. 21) conducted a critical evaluation of the work reported by Schluderberg, et. al. concentrating on the results reported for case a) above, where the flow was more readily comparable with the corresponding data for pure fluids, and where the results obtained showed a friction factor less than that for pure fluids at large Reynolds numbers. The analysis of the Babcock and Wilcox data consisted of two parts: a "parameter sensitivity evaluation", and a recalculation of the friction factor using the raw data for several of the runs.

The "parameter sensitivity evaluation" showed that the magnitude of the friction factor was particularly sensitive to the values of the measured pressure drops, the pressure level at the exit from the hairpin loop, the mass flow rate and the loading ratio. After recalculating the friction factor the Franklin Institute still found that the friction factor was less than that for a pure fluid flowing in a smooth tube at the same Reynolds number. They also found that the data were still too scattered and subject to error to be useful in deducing a correlation equation.

Peskin. - Peskin and Dwyer (ref. 22) made an effort to determine the mechanism of gas-solid flow in tubes in a similar manner to Korn (ref. 23). From their experimental work Peskin and Dwyer concluded that gas-solid flow can be divided into the following four distinct flow regimes:

(1) Particles cause viscous disturbances and increase the size of the laminar sub-layer and thus a decrease in the shearing stress at the wall. In this case, the particles are very close together but occupy a small volume.

(2) Particles cause mostly viscous disturbances, but are too far apart to affect the gas velocity profile and hence the laminar sub-layer. The shearing stress at the wall is unchanged.

(3) Particles cause inertial disturbances that alter the gas velocity profile and decrease the size of the laminar sub-layer. In this case the wall shearing stress increases.

(4) Particles occupy a large volume and change the geometry of the flow. This situation is similar to the flow in packed beds.

It would appear, therefore, that the variation of the friction factor of a gas-solid suspension with loading ratio and other parameters may depend on which flow regime is applicable and may not be generalized for all gas-solid flows.

In order to verify the drag coefficient model, Peskin and Dwyer also measured pressure drop and both fluid and particle velocity profiles for loading ratios up to 4 by using 80 and 110-micron-diameter glass beads in air in a 3-inch-square duct. For these small, relatively widely spaced particles (regime 2), Peskin found that the flow disturbances caused by the particles are entirely viscous

since the particles because of their small size do not possess enough inertia in themselves to cause an inertial disturbance in the gas. Also, because of the relatively large spacing between the particles, the gas velocity profile was found to revert back to a universal profile between the particles. The average velocity of the particles, however, showed a large deviation from the velocity calculated by using the standard drag coefficient for the settling velocity; that is, on the basis of the experimentally measured particle velocity, the drag coefficient  $C_D$  calculated from the pressure drop measurements was much higher than predicted from the standard correlation. Peskin attributes the high drag coefficients to the added drag of the longitudinal component of the turbulence of the fluid rather than to shortcomings in the assumed model. Because of the disparity between the model and Peskin's data, the drag coefficient model does not appear useful for predicting suspension pressure drops.

In another investigation, Peskin (ref. 24) also correlated some of his pressure drop data in terms of the equivalent friction factor  $f_s$  defined by

$$\Delta P_s = 2f_s \rho_s \frac{L}{D} \frac{v_g^2}{g_c} \quad (14)$$

Sets of curves of  $f_s$  against gas Reynolds number were obtained for two different glass particle sizes (80- and 110-micron diameter) at Reynolds number 100,000 to 150,000 and loading ratios up to 14 in the same 3 inch square duct. The faired variations of these curves after conversion to

$f_s'$  were presented in ref. 17 and showed that in all cases the equivalent friction factor  $f_s'$  increased with increasing solids loading ratio and with decreasing gas Reynolds number. In addition, the results indicated that at a given loading ratio and Reynolds number, the friction factor was smaller for the 80-micron particles than for the 110-micron particles. It should also be noted at this point that the results for the friction factor of the 110-micron particles are somewhat dubious in view of certain experimental inaccuracies in the runs for this particle size (private communication from R.L. Peskin).

Soo. - In order to verify some of his analytical results, Soo has performed several experimental studies with dilute gas-solid suspensions in turbulent flow. Soo, Trezek, Dimick and Hohnstreiter (ref. 25) studied distributions of concentration, mass flow, and velocity of 50-micron glass and 35-micron nominal size magnesia in air at various loadings. They utilized a closed loop system with a 5 inch diameter duct using a flow velocity of about 130 ft/sec for all experimental runs. Due to the fact that a closed loop was used in the experiments, special instruments had to be developed for the measurement of the significant parameters.

Particle concentration was measured by fiber optics. For the measurement of the particle phase velocity an electrostatic mass flow probe was developed to determine the mass flow of the particle phases.

One of the results of this study was that because of

the difference between the velocity profiles of solid and gas, the mass ratio and flow rate ratios (loading ratio) were found to be different, with the former always at a higher value. In their experiments, for example, the mass ratio varied between 6 and 12 for the glass particles and .45 and 1.65 for the magnesia; whereas, the mass flow ratio was between 4.97 and 8.13 for the glass and .249 and .876 for the magnesia. However, they found that the velocity of the particles at the center of the pipe did not differ from that of the gas in fully developed turbulent flow in their range of loading.

They also found that the concentration of solid particles increased toward the wall of the pipe; whereas, the mass flow of solid particles decreased toward the wall. Although the solids velocity is less than or equal to that of the stream at the core, it was found to be finite and nearly 20% of the core velocity at the wall. The fluid was found to follow the  $1/7$  turbulent velocity law whereas the particle velocity profile depended on the distance from the wall to approximately the  $2/3$  power.

The authors concluded that correlation of the drift of solid particles toward the wall because of electrostatic forces and diffusion of solid particles toward the core because of concentration gradient was valid.

In a later study, Soo and Trezek (ref. 26) using the same experimental system described in reference 25 presented results on concentration and mass flow distributions of

nominal 30-micron magnesium oxide particles suspended in air in turbulent pipe flow. Loading ratios of up to 3 and gas Reynolds numbers ranging from 130,000 to 295,000 were studied.

Soo and Trezek observed that the wall of their test section became deposited with a "tenacious" layer of the thickness of 1 to 2 magnesia particles after a prolonged run with the air-magnesia suspension. They found that restarting after shutdown did not lead to further deposition. This was attributed to the wall becoming insulated after the initial layer is deposited and the magnesia particles in suspension being unable to give up their charge at the wall and become deposited tend to become reentrained by turbulent diffusion. The authors felt that the deposited layer constituted a "roughness", since an increase in the friction factor (based on air alone) by 10 to 12% was observed when compared to clean air flow.

In this study it was also found that the addition of solid particles led to a decrease in pipe flow friction factors up to a certain mass ratio of solid to gas, but increased again as the loading increased. They also observed that the gas velocity profile was unaffected by the solid phase. Their results also indicated that the mass flow ratio was consistently lower than the mass ratio, and that with a similar charge mass ratio of the particles the electrostatic effect is felt more strongly at low flow velocity. They felt that this confirmed the minimum

transport velocity concept (ref. 27) and explains the need for higher suspension velocity for smaller particles, below a certain size range, than larger particles.

By studying the collision rate of the particles with the wall, the authors determined that such collision gives only a small contribution to the pressure drop in pipe flow. Their data also showed that due to large interparticle spacing and lack of collision among the particles the density of the particles was such that the whole range of their experiment was in the "free particle" range. They note that the velocity profile of the solids was therefore analagous to that of free molecule flow with slip at the wall and nearly linear velocity gradient.

The authors conclude by observing that pipe flow of a gas-solid suspension is basically a phenomenon of interaction between electrostatic and hydrodynamic effects, the potential parameter being the ratio of electrostatic force to turbulent force. Unless the particle charge is truly negligible, they conclude, steady fully developed laminar pipe flow of a suspension cannot be maintained.

McCarthy and Olson. - In recent paper by McCarthy and Olson (ref. 28) turbulent flow of dilute suspensions of lucite, glass beads and calcite in air was investigated. The loading ratio was below .6 for all runs, and the Reynolds number ranged from  $10^5$  to  $10^6$ . The pressure drops were measured in the center section of a 1 inch diameter glass tube. The size of lucite particles ranged between 147

and 417 microns with an average size of 230 microns. The glass beads were between 53 and 74 microns and averaged 64 microns. The size of the calcite particles varied from below 1 micron to approximately 10 microns with an average particle size of 3 microns. The authors carried out runs for each of three air flows and four feed rates for the lucite and the glass beads, but were only able to run at one condition for the calcite due to difficulty encountered in feeding with their open-loop set-up.

The authors measured particulate velocities photographically and compared them to velocities calculated by using the standard drag coefficient.

By defining the velocity along the tube as the sum of the mass fraction multiplied by the velocity of both the gas and the particles, McCarthy and Olson solved the one dimensional time averaged equation of motion for steady-state flow by applying the continuity equation and the ideal gas laws. The solutions were similar to those previously obtained for compressible flow of an ideal gas with the exception of the mass velocity which was based on the density of the suspension and the mass averaged velocity rather than the pure gas density and velocity.

As a result of their experimental work, they found that for the 64 micron glass beads the solid velocity approximates the gas velocity beyond the first four feet of this twelve foot test section. For the 3 micron calcite

particles the solids velocity was essentially identical to the gas velocity for all points in the pipe.

The friction factor correlation obtained in this work was based on the pressure drop measured in the 4 to 12 foot region of the test section and was represented by

$$\frac{f_s}{f_g} = 1.0 - 0.8\eta + 0.5\eta^2 \quad (25)$$

This correlation however was recommended by the authors with the precaution that it be used only in the region where tested ( $\eta < .6$ ), since at higher loadings a point of zero friction loss would be approached, which is an impossibility. This correlation predicts a minimum at  $\eta = .8$  with a standard deviation of  $\pm 0.4$ . In addition to observing the friction factor (based on mass average velocity and suspension density) decrease when solids were added to the system, McCarthy and Olson also observed that the particle velocities in the turbulent core did not show any significant variation with respect to radial position.

Although equation (25) indicates that the ratio  $\frac{f_s}{f_g}$  decreases as loading ratio increases, the ratio  $f_s'/f_g$  increases<sup>g</sup> with loading ratio (see equation (15)). Thus McCarthy and Olson did not find drag reduction in their experiments. Bureau of Mines - The results of gas-solid suspension study using a closed-loop system were first reported in a paper by Rosenecker, Coates, and Lucas (ref. 29). In this study, the main objective was to determine the effect of particle concentration on the power required to circulate a gas-solid

Particle	Gas	Particle Diameter, $D_p$ (microns)	Inside Tube Diameter $D$ (inches)	Gas Reynolds Number (Re) <sub>g</sub>	Loading Ratio, %	Source
Alumina-Silica Catalyst	Air	10 - 220 (avg. 50)	.69	17,000 - 50,000	0 - 16	Farbar* (ref. 15)
Glass	Air	36,97	.5	10,000-60,000	.7 - 7	Mehta, Smith & Comings* (ref. 16)
Graphite	N <sub>2</sub> , He, CF <sub>4</sub> , CO <sub>2</sub>	1 - 5	.313-.875	2,000 - 400,000	0 - 90	Schluderberg, Whitelaw, & Carlson (ref. 20)
Glass	Air	80,110	3.0	132,000	0 - 4	Peskin & Dwyer (ref. 22)
Glass	Air	80,110	3.0	100,000-150,000	0 - 14	Peskin (ref.24)
Magnesia Oxide	Air	10 -100 (avg. 36)	5.0	130,000 295,000	0 - 3	Soo & Trezek (ref. 26)
Lucite, Glass, Calcite	Air	147-417; (avg.230), 53-74; (avg.64) 0-10; (avg. 3)	1.0	10 <sup>5</sup> - 10 <sup>6</sup>	0 - .6	McCarthy & Olson (ref.28)

\* Some vertical test section data as well as horizontal data.

TABLE II. SUMMARY OF OPERATING CONDITIONS FOR SMALL PARTICLE RESEARCH WITH HORIZONTAL TEST SECTIONS.

suspension. The solids loading was determined by using a two-phase flowmeter designed and built by the Bureau of Mines (ref. 30). The suspensions tested consisted of 18 to 40 micron glass beads in a mixture of 89 percent  $N_2$  and 11 percent  $CO_2$  at 20 psig. Loading ratio was varied between 0 and 2.2 and gas Reynolds numbers ranged between 29,000 and 60,000 in one inch stainless steel tubing. The conclusion reached by the authors was that for an equal weight rate of gas and suspension there is no power difference required in the pumping of a suspension. Since there was no friction factor data obtained in this study it will not be included in Table II.

#### Vertical Test Section Studies.

A review of the small particle research performed in a vertical test section appears on the following pages, and a summary of the operating conditions and the physical properties of gases and solids used in each experiment is presented in Table III.

Depew. - Depew (ref. 31) studied heat and momentum transfer in a  $35\frac{1}{2}$  inch long .710 inch inside diameter vertical test section. He used suspensions of 30- and 200- micron glass beads in air at Reynolds numbers of 13,500 and 27,400. The loading ratio was varied between 0 and 3.5 at the high Reynolds number and between 0 and 7 at the low Reynolds number. Although primarily interested in heat transfer, Depew also studied the effect of solids loading on friction factor in an attempt to verify the analogy between heat and momentum

transfer at low solids concentration.

His curves of total pressure drop all increased with solids loading. At the lower air rate, the slope of the 200-micron suspension was equal to the slope of the 30-micron particle curve at zero loading. At the higher air rate, the pressure drop with the two sizes was the same at a loading ratio of 3. Depew found no minimum at either air rate, but the curves obtained with the smaller size underwent a slight upward curvature.

The friction factor relation used by Depew in analyzing his data

$$\frac{4fL}{g_c D} = \frac{1}{G^2(1 + \eta)RT_{avg}} (P_1^2 - P_2^2) - 2 \ln \frac{P_1 T_2}{P_2 T_1} \quad (26)$$

was derived by an energy balance and does not take into account the static head of the particles. Depew also showed that for the case of small pressure and temperature change through the test section this relation reduce to

$$\frac{4fL}{D} = \frac{2g_c \Delta P_t}{\rho_g v_g^2} \quad (27)$$

at zero loading which is the Fanning equation.

Depew's experimental heat transfer results with the 30 $\mu$  particles showed that the Nusselt number decreased to a minimum (below the pure gas value) and then increased as loading was increased. He found that the Nusselt number remained constant for loading ratios less than 0.5 and then decreased to a minimum which occurred between 1.0 and 1.5. His experiments with 200-micron beads showed that the Nusselt number was independent of solids loading.

His friction factor results, calculated from equation (26), were similar to the heat transfer results in that the curves decreased with loading, however for the friction factor the decrease began immediately with even very low loadings. He also observed that only in one case -  $30\mu$  spheres at  $Re = 13,500$  was there a minimum.

Depew used a Venturi followed by a  $34\frac{1}{2}$  inch long tube prior to his test section to obtain a uniform particle distribution across the test section cross section.

Tien and Quan. - In an attempt to confirm the theoretical analysis of Tien (ref. 32), Tien and Quan (ref. 33) experimentally studied local heat transfer characteristics of glass-and lead-air suspensions in turbulent flow. Although primarily interested in heat transfer, Tien and Quan did make some pressure drop measurements. The study was performed on the apparatus of Depew (ref. 31) with a special brass tube installed for the pressure drop measurements. Glass and lead powders 30- and 200-microns in size were suspended in air at gas Reynolds numbers of 15,000 and 30,000. The pressure drop test section was approximately .710 inches in diameter with some irregularities so that "very accurate results could not be expected."

The pressure drop results were presented on a plot of the ratio of the pressure drop per inch of test section for the suspension to that of air alone taken in a region of the test section where particle acceleration effects were negligible. The plot indicated that the ratio increased

as the loading ratio increased for each particle at both Reynolds numbers, the glass particles giving less pressure drop than the lead powders. The results also indicated that higher Reynolds numbers and larger diameter particles increase the pressure drop. Tien and Quan also found that for all cases considered, fully developed flow was established within 24 inches from a Venturi nozzle outlet.

From their results the authors concluded that heat-transfer characteristics could not be predicted accurately by the values of specific heat and measurements of pressure drop alone. Since, for example, both the 30- and 200-micron glass particles produced similar magnitude of pressure drop but had heat transfer characteristics which differed markedly. The discrepancy was explained on the premise that the pressure drop at the wall only provides an indication of the velocity at the wall, and does not indicate the effect of the particles on the complete velocity profile or the scale of turbulence.

Boothroyd - Perhaps the most significant study to date in the field of momentum transfer associated with suspensions composed of small particles in turbulent flow was performed by Boothroyd (refs. 34, 35). Boothroyd (ref. 34) studied pressure drops associated with the flow of 0-40-micron zinc dust (average size 12-microns) in vertical tubes with 1, 2 and 3 inch inside diameters. The loading ratio varied from 0 to 17 and the experiments were carried out at four gas Reynolds numbers ranging from 35,000 to 100,000.

By using dimensional analysis Boothroyd determined that the significant terms in any experimental study of a particular gas-solid suspension are the loading ratio, the gas Reynolds number and the time scale ratio ( $D^2 \rho_g / D_p^2 \rho_p (Re)_g$ ) Boothroyd presented his results in terms of the ratio of solid to gas friction factor ( $f'_s / f_g$ ) and discovered, among other things, that this ratio was always far less than unity in the 1 in. tube but in the larger pipes was usually higher than one. His results indicated large drag reduction in that the friction pressure drop in all cases was always less than that for a one-phase fluid of the same density.

Another interesting aspect of the experimental data was that (with the exception of the highest value of the time scale ratio - low flow in the 3 inch tube) there was a distinct minimum of the friction factor ratio in the range of loading ratio between 1 and 2.2, indicating that the solids substantially reduce the level of fluid turbulence at relatively low loadings. The results also showed that the friction factor ratio had a smaller dependence on the gas Reynolds number than on either the time scale ratio or the loading ratio.

In a later work, Boothroyd (ref. 35) used tracer techniques to study the turbulence characteristic of the gaseous phase under similar conditions of loading and Reynolds number as the friction factor experiments previously reported. The approach used in this study was similar to established tracer techniques. The sampling device used in this study

is an anemometric isokinetic sampling probe described in ref. 36. The results of the diffusion of the gaseous phase, after normalization were evaluated essentially by the analysis of Taylor (ref. 37) for the spread of fluid above a plane.

The results indicated that within the range of flow variables examined, the intensity of turbulence has a value close to that experienced without solids. In addition, there was no tendency for the intensity to vary with any of the flow parameters in a well defined manner.

For the 2 inch tube it was found that the solids reduced the dimensionless diffusivity of the carrier fluid especially in the loading ratio range between 0 and 2. The author concluded that for the 2 inch pipe the turbulence of the carrier fluid was of a weak nature but was somewhat stronger at higher values of  $\rho_f D^2 / (\text{Re})_g$ . The minimum value of the dimensionless diffusivity was well pronounced and occurred at a loading ratio between 1 and 2 which was comparable to the results previously observed for the friction factor ratio.

The results for the 3 inch tube differed from those for 2 inch tube. The dimensionless diffusivity was now found to be much higher than when solids are absent.

Boothroyd visualized the effect of the solids by attributing to them a "shredding" action in the fluid, superposing a number of small eddies on the flow near the wall. In a large eddy undergoing deformation near the wall, particles not following the fluid motion must produce many

vortices of size comparable with the particle spacing. The generation of any large scale turbulence would under these circumstances be severely inhibited by this stabilizing "shredding" action.

Boothroyd also states in his conclusions that more turbulence may probably be produced at greater distances from the wall than is the case in a solids free gas. He also concludes that the minimum of both friction factor ratio and dimensionless diffusivity observed seem to indicate a change in the form of turbulence as the solids loading is increased.

#### ANALYTICAL STUDIES

A brief description of theoretical analyses deemed to be of particular significance to this study will be presented in the following paragraphs. Although some experimental work may have been performed during the course of some of the studies, the primary focus of the investigations described below is analytical in nature.

Tien. - One of the earliest analytical studies dealing with dilute gas-solid suspensions was performed by Tien (ref. 32). This study concentrated on heat transfer by turbulently flowing fluid-solids mixture in a pipe. In the analysis, which applied only to small particles at loading ratios of less than one, Tien assumed that the solid particles are uniformly distributed throughout the flow field. Based on this assumption and others, Tien was able to solve the turbulent energy equations for both the solid and fluid analytically. His results predicted a linear relationship between the average

Particle	Gas	Particle Diameter, $D_p$ (microns)	Inside Tube Diameter, $D$ (inches)	Gas Reynolds Number, $(Re)_g$	Loading Ratio, $\eta$	Source
Glass	Air	30, 200	.710	13,500 27,400	0 - 7 0 - 3.5	Depew (ref. 31)
Glass, Lead	Air	30, 200	.710	15,000 30,000	0 - 3.5	Tien and Quan (ref. 33)
Zinc dust	Air	0 - 40 (avg. 12)	1, 2, 3,	35,000 - 100,000	0 - 17	Boothroyd (ref. 34)

TABLE III. SUMMARY OF OPERATING CONDITIONS FOR SMALL PARTICLE RESEARCH WITH VERTICAL TEST SECTIONS.

Nusselt number of the suspension and the factor  $\delta$ , where

$$\delta = \frac{(C_p)_p}{(C_p)_g} \quad (28)$$

The relevance of Tien's analysis to the present study lies in the fact that this prediction was shown to be incorrect by the experimental work later performed by Tien and Quan (ref. 33). Their experimental results showed a peculiar feature: the Nusselt number first decreased and then increased as the loading ratio was increased for fixed gas Reynolds number and particle size. This feature was not indicated by Tien's analytical study, and the authors proposed that this decrease in Nusselt number is due to the distortion of the gas flow field by the presence of solid particles that was not accounted for in the theory.

Soo. - In a series of publications, S.L. Soo investigated many phenomena associated with gas solid suspension flow (refs. 38, 39, 40, 41).

In reference (38) Soo studied fully developed turbulent pipe flow of a gas-solid suspension. In this analysis a semi-empirical model similar to the 1/7th velocity for gases, was applied to a gas-solid suspension. The data used in this approach consisted of distributed mass flow of solids in pipe flow at velocities from 50 to 100 feet per second, with glass beads of 100- to 200- micron diameter and solid to air mass ratios of 0.05 to 0.15 (ref. 42). In the range considered by Soo, compressibility of the fluid phase and the effect of gravity on the density distribution of the solid particles

were considered to be negligible. Soo also assumed that since the concentration of solid particles was small, the velocity distribution of the gas stream was not significantly affected by the particles.

Based on these assumptions and the empirical data, Soo proposed a solid particle density distribution which was parabolic in nature. Using this distribution he was then able to relate the radial drift velocity and the particle diffusivity to radial position. The relationship obtained indicates agreement with the assumption that a continuous transport of small, energy rich eddies from the wall toward the center exists, with simultaneous flow of energy-poor fluid back toward the wall, the nonuniform density distribution being sustained by diffusion and drift of particles toward the center of the pipe.

Based on empirical observations and photographic analysis, Soo then assumed a mean velocity distribution of solid particles with form analogous to the  $1/7$ th velocity law of the fluid but with a finite velocity of particles near the wall. Using this relation along with the density relation previously postulated, Soo integrated across the tube cross-section to obtain the total solids flow rate in terms of constants which depend on the particle density and velocity at the wall. By using experimental results for relative mass velocity at various distances along the wall, Soo was able to calculate the constants. The author then related the particle velocity and density at the wall by using the energy

equation for the suspension at the wall. Combining this result with the previously determined constants he obtained relations for particle density and velocity at both the tube wall and the center of the tube in terms of particle and fluid properties readily available.

The results of this analysis indicated that greater slip is to be expected at the wall for larger density and diameter of solid material; the ratio of particle to fluid velocity at the centerline would also be expected to be larger due to the greater inertia of the larger particles. A greater velocity lag at the center of the pipe due to higher loading was also indicated.

In order to develop some basic understanding, via mathematical procedures, of interaction of a gas-solid suspension with a boundary, Soo (ref. 39) treated the case of laminar boundary layer motion of a gas-solid suspension over a flat plate. The reason for studying laminar rather than turbulent motion of the suspension being the same as that for gas studies. In this analysis he considered the case of two-dimensional motion of a gas-solid suspension over a flat plate consisting of an incompressible gas phase with uniform solid concentration of particles of one size in the free stream only. The author set down the boundary layer equations and boundary conditions and applied the momentum-integral method. With the simplification of laminar motion, density and velocity distributions and the magnitude of the boundary layers of the two phases were computed. The results of this

analysis indicated that as the suspension proceeds along the flat plate, the slip velocity of the solid particles decreases, the concentration at the wall increases, the boundary-layer thickness of solid particles increases, as the solid particles develop a normal component of velocity by the viscous drag of the normal component of the fluid viscosity. His analysis showed that the normal component of the particle velocity is smaller than that of the fluid even for the case of equal fluid and particle velocities. The trend of increase in concentration also suggested the possibility of deposition of solid particles at a distance downstream from the leading edge.

Soo also investigated the contribution of the shear layer to particle motion and found that, in spite of the large shear rate at the leading edge, it takes time for the spinning of the particle to take place so as to give rise to substantial lift force. He observed that the lift due to shear motion is negligible in comparison to that due to the induced normal component of fluid velocity. In this analysis, Soo also considered the effect of Brownian motion of particles, since the magnitude of Brownian motion (though quite small) is not negligible at the wall when the fluid velocity goes to zero. Soo found that for very small particles the solution reverts to the case of incompressible flow of a gaseous mixture; the particle density being uniform.

In the same paper (ref. 39), Soo also investigated

the transport properties in a multivelocitv mixture. Using the approximation for the viscosity of a mixture presented by Hirschfelder, Curtiss, and Bird (ref. 43), Soo developed an expression for the viscosity of a gas solid suspension. His relation indicates that the viscosity of the fluid actually decreases as the loading ratio is increased. Confirmation of this result was obtained from the experimental work of Sproull (ref. 44) with dilute suspensions of talc in air.

A text written by Soo (ref. 45) covering momentum, energy, mass, and charge transfer between phases in a multiphase system is the most recent reference of its nature in the field and contains more detailed presentations of the author's analyses.

Sproull. - The pioneering research in the field of drag-reduction with dilute gas-solid suspensions was presented by W.T Sproull (ref. 44). Sproull measured the viscosity of dusty air using a rotating viscometer and found reductions in viscosity of up to 40% compared to clean air. Two types of dusts were studied: one was limestone dust consisting of 40% by weight of particles smaller than 10-microns in diameter; the other was talc dust 99% by weight smaller than  $10 \mu$ . The maximum reduction of 40% was obtained with limestone at a loading ratio of .186. The maximum reduction observed with the smaller talc was 35% at the same loading ratio. Sproull found that the concentration of the dust was the main factor in the effect,

and particle size and bulk density of the dust were relatively unimportant.

Sproull attributed the decreased viscosity to a decrease in the mean free path of the fluid brought about by the dust particles with a "boundary layer" of gas adhering to each particle.

Sproull also mentions that the addition of small amounts of dust to turbulently flowing air in pipes resulted in a decrease of 13% in the pressure difference required to maintain the flow. Although the pipe flow data was never presented, Sproull maintained that this effect is also due to a viscosity decrease of the fluid.

Saffman. - Saffman (ref. 46), in a lengthy correspondence dealing with Sproull's results, rejected the idea of a decrease in fluid viscosity caused by the addition of the dust. Saffman maintained that the effect was a result of the small downward velocity of the particles due to gravity coupled with an outward radial velocity due to centrifugal force. According to Saffman's explanation, as the particles move onwards they carry momentum with them, thus providing an extra mechanism, in addition to the normal effect of viscosity, for the transmission of stress inside the air. The extra stress perturbs the distribution of tangential velocity and alters the torques on the cylindrical viscometers.

Saffman's explanation of pressure loss reduction with dusty gases was that when the dust particles are not too small, their "relaxation time" will be comparable with, or

greater than, the time-scale of the turbulent fluctuations. The dust particles would not then follow the air motion but lag behind the turbulent fluctuation of velocity. The relative velocity of dust and air causes an extra dissipation which extracts energy from the turbulence and presumably damps it, thereby reducing the Reynolds' stresses and the loss of pressure. On the other hand, Saffman continues, with fine dust for which the relaxation time is much less than the turbulent time-scale, the dust follows the air motion closely and its main effect is to increase the effective density of the air, thereby increasing the effective Reynolds number of the flow and the Reynolds' stresses.

Intrigued by the possibilities associated with Sprouil's results (ref. 44), Saffman (ref. 47) investigated the effect of dust particles on the stability of laminar flow of a gas, in order to see how dust may affect the critical Reynolds number for transition from laminar to turbulent flow. The equations describing the motion of a gas carrying small dust particles were given and the equations satisfied by small disturbances of steady laminar flow were derived. The effect of the dust was described by two parameters; the concentration of dust and the relaxation time (a measure of the rate at which the velocity of a dust particle adjusts to changes in the gas velocity and depends upon the size of the individual particles). Saffman showed that if the dust is fine enough for the relaxation time to be small compared with the characteristic time scale associated with the flow, then the

addition of dust causes the critical Reynolds number to be lowered by the factor  $(1 + \eta)^{-1}$  (dust destabilizes the gas flow); whereas, if the dust is coarse so that the relaxation time is relatively large, then the dust has a stabilizing action (dust causes a higher critical Reynolds number).

Saffman also observed that for a relaxation time very much greater than the characteristic time scale, increasing the size of the coarse dust particles reduces the stabilizing effect. He implies that at a given concentration there is a value of relaxation time for which the stabilizing effect is maximized; and for values of relaxation time greater than this particular value it is not correct to say the coarser the dust, the more stable the flow. Saffman explained that the larger the particles at fixed concentration, the fewer particles in the flow; and implies that the decrease in the number of particles more than outweighs the increase in size of the individual particles when the size is relatively large.

Saffman's analysis was based on the following assumptions:

- a) dust particles are uniform in size and shape,
- b) particles occupy little volume compared to gas,
- c) incompressible gas flow,
- d) flow is unidirectional,
- e) negligible velocity of sedimentation.

If the last assumption is not true, then the velocity of particle and gas will not be equal in basic flow and the

number density will not be constant. It is therefore clear that for very large particles or small velocity, Saffman's analysis is of questionable utility. Saffman also neglected the effect of electrostatic forces in his analysis.

Using these assumptions, Saffman also modified the Orr-Sommerfield equations for plane parallel flow of a dusty gas. Michael (ref. 48) extended the analysis of Saffman to consider the case of plane Poiseuille flow. In his paper approximate results were presented for the stability of plane Poiseuille flow of a dusty gas. He assumed that the mass concentration of the dust was small and his results were obtained by making a perturbation of the curve of neutral stability for a clean gas. The results were illustrated for  $\eta = 0.05$  by a set of perturbed neutral stability curves at different values of the time relaxation parameter varying from 0 - 500. His results attempted to qualitatively indicate how the curve of neutral stability is modified by the presence of the dust.

Julian & Dukler. - In a recent paper, Julian and Dukler (ref. 49) attempted to find a correlation for pressure drop caused by a gas-solid suspension by use of an eddy viscosity model. In their work they suggest that for dilute-phase transport the solids make their presence felt primarily by modifying the local turbulence in the gas phase, increasing the turbulent fluctuations, mixing length, and eddy viscosity, and consequently, frictional pressure drop.

Julian and Dukler's analysis was based on a modification of Gill and Scher's expression (ref. 50) for the eddy viscosity

of a pure fluid flowing through a tube. Julian and Dukler modified the Gill and Scher equation to take into account the effect of particles by redefining the von Karman constant for a suspension as,

$$K = k(1 + \eta)^m \quad (29)$$

where the unknown constants  $k$  and  $m$  were determined from previous experimental data. For loading ratios below 12 they found that  $k$  has the value of .36 and  $m$  was equal to .25. This was especially encouraging since at  $\eta = 0$ ,  $K$  reduces to 0.36 which is the accepted value for flow of a particle free gas. Based on the value of  $K$  given by equation (29), the dependence of  $f_s'$  on gas Reynolds number and loading ratio was obtained by Julian (ref. 14). He found  $f_s'$  to be independent of particle diameter and particle density and dependent on  $(Re)_g$  to the  $-.2$  power, which indicates that the effect of gas Reynolds number on the suspension flow is approximately the same as it is for pure gas flow. Pfeffer, Rossetti and Lieblein (ref. 17) fitted Julian's results to the equation

$$f_s' = .046 (Re)_g^{-0.2} (1 + \eta)^{0.3} \quad (30)$$

so that after dividing by equation (19)

$$\frac{f_s'}{f_g} = (1 + \eta)^{0.3} \quad (31)$$

It should be pointed out that Julian and Dukler's analysis is strongly dependent upon the results of the experimental investigations analyzed. The major portion of these experimental studies involved large particles (particle diameter greater than 100-microns); and, of the studies

using small particles, only a very small portion presented results in the loading ratio region below 2.

Pfeffer, Rossetti and Lieblein - In an effort to determine the feasibility of using a suspension as the working fluid in a gas Brayton cycle, Pfeffer, Rossetti and Lieblein (ref. 17) performed an analysis and correlation of heat-transfer coefficient and friction factor data for dilute gas-solid suspensions. After an analysis of existing heat transfer data, the authors were able to obtain a correlation for the heat transfer coefficient ratio of a suspension to a gas. Due to the fact that the existing friction factor data was sparse and scattered the authors did not attempt to obtain a correlation based on the data, but instead turned to the Reynolds analogy.

The Reynolds analogy can be applied to gas-particle suspensions if the suspension is assumed to behave as a homogeneous fluid and if an accurate heat transfer coefficient of suspensions is available. By applying the Reynolds analogy to the gas and solid phases separately, a relation between  $f_s'/f_g$  and the heat transfer coefficient ratio  $h_s/h_g$  was obtained

$$\frac{f_s'}{f_g} = 1 + \frac{1}{\delta} \left( \frac{h_s}{h_g} - 1 \right) \quad (32)$$

Using the previously obtained relation of  $\frac{h_s}{h_g}$  in equation (32) the authors obtained

$$\frac{f_s'}{f_g} = 1 + 4.0 (Re_g)^{-0.32} \eta \quad (33)$$

In the region of Reynolds number greater than 25,000 but less than 100,000 equation (31) and equation (33) were found to be in good agreement with each other and with certain of the data for large particle size for  $2 \leq \eta \leq 10$ . It should be pointed out, however, that equation (33) was obtained from the heat transfer relation Pfeffer, Rossetti, and Lieblein deduced from experimental data for loading ratios greater than 2 neglecting a particle size effect.

#### DRAG REDUCTION WITH LIQUIDS

Drag reduction with liquids in turbulent flow is a well established phenomena. It has been found to occur in solutions, gels, and suspensions. Due to its spectacular effectiveness, drag reduction obtained by the addition of soluble polymer to Newtonian liquids has received the most study (refs. 51, 52, 53, 54, 55, etc.) The variables most affecting the level of drag reduction for a given polymer solution are the bulk mean velocity, polymer concentration and pipe diameter. Polymer solution drag reduction seems to occur from one of two effects:

- 1) the extension of laminar behavior to abnormally high Reynolds numbers,
- 2) the reduction of friction factor in fully developed turbulence.

Savins (ref. 51) and Astarita (ref. 55) suggested that drag reduction by polymer solutions is caused by viscoelasticity. Their conception was of a reduction of turbulent energy dissipation because of the conservative nature of viscoelastic

materials at high shear strain fluctuation frequencies. Thus, if the dissipation frequencies in the turbulence were greater than the reciprocal of the solution relaxation time Astarita postulated that drag reduction would occur.

A second type of drag reduction has been observed to occur with soap solutions (refs. 56, 51, 58). Little is apparently known regarding the mechanism of soap solution drag reduction, and its utility would appear to be limited to situations where polymers may not be used as additives.

The third type of liquid drag reduction reported in the literature appears to be most analagous to gas-solid studies This is drag reduction associated with addition of fine particles to the liquid to form a dilute suspension (refs. 59, 60). The mechanism of drag reduction by suspended additives is not well understood, although it has been attributed to the damping effect of the solid particles on the turbulent fluctuations thereby decreasing radial momentum transport (refs. 59, 60, 61). A recent survey of drag reduction with liquids has been prepared by Patterson, Zakin and Rodriguez (ref. 62) and is the most comprehensive survey of this field presented to date.

### III. DESCRIPTION OF APPARATUS, MATERIALS, AND EXPERIMENTAL PROCEDURE

The apparatus employed in this study was based on the use of a circulating compressor capable of pumping both gas and solids through a closed experimental loop. Pressure drops across both horizontal and vertical test sections were measured by means of micromanometers. Velocity and turbulence measurements were made by applying some of the most recent advances in anemometry to the gas-solids system. Particle concentration was determined with a specially designed mass flow meter employing strain gages. In order to properly calibrate the mass flow meter, an open loop system was also designed and employed. Five different sizes of glass beads were used in the experiments in order to determine the effect of particle diameter on frictional pressure loss. The details concerning apparatus and materials employed during the study as well as the experimental procedure will be presented in the following paragraphs.

#### Apparatus

The apparatus to be described in detail in this section includes the gas-solids circulator, the closed experimental loop, the anemometry and the mass flow meter as well as the open calibration loop.

Gas-solids circulator. - When both gas and solids are continuously recirculated without removal of the solids from the gas stream the flow may be classified as a closed loop operation. In order to achieve such as closed loop recirculation, however, a blower or compressor must be available which can pump both solids and gas together without damage to its internal parts

or contamination of the suspension. Such a circulator was designed and built by the Franklin Institute and donated to the current study by the Bureau of Mines at Morgantown, West Virginia.

The circulator components are constructed of Armco 17-4 PH stainless steel. Most of the parts were first rough machined, heat-treated to the 1050H condition and then finish machined. No castings or forgings were required. Balancing of the shaft assembly was done by the International Research and Development Company. Clearance on the face of the rotor was set at 0.010 to 0.015 inches depending on combined differential expansion and on pressure deflection. Figure 1 is a photograph of the open faced impeller and the housing scroll in which the rotor operates. The flow area from the point of the impeller nose cone to the leading edge of the impeller blades is constant. The inlet angle of the blading was designed to minimize entrance shock losses and consequent particle attrition rate. Figure 2 shows the rotor installed with nose cone in place. Figure 3 is an exploded view of the major components of a circulator assembly. The circulator assembly is shown in figure 4.

The circulator was driven by a 15 horsepower variable speed induction motor powered by a 25 horsepower motor coupled with a variable frequency generator shown in figure 5. The motor-generator was built by U.S. Electric Motors and provides stepless speed variations in two ranges of from 1600 to 6600 and from 2640 to 13,200 rpm. During the course of this study shaft speeds were determined by use of a General Radio Company

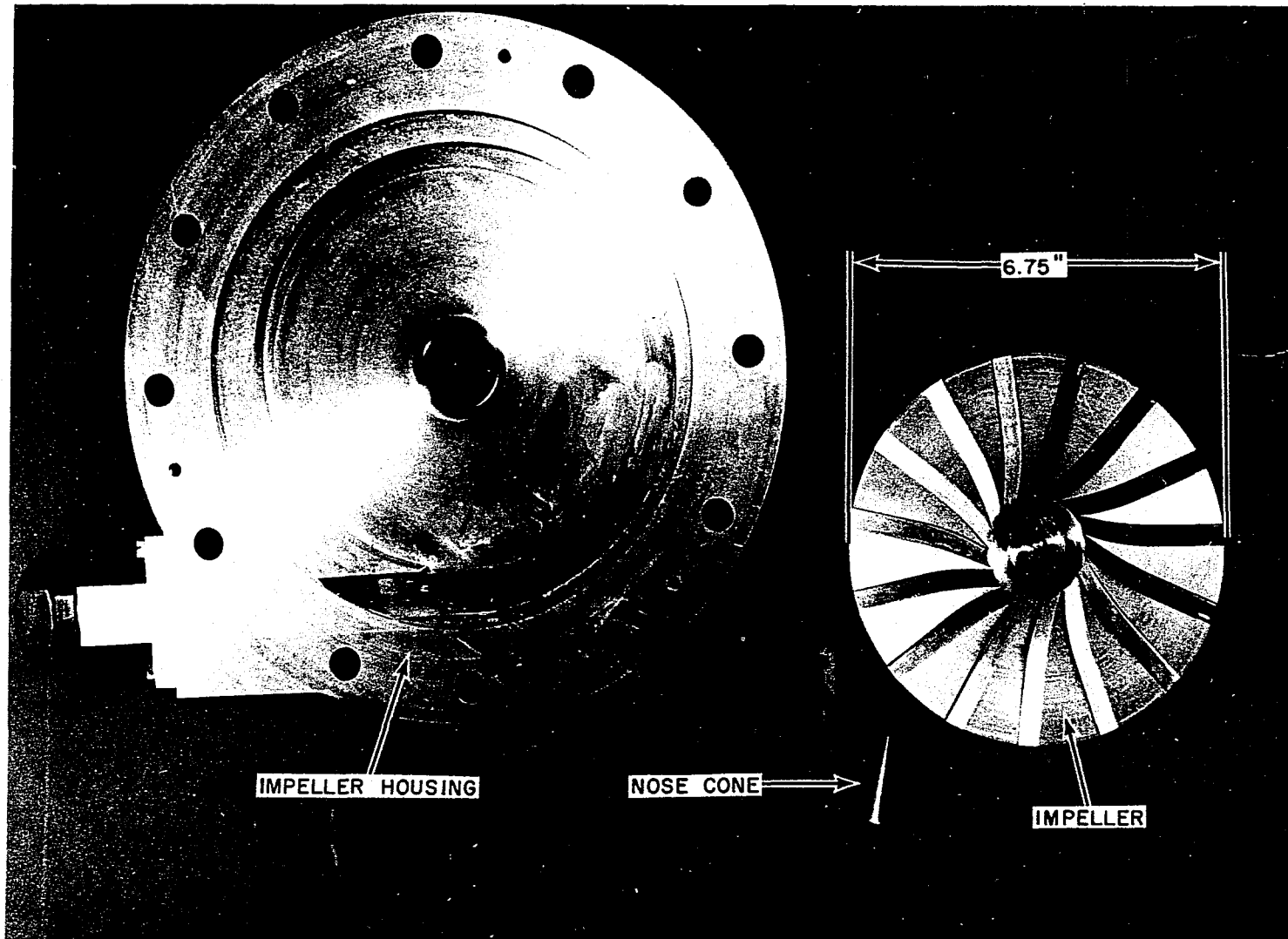


Fig. 1 - VIEW OF CENTRIFUGAL IMPELLER AND HOUSING VOLUTE

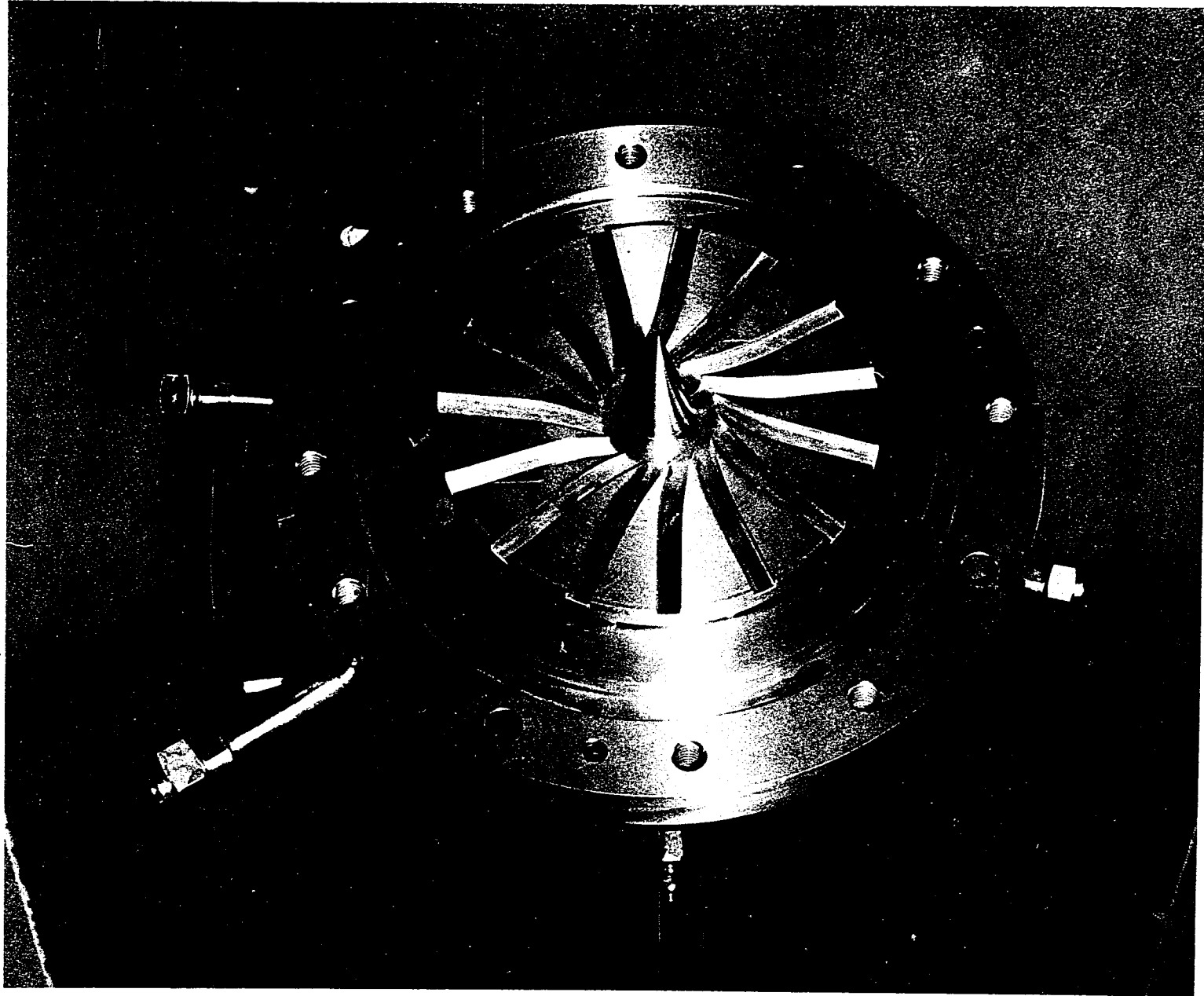


Fig. 2 - IMPELLER AND NOSE CONE ASSEMBLY

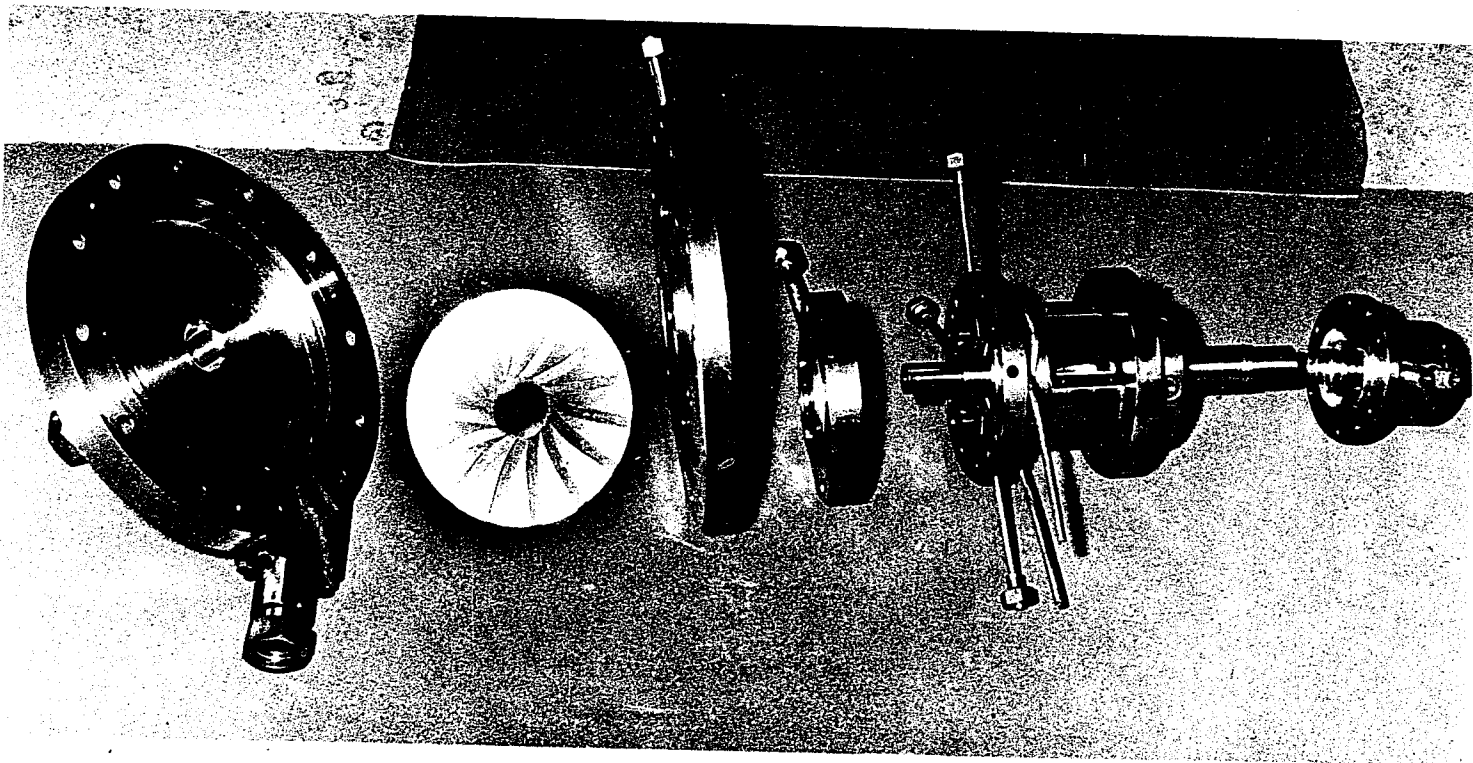


Fig. 3 - EXPLODED VIEW OF CIRCULATOR ASSEMBLY.

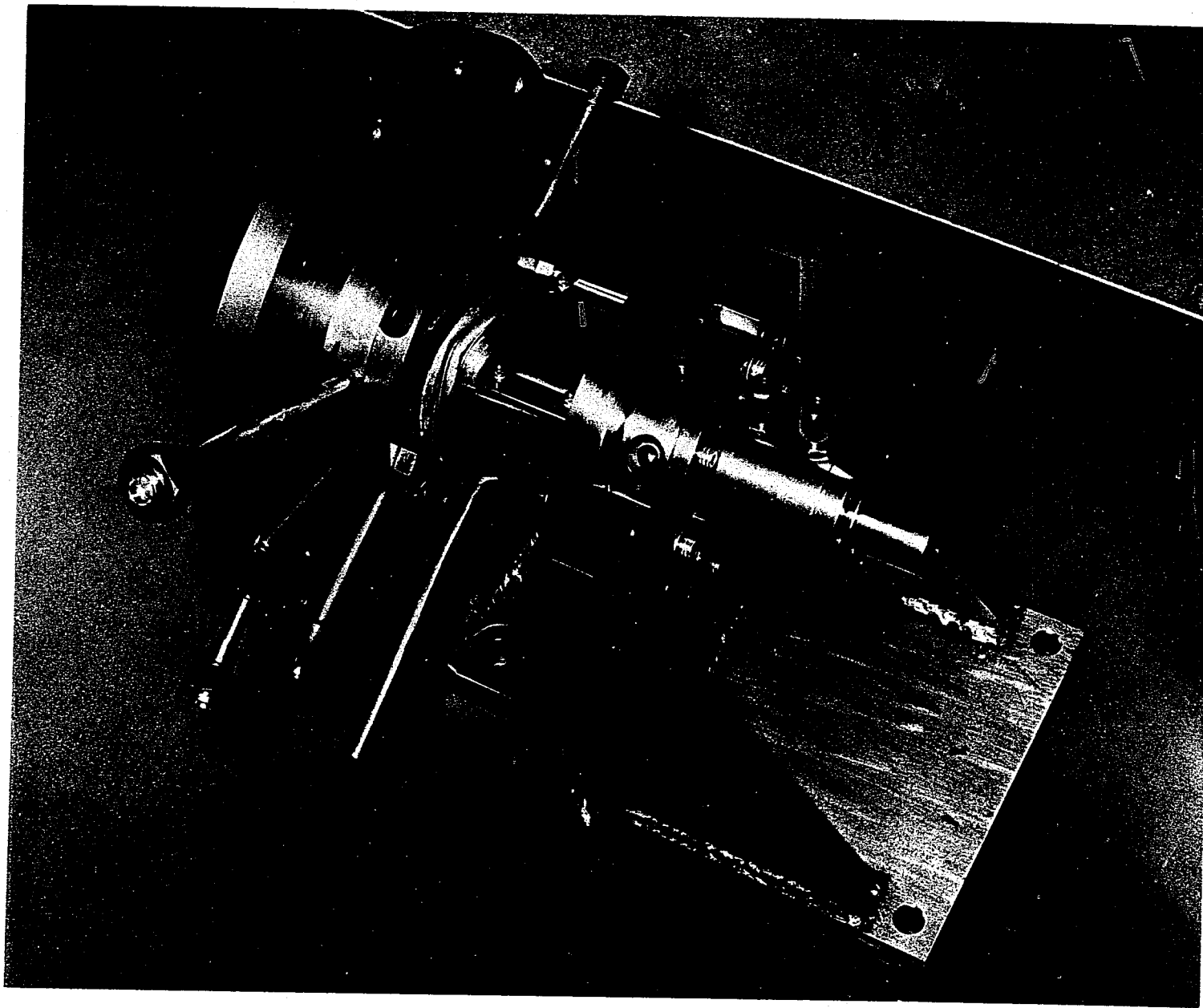


Fig. 4 - PRELIMINARY ASSEMBLY OF CIRCULATOR.

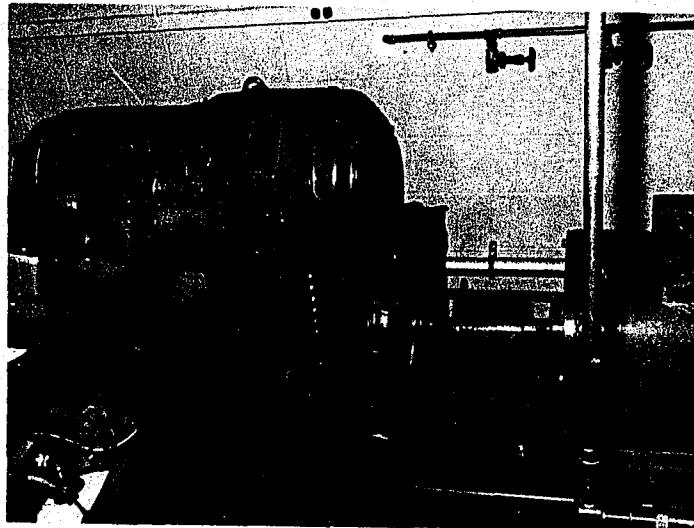


Figure 5a.: 25 hp Motor-Generator.

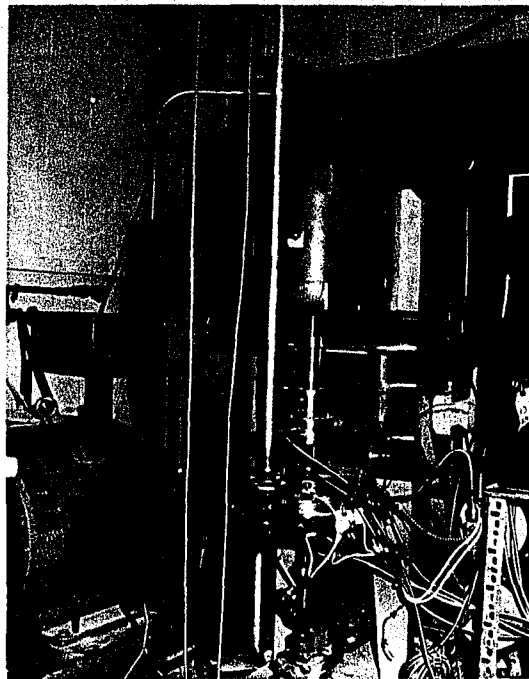


Figure 5b.: Slave motor coupled to  
gas-solids circulator.

type 1531-A Strobotac electronic stroboscope focused on the flexible coupling connecting the circulator and the 15 hp slave motor.

Closed experimental loop. - The closed experimental loop employed in this study is primarily constructed of 1" O.D. type 304 seamless stainless steel tubing with a 1/16" wall thickness but the loop also contains four pyrex glass sections with a one inch inside diameter. The metal to metal joints used in the construction of the loop consisted either of using flanges or one inch Swagelok unions. Joining of two pieces of metal tubing by flanging involved facing off the ends of the tubes and using flanges fitted with 1" inside diameter bushings soldered on each piece so that the tube ends met flush within the outer bushing. Either method provides a leakproof metal-metal joint with no protrusions into the fluid stream and essentially no disturbance of flow patterns.

The pyrex-metal joints were formed by using standard glass-metal flanges and teflon gaskets with a one inch inside diameter. The pyrex sections contain a slightly outward tapered inlet and exit portion into which the stainless steel tubing was fitted. The inside diameter of the metal tubing was tapered out at a very slight angle by fine machining so that the wall thickness at the end of the tubing approximated a razor's edge. This type of coupling resulted in a leakproof joint with a minimum disturbance of the flow pattern and essentially no step protruding into the fluid stream.

A schematic diagram of the closed loop used for this study is shown in figure 6. As can be seen from the figure, the loop is approximately rectangular in shape with two horizontal and two vertical sections. In order to promote uniform particle distribution and prevent particle accumulation, sharp  $90^\circ$  elbows were installed before every section of the loop where measurements were taken. These elbows were made from 2" diameter stainless steel bar stock and were milled in such a manner as to allow the metal tubing to seat in the elbow and maintain the inside diameter of the tubing through the elbow with no steps or spaces where the particles could accumulate.

Since flow is in the counter clockwise direction, figure 6 indicates that the first portion of the loop encountered by the fluid leaving the circulator is vertical with flow in the upward direction. This leg of the loop, which is preceded by a sharp  $90^\circ$  elbow is 97" long and contains a 36" pyrex test section 57 inches from the elbow. This pyrex test section has two glass pressure taps 30 inches apart and 3 inches from each end. These taps were filled in with epoxy resin leaving a smooth  $1/16$  inch diameter hole for pressure measurements and also prevented any ripples, steps or irregularities in the glass tube at the tap junctions.

After the upward vertical leg of the loop is another sharp  $90^\circ$  elbow followed by a 12 foot long horizontal portion. This horizontal part is composed of an  $82\frac{1}{2}$ " metal calming section followed by a 12" pyrex viewing section and a 44" metal test section. The 44" section contains two pressure taps 40 inches

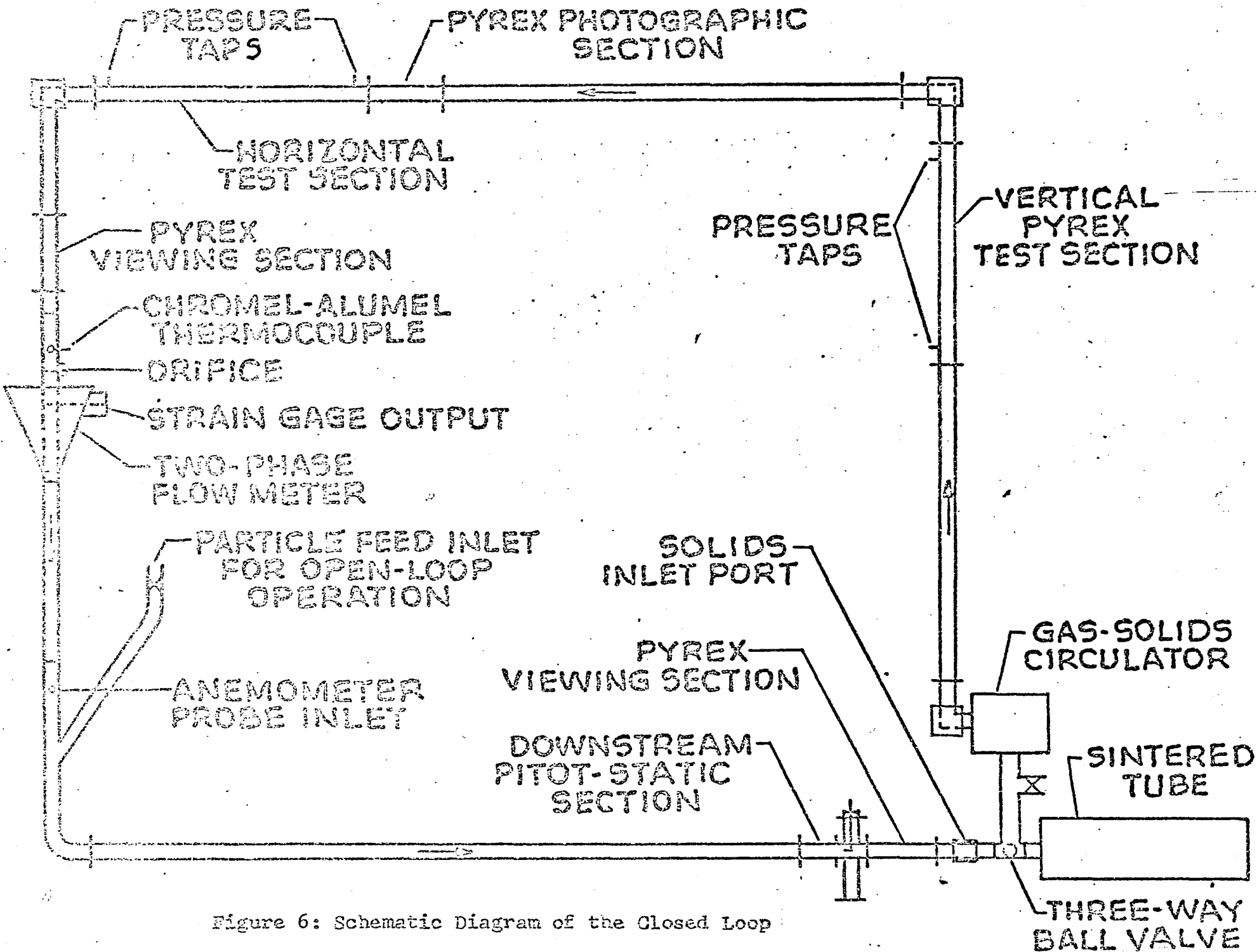


Figure 6: Schematic Diagram of the Closed Loop

apart two inches from each end of the section. These taps consist of 1/16" outside diameter spring steel tubing with a .020" hole which was soldered into the test section. A 20/1000 drill was used to bore holes through the test section where the taps are located. The test section was reamed and lightly polished so that no burrs or irregularities were present in the tubing at these tap holes.

The downward vertical portion of the loop follows another sharp 90° elbow connected to the end of the upper horizontal leg. This second vertical part of the loop contains an orifice, mass flow meter, and anemometer probe inlet. It is 113 inches long and, following the elbow, consists of an 18½" metal section, a 12" pyrex viewing section, and 12½" of metal tubing prior to a sharp edged orifice. Following the orifice is the mass flow meter, 30 inches of metal tubing and the anemometer probe inlet. A particle inlet port used in open loop operation is 5" past the anemometer inlet and 15½" above the long radius elbow connecting the downward vertical to the lower horizontal portion of the loop.

The lower horizontal leg of the loop is 13 feet long and terminates 14½ inches below the circulator. It is comprised of 121½" of metal tubing followed by a 10" metal section, a 12" pyrex viewing section and a 12-3/4" long metal section leading to a three way ball valve. The 10" metal section houses the downstream testing section of the loop. This section contains an impact tube made of 1/16" O.D. spring steel tubing and a piezometer ring composed of eight static

pressure taps spaced  $45^{\circ}$  apart around the tubing before the impact tube. The static pressure taps were constructed in the same manner as the metal pressure taps previously described. This pitot-static arrangement was found to give the same results for pure air runs as a commercially purchased pitot tube with a known coefficient of unity. The pitot tube assembly was used for calibrating the anemometer probes as well as for taking velocity traverses with pure gas as the circulating fluid. The closed loop particle inlet is located  $3\text{-}3/4$ " from the end of the pyrex viewing section. This inlet is simply a metal plug which has been carefully machined so that the bottom of the plug has the same radius of curvature as the inside diameter of the tubing. There is, therefore, no step or disturbance in the flow stream when the plug is in place.

At the end of the bottom horizontal portion on the loop there is a three way ball valve with a tee port and a one inch port size. The ball valve was used in two ways. While circulating the suspension, the ball was turned so that the valve served as a sharp  $90^{\circ}$  elbow and the suspension flowed through the compressor thus permitting closed loop operation. When it was desired to remove the solids from the loop, the valve was turned to allow the suspension to flow straight through and prevent it from going through the circulator. A one inch ball valve located between the three way valve and the compressor was opened allowing room air to be sucked through the compressor and causing the suspension to be blown

into a sintered stainless steel tube attached to the three-way valve. The blown steel tube acted as a filter and allowed the air to pass through but trapped the particles.

Some of the auxiliary equipment associated with the closed loop circulation of the suspension are the pressure measuring instruments and probe positioning equipment. All of the test section pressure drop measurements for suspension flow were made using an R. Feuss model 134b micromanometer. These micromanometers can be read down to .002" of water and as high as 6.25 inches of water by use of five different scales corresponding to five positions on a fixed graduated arc. Static pressure measurements were made at the first pressure taps on each test section by use of standard U-tube manometers. These manometers read up to 10 inches of Hg with an accuracy of .1 inch. Orifice pressure drops were also measured with a U-tube manometer with a 31" range and an accuracy of .1" of fluid. The fluid in this manometer was a Dwyer gage fluid with a specific gravity of 1.75.

Manual traverses were used to position both the anemometer probe and the downstream impact tube. The traverses were manufactured by United Sensor and Control Corp. and have a 6" scale allowing a positioning accuracy of .01 inches. The units also have a protractor and rotary vernier so that directional accuracy of within  $1^{\circ}$  can be obtained.

The complete closed-loop system was periodically checked for leaks at all stages during construction and experimentation by soap bubble testing and by use of a commercial leak

detection lacquer. No leaks were found to develop after final construction of the loop was completed.

Anemometry. - In a closed loop system for recirculating gas-solid suspensions, one of the greatest difficulties lies in obtaining air flow rate measurements. Rotameters or wet test meters cannot be used due to the adverse effects of the solids on instruments. For larger diameter pipes pitot tubes with large openings have been used to obtain air velocities. For use in a 1" tube the pitot tube must be very small so as to create as little flow disturbance as possible. In this study, however, it was found that the use of a small pitot tube is not practical for gas-solids flow since this opening will continuously become blocked with particles so that measurements cannot be taken. The use of an orifice or a venturi to determine the volumetric flow rate of the fluid is also questionable, since it is not known how the solids effect the orifice coefficient.

Due to its delicate nature, it is difficult to use a hot wire anemometer probe even to obtain air velocities with pure air flow. With solids suspended in the flow it is impossible to use standard hot wire probes for these measurements. During the course of this study hot wire and film probes of various configurations were tested and were found to break before any measurements could be made.

Recent advances in electronics have made possible the development of solid state anemometry units with which a thermistor probe may be used. One such thermistor probe developed by the DISA S&B Corp. was field tested in the closed

loop for  $\frac{1}{2}$  hour of continuous operation under conditions of heavy loading using large diameter particles. At the end of this time it was found that the probe had not changed calibration. A close-up of this type of probe, which was used to measure fluid velocity, velocity profiles and relative percent turbulence during this study, is shown in figure 7. The probe is L-shaped and has a glass coated thermistor bead suspended at the tip. The L-shape of the probe allows velocity measurements to be taken without interference from the support rod. The thick glass coating prevents the particles from damaging the thermistor or interfering with the measurement. The disadvantage of using this type of thermistor probe is that it is more sensitive to fluid temperature and therefore requires a more extensive initial calibration than standard hot wire probes.

The anemometer used in conjunction with the thermistor probe was the 55D00 Universal Anemometer manufactured by the DISA S&B Corp. This anemometer consists of four components: an Anemometer Unit, an Auxiliary Unit, a Digital DC Voltmeter, and an RMS Voltmeter. The Anemometer Unit is a multipurpose precision instrument designed primarily for measurement of the instantaneous mass flow of gases and liquids, using either a hot-wire, a hot-film or a thermistor probe. The unit was operated as a constant-temperature anemometer but is switchable for constant-current operation.

The Auxiliary Unit is intended for use in conjunction with the Anemometer Unit. It features a high-stability, high-

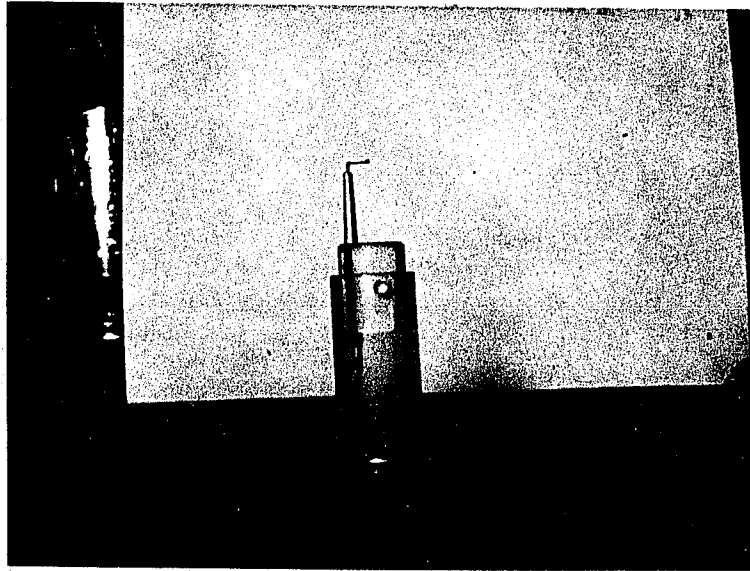


Figure 7: Close up of Thermistor Probe.

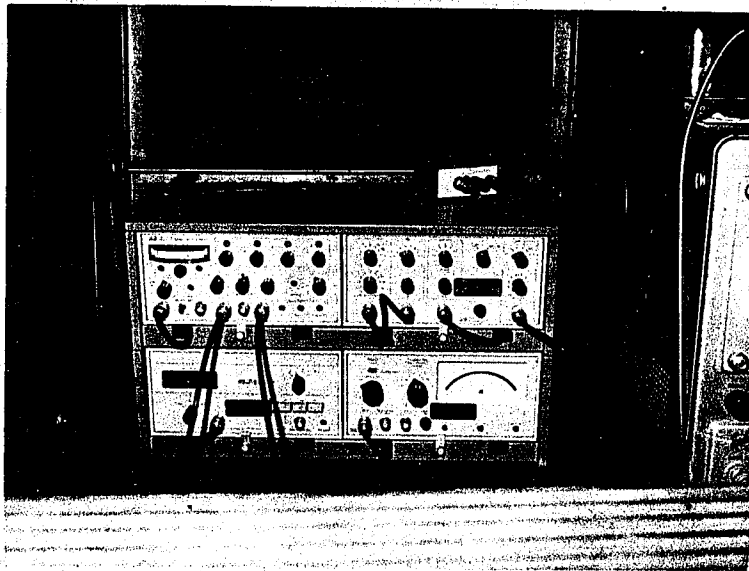


Figure 8: Front panels of four Anemometer Modules.

frequency DC amplifier with high-pass and low-pass filters, zero adjustment, and a square-wave generator. The instrument is entirely solid-state, using state-of-the-art silicon transistors and integrated circuits.

The all-transistor RMS Voltmeter is designed for measurement of the actual root-mean-square value of AC voltages (RMS voltages) between  $300 \mu V$  and 300V inside the frequency range of 1 Hz to 400kHz. These voltages may be sinusoidal or non-sinusoidal and have crest factors as high as 5 at full scale deflection and 15 at one-third of full-scale deflection. The ability of the voltmeter to accept waveforms having such high crest factors ensures a high degree of accuracy, even in measurement of nonsinusoidal wave forms such as noise and pulse trains. The Voltmeter also permits varying the integrator time constant for best possible response time, depending on the wave form and frequency of the voltage under measurement. The time constant varies from 0.1 to 30 sec.

The Digital Voltmeter is another fully transistorized instrument. It incorporates a self-balancing servo system and provides digital readout of DC voltages from 1 millivolt up to 100 volts. A damping circuit with stepwise variable time constant (1, 3, and 10 secs.) permits measurement inside the limits determined by the time constant, of the arithmetic mean of the signal from an anemometer whose probe is exposed to a turbulent flow. A photograph of the front panels of these four modules is shown in figure 8.

Mass-flow meter. - In order to determine the average solids concentration in the suspension a two phase flow meter designed, built and developed by the Bureau of Mines at Morgantown, West Virginia was employed. A cross section of this flow meter is shown in figure 9. As received from the Bureau of Mines, the meter had a filler which did not possess smooth surfaces and had a tendency to deteriorate when attacked by the suspension. For the purposes of this study a special casting was prepared and a silastic rubber was poured into the meter. When cured this rubber provided a filler which did not sag, was smooth and was impervious to suspension flow.

The metering element is a circular target that is inserted in the two phase flow stream. The target is attached to a rod at the end of a cantilevered metal strip to which are affixed metal-foil strain gages. Elimination of temperature effects upon the meter performance is achieved by having the strain gages mounted in tension and compression, one on each side of the metal strip. The metal-foil strain gages sense the deflection of the flexible metal strip caused by the solids and gas acting on the target.

The gages form an active compensated half-bridge and were used in conjunction with two fixed resistors, all comprising a complete Wheatstone bridge. Because of the large rapid fluctuation in the bridge-output signal, a long-time constant resistor-capacitor filter was incorporated. The filter was used primarily to obtain long-term average flow readings, with a time constant of about 1.4 seconds. The filter also

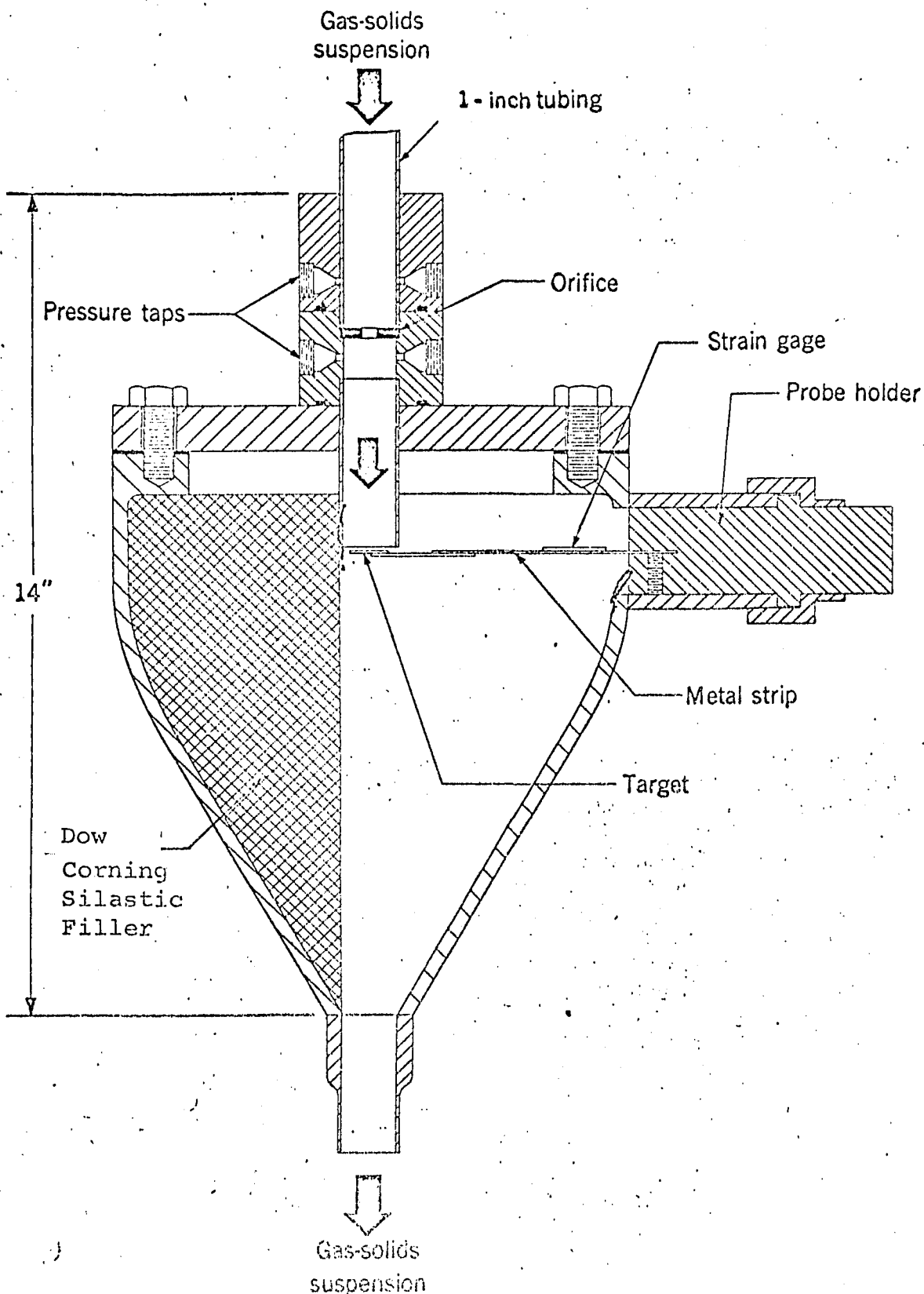


FIGURE 9 Two Phase Flowmeter

removed electrical "ringing" at the natural resonant frequency of the flexible metal strip. A third resistor section was included in the bridge for balancing the fixed resistors and a potentiometer performed this function.

A Mark 280 Brush two channel recorder with preamplifier was used to record the output from the two-phase flow meter as well as the output of a chromel-alumel thermocouple. The thermocouple was used to measure the fluid temperature at a point in the downward vertical portion of the loop a few inches before the two phase flow meter. The recording system used in this study was able to measure an output as small as one micro-volt and was capable of step variation in sensitivity.

In order to obtain meaningful results with the two phase flow meter, however, it must be calibrated in an open loop system under various conditions of solids loading and gas flow rate.

Open Calibration Loop. - A schematic diagram of the open loop system used for the calibration of the two phase flow meter is shown in figure 10. As can be seen from the figure the major difference between the open and closed system are in the need for both a continuous particle feeding and collection system. A continuous and fairly steady feeding of the particles into the air stream was accomplished by means of a feeder-air lock combination installed at the top of the feeding "Y" shown in the figure. The feeder is a BIF helix type volumetric dry

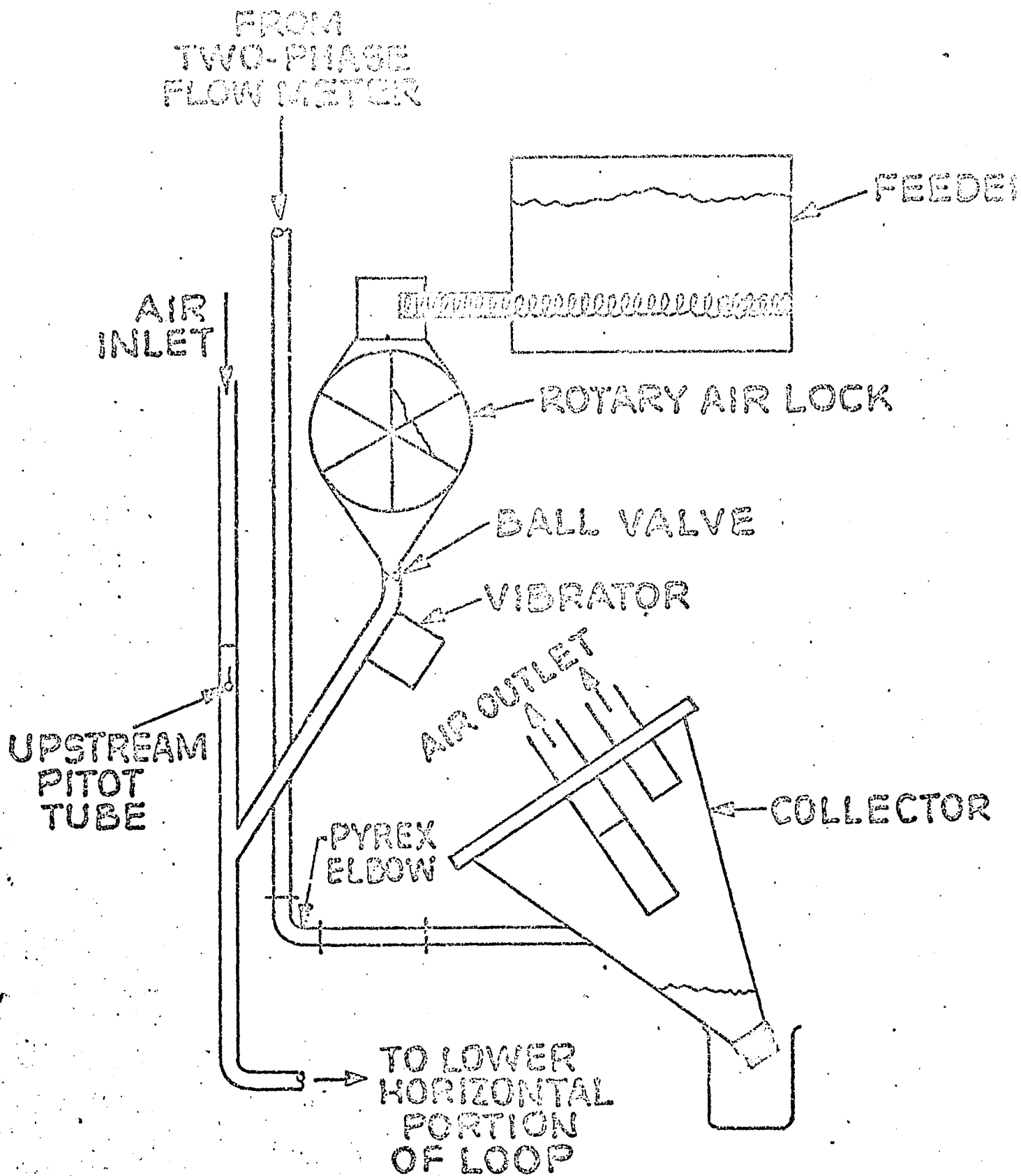


Figure 10: Schematic Diagram of the Open Loop

feeder with interchangeable helices. Solid particles placed in the feeder hopper flow by gravity into a chain-driven rotating horizontal helical feed screw. As the helix rotates, it moves the material along the base of the hopper and out through the discharge spout. From the discharge spout the material falls into a Prater rotary air lock with six individual feeding compartments. This combination feeder-airlock permits continuous feeding without permitting additional air to be introduced to the system.

The design of the collection system for the open-loop operation presented several difficulties. Since the study was carried out in an enclosed area, no dust could be permitted to contaminate the air. Since no cyclone can be designed (within the space limitations of the study) that is 100% efficient, the use of a cyclone would represent a potential health hazard. The use of a sintered tube for solids collection and weighing although capable of nearly total efficiency was also found to be impractical for this system. It was found that after a short period of time the sintered tube became clogged thus causing a large pressure drop across the tube and a decrease in the fluid flow rate through the loop. It was therefore difficult to make meaningful measurements.

A cross-section of the collection system finally evolved is shown in figure 11. It can be seen that the collector represents a compromise between a cyclone and a sintered

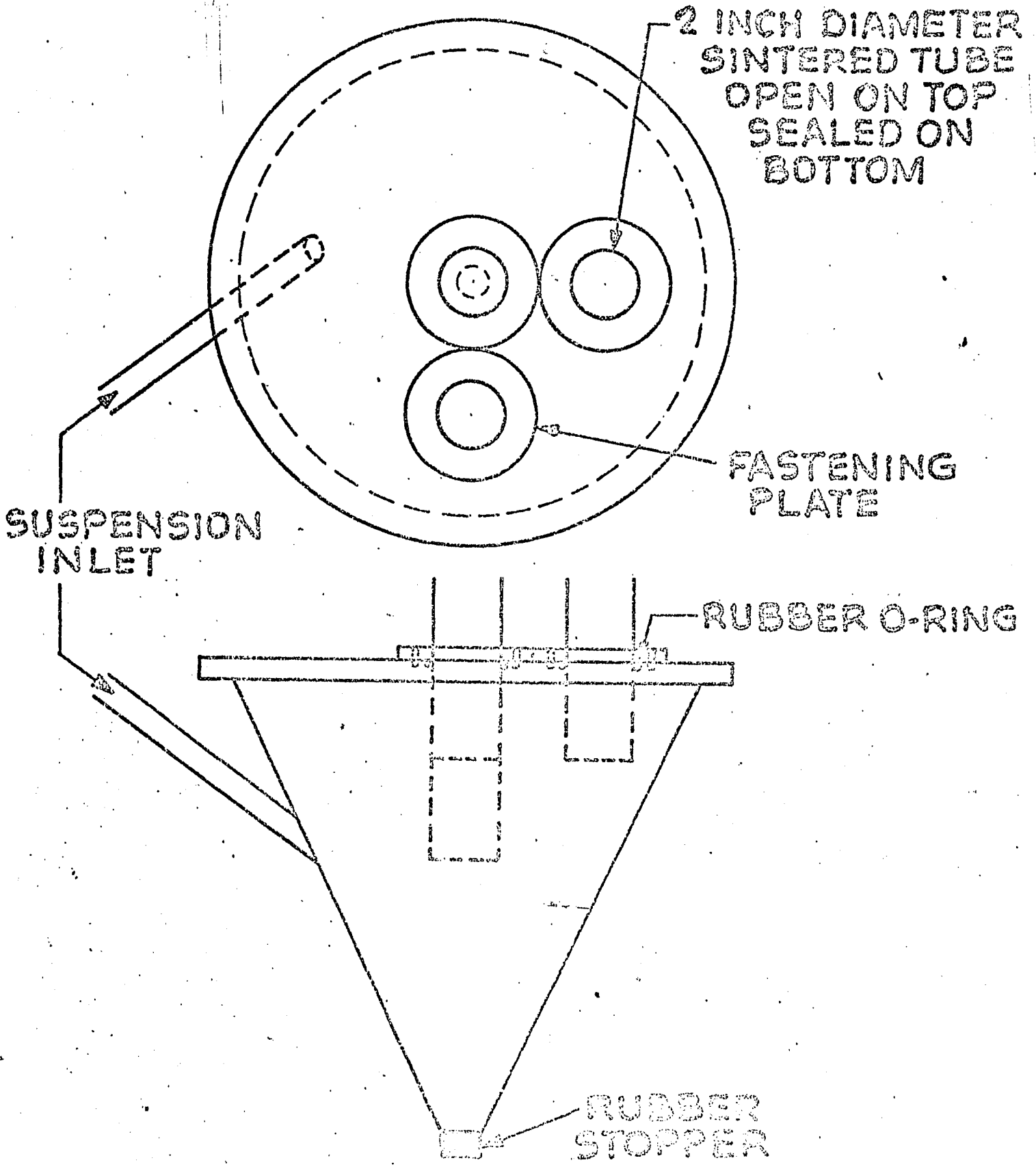


Figure 11: Particle Collector

tube. In this design the collector is essentially a cyclone with sintered tubes providing the air outlet. The suspension enters the collector at a downward angle tangential to the side of the cone. The decrease in air velocity experienced upon expansion into the cyclone caused most of the solids to drop to the bottom of the cone. The small portion of solids still entrained by the air are deposited on the sintered tubes. This design prevents solids contamination of the air as well as extensive clogging of the sintered tubes. The two-phase flow meter was calibrated by weighing the particles collected per unit time during open loop operations. The air flow rate was determined using a commercial pitot tube in the air inlet section of the loop. This commercially purchased pitot tube was checked while in this upstream location during pure air open loop operation by means of the pitot-static testing section previously described. Velocities obtained from each instrument were found to be essentially the same for the Reynolds number range in this study.

#### Materials

The materials used in this study consisted of five different size distributions of Scotchlite glass beads purchased from the Minnesota Mining and Manufacturing Company. Atomized aluminum particles with a mean diameter of approximately five microns were also experimented with during the course of this study. Unfortunately, however, it was found that these aluminum particles tended to

agglomerate as well as thickly coat the tubing walls. These particles could not, therefore, be studied with any degree of reproducibility of measurement.

The five different types of glass beads studied are listed in Table IV and ranged in size from average particle diameters of 10 to 59 microns. Microphotographs of these particles both before and after being circulated are shown in figures 12-16 and indicate no change in the sphericity of the particles. The size distribution of these particles both before and after circulation in the closed loop system were obtained by use of a Coulter counter. These distributions will be presented in a later section of this dissertation.

#### Experimental Procedures

Three separate experimental procedures were adhered to during the course of this study. These correspond to the situation of pure air runs, open loop calibrations, and closed loop experiments respectively and are described in the following sections.

Pure air runs. - The pure air runs were primarily performed with the closed loop configuration, but some runs were also made with the open-loop system. These runs were carried out in order to calibrate and check the entire system for the condition of zero loading ratio. During these runs pressure drops across both horizontal and vertical test sections were taken and pure air friction factors for each of these sections were calculated. The thermistor anemometer probe was also

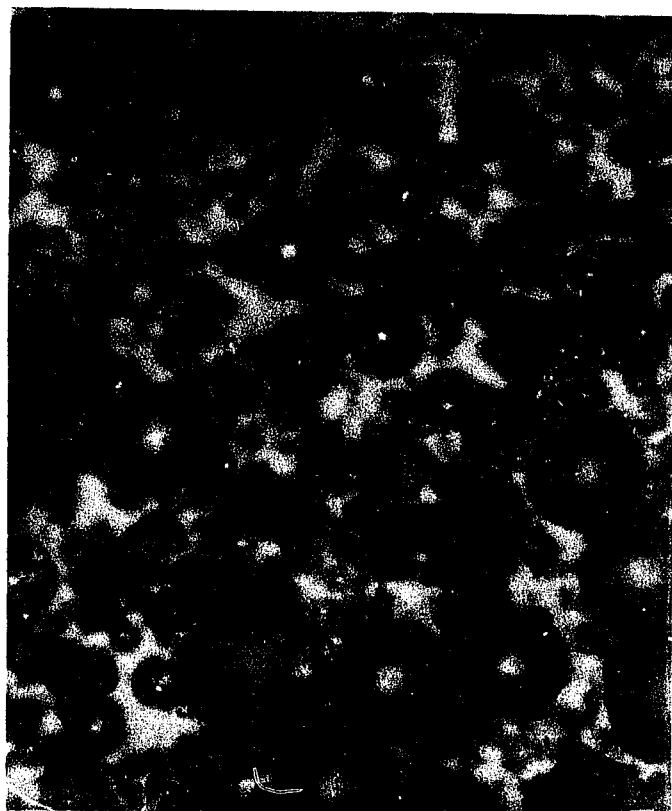
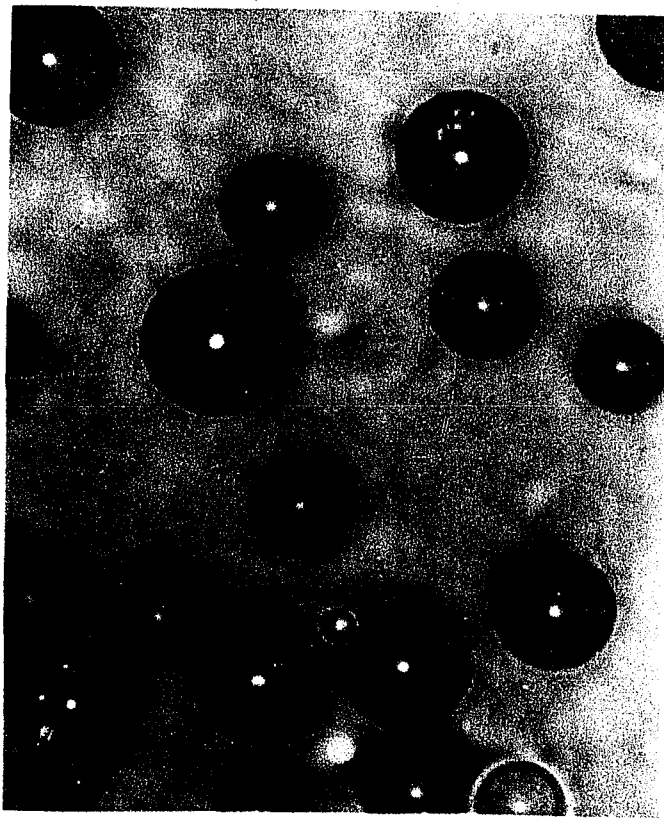
Table IV. Particle Sizes

Descriptive Title	Actual Nominal Particle size*
50	59
30	34
#279	25
#981	20
#980	10

\*Determined by Coulter Counter Analysis

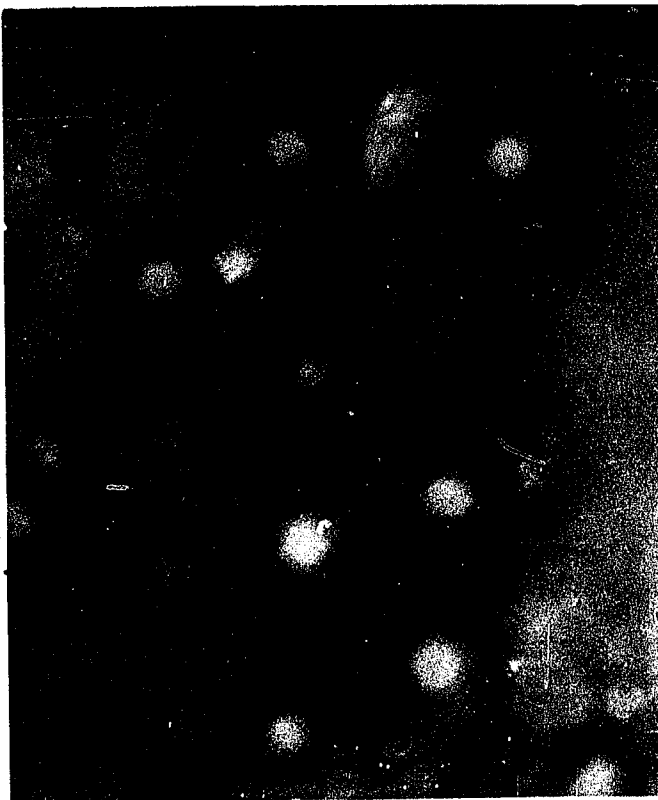
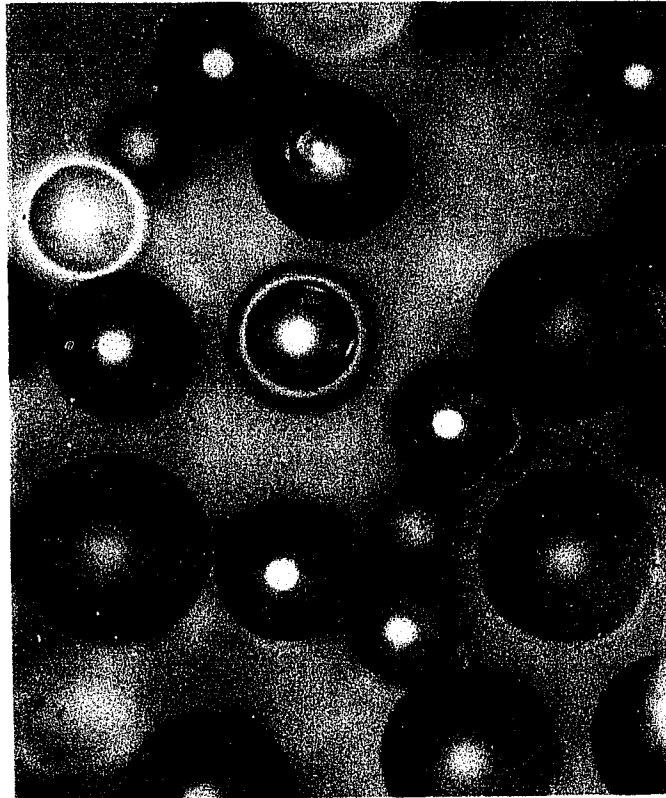
Figure 12: Photographs of 50 $\mu$  Glass Beads.

a) Before recirculation -  
300 x magnification.



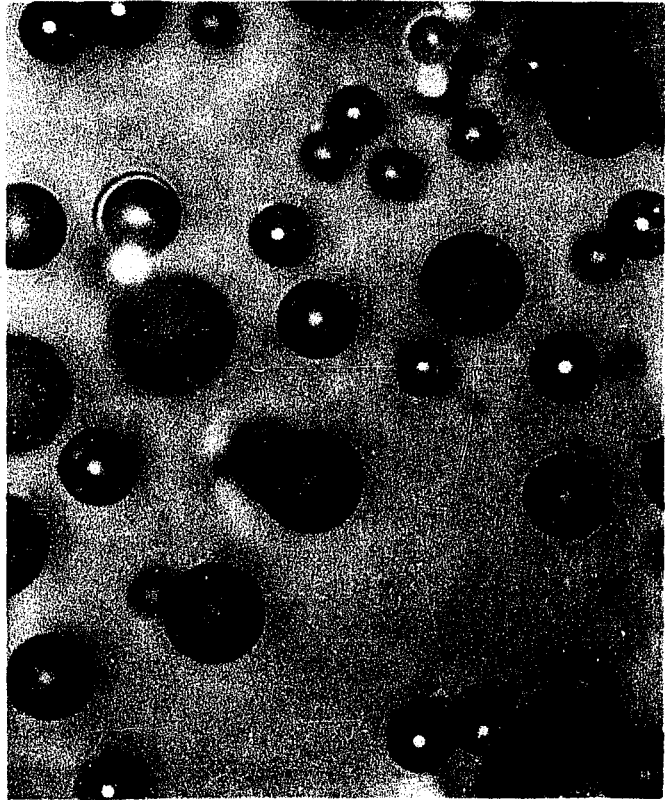
b) After recirculation for  
4700 seconds in the closed  
loop - 300 x magnification.

a) Before recirculation -  
700 x magnification.



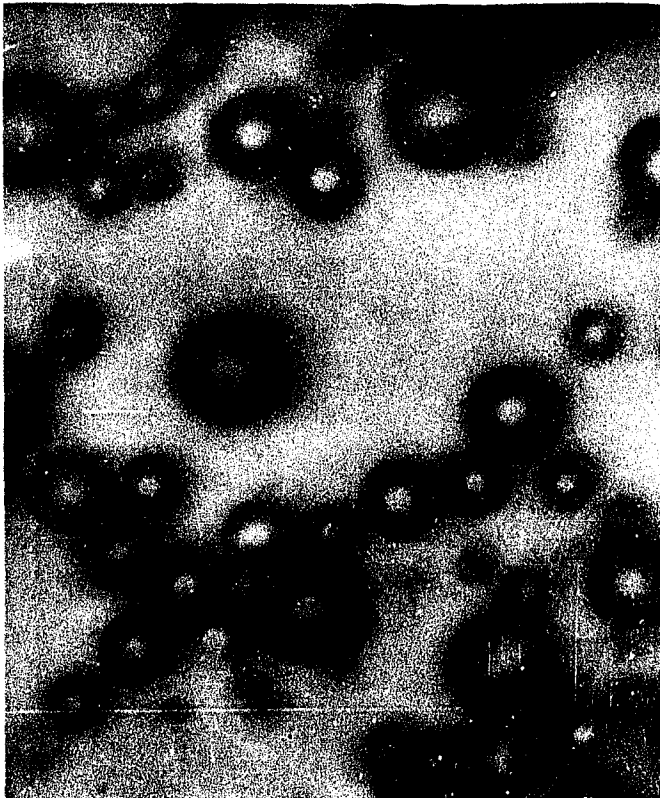
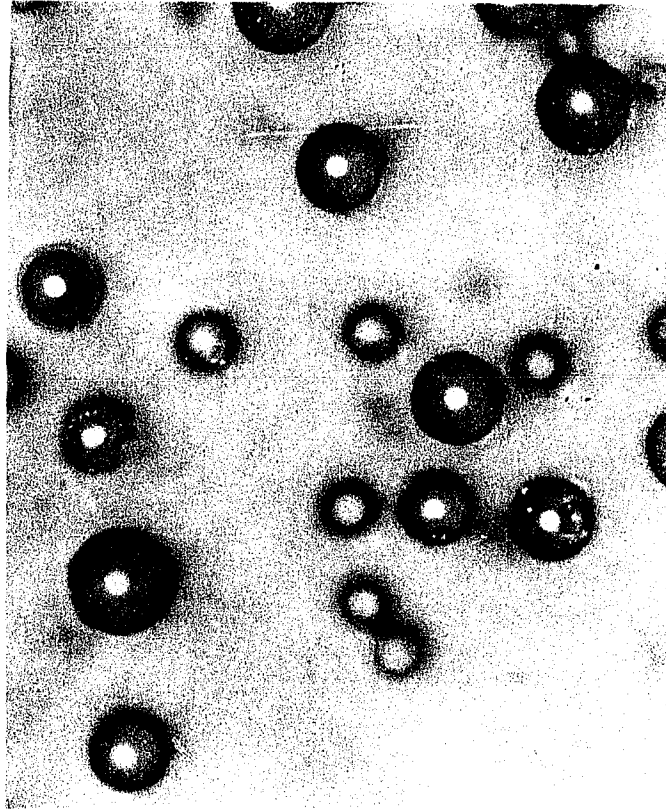
b) After recirculation for  
3480 seconds in the closed  
loop - 700 x magnification.

a) Before recirculation  
- 700 x magnification.



b) After recirculation for 3800  
seconds in the closed loop  
-700 x magnification.

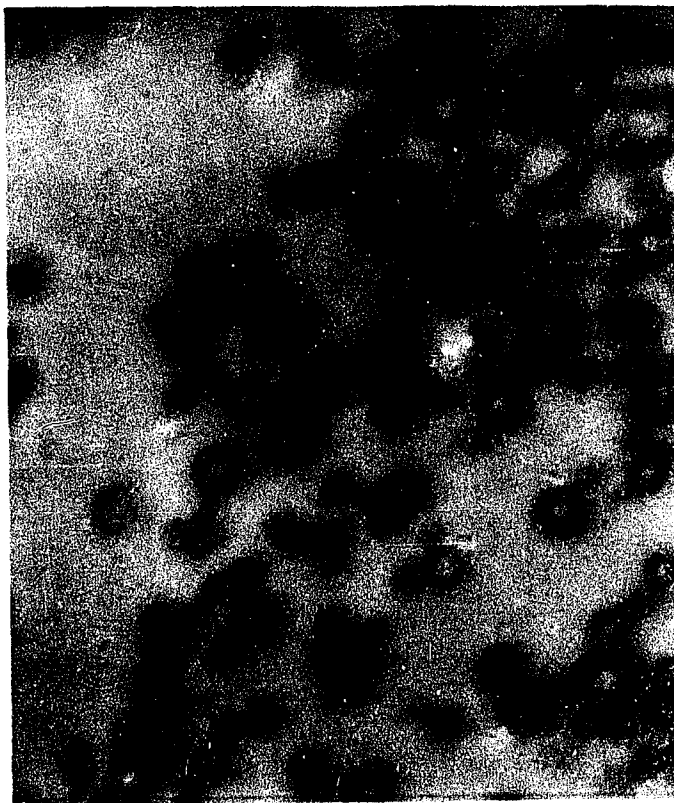
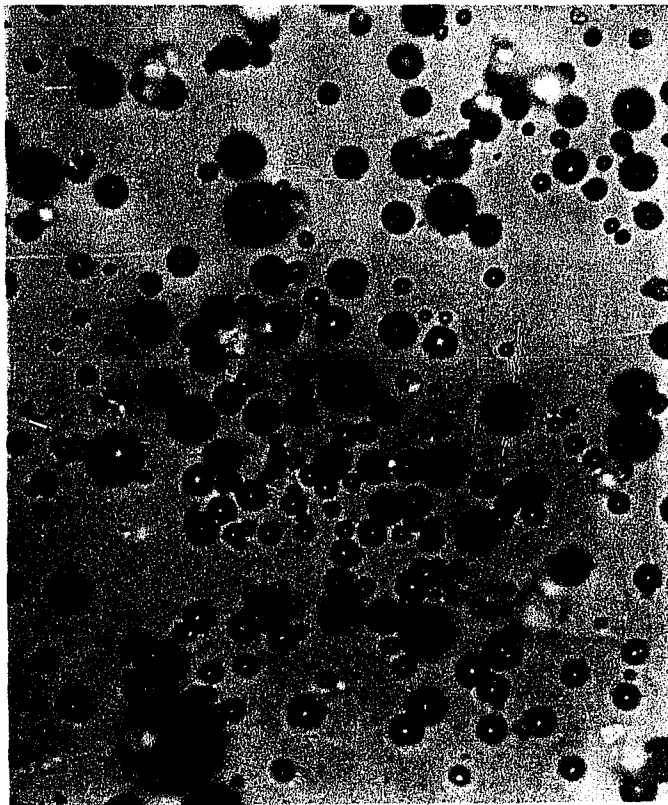
a) Before recirculation  
~700 x magnification.



b) After recirculation for 4420  
seconds in the closed loop  
~700 x magnification.

Figure 16: Photographs of the #980 Glass beads.

a) Before recirculation  
- 700 x magnification.



b) After recirculation in the  
closed loop for 7130 seconds  
- 700 x magnification.

calibrated using the downstream pitot-static testing section at the fluid flow rates and temperatures encountered during the study. The two-phase flow meter readout resulting from clean air flow at different mass flow rates was also obtained. No significant difference was found when these strain gage readouts were compared for open and closed loop systems at equivalent mass flow rates.

The experimental procedure during these runs can be described as follows. After an equipment warm up period of between 30 minutes and one hour, the readout from the two phase flow meter was set to zero. At this time the voltage from the anemometer was also checked for agreement with a previously obtained voltage-temperature correlation. This voltage-temperature relationship was determined by regulating the temperature of the loop by means of the room air-conditioner and recording the anemometer voltage and corresponding loop temperature over a long time period without flow. In order to obtain consistent and useful anemometer calibrations for all flow conditions and temperatures it was necessary to have the zero flow voltage agree with this relationship before any flow measurements could be taken. If necessary, the no flow voltage was adjusted, after which the no flow root mean square voltage was recorded. In the remainder of this dissertation the voltage and root mean square voltage under conditions of no flow through the system will be referred to as  $V_0$  and  $V_{rms0}$  respectively.

Both micromanometers were then prepared by filling them with 200 proof ethyl alcohol until zero readings were obtained. Both the impact tube and the anemometer probe were initially set at the center of the tubing by means of manual traverses. the compressor was started and the desired RPM of the motor was obtained by adjusting the speed of the motor until a slot on the coupling shaft appeared to stop turning when viewed with the electronic stroboscope. When steady pressure drop readings were observed, the pressure drops across the test sections were recorded as well as the pitot-static section pressure drop. The anemometer readings were then recorded while an identification mark was made on the flow meter and thermocouple readout on the recorder. Static pressure and orifice pressure drop measurements were then made. Continuous readings of the room temperature and humidity were made using a Serdex hygrothermograph.

Modification of the above procedure during some pure air runs depended upon the required measurements. During the initial runs it was desired to check the pressure measuring instruments. It was therefore necessary to design and construct a pressure manifold. The pressure manifold contained toggle valves and was used when several pressure drops or instrument readings were to be made. The manifold was thoroughly checked for leaks by means of a high pressure compressed air line and soap bubble testing prior to installation in the experimental system. Using the manifold it was possible to compare the test section pressure drop and pitot tube readings of several

instruments during the same run. The instruments field tested along with the R. Feuss micromanometers included a movable leg manometer, a hook gage and a Flow Corporation MM3 micromanometer. The R. Feuss micromanometers were found to give the most reliable readings and showed the quickest response to changes in flow or pressure drop. Subsequent to these initial runs the R. Feuss micromanometers were used exclusively for pressure drop measurement.

Though the calibration of the anemometer probes was carried out with both the impact tube and the thermistor probe in the center position, it was also necessary to obtain velocity profiles for a number of the pure air runs. These profiles were obtained by moving the impact tube to predetermined positions across the test section using a manual traverse. The profiles were always made subsequent to the previously described measurements with fluid temperatures being continuously recorded.

Pure air runs were also made after each set of closed loop suspension runs. The purpose of these air runs was to determine whether the anemometer probe calibration had been altered by the solids. During these runs the impact tube was not employed. The pressure drops across each test section were measured by the micromanometers directly and the anemometer voltage reading was used together with the previously obtained calibration to determine the air velocity. Friction factors were calculated from this data. If the calculated friction factors agreed with those previously obtained for each test

section, then it was concluded that the probe had not been damaged by the particle flow. When a difference was found, the suspension runs performed subsequent to the previous calibration check were repeated using another calibrated probe.

Open loop calibration runs. - In order to obtain a correlation between the output from the two phase flow meter and solids loading ratio an extensive series of open loop calibration runs was performed. During these runs it was necessary to separately measure the solids and air flow rates and relate these measurements to the flow meter output, subsequently to be referred to as  $V_{ST}$ .

After the compressor was adjusted to the proper RPM by using the stroboscope, the one inch ball valve beneath the rotary air lock (see figure 10) was opened, and the rotary air lock put into operation. A switch was then activated which allowed the BIF feeder, an electric timer and the electric vibrator to begin operating simultaneously. The BIF feeder could be approximately set for the desired solids flow rate before the start of a run by using a calibration obtained prior to the installation of the feeder airlock combination into the experimental system for the no flow condition. Feeder settings could not be used to precisely determine the solids flow rate since it was found that the feeder rate at a given setting was dependent upon the air flow rate.

The upstream pitot tube was used for the determination of air flow rates. The solids flow rate was determined by

weighing the collected particles in a measured time. The particles were removed from the collector by mechanically rapping the top and sides, removing the rubber stopper at the bottom of the collector and allowing the solids to fall into a previously weighed beaker. Visual inspection following this procedure indicated that there was very little if any particle residue in the collection cone. Weighings were made using a triple beam balance capable of weighing 2610 grams to the nearest .1 gram.

Pitot tube readings were made and recorded several times during each run with recorder output being marked each time. When the pitot tube pressure drop decreased to 10% below its initial value the run was terminated. This decrease in pitot tube reading was caused by clogging of the sintered tubes and consequent decrease of the loop velocity. Due to the design of the collection system at least 100 gms. of particles could be collected even at the highest solids flow rate before it was necessary to terminate the runs. After each run it was necessary to remove the sintered tubes from the collector and clean them by use of a compressed air line. Weighing of the sintered tubes before and after cleaning indicated that less than 5 grams of particles were required to clog the tubes.

Shut down procedure for the open-loop runs consisted of shutting the feeder, timer and vibrator simultaneously, then stopping the airlock, closing the ball valve, and turning off the compressor and motor-generator.

During the open loop calibration runs pressure drop readings were also made across the upper horizontal test section. Unfortunately, the fact that the feeder airlock combination did not feed at a perfectly steady rate caused pulsations in those readings and led to scatter in the data.

Due to the large inventory of particles required and its time consuming nature, open-loop strain gage calibration was performed only with the  $30\mu$  glass particles.

Closed-loop experiments. - Measurements obtained during both the pure air and open-loop calibration runs were used to obtain calibrations and correlations necessary in order to analyze the closed-loop results. During these closed-loop runs pressure drops across each test section and the orifice as well as velocity and turbulence measurements were recorded. From these data the effect of particle size and concentration, as well as fluid flow rates, upon friction factors, gas velocity profiles and orifice coefficient was studied.

The operating procedure for these runs was somewhat less complicated than that for the open-loop calibration runs. After the initial warm up period, setting the instruments to appropriate no flow values and recording  $V_o$  and  $V_{rmso}$ , a pre-weighed sample of particles was poured into the loop through the closed-loop feeding inlet previously described. The motor-generator was turned on and the compressor put into operation. The stroboscope was set at the highest RPM under consideration and the compressor speed adjusted to maintain this RPM. The pressure drops across the two test sections

27.

were measured directly by means of the two R. Feuss micromanometers. When these pressure drops and the output from the two phase flow meter showed no change with time, readings were taken. The anemometer voltage and root mean square voltage were recorded while the thermocouple and flow meter recorder output was marked. The test section and orifice pressure drop measurements were then taken followed by the static pressure measurements. With the same particles still in the circulating loop the compressor speed was set for each of the remaining RPM to be studied and the same procedure of data recording was followed.

For the closed-loop study, solids loading was determined by means of the calibrated mass-flow meter and air velocities and turbulence measurements were made using the calibrated thermistor probes. Velocity profiles were obtained for a number of suspension runs using the thermistor probe and a manual traverse. These profiles were always made subsequent to pressure drop and centerline velocity measurements. The entire closed loop system was electrically grounded through the compressor by means of cables connected across each glass test section for all suspension runs.

Since attrition of larger diameter particles during closed-loop operation was felt to be more likely than with the smaller particles, the loop was cleaned more frequently when the two largest size particles were studied. For these particles, runs were made at 10 gram increments and the loop cleaned every other run. For the two middle size particles employed in this

study, runs were also made at 10 gram increments but the loop was cleaned after every fourth run. For the smallest sized particle the loop was not cleaned until a complete series of eight runs were completed. The high cost and difficulty of obtaining the three smaller diameter particles along with the very small inventory of these particles available for this study strongly influenced the foregoing method of operation.

The particles were collected in the sintered tube shown in figure 6 by use of the three-way ball valve in the flow-through position. Particles from different runs were saved in labeled jars for subsequent particle size distribution analysis so that particle attrition could be studied on representative samples.

The mass flow meter output was used to determine whether the loop was completely clean. After every loop clean-out pure air runs were made to check out all parts of the experimental system.

#### IV EXPERIMENTAL RESULTS AND DISCUSSION

The results obtained during pure gas studies, open-loop mass flow meter calibration as well as closed-loop investigations with circulating suspensions will each be presented separately in the following sections.

##### Pure Gas Results

During closed-loop experimentation (with pure gas as the circulating fluid), velocity profile, pressure drop, anemometer and orifice calibration data were obtained. The results obtained from these data are presented below.

Velocity profiles. - Velocity profiles were obtained for tube Reynolds number ranging from 3450 to 41200 by use of the downstream pitot-static testing section previously described. Typical velocity profile data across the tube are shown in figure 17. The figure also shows a plot of the curve obtained using 1/7th power law based on the centerline velocity experimentally determined. The agreement between the experimental data and the theoretical curve is seen to be better than 3% at all points. The experimental data were obtained with three measuring instruments: the R. Feuss micromanometer, a movable leg manometer, and a specially designed hook gage. The data from the three instruments were practically identical, so that only one experimental point is discernible at some of the traverse positions.

The velocity data obtained from each traverse were also plotted against the radial distance from the center of the tube. The area under these curves was determined using a

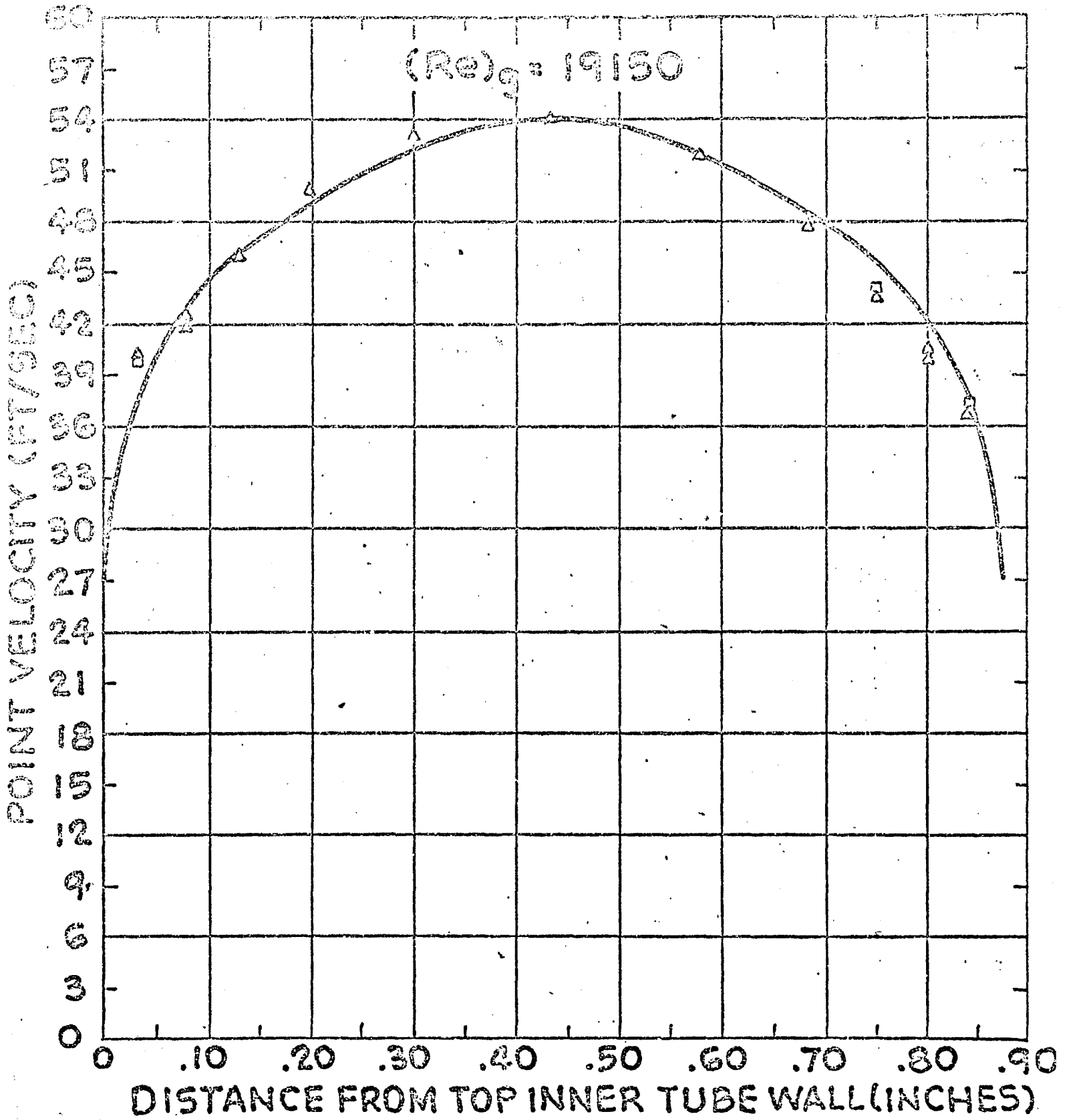


Figure 17: Gas Velocity Profile

polar planimeter and the average gas velocity was calculated. The reader is referred to Appendix A for details of this operation. The ratio of the average to centerline gas velocities as determined by this procedure are presented in Table V. From this table it would appear that in a Reynolds number range of between 3670 and 41200 the average to centerline velocity ratio is  $.80 \pm 2.5\%$ , which is what would be expected upon integration of a velocity profile for a fluid obeying the 1/7th power law.

Friction factors. - Friction factor results were determined by measuring pressure drops across both the horizontal and vertical test sections. For runs in which velocity profiles were taken, the experimentally determined average velocity was used in the friction factor calculation otherwise a value of .8 times the centerline velocity was taken as the average velocity. Since the pressure drop across each test section is relatively small and the flow is isothermal in nature, the incompressible flow equations were used to determine friction factors. The method of calculation is indicated in Appendix A along with a sample calculation.

A plot of the calculated Blasius friction factor (Blasius friction factor equals 4 time the Fanning friction factor) as a function of the gas Reynolds number for the horizontal test section is shown in figure 18. Two empirical equations are commonly used to represent the relation between the gas friction factor and the Reynolds number for flow

TABLE V.

VARIATION OF RATIO OF AVERAGE CENTERLINE GAS VELOCITY WITH GAS REYNOLDS NUMBER.

$(Re)_g$	$\frac{\bar{v}}{v_c}$
3450	.736
3670	.783
4300	.777
11500	.823
19150	.788
31835	.789
41200	.830

through smooth tubes (ref. 63). The first equation is valid the Reynolds number range between 5000 and 200,000 and corresponds to

$$f_B = \frac{0.184}{(Re)_g^{.2}} \quad (34)$$

Equation (34) is plotted along with the data in figure 18. Curves corresponding to  $\pm 5\%$  deviation from this correlation are indicated by the dashed lines. As can be seen from the figure, equation (34) provides an adequate description of the data since the bulk of the experimental results fall between the  $\pm 5\%$  curves on the figure.

The second correlation commonly used to represent friction factor data for turbulent flow through smooth tubes is presented below

$$f_B = .00560 + \frac{.5}{(Re)_g^{.32}} \quad (35)$$

This empirical relation is a more exact equation and is reportedly (ref. 63) valid in a wide Reynolds number range of between 3000 and 3,000,000. The calculated friction factor data from the vertical test section is presented in figure 19 as a function of Reynolds number along with a curve of the friction factor calculated using equation (35). The  $\pm 5\%$  deviation curves are again indicated by dashed lines. Since most of the calculated data fall within these deviation curves, equation (35) can be used to represent the pure gas vertical test section friction factor results. The differences between the friction factors of the horizontal and

Figure 18: Variation of Friction Factor with Gas Reynolds Number

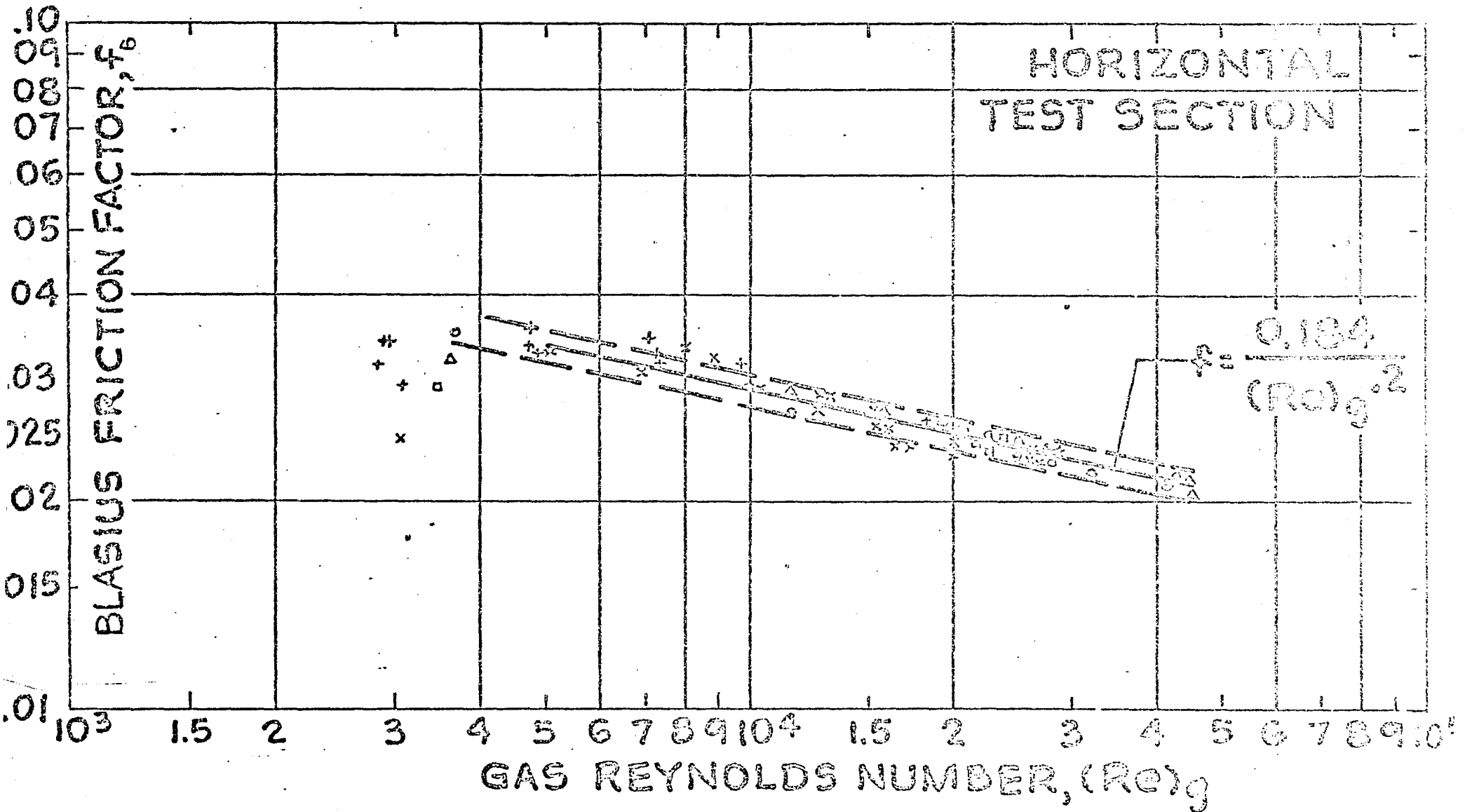
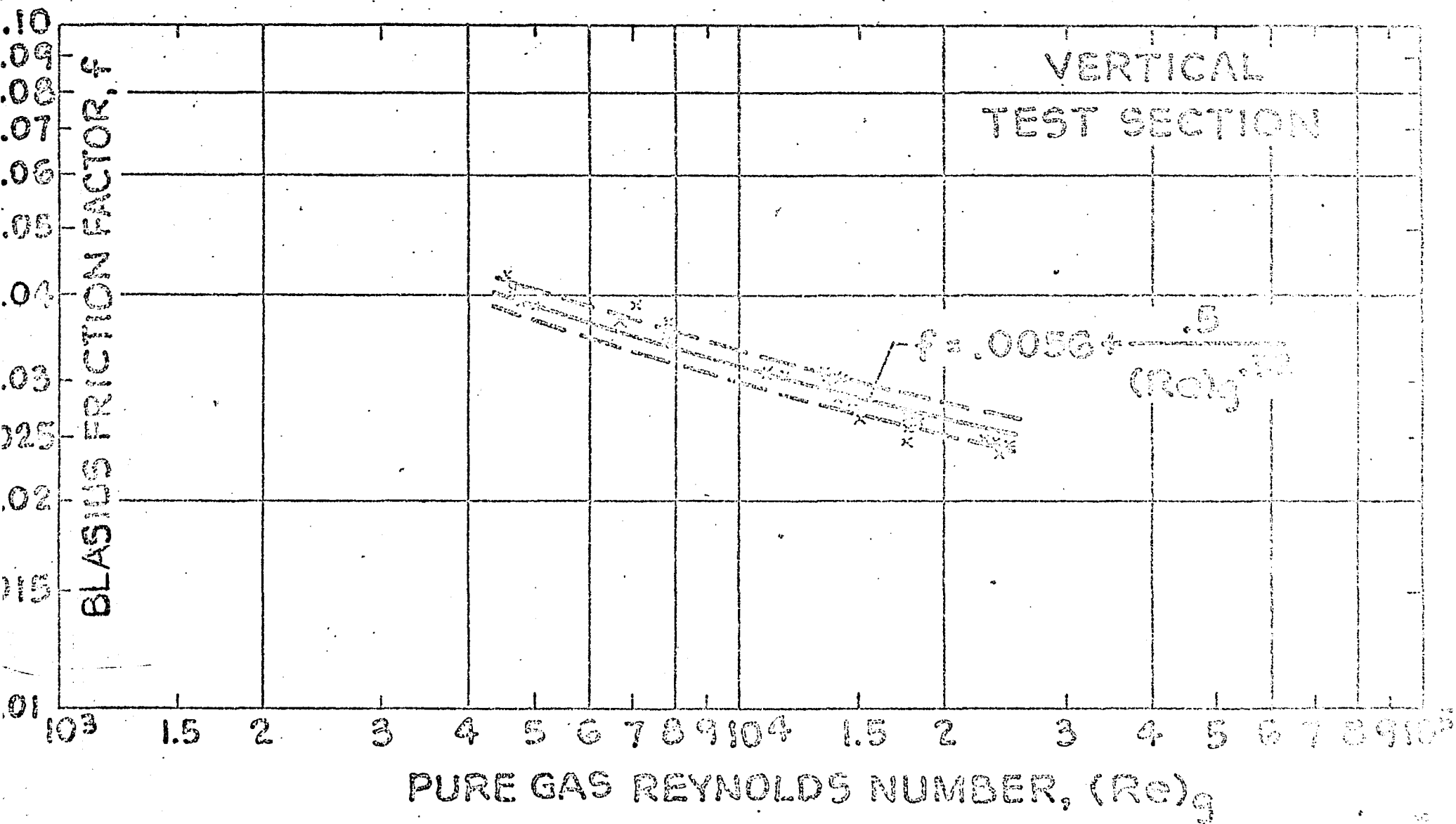


Figure 19: Variation of Friction Factor with Gas Reynolds Number



vertical test sections can be attributed to the fact that the horizontal test section is metal while the vertical section is glass and each has different surface properties. Another factor possibly influencing this difference could be the different location of the two sections, with the vertical section being closer to the gas-solids circulator. In any case, the friction factor data obtained from each section can be adequately represented by commonly used empirical relations, namely equation (34) for the horizontal and equation (35) for the vertical test section.

Anemometer Calibrations. - In order to determine gas velocities in suspension flow, a calibrated anemometer probe was required. The calibration of these probes was carried out with pure gas circulating in the closed loop system through the use of the downstream pitot-static section. Since the thermistor probe is very sensitive to the temperature of the flowing gas, a number of curves of anemometer output voltage as a function of fluid velocity at different temperatures was required for each calibration. A cross plot of these curves was then made in order to obtain a single plot of voltage versus temperature with fluid velocity as a parameter. During the course of this study, five probes were calibrated in this manner. The final voltage versus temperature plot for probe #5 is shown in figure 20. A typical curve of voltage as function of velocity at an arbitrary temperature using probe #5 is presented in Appendix A. As can be seen from figure 20, when the temperature increases

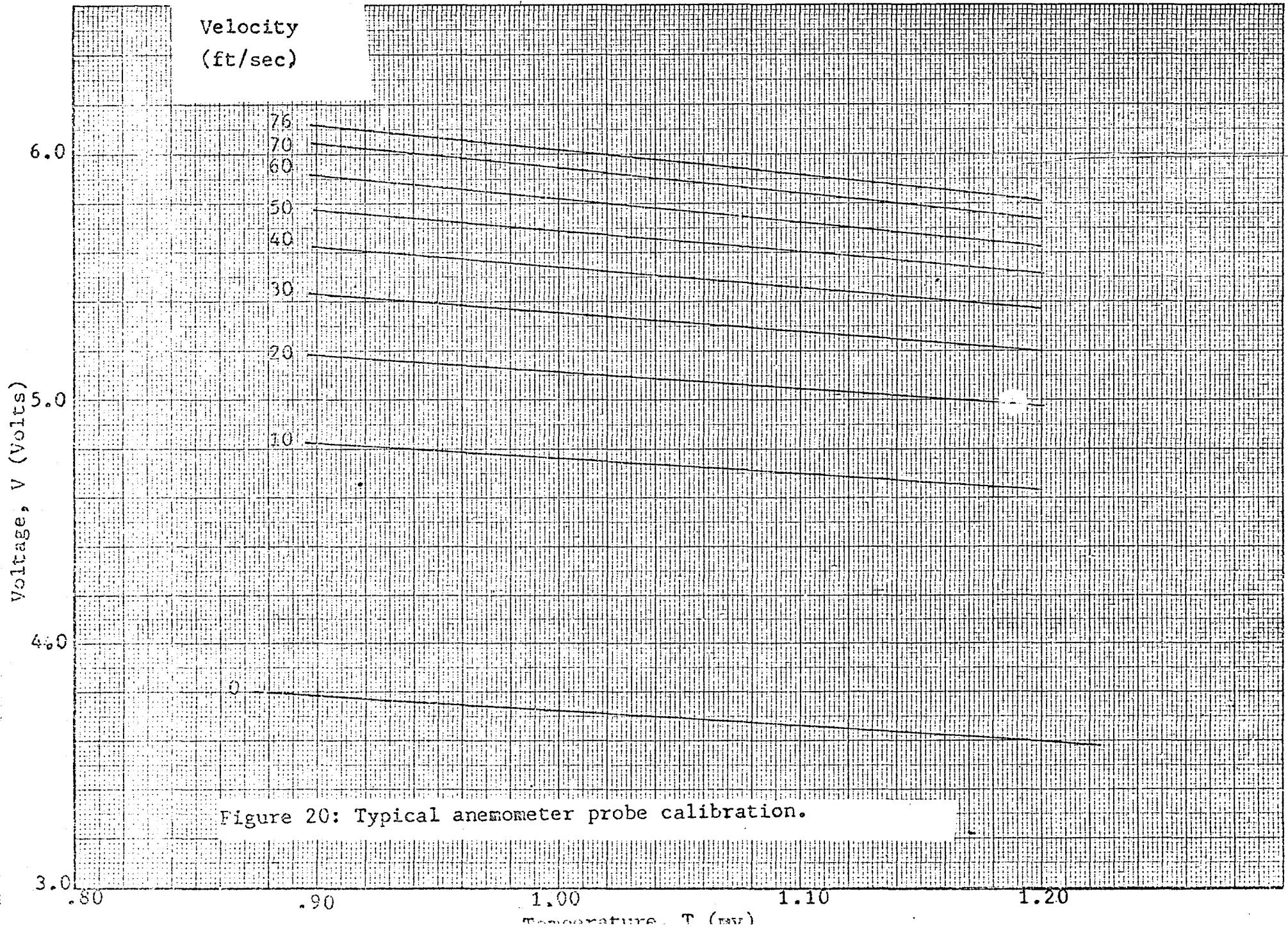


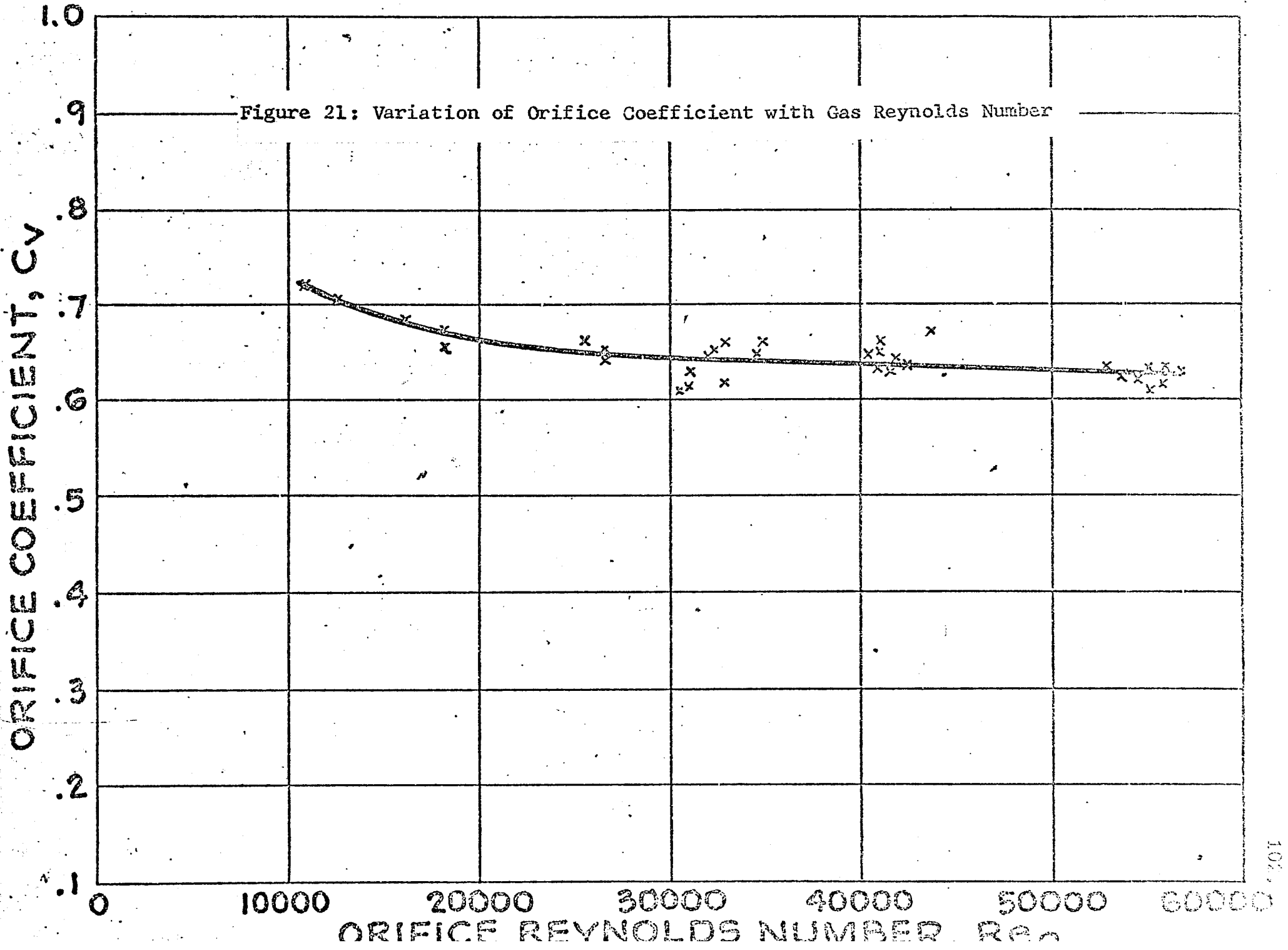
Figure 20: Typical anemometer probe calibration.

the output voltage decreases at any given velocity, typical of a thermistor type transducing element. At the outset of this project it was thought that these probes could be made with such an accuracy as to allow the calibration of one probe to be within  $\pm 1\%$  of the calibration of another. Calibration of each of the five probes, however, showed this to be true for only two cases.

Orifice Calibration. - Orr (ref. 64) maintains that an orifice is essentially unaffected by the presence of solids and may be used to meter gas-flow rates in suspension flow. In order to determine the validity of using an orifice to meter gas flow rates of suspension an orifice calibrated for pure gas flow is required. This was obtained by installing pressure taps across the aiming orifice located above the strain gage as shown in figure 9, and taking pressure drop measurements for pure air runs using the anemometer to determine the air flow rates. Knowing the pressure drop across the orifice and the air flow rate, orifice coefficients were calculated (see Appendix A). The variation of these orifice coefficients with orifice Reynolds number is shown in figure 21. As can be seen from the figure, above a Reynolds number 20,000 the orifice coefficient is essentially a constant of .63.

#### Open-Loop Calibration Results

In order to determine suspension loading ratios during closed-loop operation the two phase flow meter was calibrated using the open-loop system and experimental procedure previously



described. During these open-loop calibration runs, which were carried out with both pure gas and suspensions as the working fluids, the centerline mass flow rate was varied between 2.2 and 5.5. The suspension runs were made with feeder rates between .25 and 14.5 gms/sec. achieved by changing the setting on the BIF screw type feeder. The data obtained were correlated in the form predicted by a simple momentum analysis presented below.

The strain gage reading obtained from the two-phase flow meter is proportional to the force which the fluid exerts on the circular target inserted in the stream. This force is equal to the time rate of change of momentum of the fluid, so that

$$V_{ST} \propto F = \frac{dm_f v_s}{dt} \quad (36)$$

The fluid in this case is composed of both gas and solids, therefore, equation (36) can be written as

$$V_{ST} = k_1 \frac{d(m_g v_g)}{dt} + k_2 \frac{d(m_p v_p)}{dt} \quad (37)$$

Expansion of this equation yields

$$V_{ST} = k_1 v_g \frac{dm_g}{dt} + k_2 v_p \frac{dm_p}{dt} + k_1 m_g \frac{dv_g}{dt} + k_2 m_p \frac{dv_p}{dt} \quad (38)$$

Assuming that there is no slip between the particle and gas ( $v_p = v_g$ ) and that the particles and gas are not accelerating,

$$V_{ST} = k_1 v_g \left( \frac{dm_g}{dt} + \frac{k_2}{k_1} \frac{dm_p}{dt} \right) \quad (39)$$

However,

$$\frac{dm_g}{dt} = \rho_g v_g A \quad (40)$$

and

$$\frac{dmp}{dt} = W_p \quad (41)$$

so that,

$$V_{ST} = k_1 v_g \left( \rho_g v_g A + \frac{k_2}{k_1} W_p \right) \quad (42)$$

Rearranging equation (42) by multiplying and dividing each part of the right hand side by  $\rho_g$  gives

$$V_{ST} = \frac{k_1 A}{\rho_g} \rho_g^2 v_g^2 + \frac{k_2}{k_1 \rho_g} \rho_g v_g W_p \quad (43)$$

Assuming the density of the gas to be approximately constant, equation (43) can be rewritten as

$$V_{ST} = k_1' \rho v_g (\rho v_g) + k_2' \rho v_g (W_p) \quad (44)$$

where

$$k_1' = \frac{k_1 A}{\rho_g} \quad \text{and} \quad k_2' = \frac{k_2}{k_1 \rho_g}$$

Since the area of the target does not occupy the entire flow area of the tube, it is entirely possible that the relation between  $V_{ST}$  and the mass flow rate of gas and solids is not linear so that an equation of the form,

$$V_{ST} = k_1' \rho v_g (\rho v_g)^a + k_2' (\rho v_g) (W_p)^b \quad (45)$$

may be expected.

In order to facilitate the calibration of the meter, equation (45) was modified in terms of centerline velocity as follows

$$V_{ST} = k_1'' \rho v_c (\rho v_c)^a + k_2'' \rho v_c (W_p)^b \quad (46)$$

where

$$k_1'' = k_1' (.8)^{1+a} \quad \text{and} \quad k_2'' = .8 k_2'$$

The pure gas ( $W_p = 0$ ) strain gage output was plotted as a function of the centerline mass flow rate in figure 22. According to equation (46) when  $\log V_{ST}$  is plotted as a function of  $\log v_c$ , with  $W_p = 0$ , a straight line should result with slope  $1 + a$  and an intercept ( $\rho v_c = 1.0$ ) of  $k_1''$ . The log plot of  $V_{STO}$  versus  $\rho v_c$  shown in figure 23 indicates that  $a = .808$  and  $k_1'' = .0128$ . A typical readout from the Brush recorder for  $V_{ST}$  is shown in figure 24.

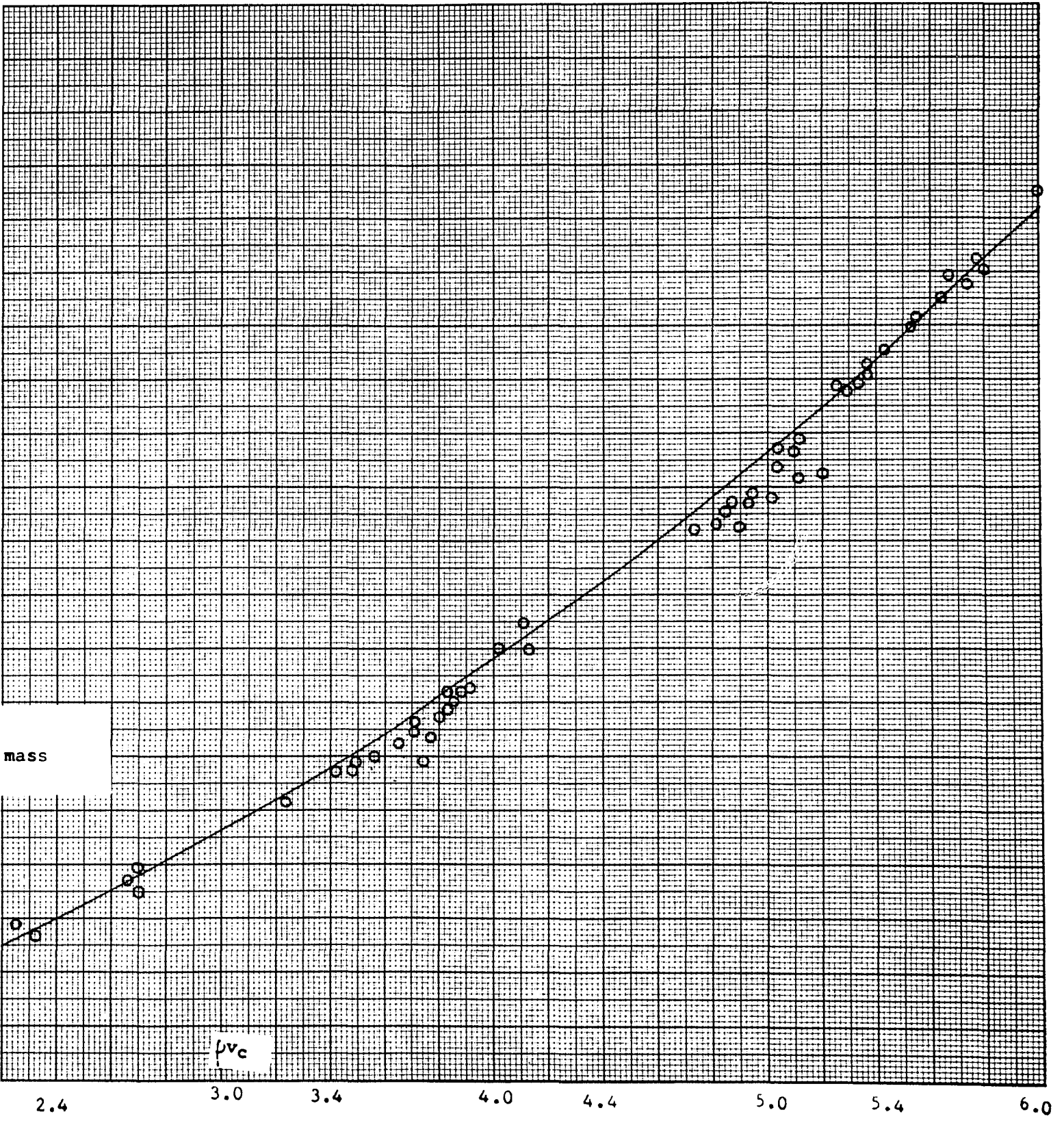
The suspension data were treated in a similar manner with equation (46) indicating that an arithmetic plot of  $V_{ST} - V_{STO}$  versus  $v_c$  should yield a family of straight lines passing through the origin with a varying slope equal to  $k_2'' (W_p)^b$ . This is illustrated by figure 25. The value of  $k_2''$  and  $b$  are readily obtained by plotting the log of  $V_{ST} - V_{STO} / v_c$  versus the log of  $W_p$  as shown in figure 26. It was interesting to note that the slope  $b$  was equal to  $.808$  exactly the same value as obtained from the pure gas results. Substituting the values of the experimentally determined constants, equation (46) can be written as

$$V_{ST} = .0128 (\rho v_c) (\rho v_c)^{.808} + .0155 v_c (W_p)^{.808} \quad (47)$$

Since the ratio of the particle flow rate,  $W_p$  and the gas mass flow rate  $.8\rho v_c A$  is the calibration correlation in terms of  $\eta$  is

$$\eta = \left[ \frac{V_{ST}}{.0217 (\rho v_c)^{1.808}} - .590 \right]^{1.238} \quad (48)$$





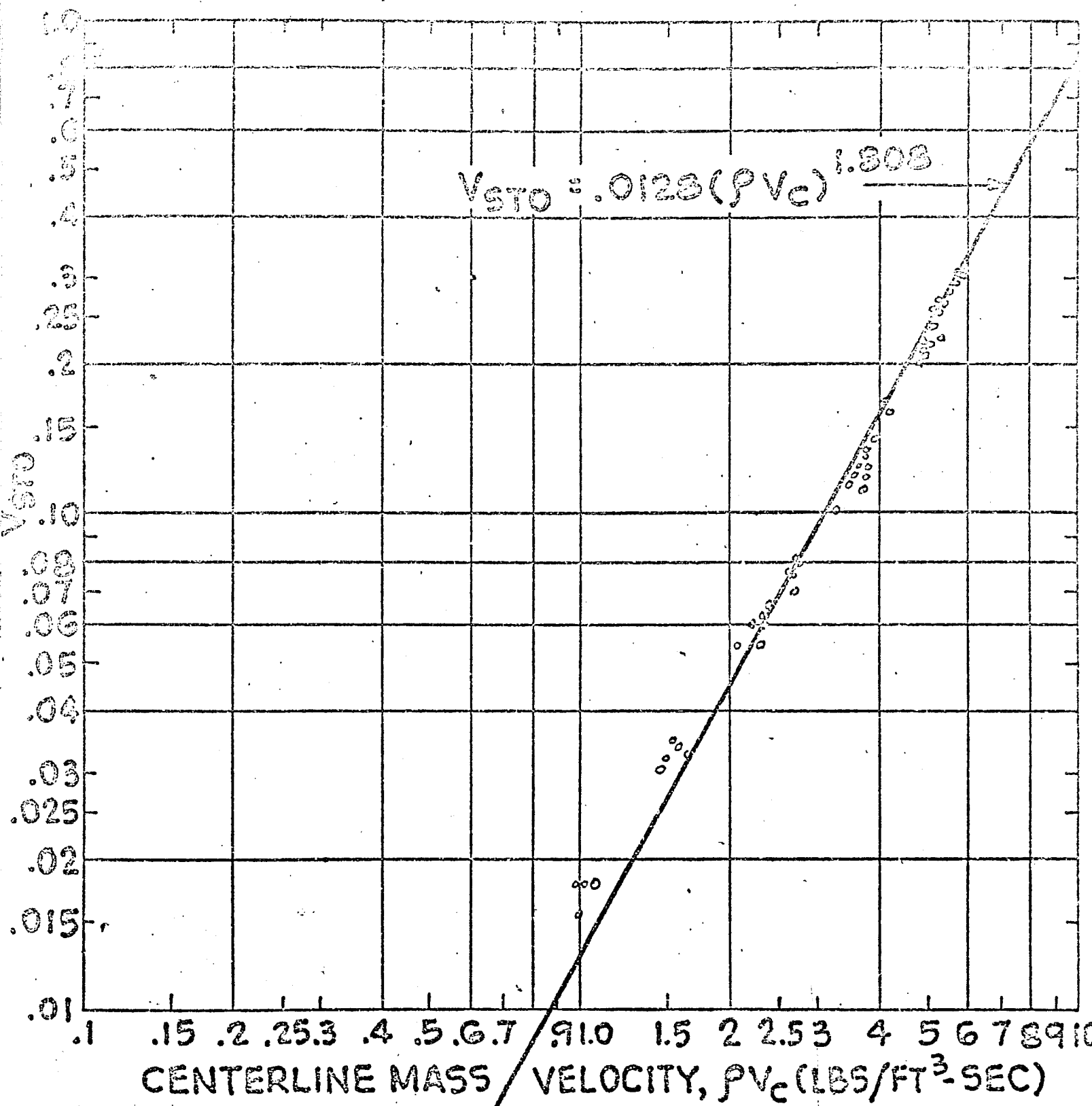
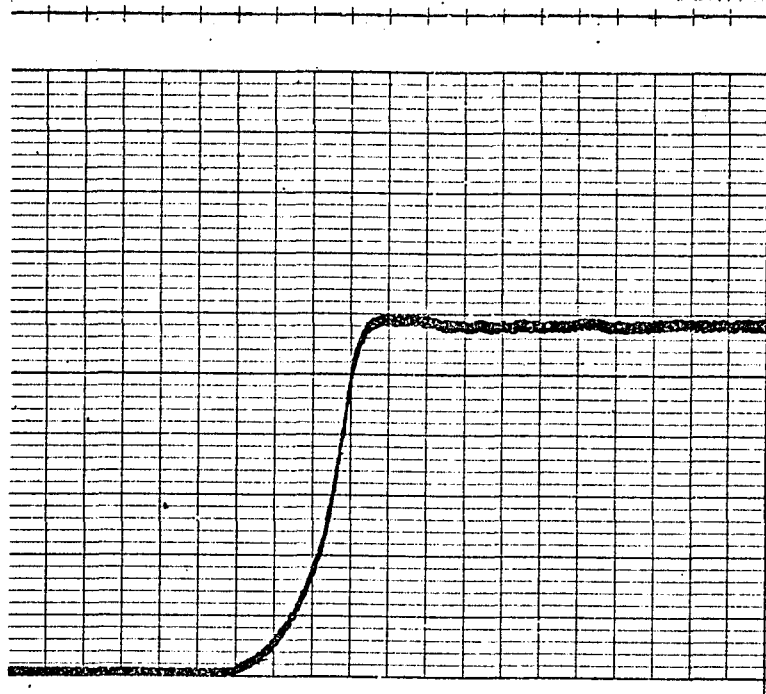
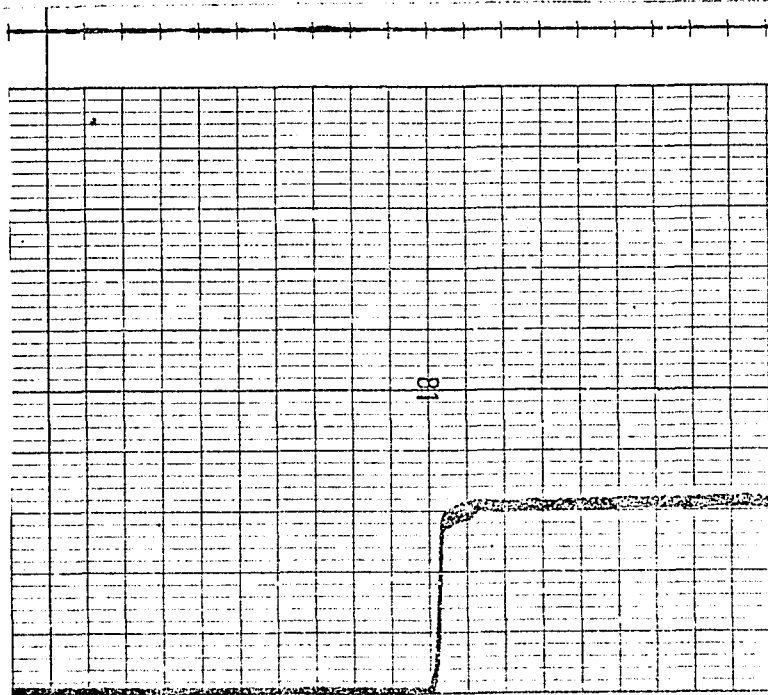


Figure 23: Variation of Pure Gas Strain Gage Reading with Centerline Mass Velocity



a) High Reynolds number - 10  $\mu$ v/div

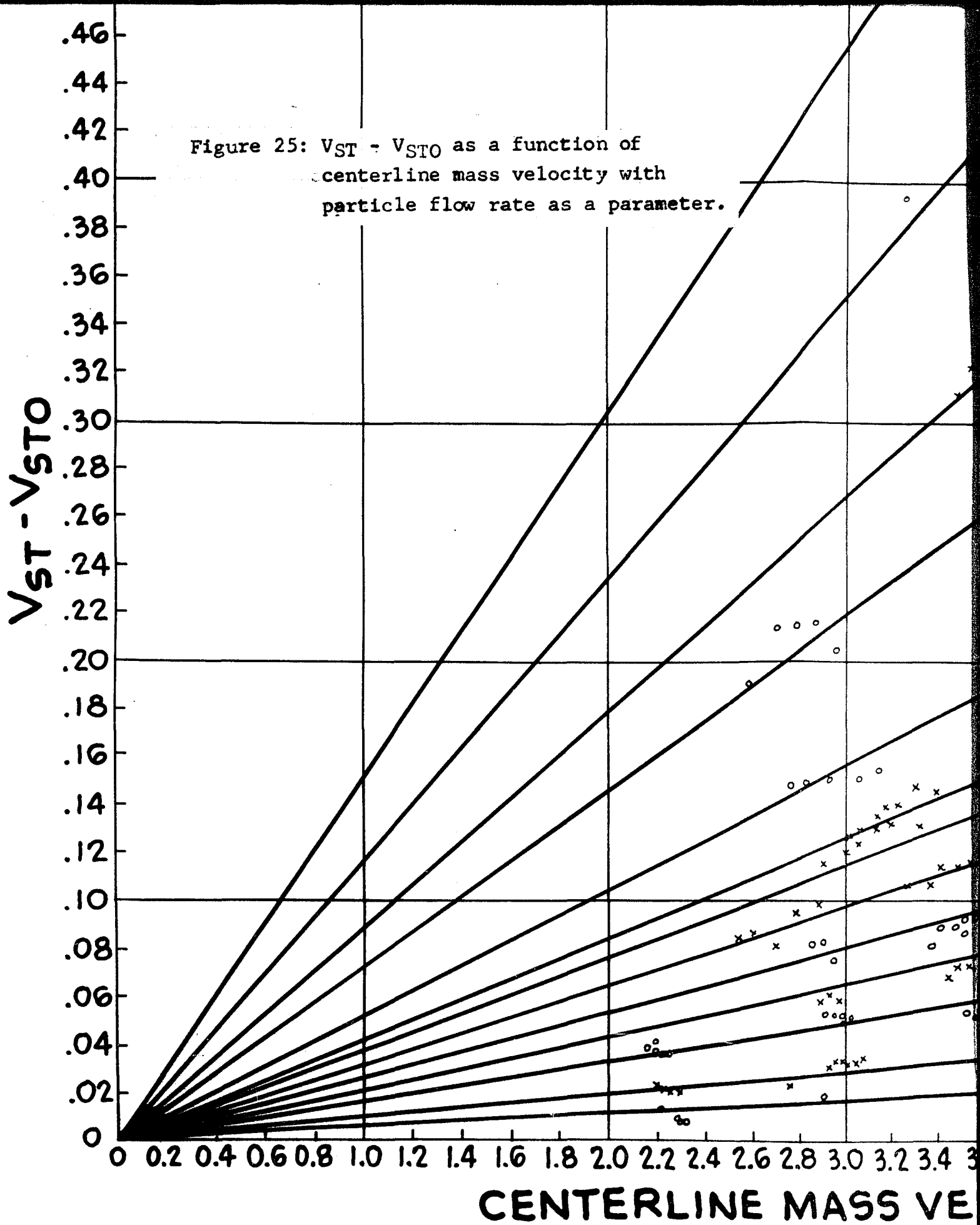


PRINTED IN U.S.A.

b) Moderate Reynolds number - 10  $\mu$ v/div

Figure 24: Typical pure gas recorder output.

Figure 25:  $V_{ST} - V_{STO}$  as a function of centerline mass velocity with particle flow rate as a parameter.



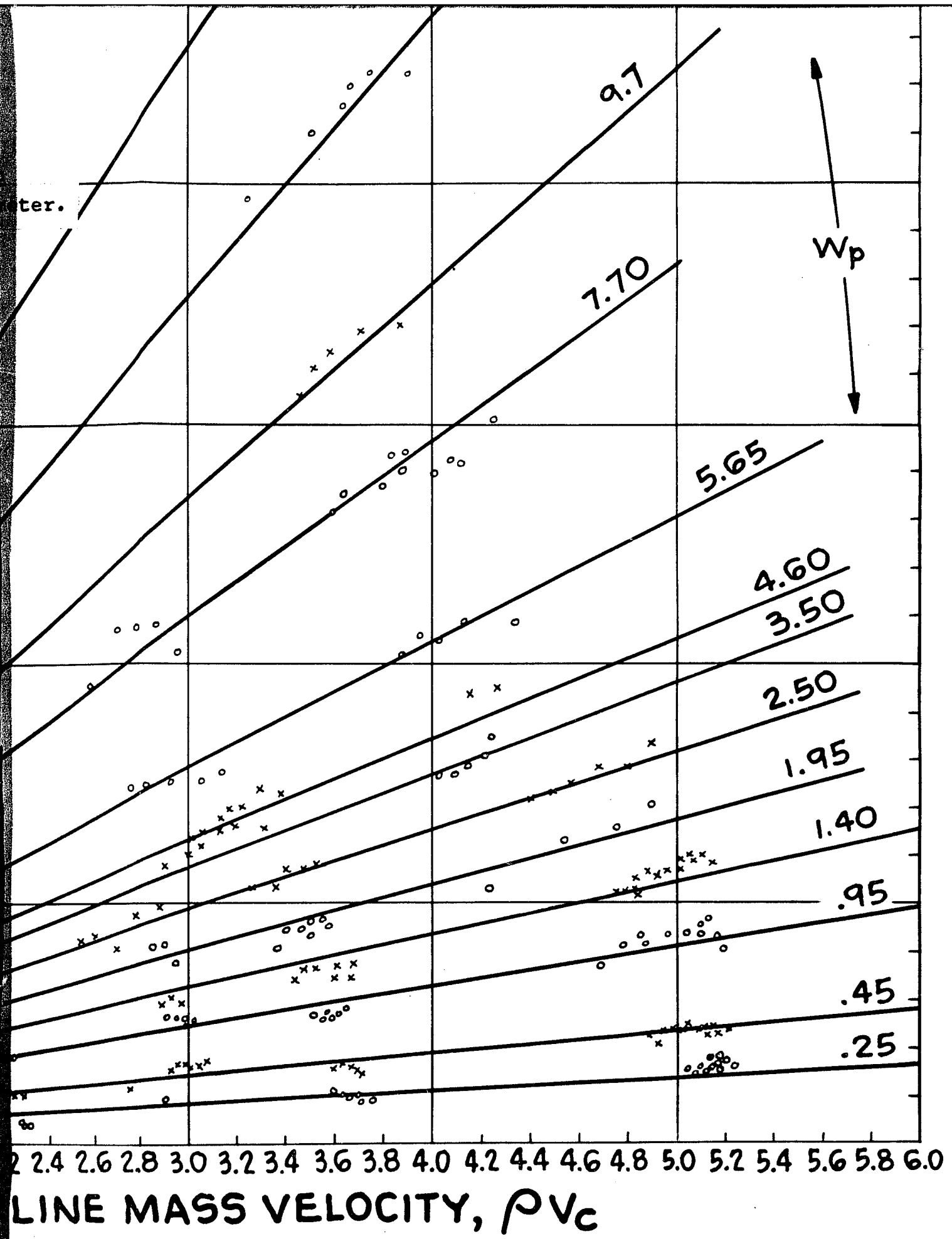
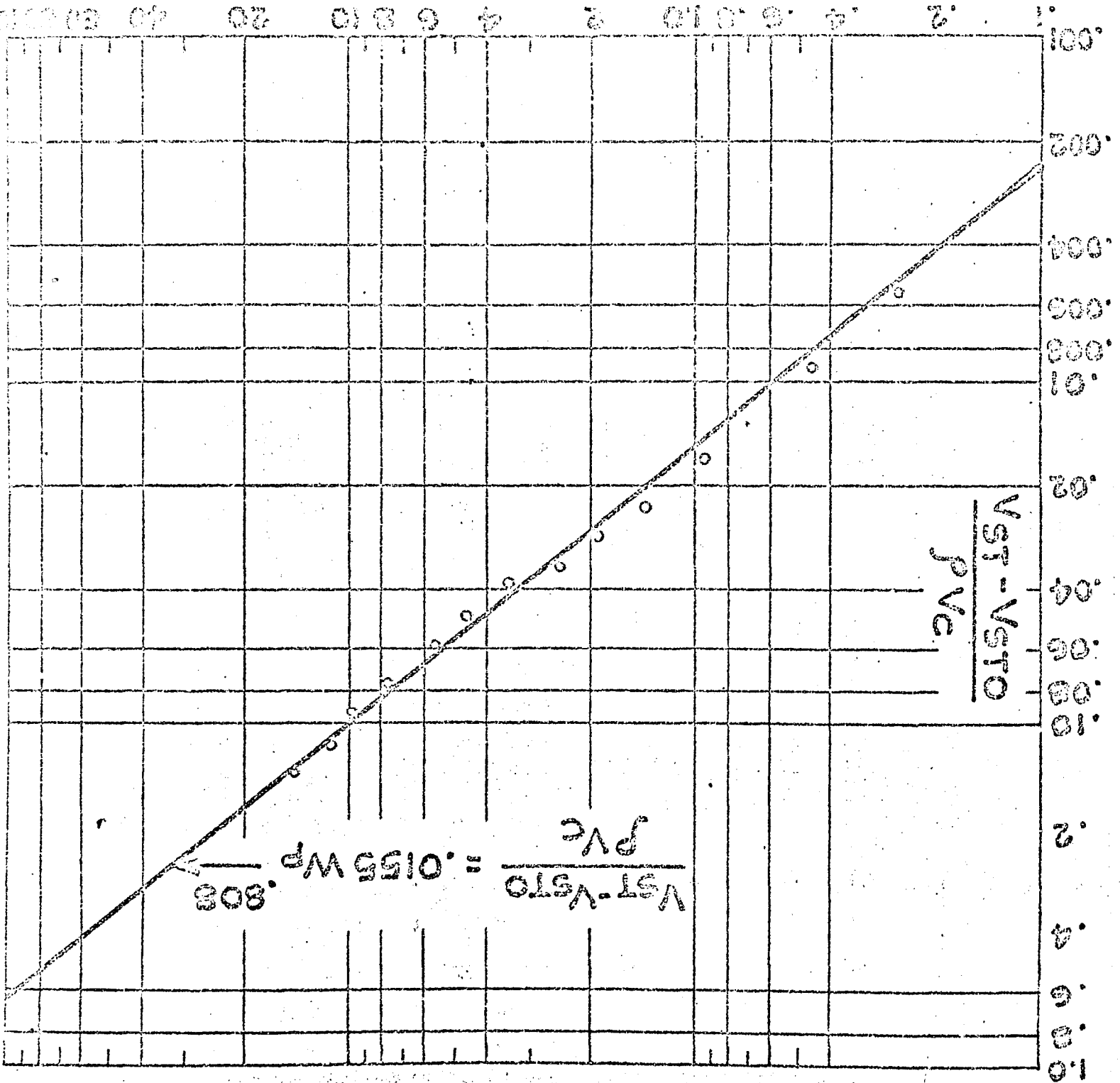


Figure 26: Variation of  $V_{ST} - V_{ST0}$  with Particle Flow Rate  
 & Ve

WP (g of particles/sec)

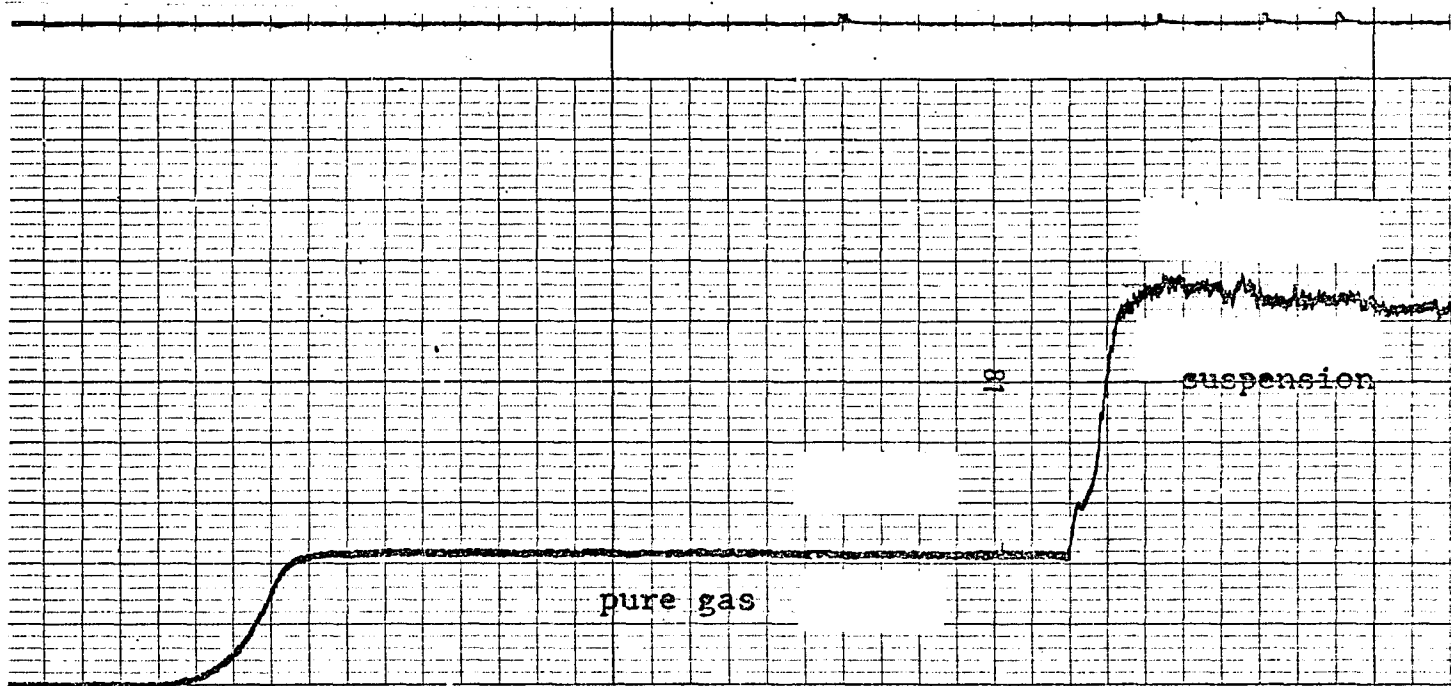


Although technically only valid for the  $30\mu$  particles this correlation was used to determine loading ratios for all the glass particles studied in this work. Recorder outputs for two cases of strain gage output, one each for high and low feed rates, is shown in figure 27. The pulsing observed on the low feed rate sample output is a result of the feeding characteristics of the screw type feeder. Whenever pulsing was obtained an average value of strain gage output at any given point was used to determine the solids loading.

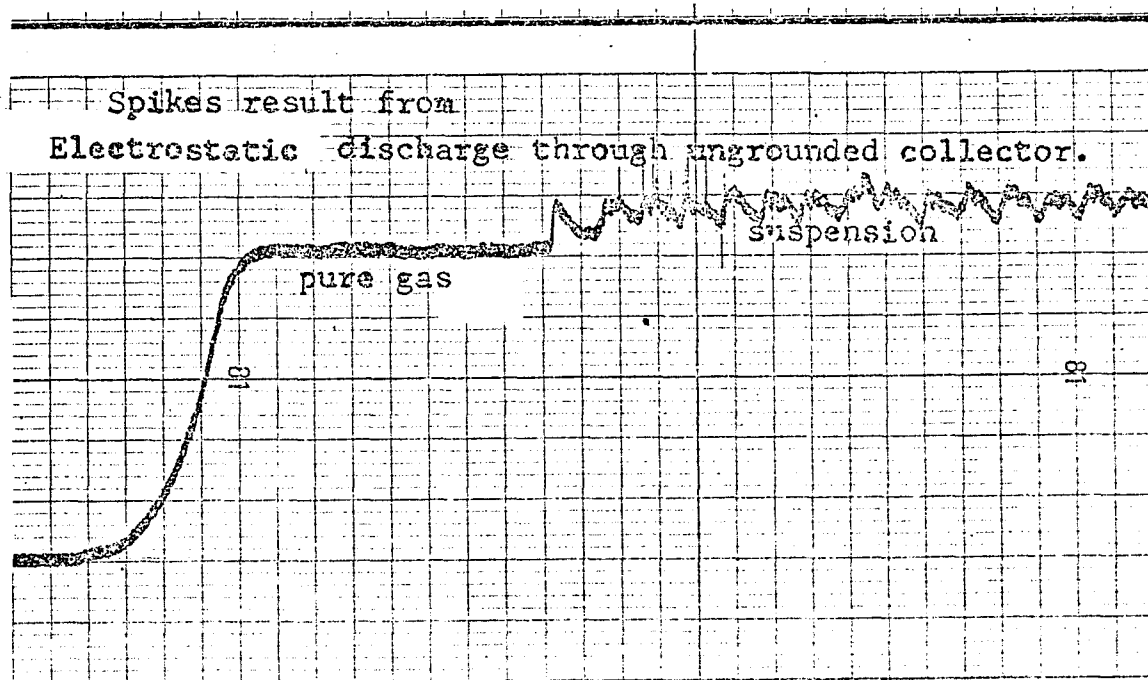
#### Closed Loop Results

During closed-loop operations with a suspension as the working fluid, mass flow ratios, friction factors for both vertical and horizontal test sections, centerline and percent turbulence as well as orifice coefficients were determined. In addition, a photographic analysis using the pyrex section preceding the horizontal test section (see fig. 6) was performed for representative Reynolds number and loading ratio conditions. Particle size distribution analyses were also made on representative particulate samples both before and after circulation through the loop. The results of each of the analyses and experiments mentioned above are presented separately in the following sections.

Mass flow ratios. - Loading ratios were determined by use of the two-phase flow meter previously described along with the open-loop calibration represented by equation 48. Samples of the flow meter output for closed-loop operation are shown in figure 28. Velocities were obtained from anemometer

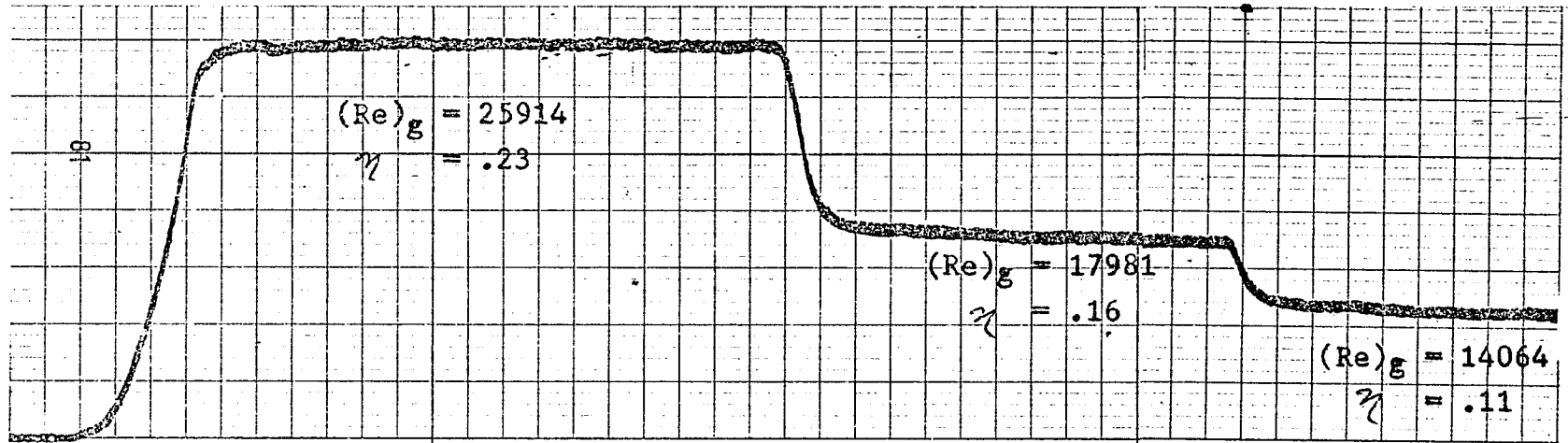


a) High particle feed rate.  $W_p = 15.5$ .  $V_{ST} = 20 \mu\text{v/div}$ .

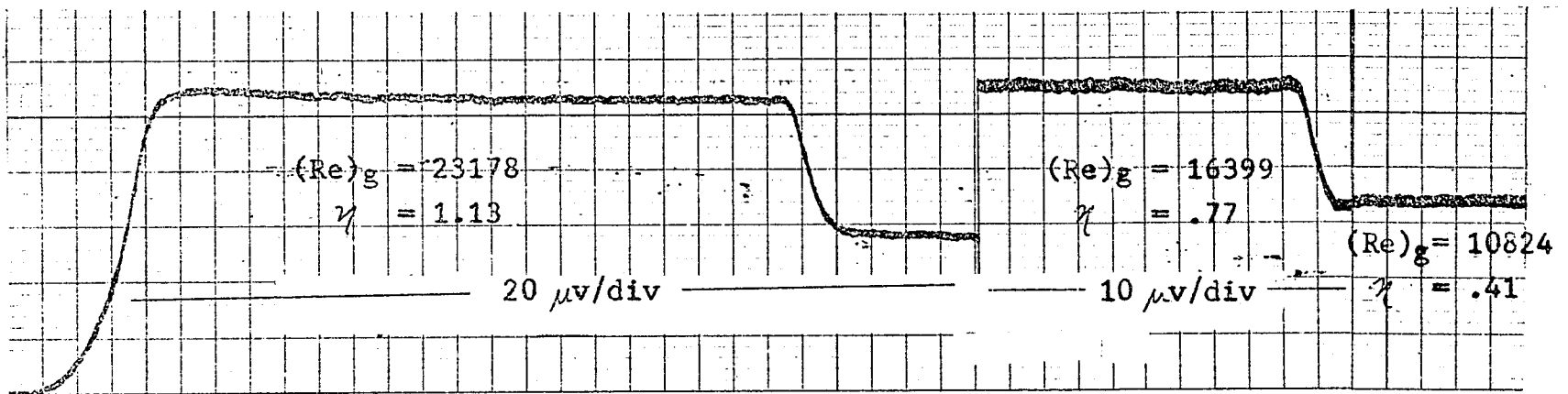


b) Very low particle feed rate.  $W_p = .5$ .  $V_{ST} = 10 \mu\text{v/div}$ .

Figure 27: Open loop strain gage output for high and low feed rates.



a) Low loading.  $V_{ST} = 10 \mu v / div.$



b) High loading.

Figure 28. Typical closed loop flow meter output for 30  $\mu$  Glass Beads.

readings using calibrated thermistor probes. Curves of loading ratios as a function of weight added to the system were obtained for the five particle sizes at each of three different Reynolds number ranges. These curves are presented in figures 29 - 37. The data from which the curves were faired is also indicated in each figure. As can be seen from the figures, with the exception of the 980 glass beads (avg  $D_p = 10\mu$ ) all of the curves are roughly S-shaped. For each particle size a comparison of the plots for the three different Reynolds numbers indicate that the higher the Reynolds number the higher the loading ratio at any given weight added to the system. This effect is more pronounced as the weight added to the loop is increased. This phenomena is explained by the fact that a larger percentage of particles are entrained by the gas when its velocity is high as compared to when it is low. At lower air velocities it is more likely to have particles caught in the compressor, elbows or other sections of the system, or coating the loop. It should also be pointed out that particles will remain in suspension at higher concentrations for higher air velocities. This accounts for the decreasing magnitude of the flattened upper portion of the S-shaped curves with decreasing gas Reynolds number for each particle size.

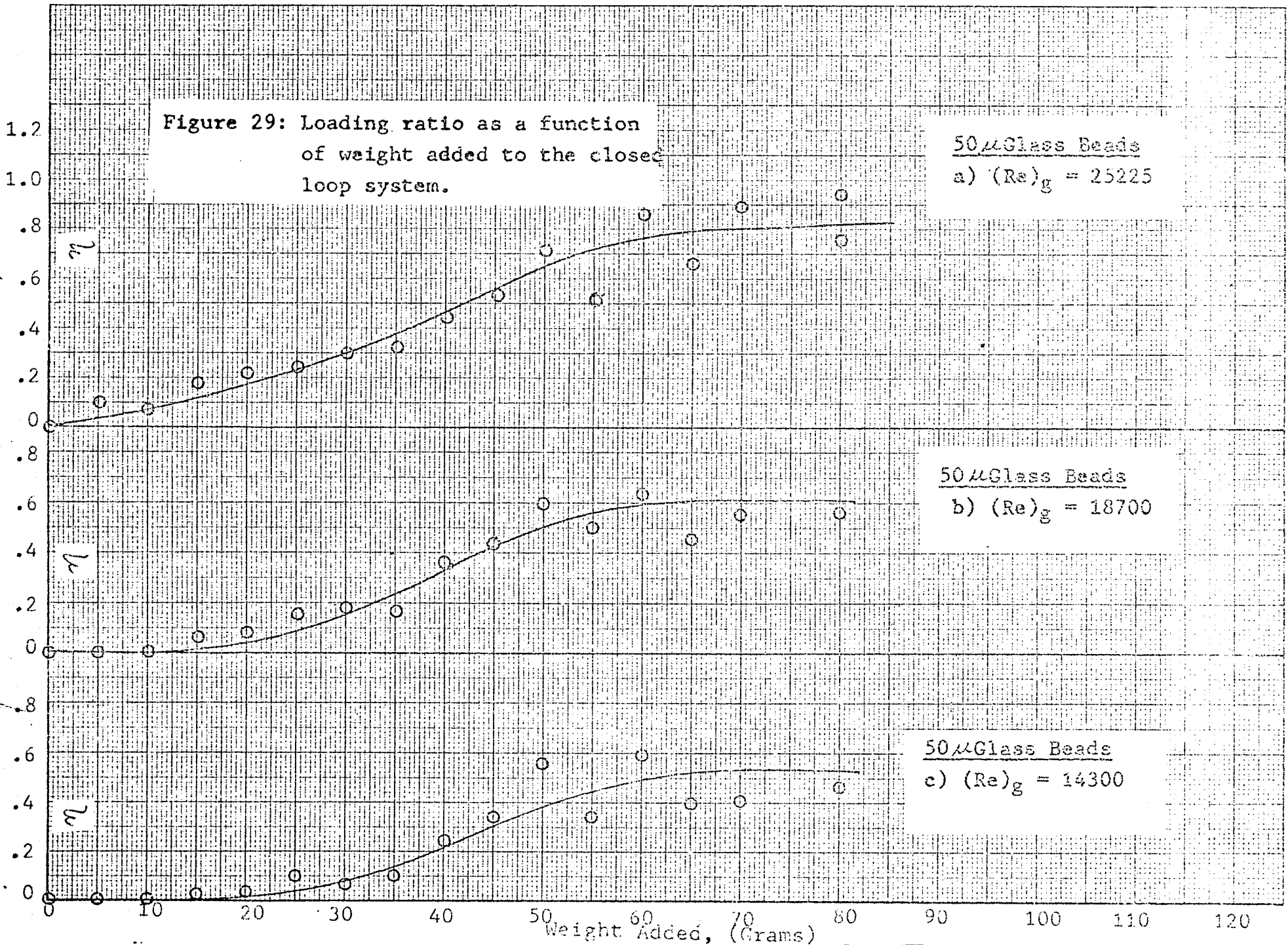
The shape of these curves could be explained on the basis of differing interacting effects. The lower portion of the curves is less steep and indicates that a small percentage of the particles added to the system are

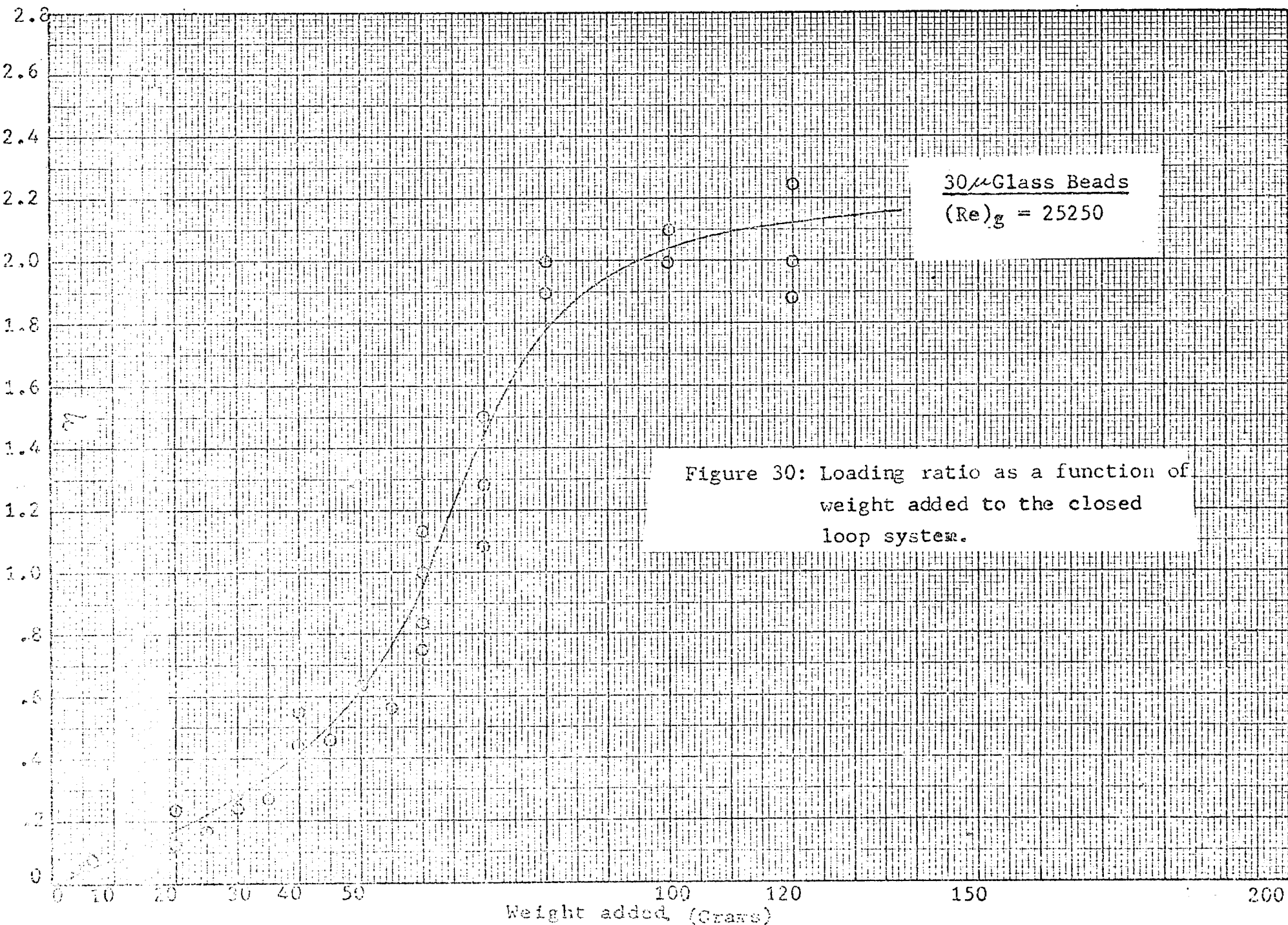
Figure 29: Loading ratio as a function of weight added to the closed loop system.

50  $\mu$  Glass Beads  
a)  $(Re)_g = 25225$

50  $\mu$  Glass Beads  
b)  $(Re)_g = 18700$

50  $\mu$  Glass Beads  
c)  $(Re)_g = 14300$





30 μ Glass Beads  
 $(Re)_g = 25250$

Figure 30: Loading ratio as a function of weight added to the closed loop system.

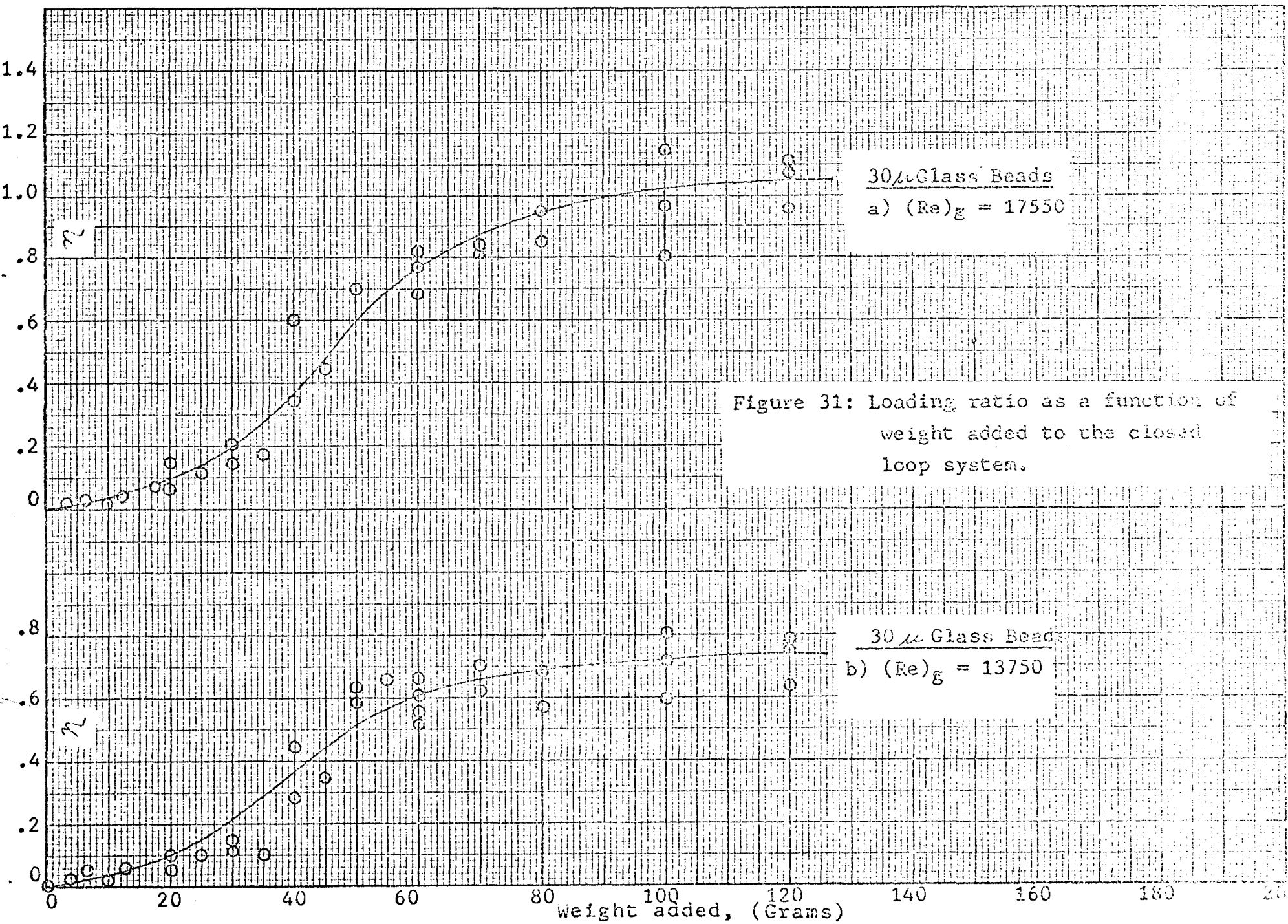


Figure 31: Loading ratio as a function of weight added to the closed loop system.

Figure 32: Loading ratio as a function of weight added to the closed loop system.

#279 Glass Beads  
(Re)<sub>g</sub> = 25900

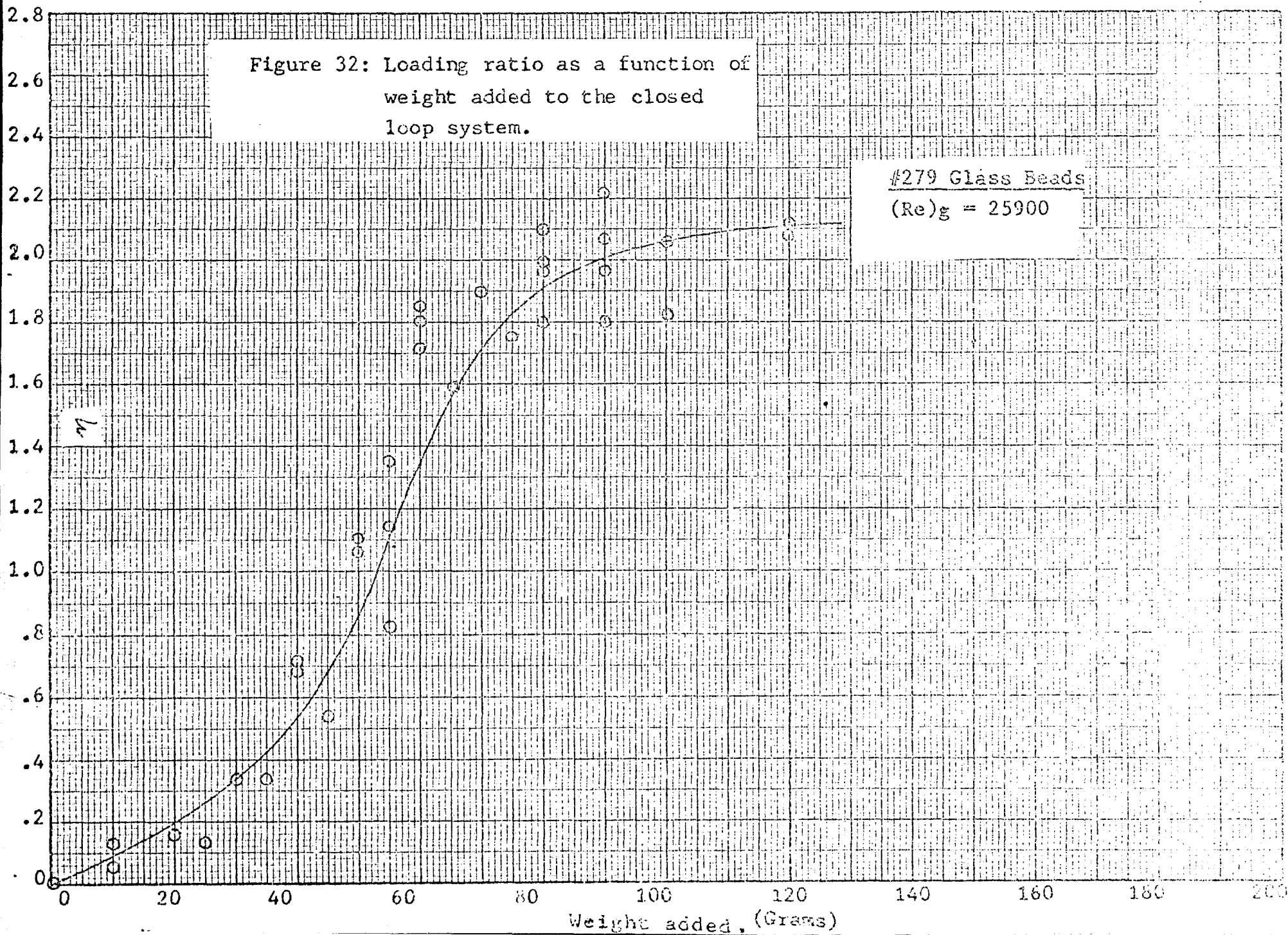


Figure 33: Loading ratio as a function of weight added to the closed loop system

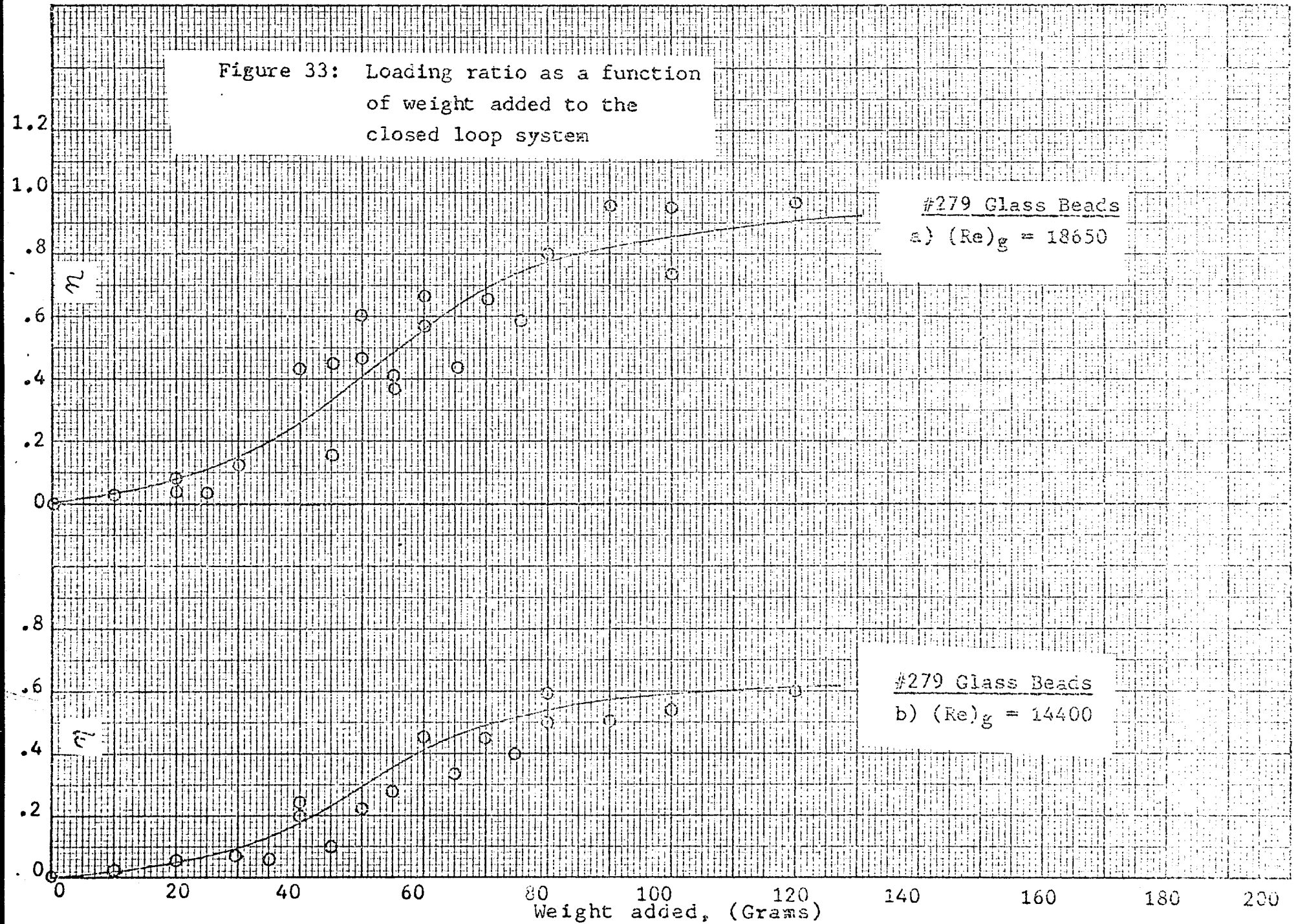


Figure 34: Loading ratio as a function of weight added to the closed loop system at high Reynolds number.

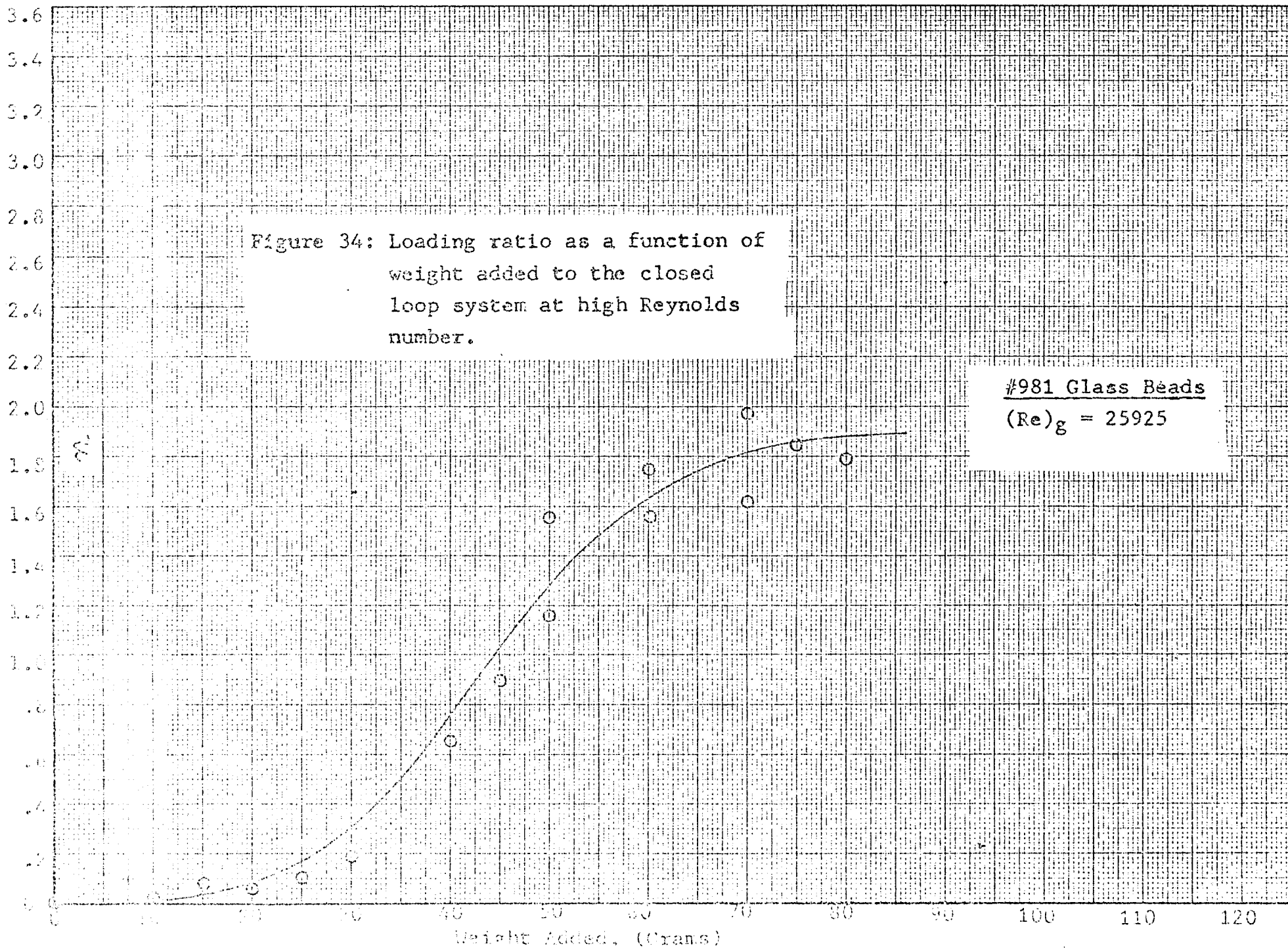


Figure 35: Loading ratio as a function of weight added to the closed loop system.

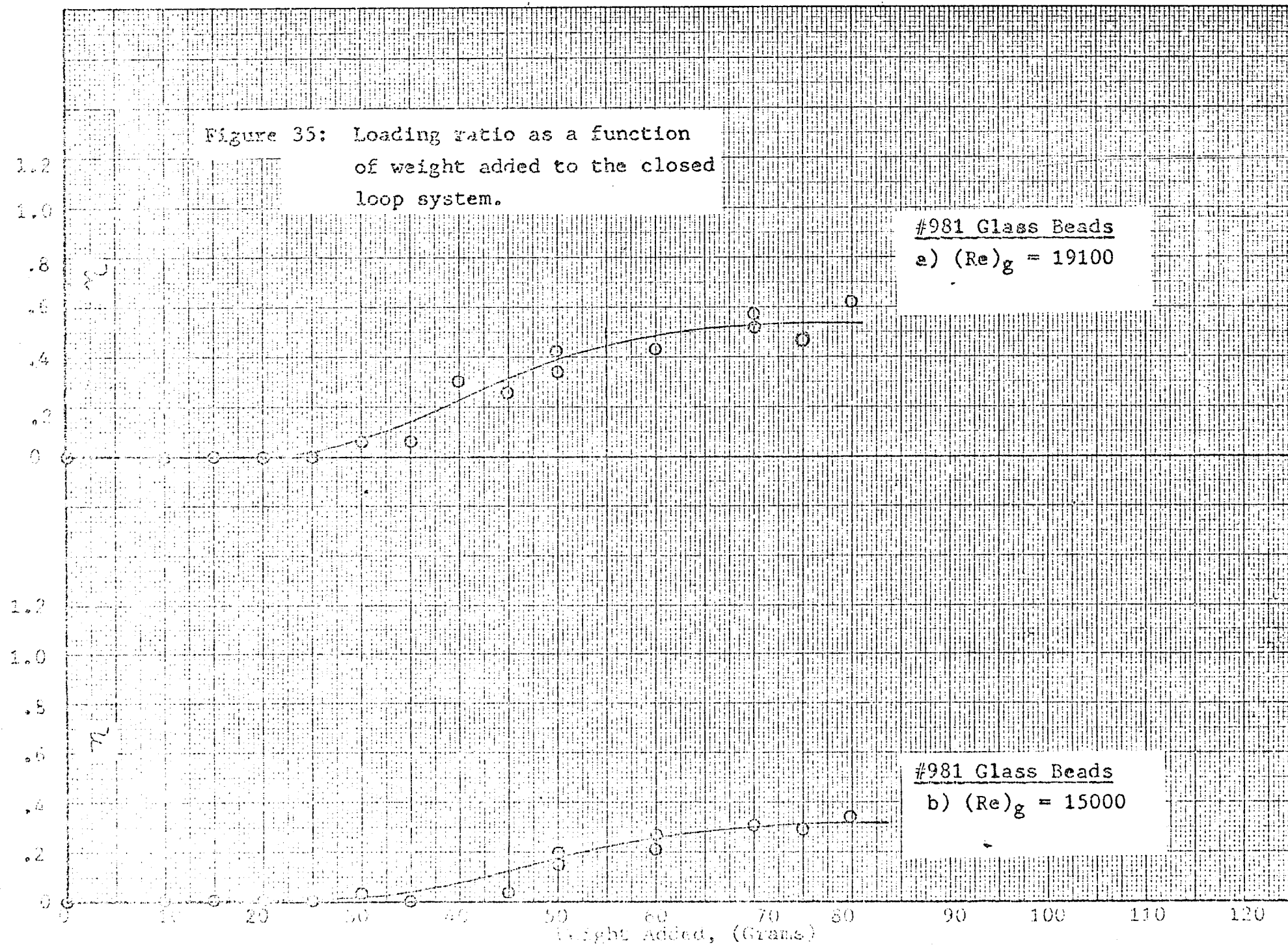
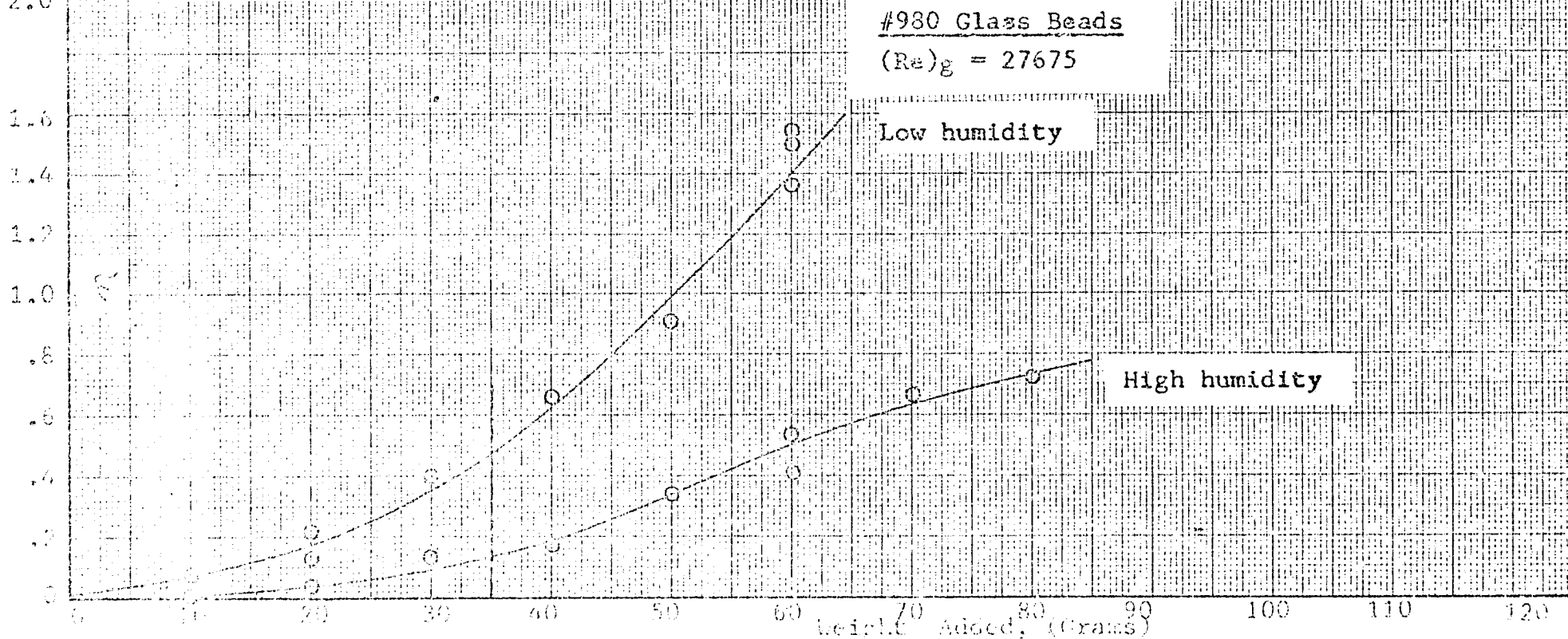


Figure 36: Loading ratio as a function of weight added to the closed loop system at high Reynolds number.



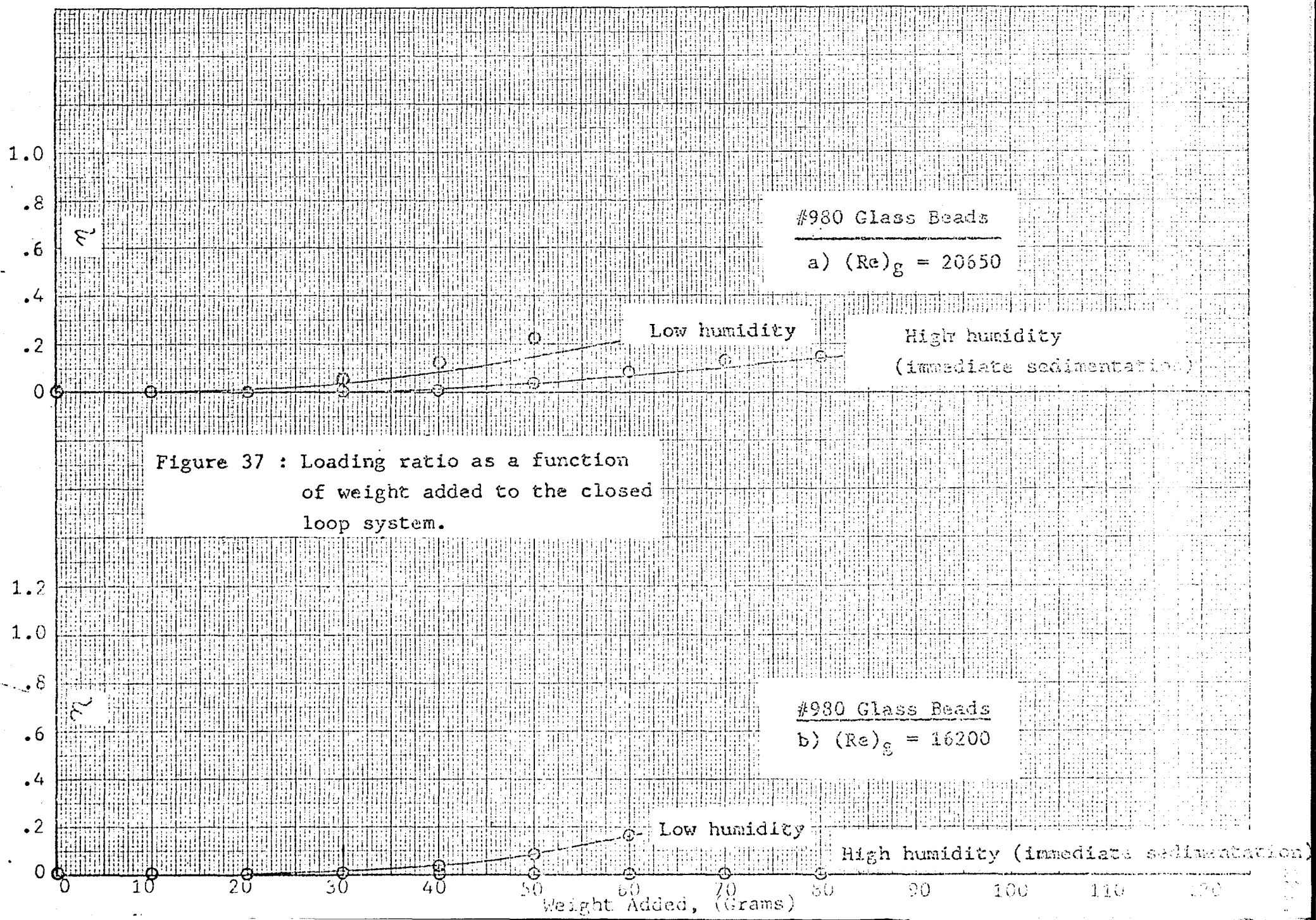


Figure 37 : Loading ratio as a function of weight added to the closed loop system.

actually circulating. For larger particles ( $D_p \approx 50\mu$  and  $30\mu$ ) this effect is less pronounced than for the smaller particles (#279, 981, and 980) and is primarily due to the particles accumulating in irregularities of the loop. For the smaller particles the effect can also be attributed to their cohesiveness which initially makes them more difficult to circulate and possibly indicates a tendency for these particles to coat the loop (although this was not visually observed except for the smallest size glass beads).

The steep portion of these curves appears to occur after the surface irregularities are filled and after cohesive forces are no longer sufficient to prevent additional particles from being circulated. The steepness of this portion of the curve depends on the particle size. The smaller particles being more easily entrained by the flowing gas show a steeper slope than the larger particles which are not as easily carried by the fluid.

After this steep portion, the figures indicate a second flattened part in the curves. In this region adding more particles to the system does not appear to significantly increase the amount of circulating material. This area of the curve is a result of particle sedimentation, so that as particles are added other particles settle out at approximately the same rate. This sedimentation can be partially attributed to the size of the particles, as the  $50\mu$  particles exhibit this second flattened portion of the curve at the lowest concentration for the highest

Reynolds number. However, since this flattening out occurs at approximately the same loading ratio for the other particles and since at the lower Reynolds numbers the smaller particles exhibit flat portions at the same or lower concentrations than the large particles, a more complicated explanation is indicated. The cohesiveness of the fine particles almost certainly will tend to cause sedimentation at lower concentrations than would be otherwise expected. Furthermore, the lower the gas velocity, the more important the cohesive force since reentrainment in the fluid stream becomes more difficult. The visual observations through the pyrex viewing sections of the loop indicated when accumulation of particles at the bottom of the horizontal section occurred. Concentrations at which this "salting out" was visually observed are indicated by vertical dashed lines in figures 29-37. It should be noted that sedimentation was somewhat difficult to see for the large particles due to their small volume at the incipient point of sedimentation. Smaller particles presented a different problem in that since the flow appeared very thick even at relatively low concentrations (due to the large number of dispersed particles), it was difficult to see particles at the bottom of the pyrex section.

For any given particle size, the visual observations indicate that particle accumulation begins at lower concentrations for the lower Reynolds numbers. This is not unexpected since the carrying capacity of the fluid is reduced when the gas velocity is decreased. The 50%

particles were not observed to "salt out" at the concentrations and Reynolds numbers considered in this investigation. It was observed, however, that although these particles did not accumulate at the bottom of the tube, they did exhibit what has been described as "bouncing flow" (particles are transported by bouncing along the bottom of the tube) through many of the runs. Furthermore, these particles also visually appeared to be flowing in a somewhat "segregated" manner with a higher particle density appearing at the bottom of the tube than at the top.

Accumulation of the  $30\mu$  particles visually appeared to occur at loading ratio of about 0.7 for the lowest Reynolds number range ( $(Re)_g = 13700$ ) and approximately 1.0 for the middle Reynolds number range ( $(Re)_g = 17500$ ). No accumulation was noted for the high Reynolds number runs ( $(Re)_g = 25,500$ ), although the "bouncing flow" and "segregated" flow phenomena were evident.

The #279 glass beads were found to accumulate at all three gas Reynolds numbers, as indicated by the figures. However, "segregated" flow was not noticeable by eye although some "bouncing flow" was observed for high concentrations in the lowest Reynolds number runs.

The #981 glass beads appeared to behave almost identically to the #279 beads. Accumulation of particles for the two lower Reynolds number conditions occurred at about the same concentrations. No accumulation was observed at the higher Reynolds number for loading ratios up to approximately

1.9; accumulation for the #279 beads at this Reynolds number was observed at a loading ratio of 2.1. It should be pointed out, however, that no signs of either "bouncing" flow or "segregated" flow were visually observed for the #981 beads at any of the flow conditions considered. The 980 glass beads were found to be the most difficult glass particles to work with. Because of their extremely cohesive nature they began accumulating at the lowest particle concentrations for all Reynolds number conditions. They were also difficult to remove from the loop during clean-out. Accumulation or coating was observed in both vertical and horizontal sections and was of a different nature than observed for the larger particles. It appeared that this accumulation was quite fine, covered large areas of the tube and had a dendritic type structure. A photograph of this phenomenon will be presented in a later section of the dissertation.

The #980 glass bead were also found to be affected by the moisture in the air. Figures 36 and 37 show the difference in concentrations obtained when the same amount of #980 glass beads were added under different conditions of room and particle moisture content. In the condition labelled "high humidity" the 980 particles were exposed to room air for approximately two weeks and the experimental runs were made on relatively humid days. For the condition labelled "low humidity", runs were made with fresh #980 glass beads on days of relatively low humidity. As indicated by the figures the higher moisture content caused lower concentrations for

any given weight of particles added at all Reynolds numbers. As can be seen from figure 37, no particle flow at all was obtained for the lowest Reynolds number run. However, no difference between friction factor data for the high and low humidity runs was observed at any given loading ratio. The fact that humidity affects the number of small particles flowing through the system but not the frictional pressure loss associated with a given loading ratio for these particles, further indicates that the cohesiveness of the smaller particles rather than gravitational forces is the primary factor in determining the concentration at which accumulation occurs at any given gas velocity. It should also be pointed out that data for the #980 glass beads were not obtained at higher loadings due to the fact that at higher loadings than shown in figure 36 and 37, clogging of the pressure taps in both the vertical and horizontal test sections occurred.

Friction factors. - Friction factors for both the vertical and horizontal test sections were calculated using measurements of pressure drop, inlet static pressure, centerline velocity, temperature and loading ratio. The calculations were performed by using the incompressible flow equation for friction factor based on the density of the pure gas. This equation may be represented by

$$f_s' = \frac{2g_c \Delta P_{fD}}{\rho_g v_g^2 L} \quad (49)$$

where

$$\Delta P_f = \Delta P_{mc} - \Delta P_h - \Delta P_a \quad (50)$$

with  $\Delta P_{mc}$  = measured pressure drop corrected for length of manometer leads in vertical section.

$\Delta P_h$  = gravity pressure head in vertical test section.

$\Delta P_a$  = acceleration pressure losses.

In these closed loop experiments the pressure loss across each test section was very small compared to the static pressure and the flow was essentially isothermal in nature so that  $\Delta P_a$  was found to be negligible. The gravity pressure head is a function not only of the gas properties but the solids loading as well and can be described as

$$\Delta P_h = (1 + \eta) L \rho_g \quad (51)$$

The corrected measured pressure drop is the measured pressure drop plus the head of air in the manometer leads between the pressure taps in the vertical section,

$$\Delta P_{mc} = \Delta P_m + L \rho_g \quad (52)$$

so that for the vertical section

$$\Delta P_f = \Delta P_m - \eta \rho_g L \quad (53)$$

In the horizontal test section the gravity pressure head is zero and  $\Delta P_{mc} = \Delta P_m$  so that

$$\Delta P_f = \Delta P_m$$

The gas densities used in the calculation for the friction factor in each test section were corrected for the average static pressure across the test section. Measured values of the static pressure at different centerline velocities are presented in figure 38 for the horizontal test section and

Figure 38: Variation of Horizontal section static pressure with centerline mass velocity for the closed loop system.

Static pressure (in. Hg. gage)

$\rho v c_s \left( \frac{lb}{ft^2 sec} \right)$

10 X 10 TO THE CENTIMETER 46 1513  
MADE IN U.S.A.  
KEUFFEL & ESSER CO.

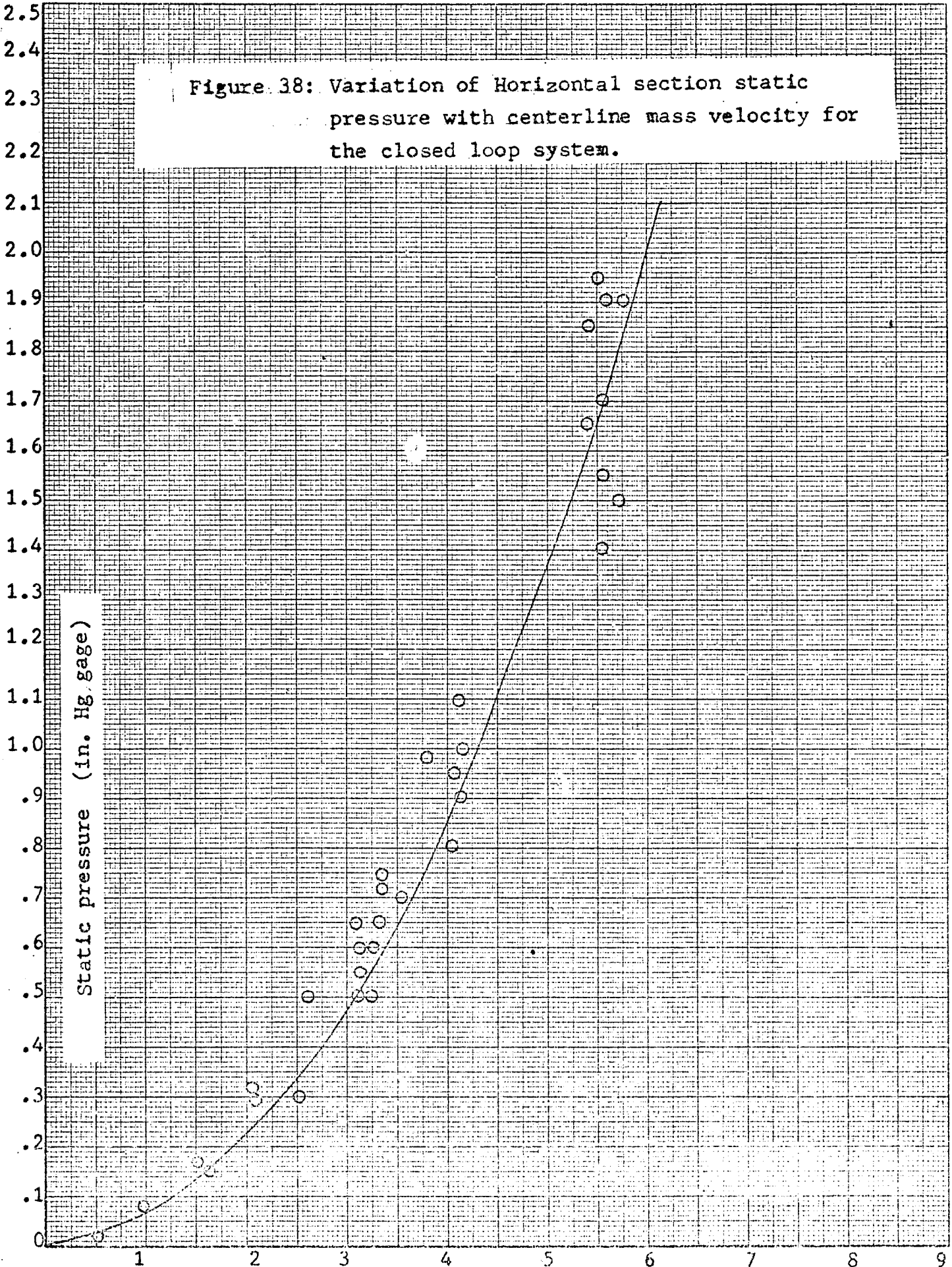


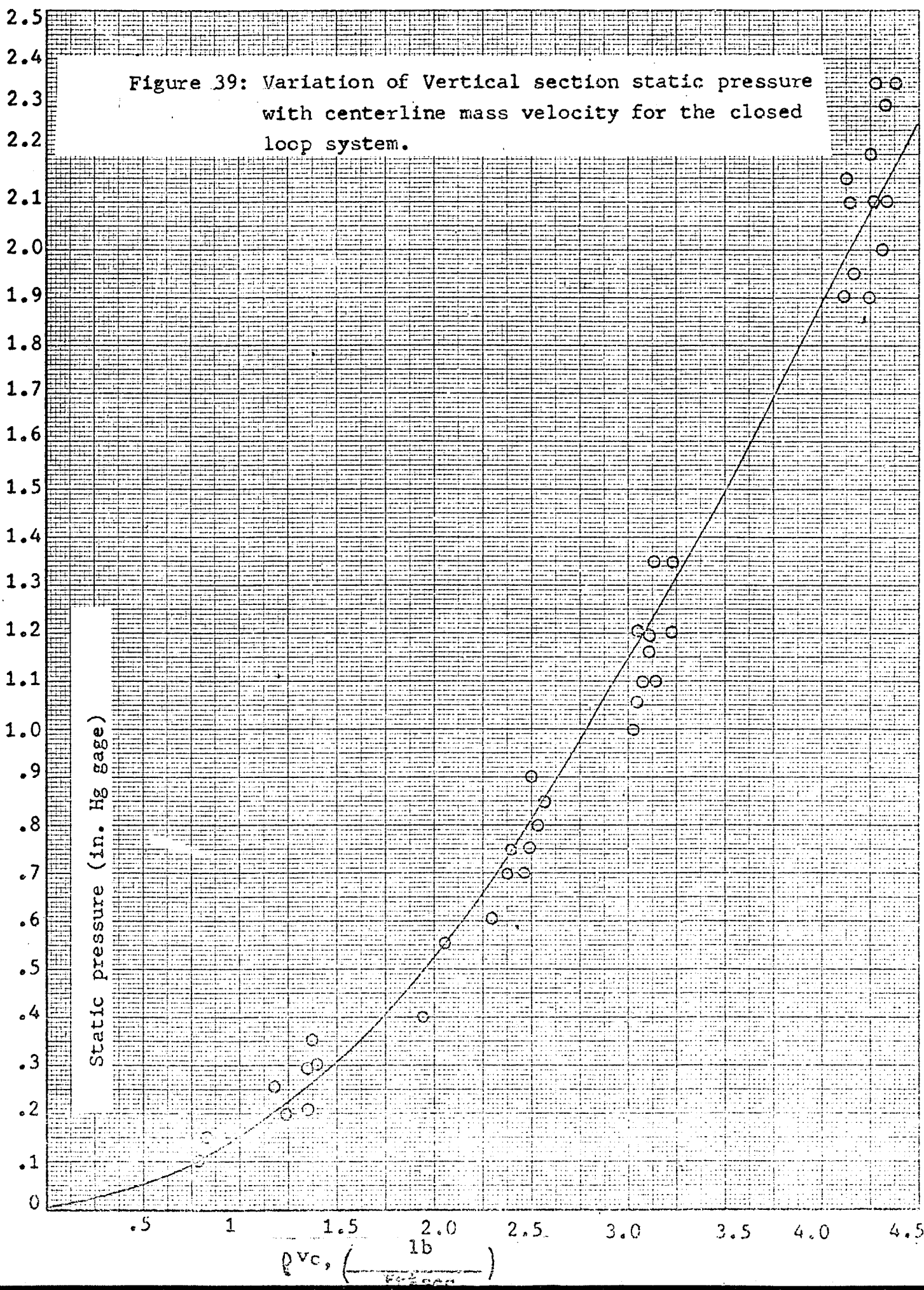
figure 39 for the vertical test section. The velocities required for the calculations were determined from centerline velocities measured on the anemometer, multiplied by .8 and corrected for flow area and pressure differences in each test section, assuming constant gas mass flow rate through the loop.

In order to present the results for each test section in a convenient manner, the calculated suspension friction factor based on equation 12 was divided by the appropriate pure gas friction factor for each test section. Equation 34 for the horizontal section and equation 35 for the vertical section. This friction factor ratio was then plotted as a function of solids loading ratio for the case of either the horizontal or vertical test section for each of the five particle sizes and each of three Reynolds number ranges. These plots are shown in figures 40 - 64. Curves indicated on the figures were faired by eye to represent the data points on each plot.

Figures 40 and 41 are plots of the  $50\mu$  particle data for the horizontal section. As can be seen from the data there is an increase in the friction factor ratio as the loading ratio is increased for each of the Reynolds numbers; the increase at any given loading ratio being greatest for the lowest Reynolds number and least for the highest Reynolds number. Figures 42 and 43 are plots of the  $50\mu$  particle data for the vertical test section. These plots indicate a large decrease in the friction factor ratio as loading ratio

Figure 39: Variation of Vertical section static pressure with centerline mass velocity for the closed loop system.

10 X 10 TO THE CENTIMETER 46 1513  
19 X 25 CM.  
KEUFFEL & ESSER CO.



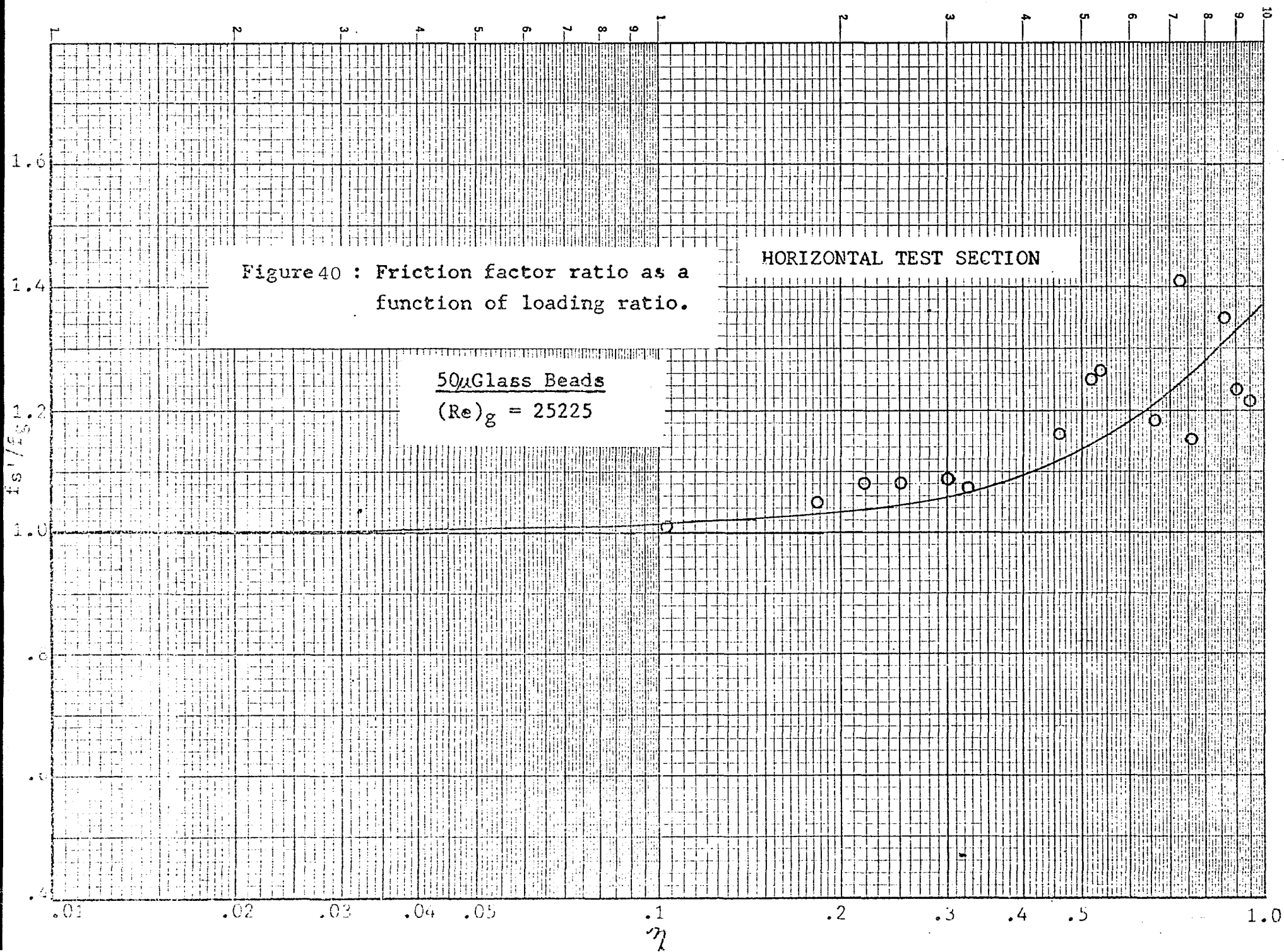
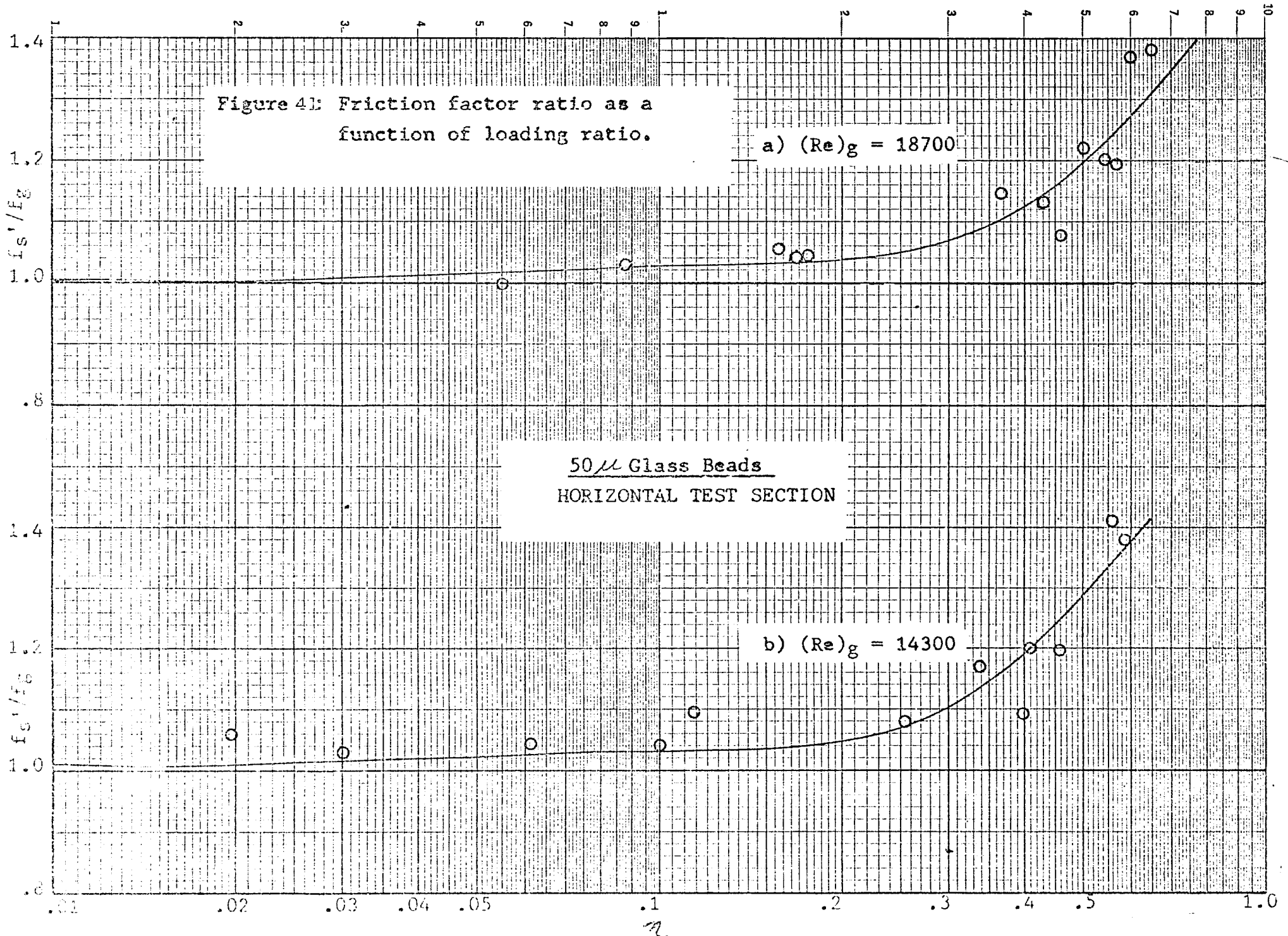


Figure 4B: Friction factor ratio as a function of loading ratio.

a)  $(Re)_g = 18700$

50  $\mu$  Glass Beads  
HORIZONTAL TEST SECTION

b)  $(Re)_g = 14300$



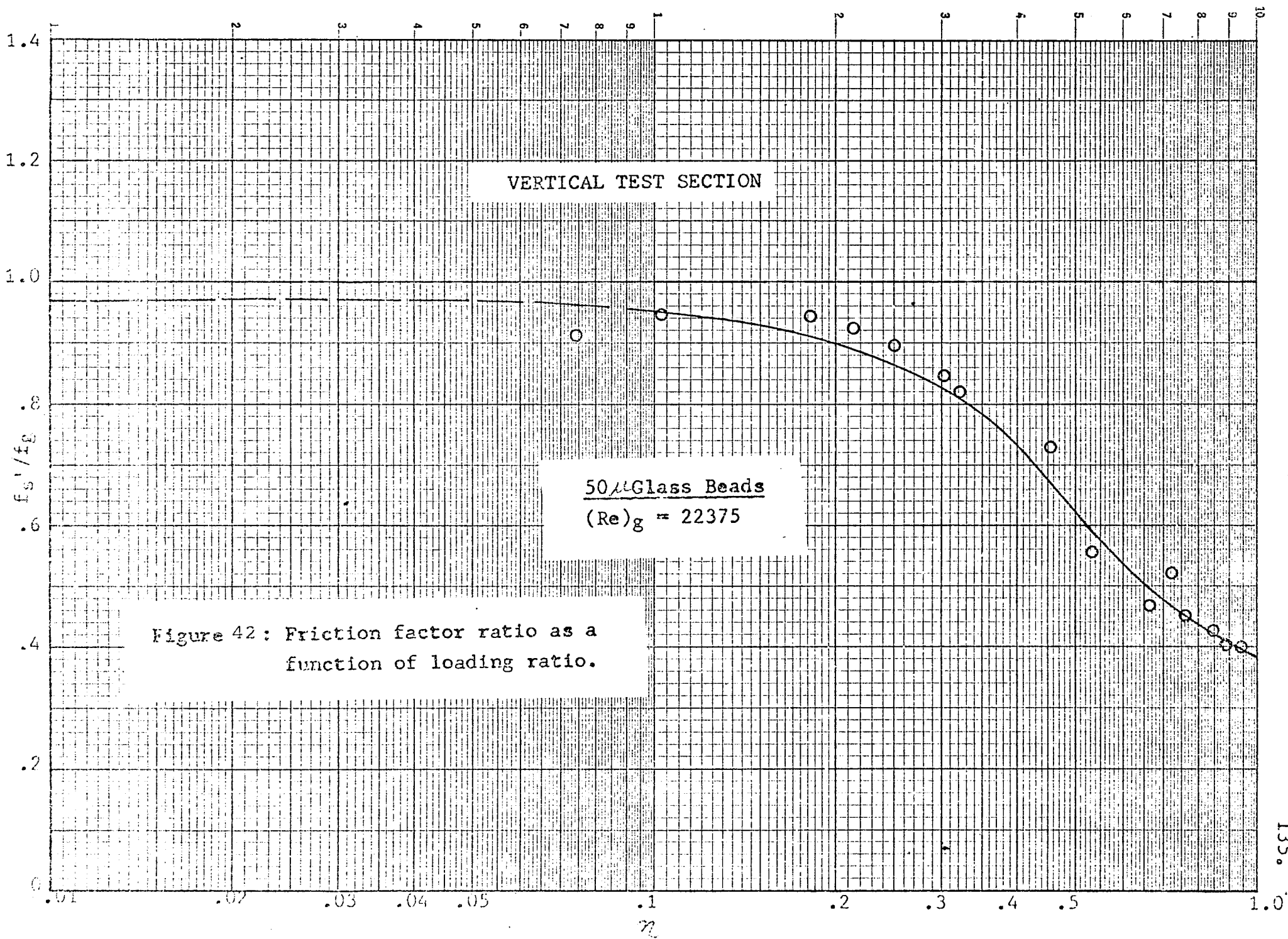
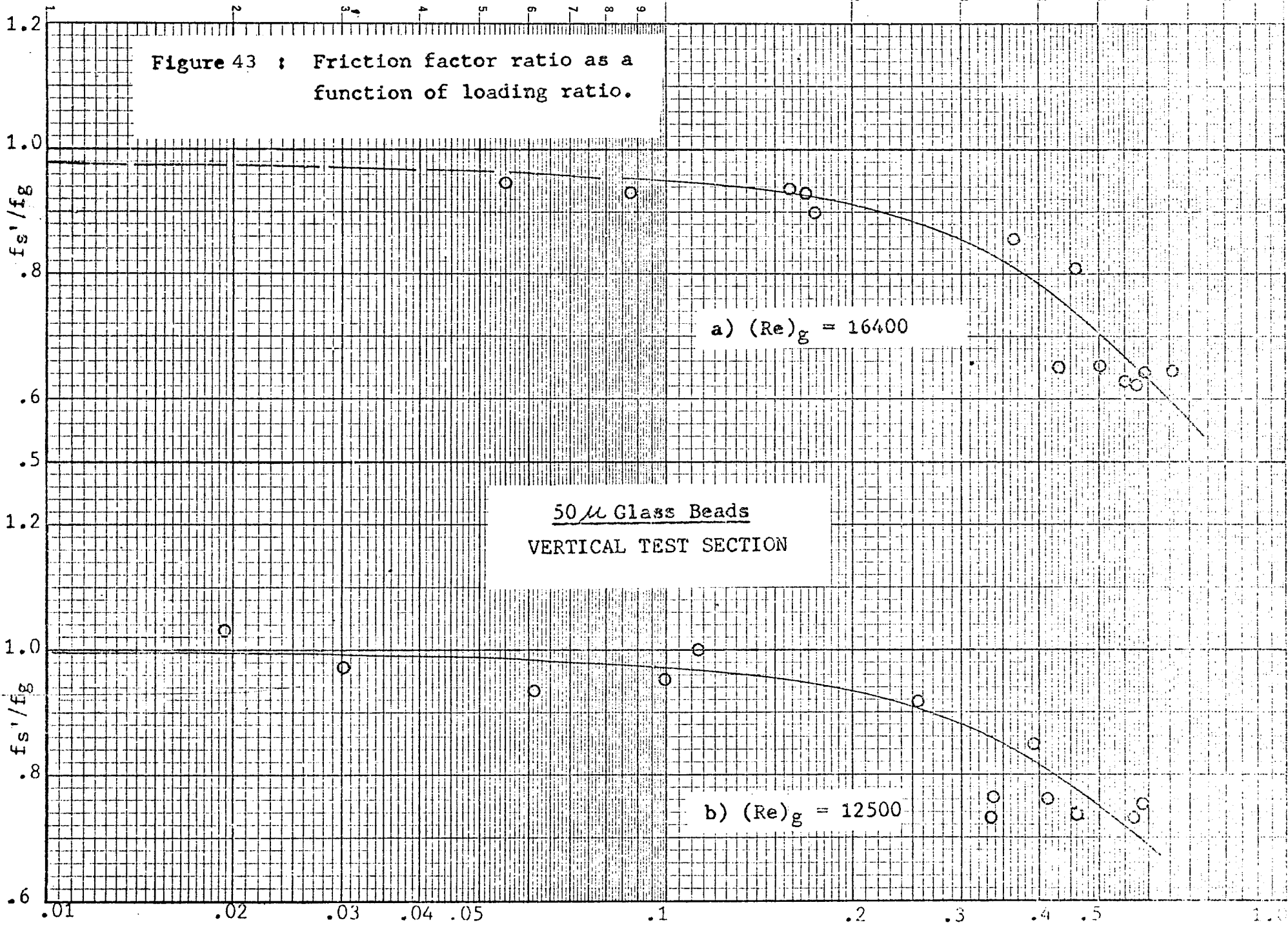
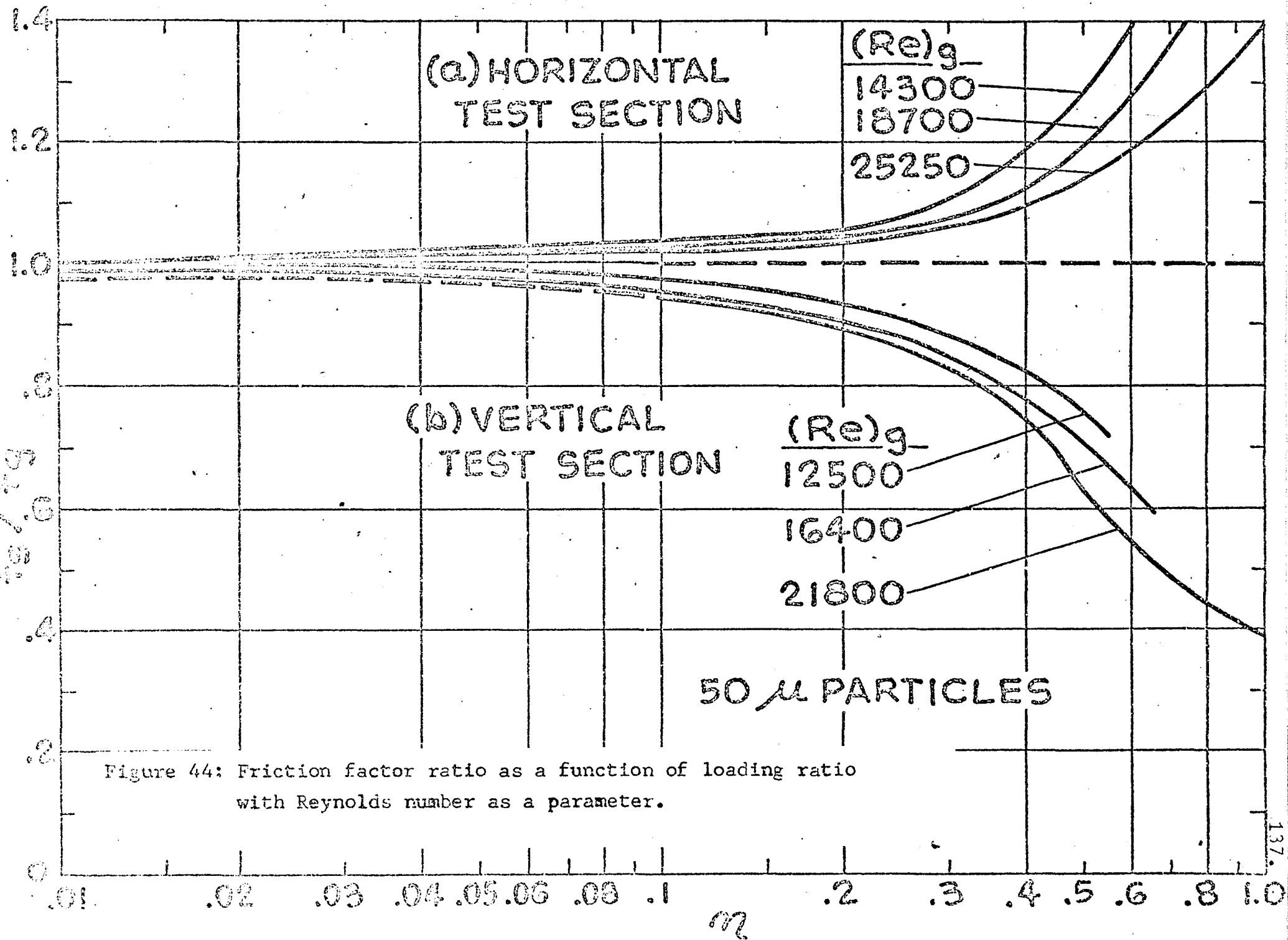


Figure 42: Friction factor ratio as a function of loading ratio.

Figure 43 : Friction factor ratio as a function of loading ratio.





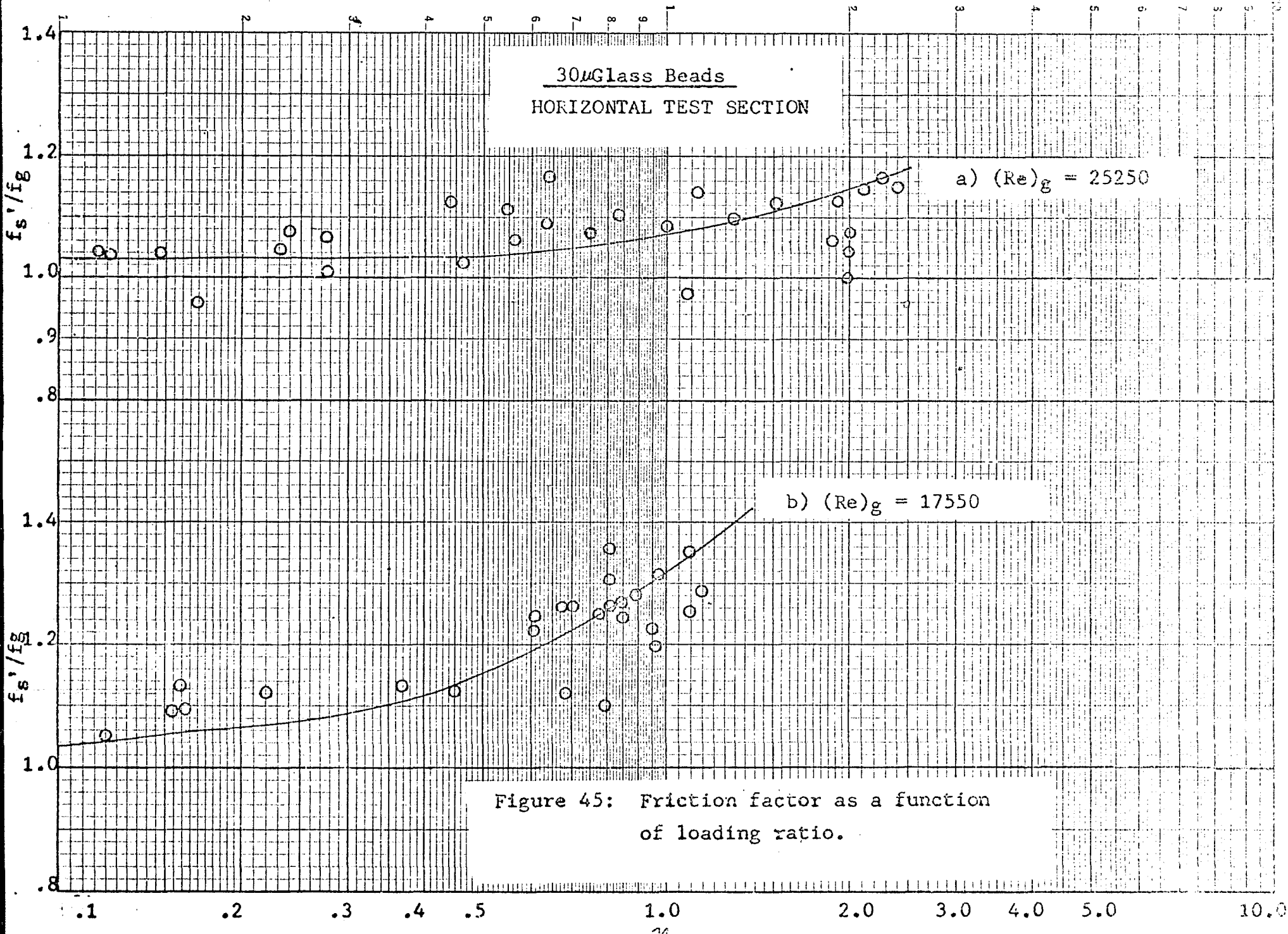


Figure 45: Friction factor as a function of loading ratio.

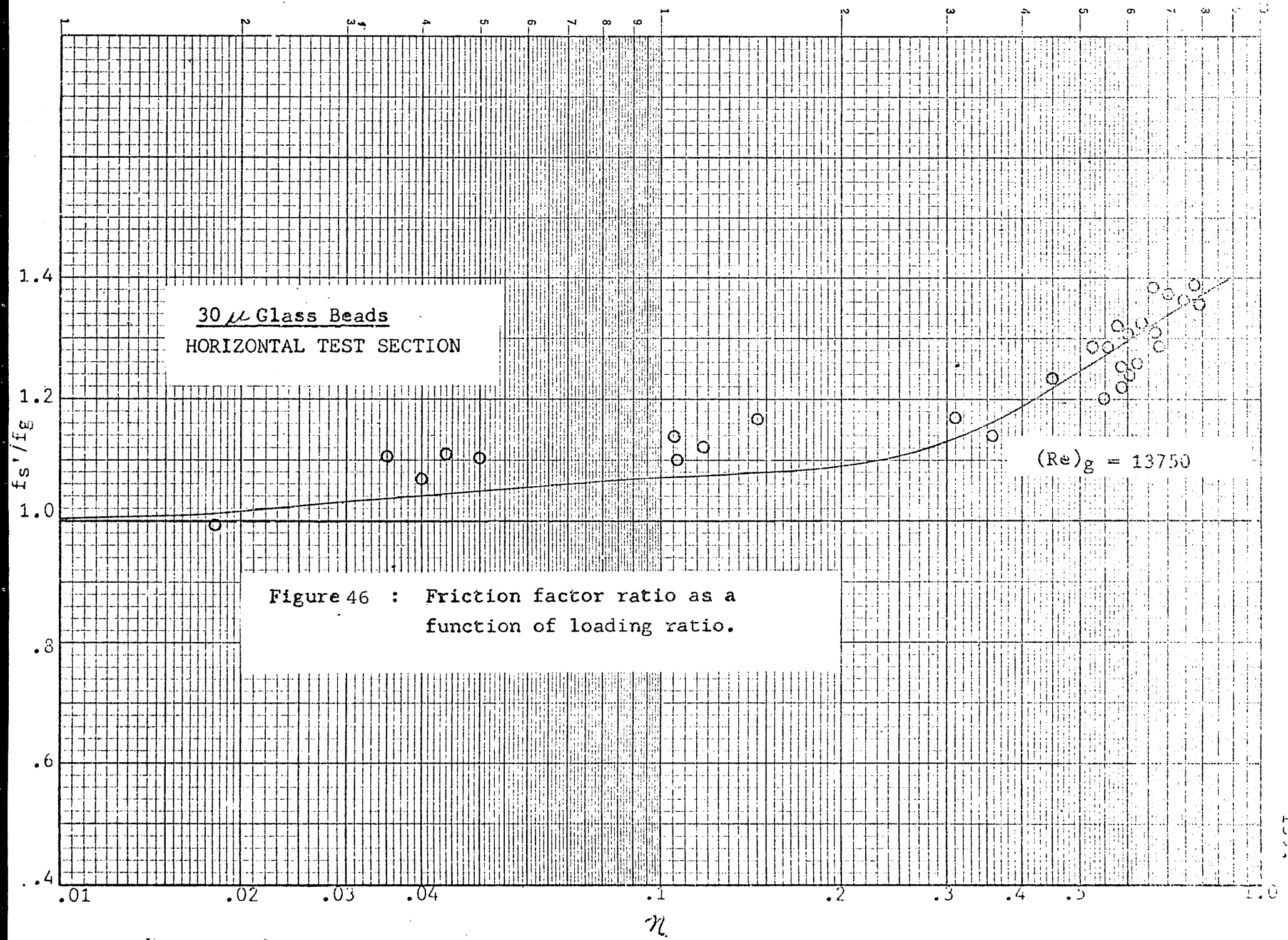
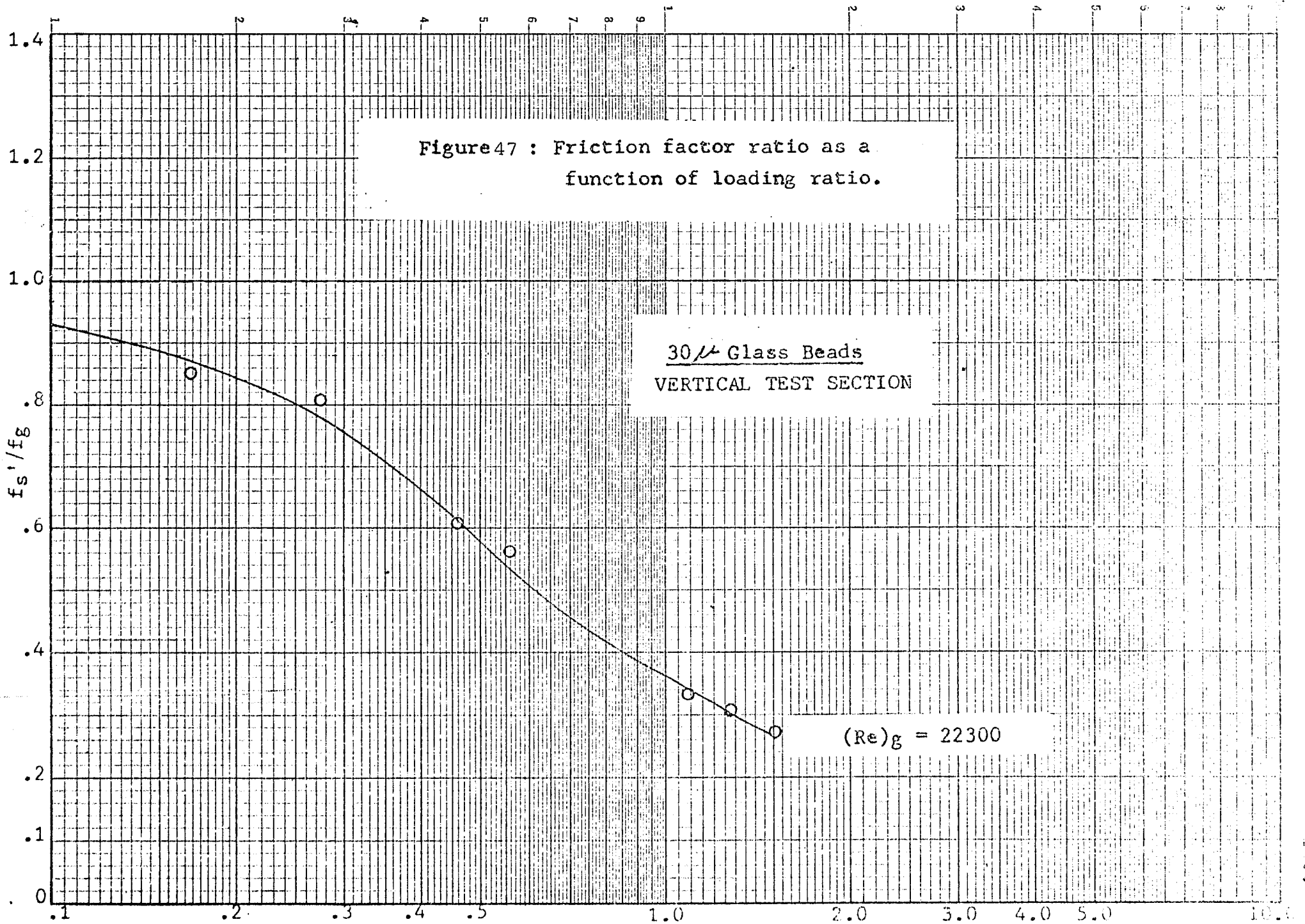
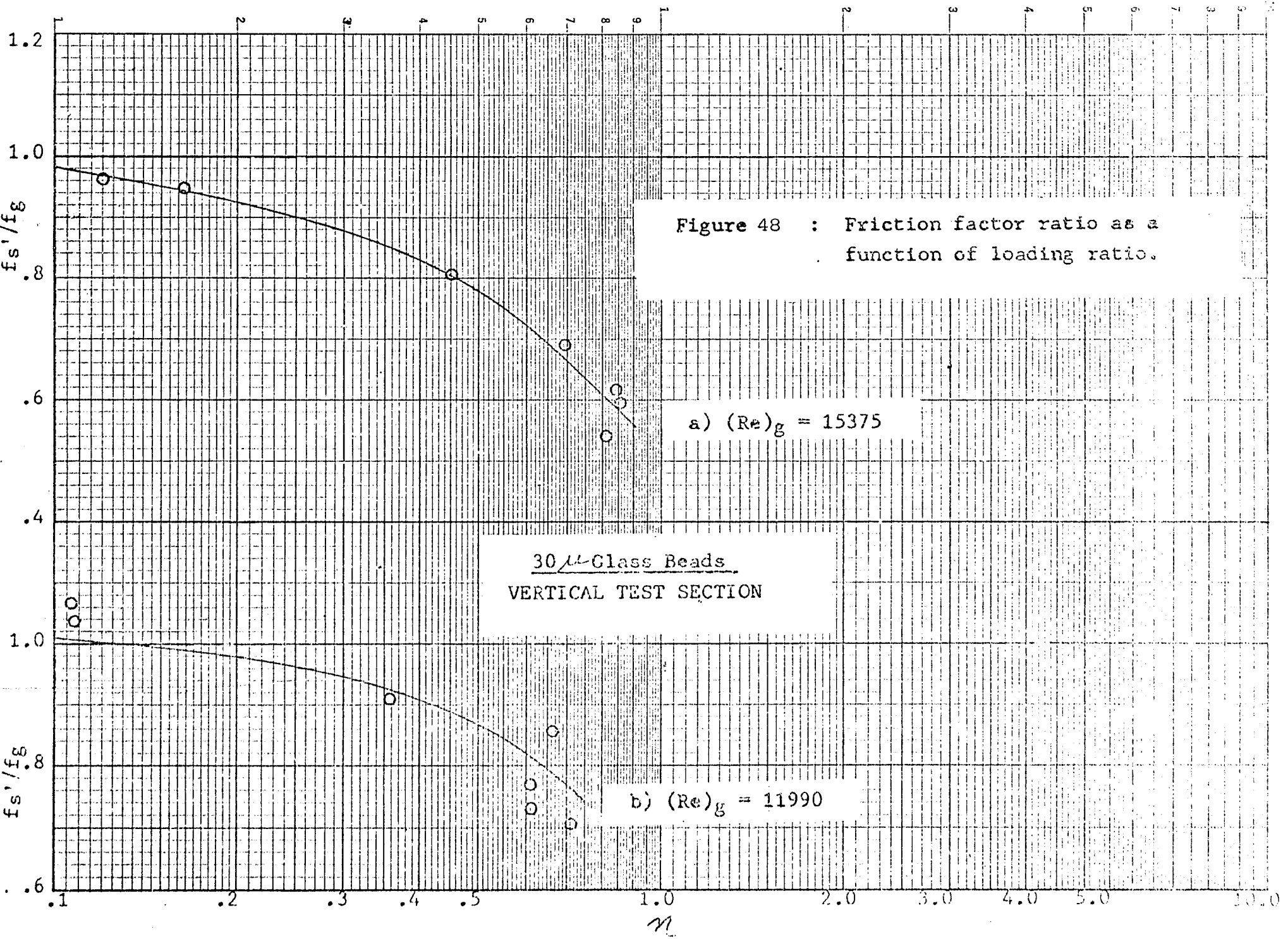


Figure 46 : Friction factor ratio as a function of loading ratio.





is increased. This "drag reduction" is found to be greatest at the highest Reynolds number and smallest with the lowest Reynolds number. In other words, the lower the Reynolds number the higher the friction factor ratio for both the vertical and the horizontal test sections. Figure 42 also indicates that at the higher Reynolds number the "drag reduction" appears to have an inflection, perhaps indicating a tendency to reach a minimum. Figure 44 is a composite of the curves drawn through the data for the six different conditions studied using the  $50\mu$  particles, and clearly indicates both the difference between the horizontal and vertical test sections as well as the Reynolds number effect in each section.

The results obtained using the  $30\mu$  particles are indicated in figures 45 - 48 and appear to exhibit similar trends as the  $50\mu$  particles, with less drag increase in the horizontal test section but slightly greater "drag reduction" in the vertical section for the highest Reynolds number condition. Figure 47 also indicates a slight inflection in the friction factor curve for the highest Reynolds number in the vertical test section. The Reynolds number effect is perhaps most dramatically indicated by figure 49 which is a composite showing the curves representing the three different Reynolds number conditions in the horizontal and vertical test sections using the  $30\mu$  glass beads.

The results of the friction factor study using #279 glass beads (approx. avg.  $D_p = 25\mu$ ) are shown in figures

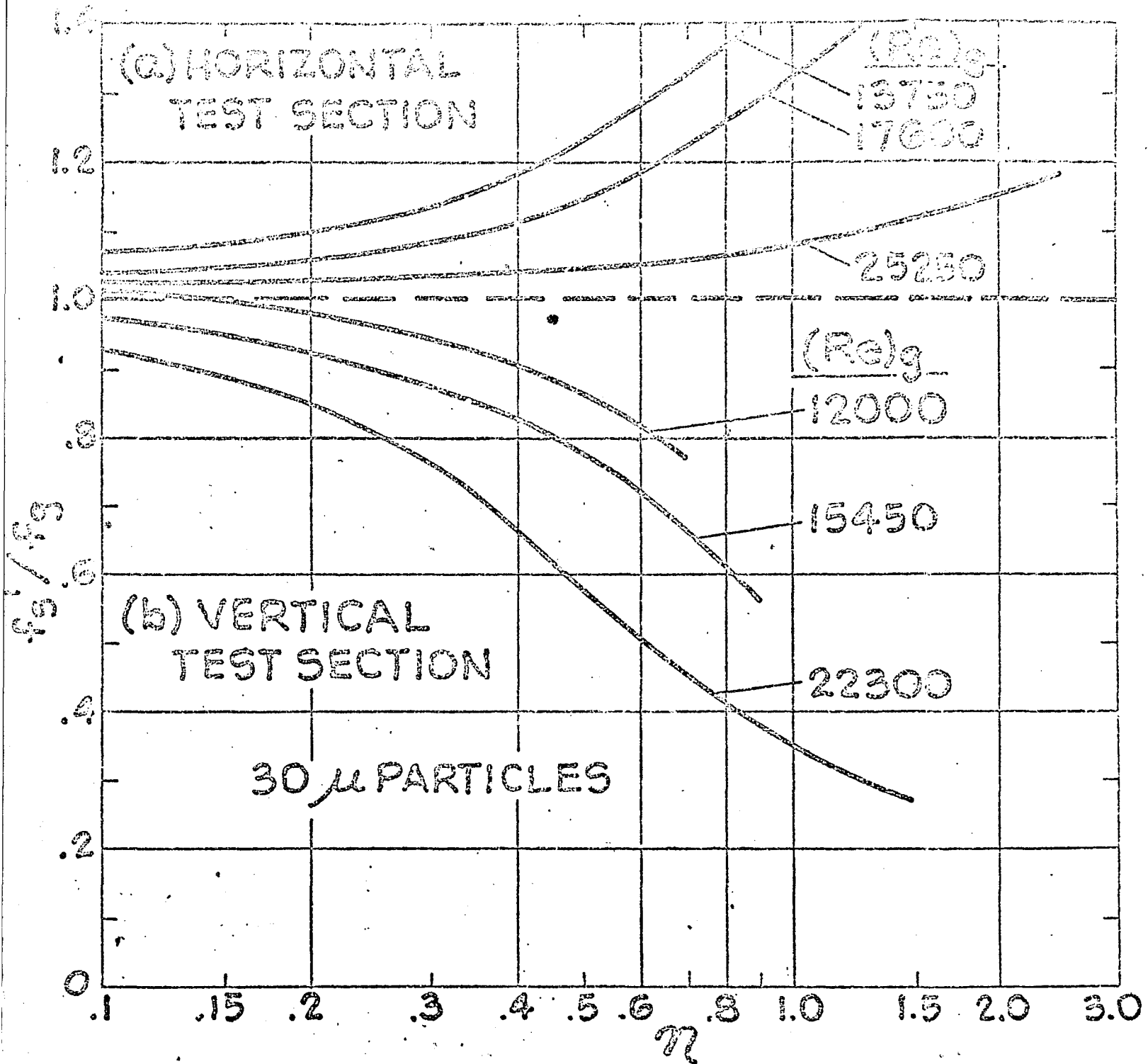


Figure 49: Friction factor ratio as a function of loading ratio with Reynolds number as a parameter.

50 and 51. The figures, representing the results in the horizontal test section, indicate that although "drag reduction" is obtained at the two lowest Reynolds numbers this decrease is only 18% maximum and there is actually a slight drag increase for the lowest Reynolds number condition. The results with the vertical test section shown in figures 52 and 53, again indicate "drag reduction" but not to the extent indicated with the larger particles. No inflection point is exhibited in the vertical test section results but an inflection point and a minimum friction factor ratio seem to be shown for the two highest Reynolds numbers in the horizontal test section. These results are more clearly illustrated by the composite for the #279 glass beads shown in figure 54.

Figures 55 - 58 indicate the friction factor results obtained using the #981 glass beads. The 3M Corporation had indicated that these beads have an average diameter of approximately  $15\mu$ , however, subsequent analysis using a Coulter counter has indicated that these particles have a mean diameter of approximately  $20\mu$  with a somewhat different size distribution than the #279 glass beads. These particle size analyses will be presented in a later section of this dissertation. In view of the fact that the #279 and #981 particles have approximately the same mean particle size it is not surprising that the results in both the horizontal and vertical test sections as indicated by figures 50 - 53 and 55 - 58 show the same general trends and are approximately

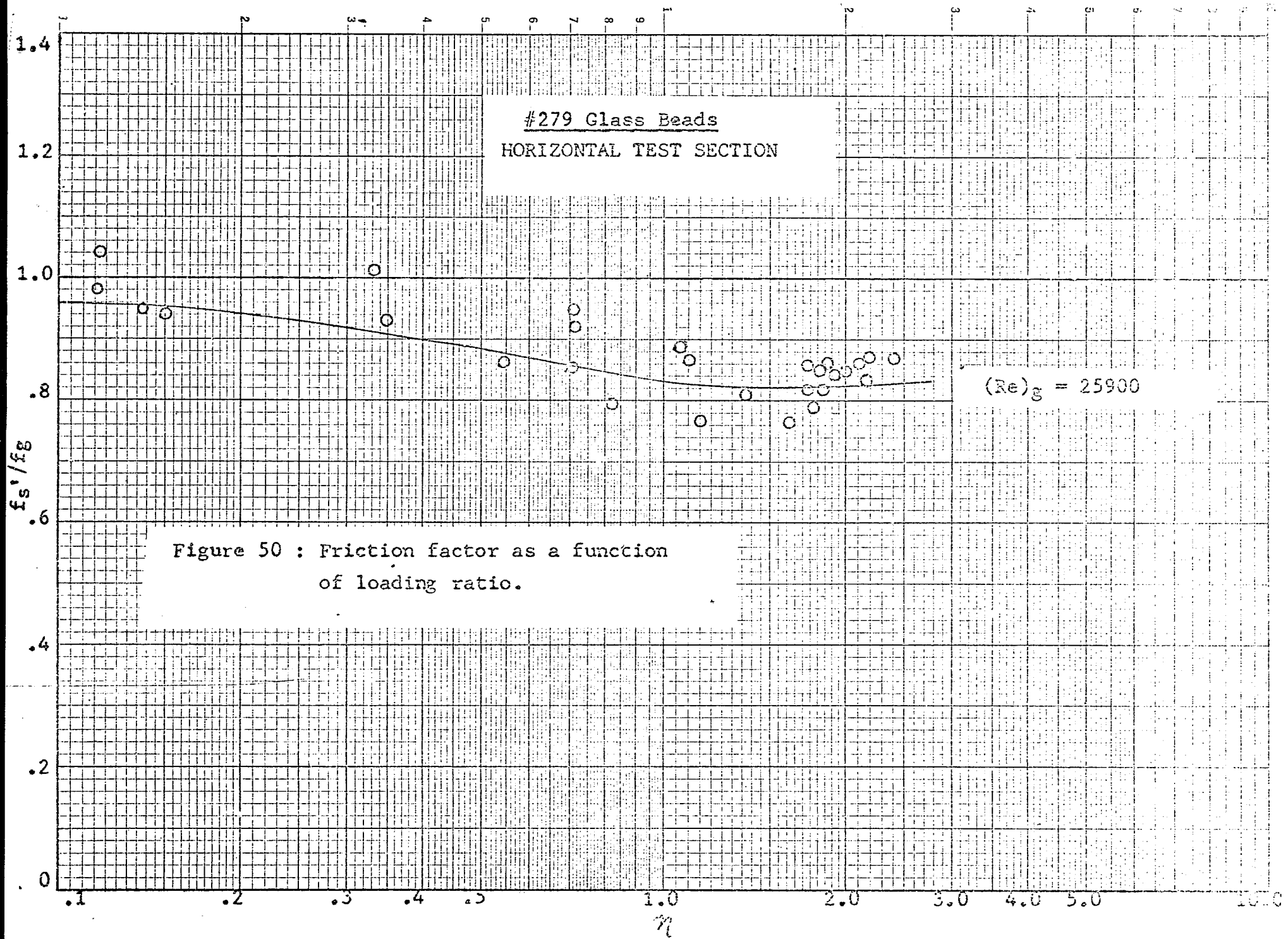
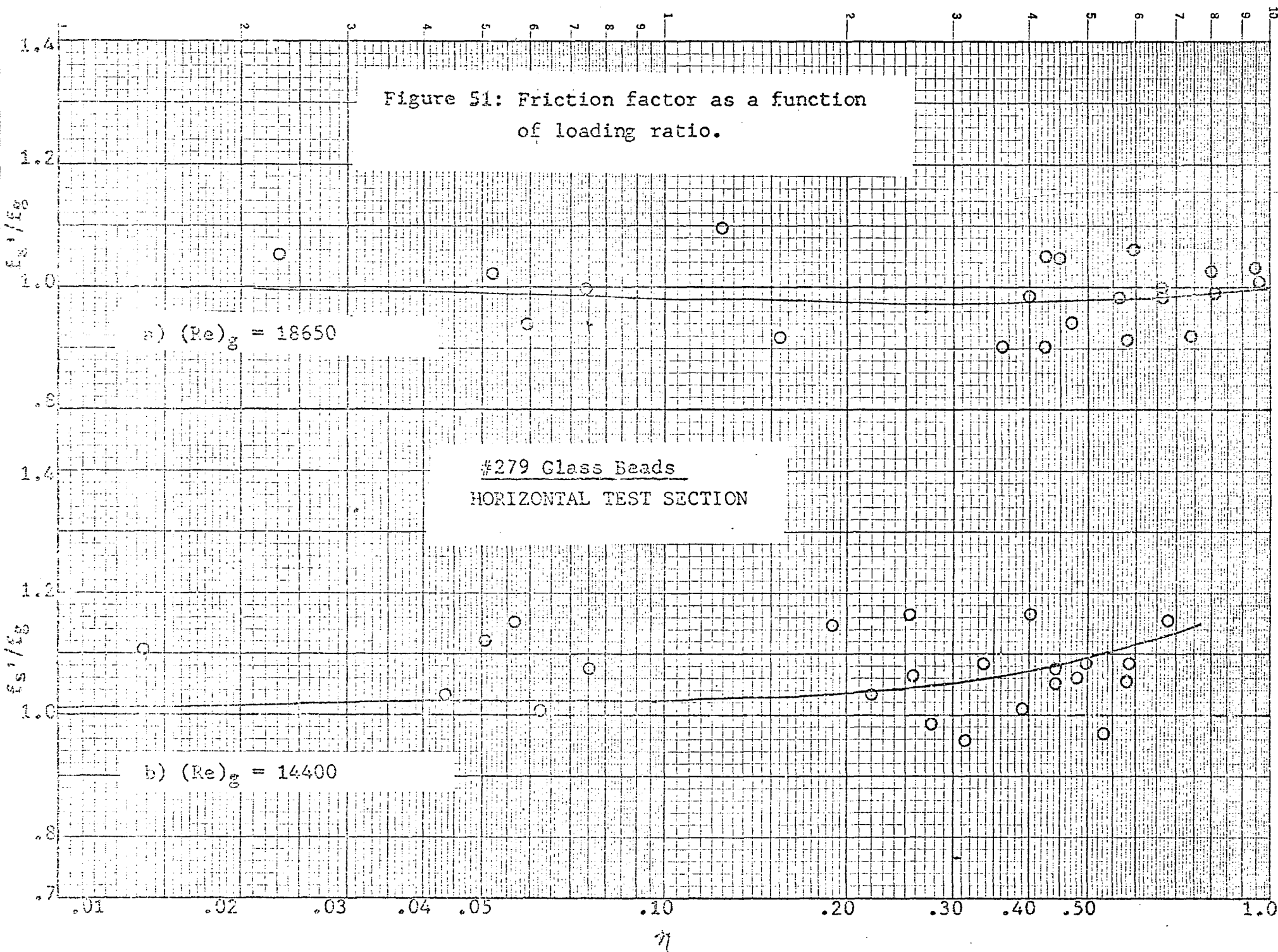


Figure 50 : Friction factor as a function of loading ratio.

Figure 51: Friction factor as a function of loading ratio.



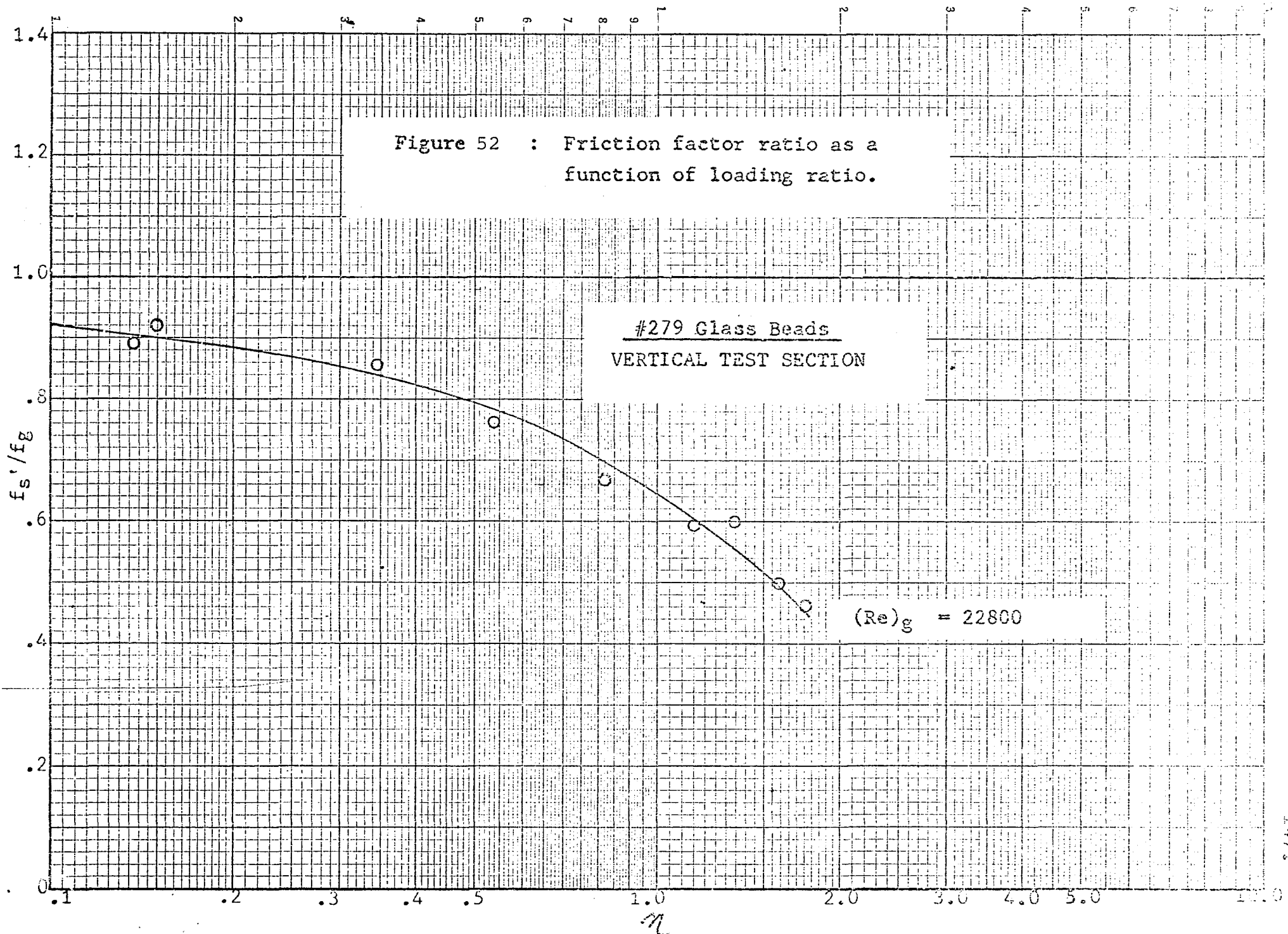
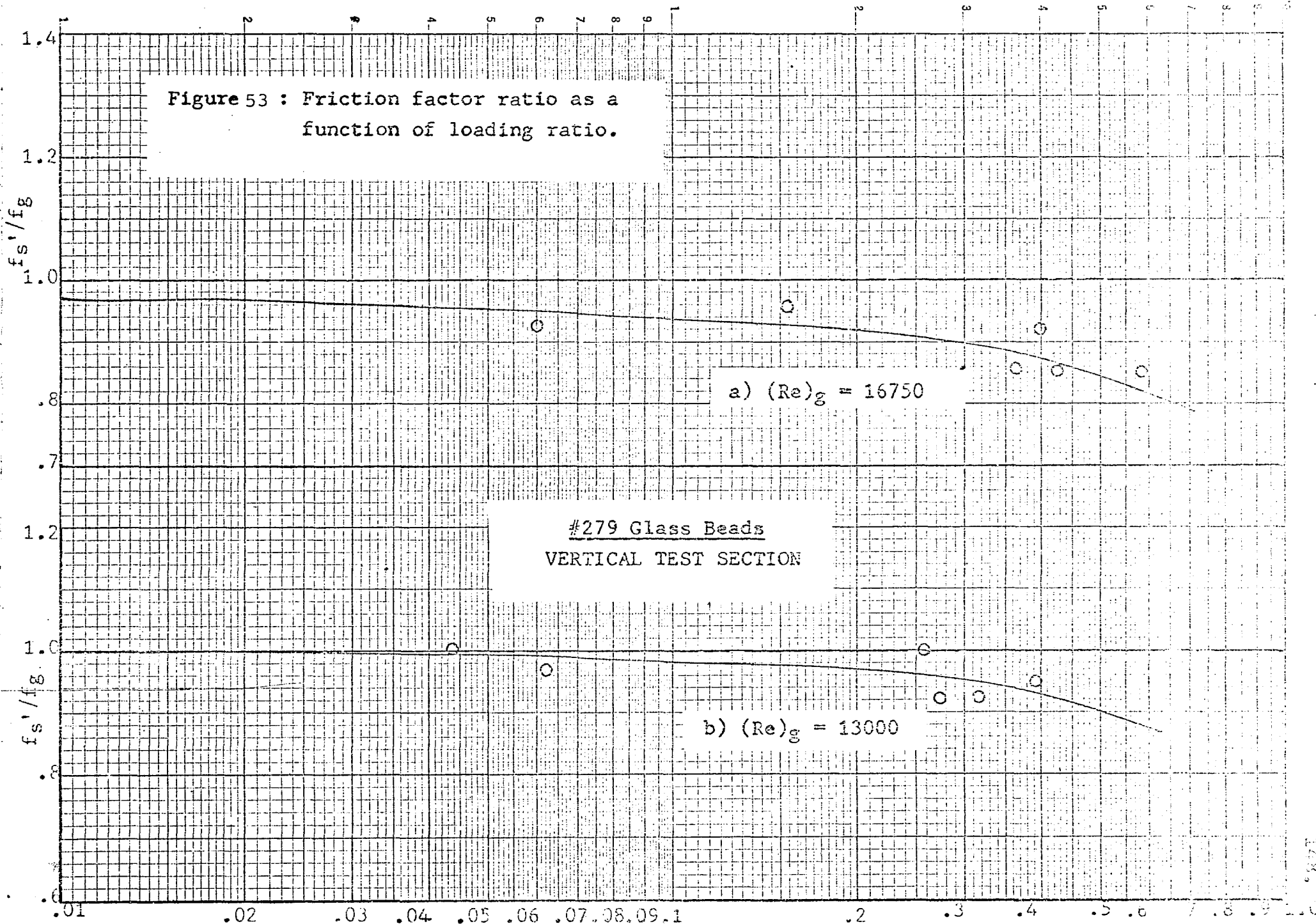
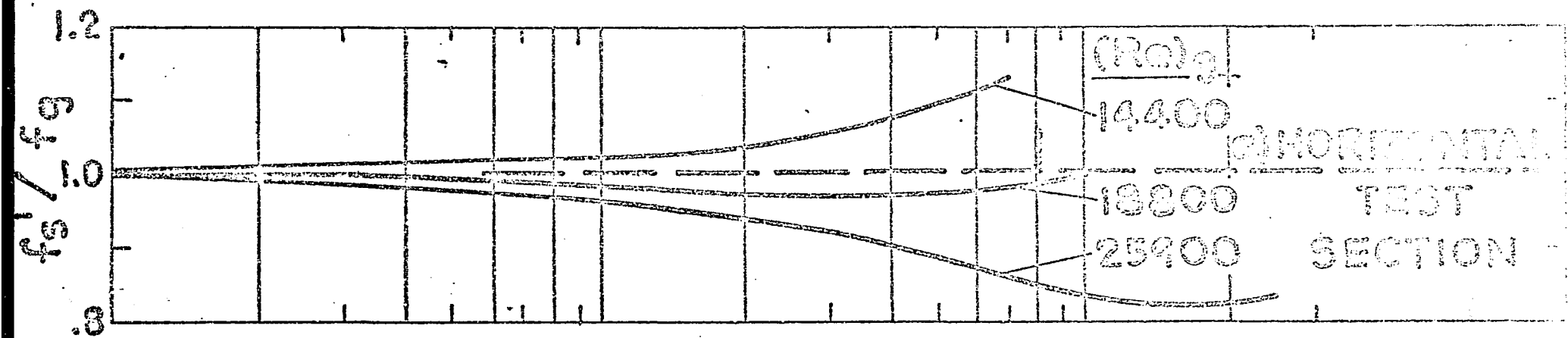


Figure 53 : Friction factor ratio as a function of loading ratio.





#279 GLASS BEADS

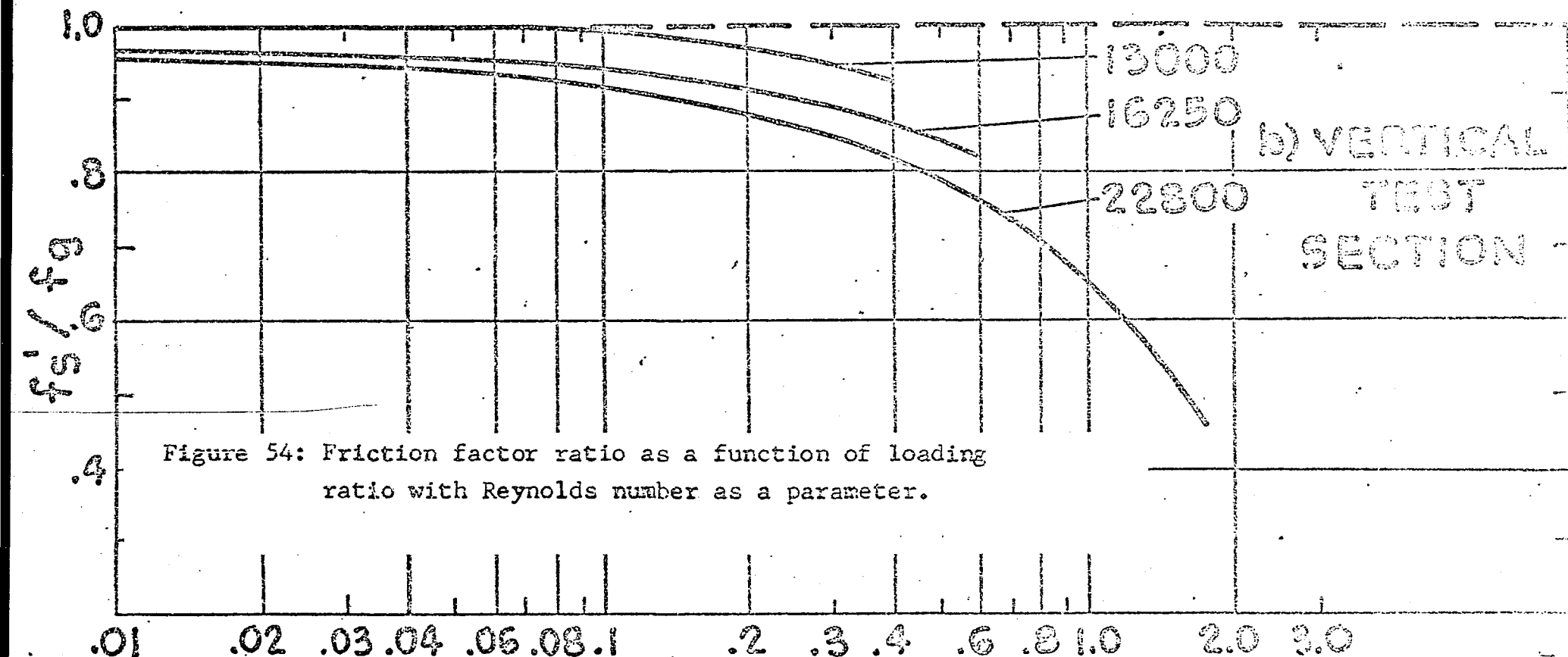


Figure 54: Friction factor ratio as a function of loading ratio with Reynolds number as a parameter.

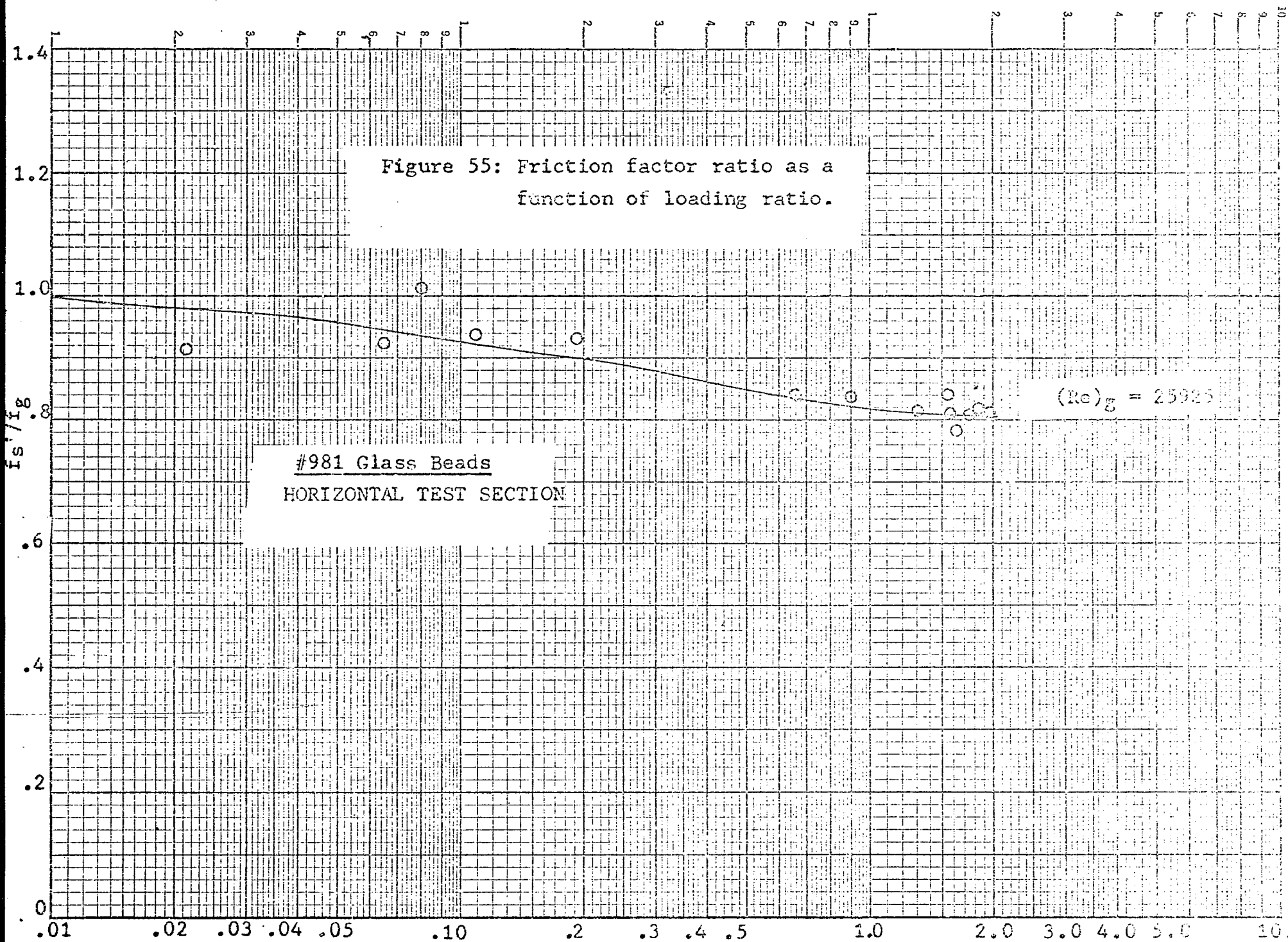


Figure 56: Friction factor as a function of loading ratio.

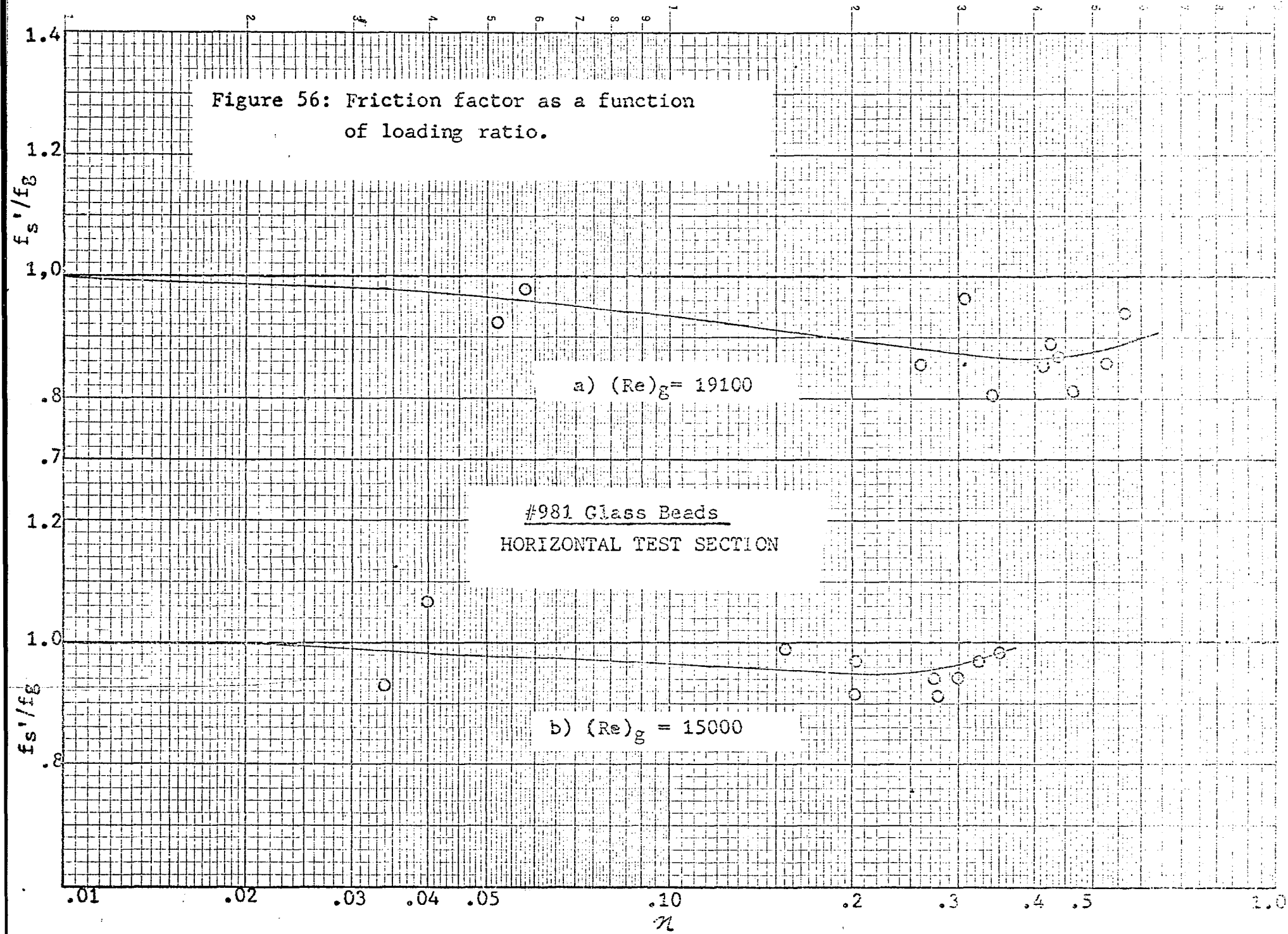


Figure 57: Friction factor ratio as a function of loading ratio.

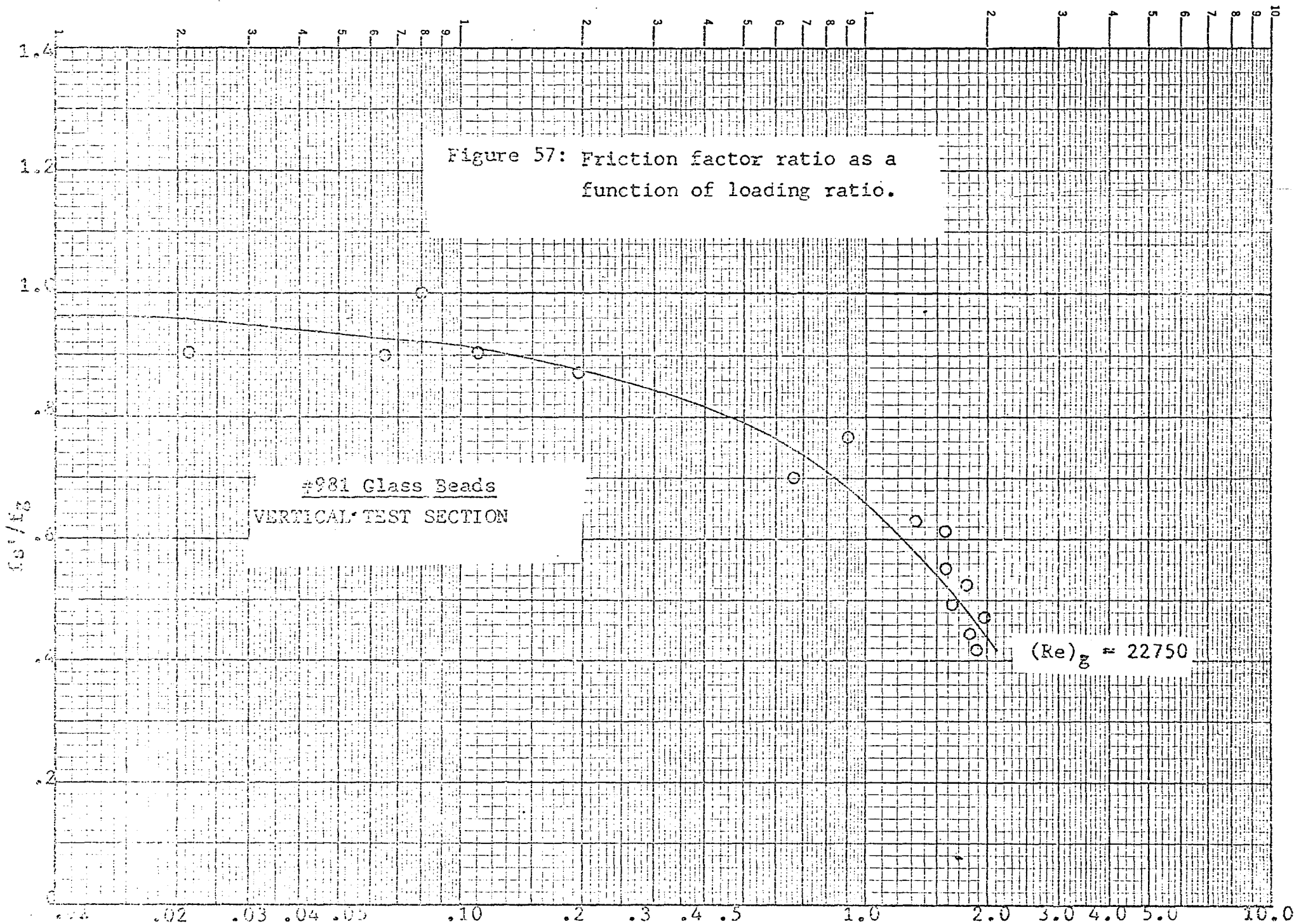
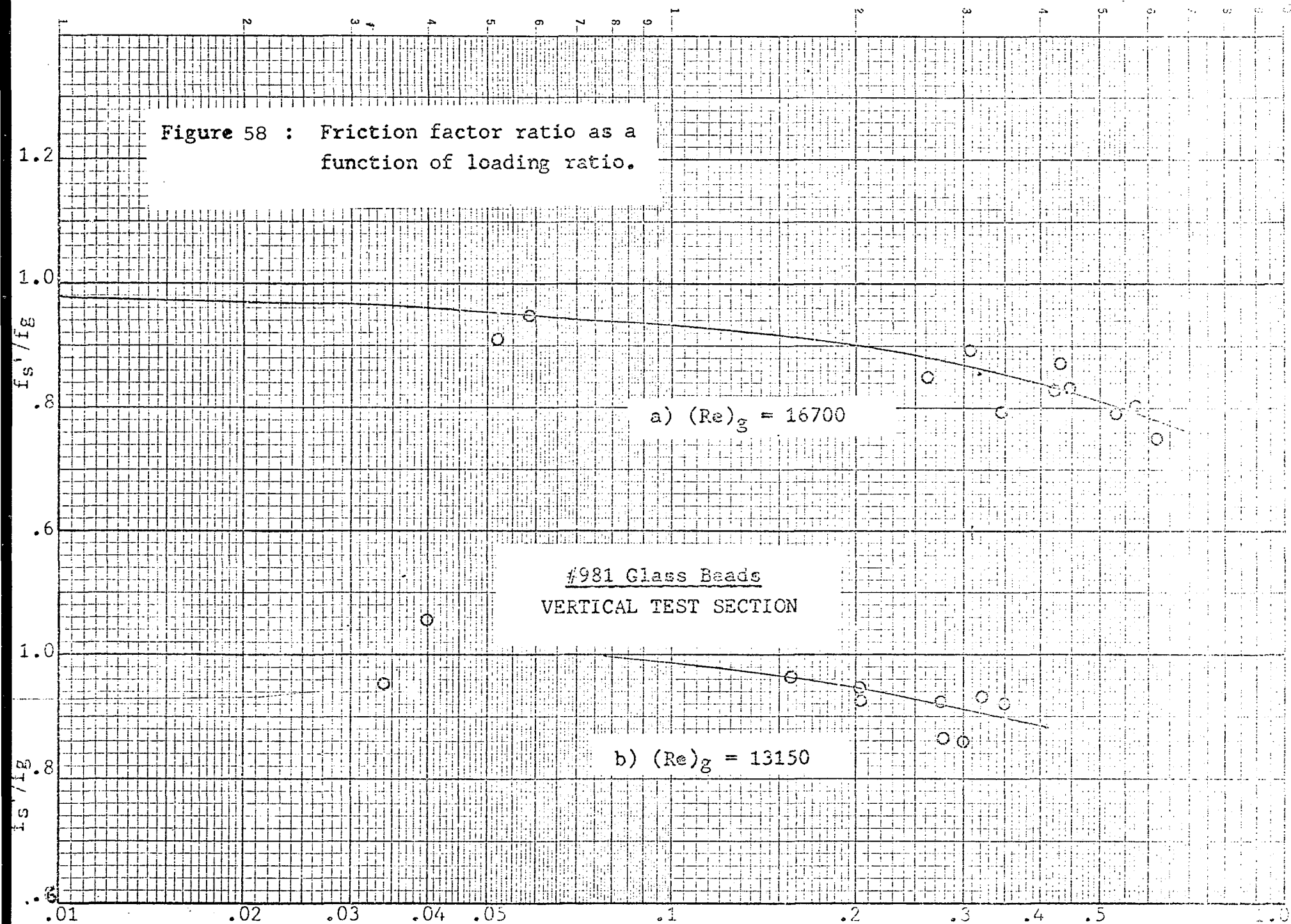


Figure 58 : Friction factor ratio as a function of loading ratio.



a)  $(Re)_g = 16700$

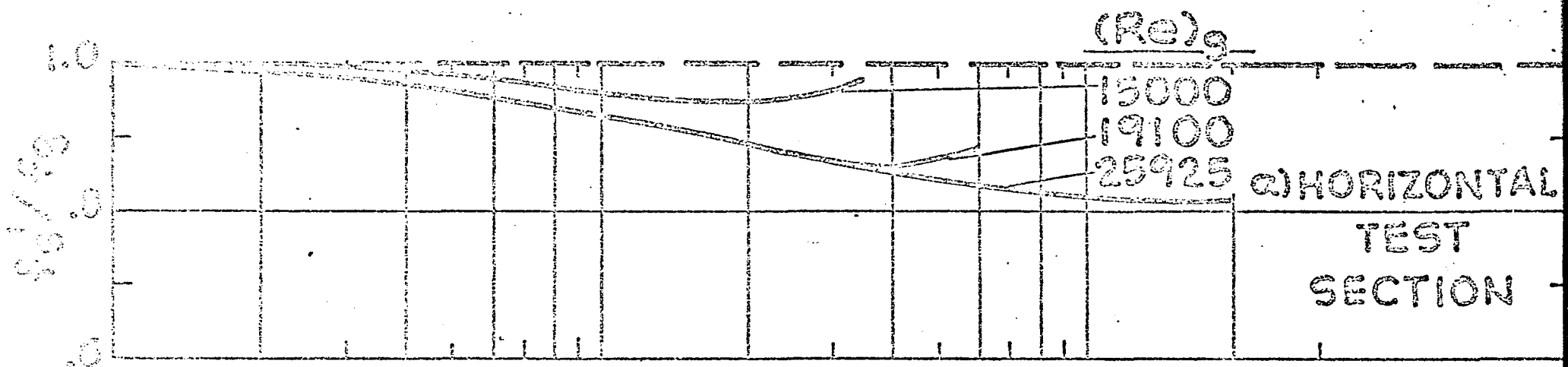
#981 Glass Beads  
VERTICAL TEST SECTION

b)  $(Re)_g = 13150$

the same in magnitude. The lone exception to this agreement appears in the horizontal data at the lowest Reynolds number where a slight drag reduction rather than a slight drag increase is shown. This could be attributed to the fact that the #279 glass beads contain more large particles than the #981 glass beads. This could also be the reason that all of the horizontal test section friction factor results are very slightly lower than the corresponding results for the #279 glass beads. The results for the three different Reynolds numbers and the two different test sections are indicated in figure 59. The figure also shows that at any given loading ratio the "drag reduction" is still somewhat greater for the vertical test section than the horizontal test section for all Reynolds numbers.

The smallest particles used in this investigation were the #980 glass beads (average  $D_p$  approximately equal to  $10\mu$ ). The friction factor results obtained using these particles are indicated by figures 60 - 63. The figures show slight "drag reduction" for all Reynolds numbers in both the horizontal and vertical test sections. The results also show that the friction factor ratio for both the horizontal and vertical test sections are nearly identical for these very small particles (see figure 64).

In order to show more clearly the effect of particle size on the friction factor ratio, two additional composites have been prepared. The composites shown in figures 65 and 66 represent the results of friction factor ratio as a



#98: GLASS BEADS.

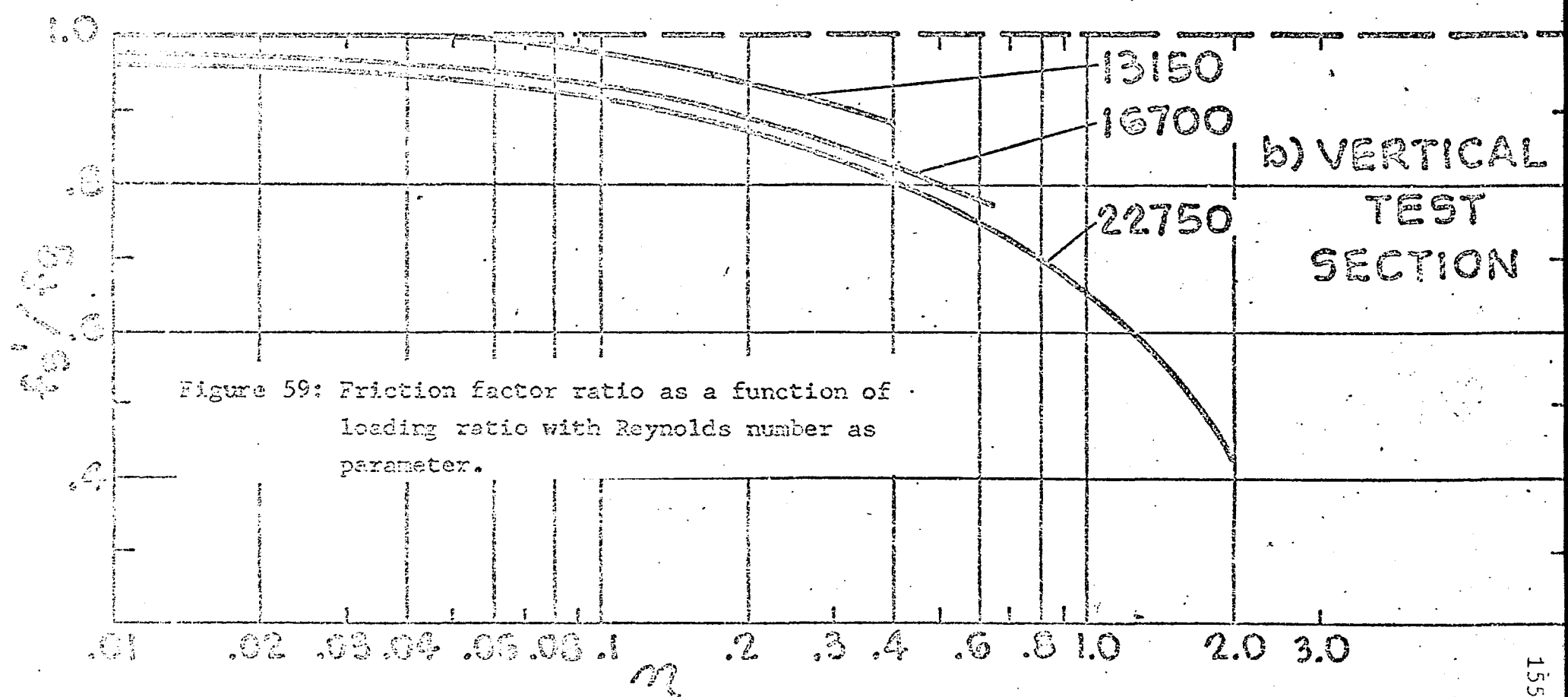


Figure 59: Friction factor ratio as a function of loading ratio with Reynolds number as parameter.

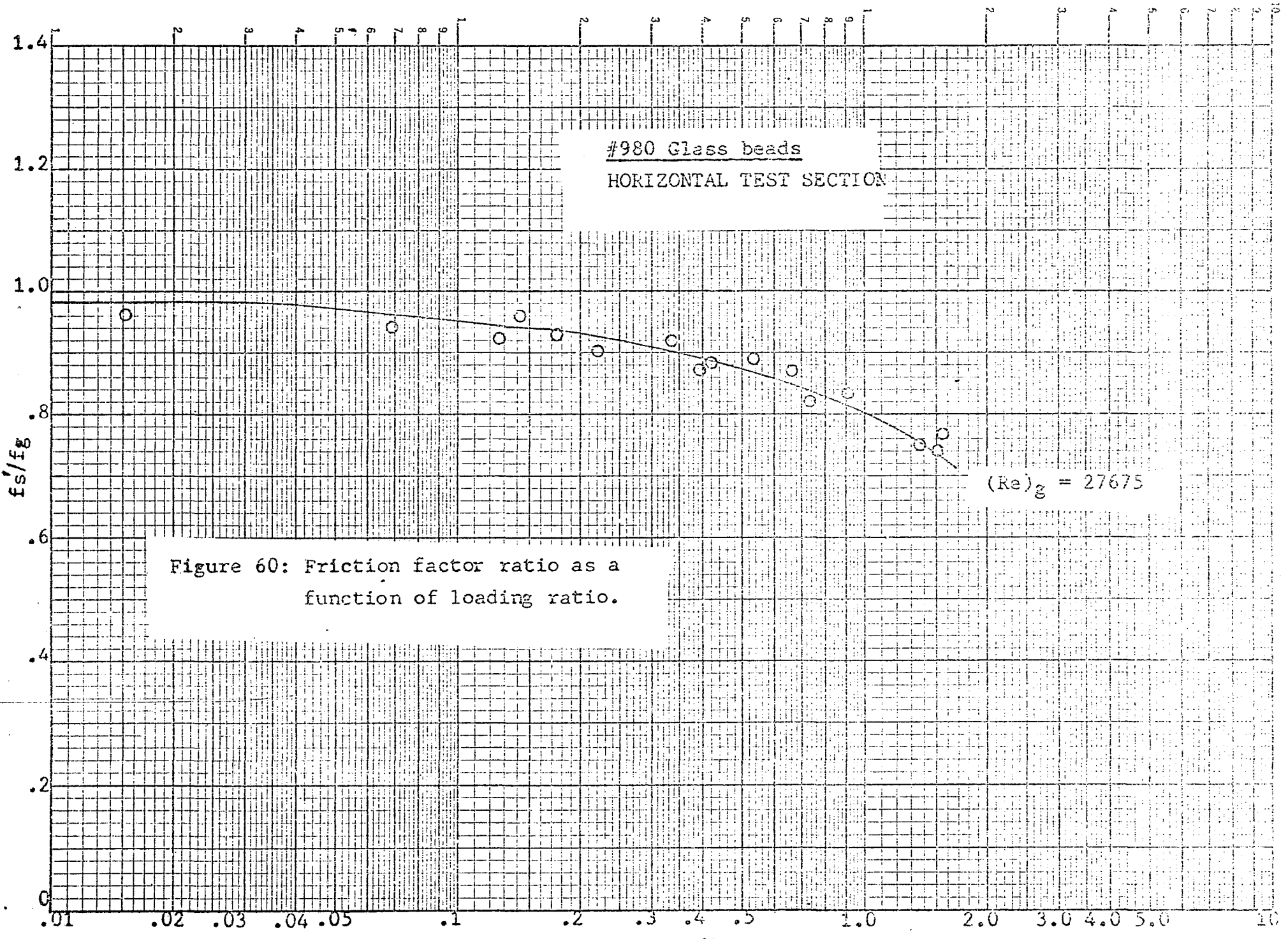


Figure 60: Friction factor ratio as a function of loading ratio.

Figure 61 : Friction factor ratio as a function of loading ratio.

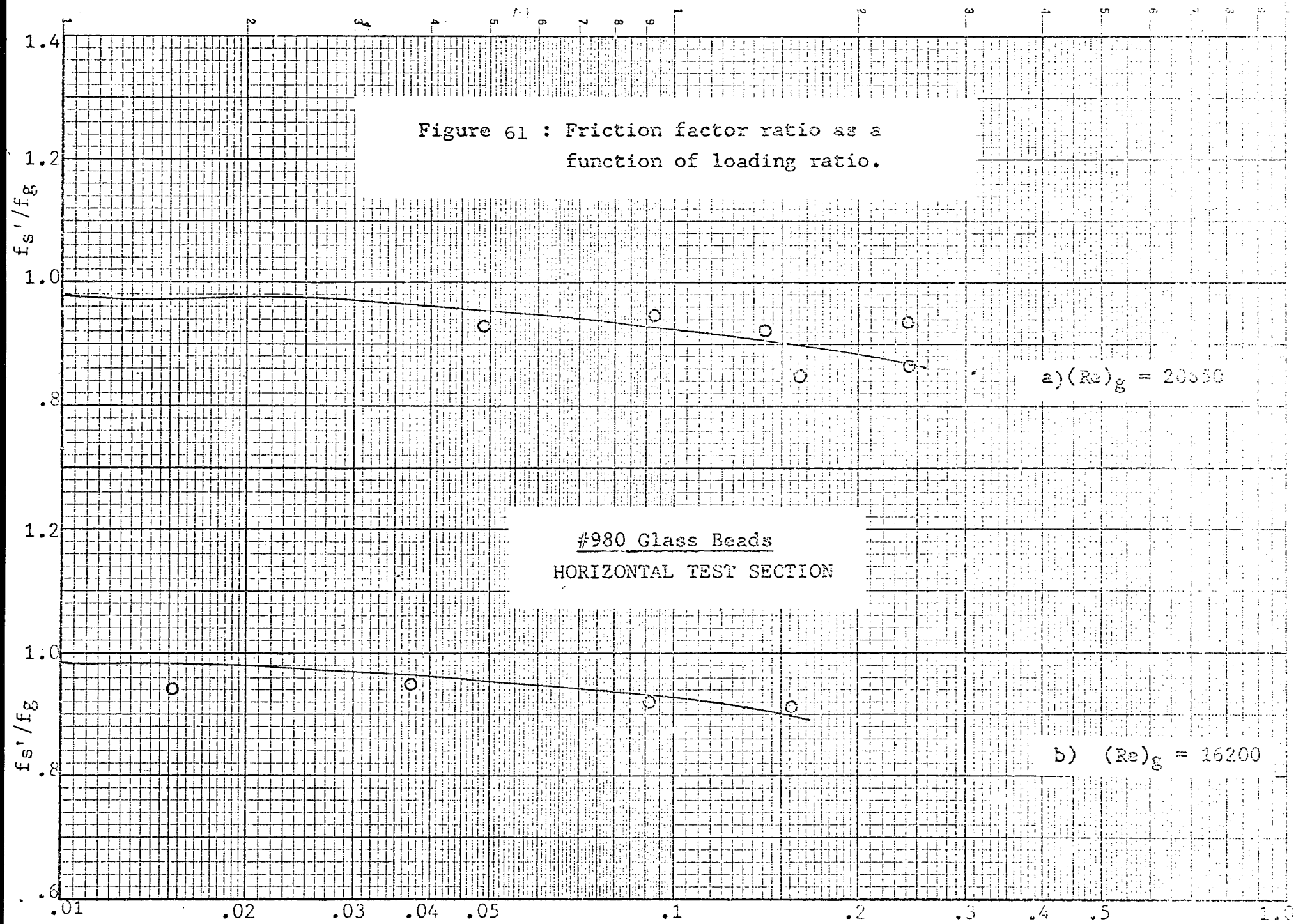


Figure 62: Friction factor ratio as a function of loading ratio.

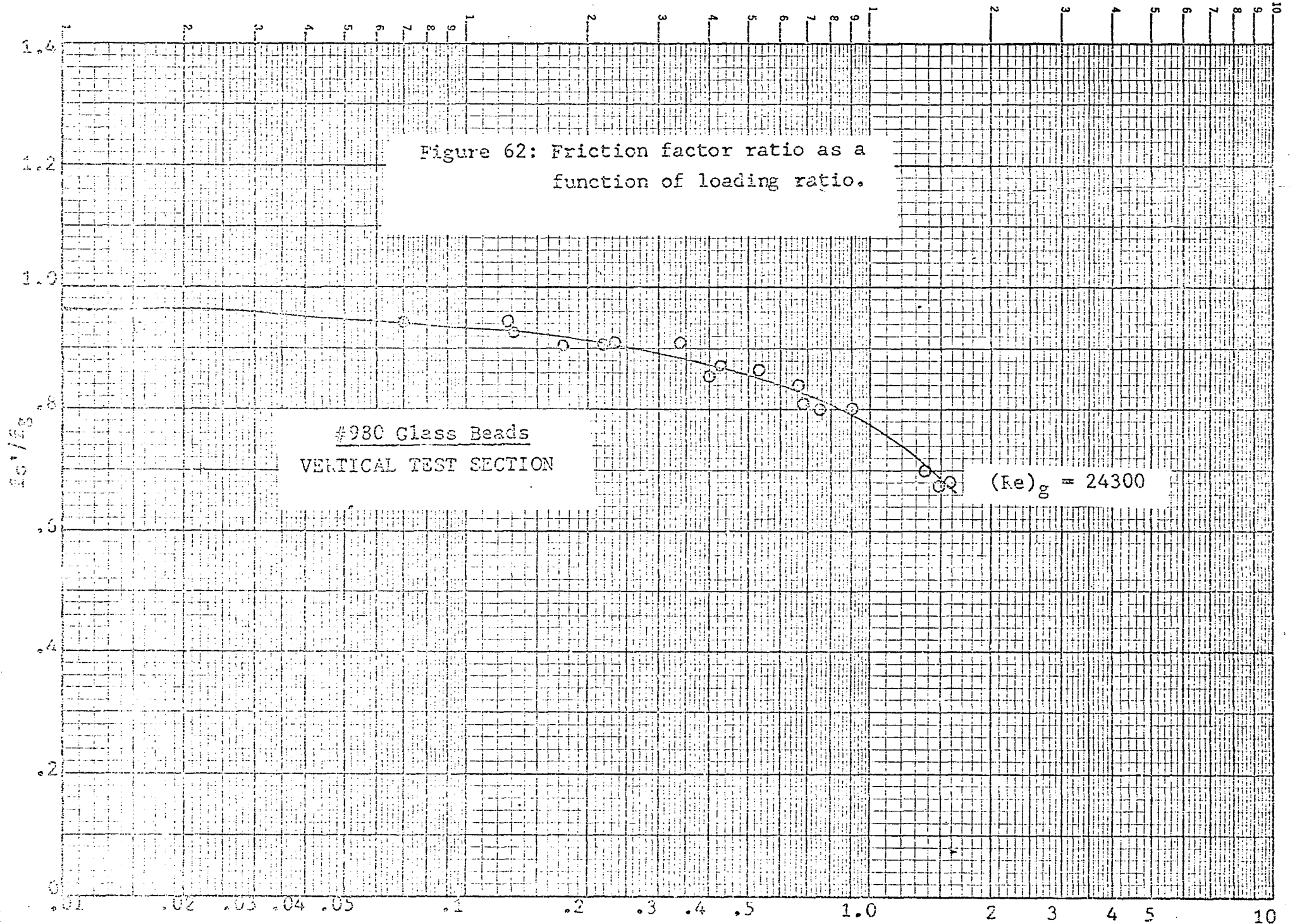
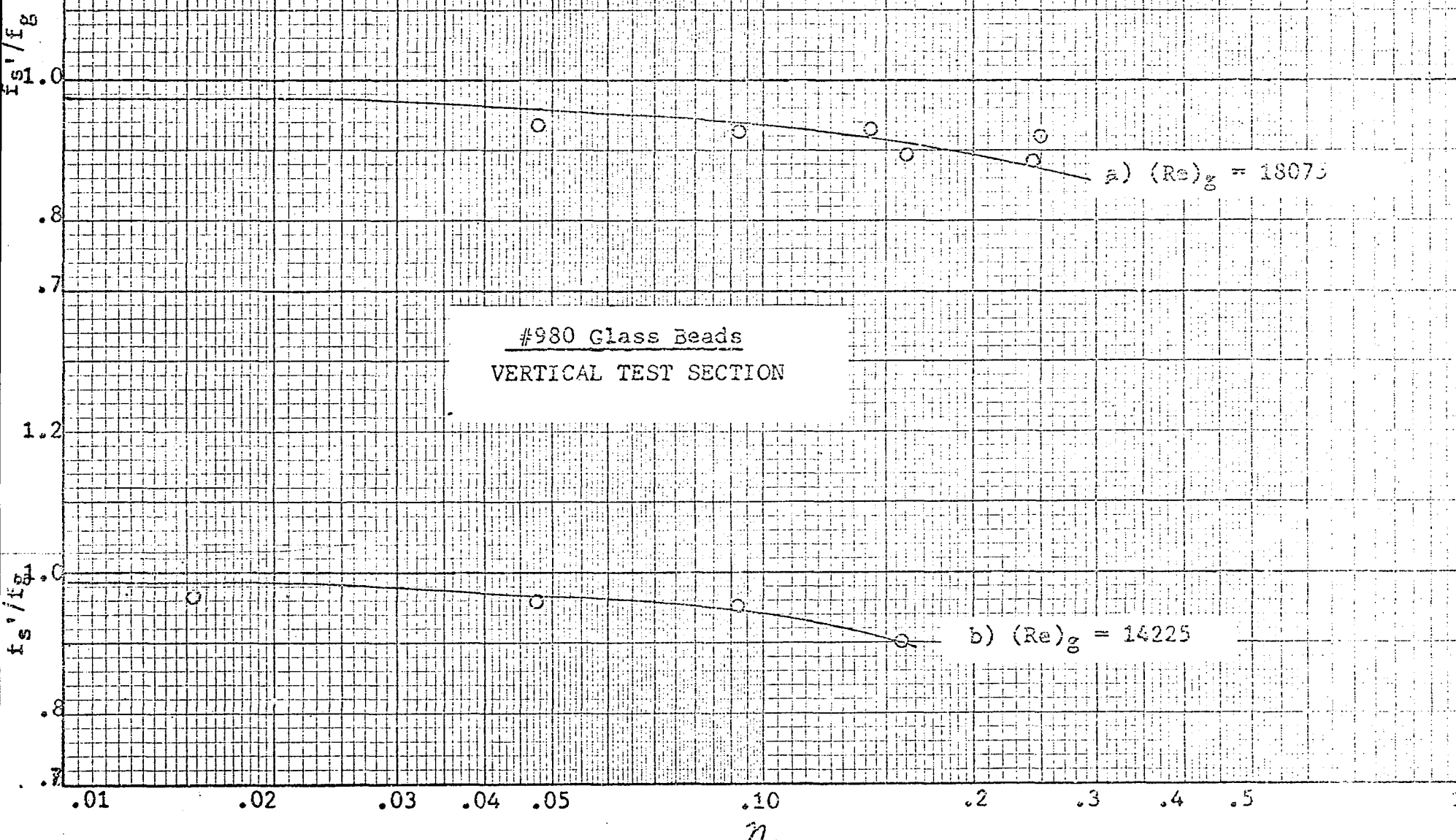


Figure 63: Friction factor as a function of loading ratio.



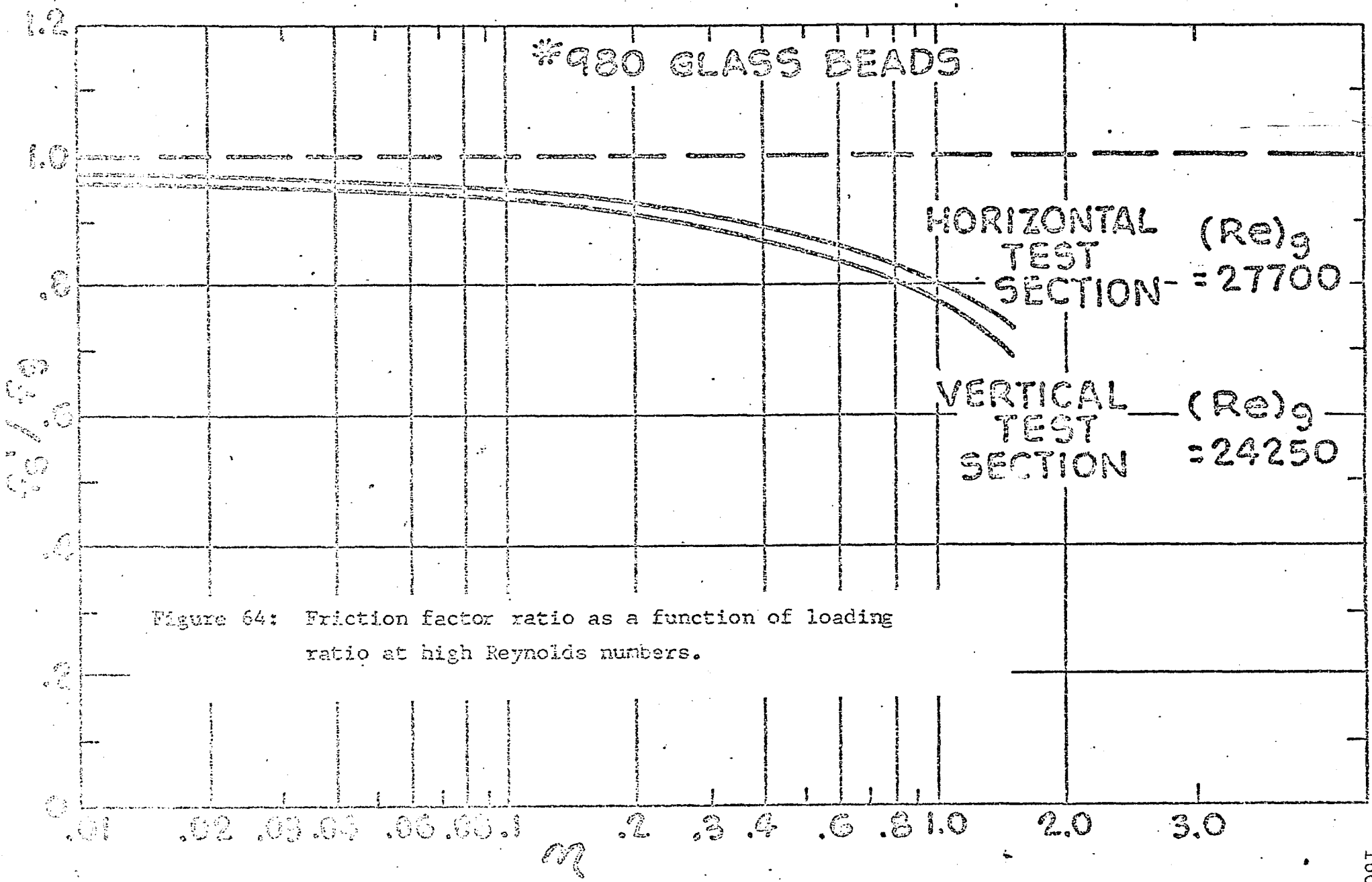


Figure 64: Friction factor ratio as a function of loading ratio at high Reynolds numbers.

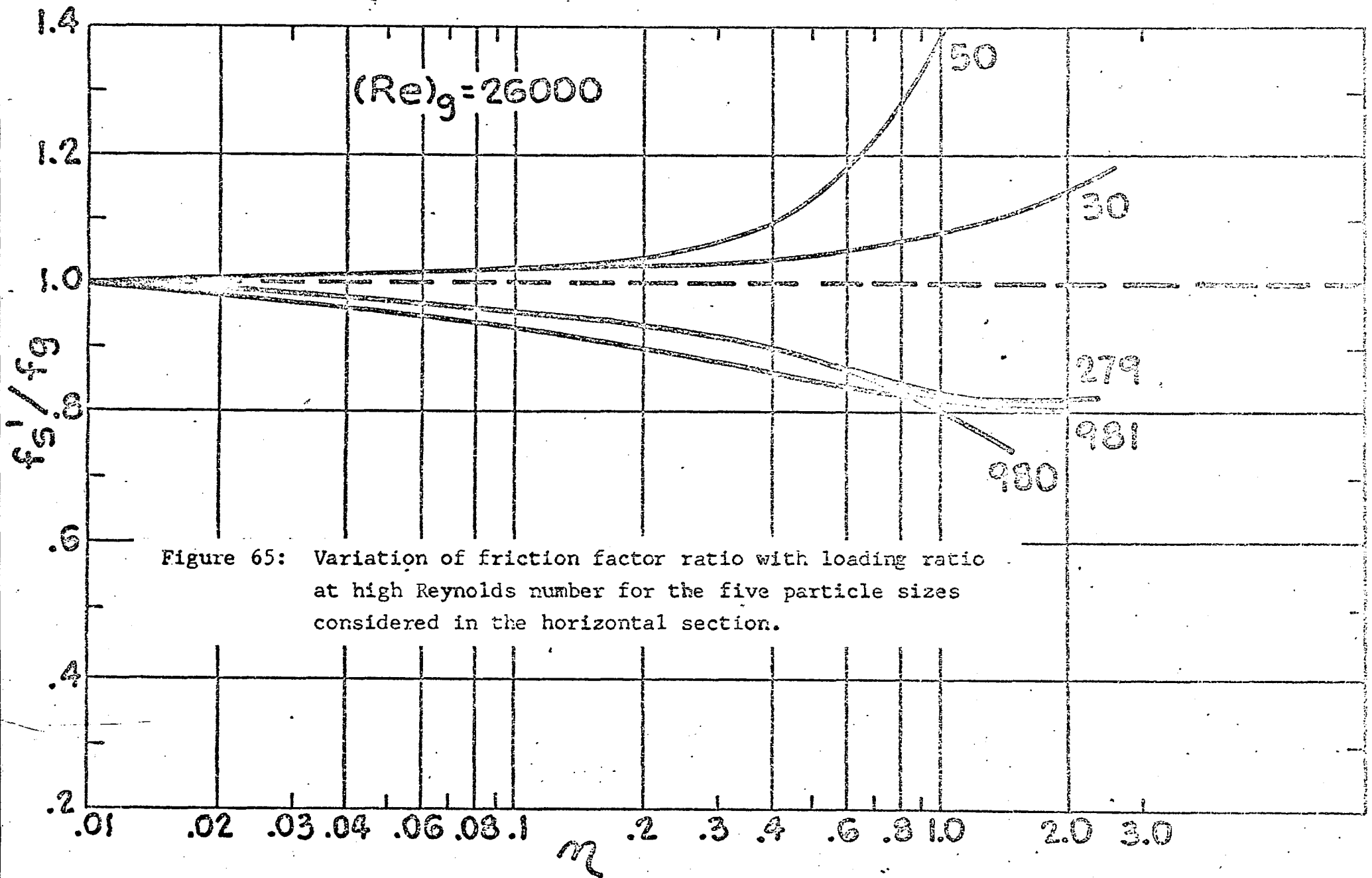


Figure 65: Variation of friction factor ratio with loading ratio at high Reynolds number for the five particle sizes considered in the horizontal section.

$(Re)_g = 23000$

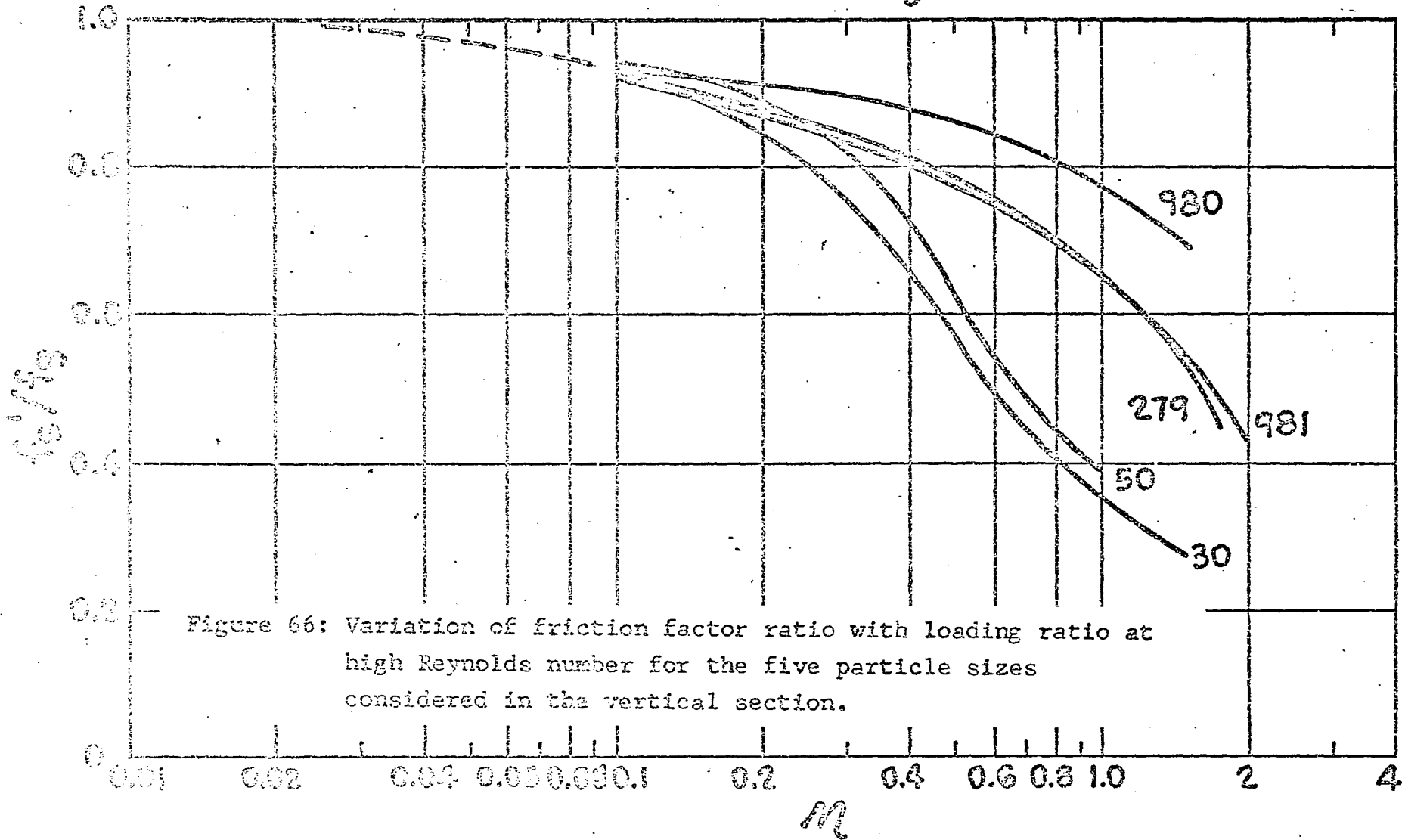


Figure 66: Variation of friction factor ratio with loading ratio at high Reynolds number for the five particle sizes considered in the vertical section.

function of loading ratio for the five different particle sizes at the highest Reynolds number in the vertical and horizontal sections respectively. For the vertical section results it is observed that the maximum "drag reduction" is obtained for the  $30\mu$  particles, with the  $50\mu$  particles giving only slightly more drag. The #981 and #279 glass beads give approximately the same magnitude of "drag reduction" - a value less than achieved with the larger particles. The smallest particles appear to give the least "drag reduction".

Figure 65, the composite for the horizontal test section, indicates that the  $50\mu$  and  $30\mu$  glass beads result in drag increases; whereas, the #279 and #981 particles cause "drag reduction" of approximately the same order of magnitude, but less than that exhibited for the same particles in the vertical section. The #980 particles gave approximately the same results for both the horizontal and the vertical test section.

The best explanation for the vertical test section results appears to be given by the theoretical analysis performed by Saffman (ref. 47). In his analysis, Saffman showed that if the particles are fine enough for the relaxation time (a measure of the rate at which the velocity of a particle adjusts to changes in the gas velocity) to be small compared with the flow, then the addition of particles causes the critical Reynolds number for transition from laminar to turbulent flow to be decreased and a drag increase results.

However, he predicts that if the particles are coarse so that the relaxation time is relatively large, then the suspension has a stabilizing action (the particles cause a higher critical Reynolds number and less frictional pressure loss). In other words, the finite slip velocity between the particles and the gas causes energy to be extracted from the turbulent eddies resulting in a smaller frictional dissipation at the wall. As indicated by Soo (refs. 38, 45) this energy extraction would be especially prominent in the vicinity of the wall where the velocity of the particles greatly exceeds that of the gas.

From Saffman's analysis it would be expected that the larger particles which lag behind the turbulent fluctuations of the flowing air but follow the bulk motion of the air will yield higher "drag reduction" than smaller particles which to some extent follow the turbulent fluctuations of the fluid. The fact that the  $50\mu$  particles yield slightly less drag reduction than the  $30\mu$  particles in the vertical test section may also be explained on the basis of Saffman's analysis. According to his model, for a relaxation time very much greater than the characteristic time scale (particle sizes much greater than those required to obtain the characteristic relaxation time) increasing the size of the particle lessens the stabilizing effect. At the gas Reynolds numbers studied in this investigation it would appear that the  $30\mu$  particles yield the optimum relaxation time since both larger and smaller sized particles result in less "drag

reduction". Although not verified experimentally, Saffman's theory would predict higher friction factor ratios for particles larger than  $50\mu$ .

The results for the horizontal test section cannot be fully explained on the basis of the theory presented above. The reason for this is apparently due to gravitational effects which cause the particle number density to vary across the tube and not remain constant as required by Saffman's analysis. As the particles become smaller, their sedimentation velocity decreases, hence decreasing the tendency toward "segregated flow" resulting in the friction factor ratios for the two sections to approach one another. The fact that the smallest particles used in this study yielded essentially the same results in the horizontal and vertical test sections further confirm this theory. With the larger ( $50\mu$  &  $30\mu$ ) particles a drag increase was observed in horizontal flow which may be attributed to the observation of "segregated flow" to such an extent that many of the particles were transported through the horizontal sections in "bouncing flow". This "bouncing flow" causes additional frictional pressure drop and in view of the fact that the cross-sectional density of the particles is not uniform and, therefore, the upper portion of the horizontal sections are less affected by the particulate flow, the net result is a drag increase for these larger particles. As the flow becomes more dispersed (smaller particles) the "segregated flow" is minimized, hence "drag reduction" results. An interesting conclusion which may

be drawn from this investigation is that in a 7/8" tube the maximum "drag reduction" in the horizontal section may be obtained with  $10\mu$  avg. diameter particles since for particles below  $10\mu$  the relaxation time would be smaller and "drag reduction" would decrease; whereas, for particles above  $10\mu$  "segregated flow" would tend to cause an increase in drag.

Photographs showing the gross flow patterns of the particles under varying conditions of loading and Reynolds number appear to confirm the fact that the smaller particles respond to the turbulent fluctuations of the fluid to a greater extent than the larger particles. The photographs also show segregated flow in the horizontal pyrex section. These results will be presented in detail in a later section of the dissertation.

Orifice Coefficient. - By measuring the pressure drop across the orifice and assuming an average velocity of .8 times the centerline velocity measured by the anemometer, orifice coefficients were calculated for all of the closed loop runs at different particle loading ratios and Reynolds numbers. The results of these calculations are plotted on figure 67 along with a curve representing the orifice calibration obtained with pure air as the circulating fluid. Dashed curves representing a  $\pm 5\%$  deviation from this curve are also shown. Since very few data points fall outside of these dashed curves it appears that the orifice coefficient calibration was not affected by the presence of particles in the flow stream.

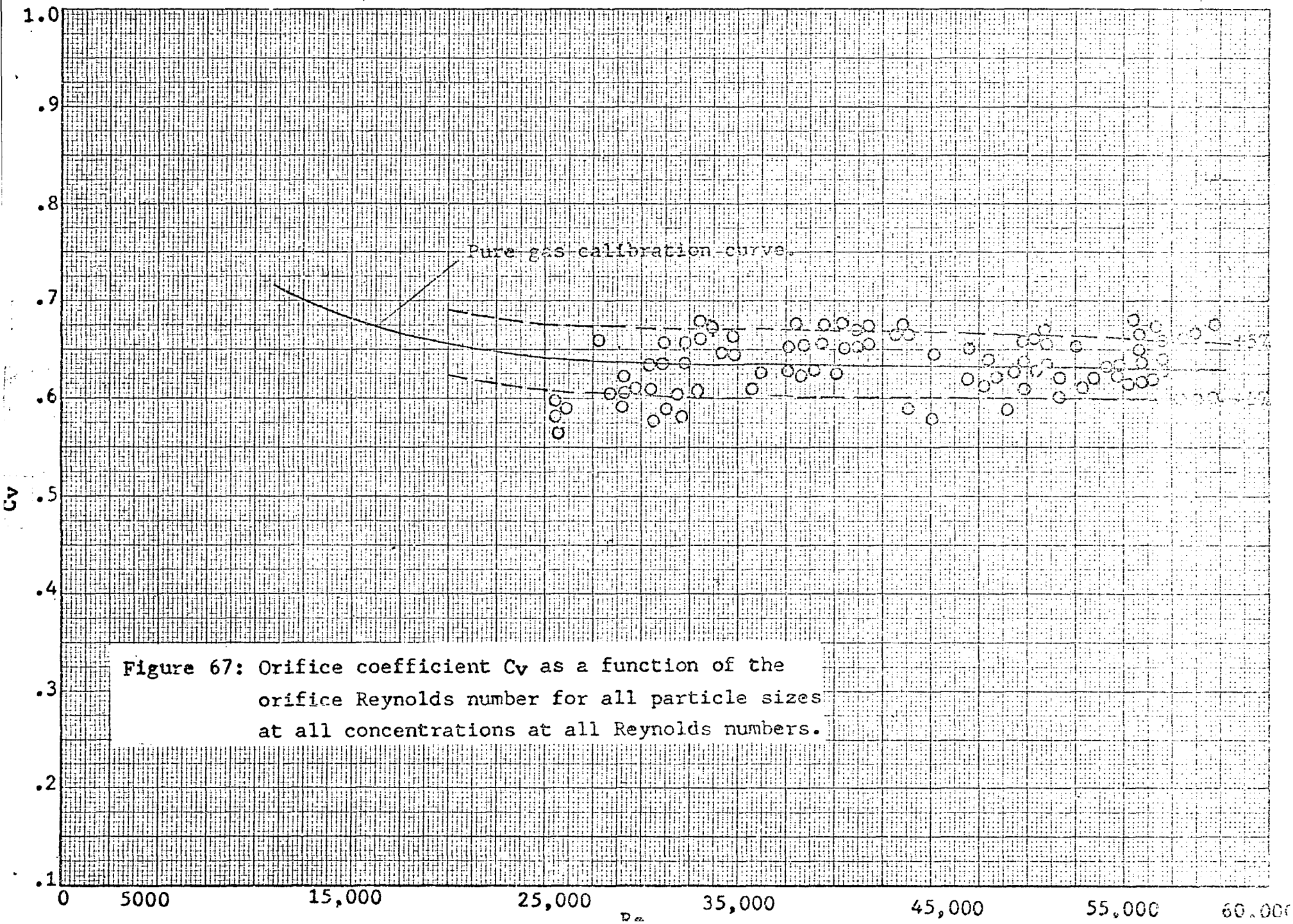


Figure 67: Orifice coefficient  $C_v$  as a function of the orifice Reynolds number for all particle sizes at all concentrations at all Reynolds numbers.

The data points which fell outside the  $\pm 5\%$  deviation curves were examined and no clear cut trend could be discerned with regards to particle size or concentration. Therefore, it would appear that these points are the result of experimental inaccuracies in either the velocity measured by the anemometer or the orifice pressure drop or a combination of both.

The results of this study therefore, seem to confirm Orr's contention (ref. 64) that a properly calibrated orifice can be used to determine gas mass flow rates for dilute suspensions.

Turbulence measurements. - Measurements of the percent turbulence at the centerline position of the tube were also made for closed loop experiments with both pure air and suspensions using the thermistor probe previously described. In order to obtain useful turbulence data from these measurements it is necessary to relate the D.C. voltage and the root mean square readings from the anemometer to the bulk velocity ( $\bar{U}$ ) and the RMS value of the velocity fluctuations in the direction of mean flow,  $\sqrt{u^2}$ . This can be obtained from the relation between the velocity and the D.C. voltage for the Disa anemometer unit which is:

$$V^2 - V_o^2 = BU^n \quad (54)$$

where B and n are experimental constants and U is the point bulk velocity. Therefore, assuming u is small compared to the bulk velocity,  $\bar{U}$  we obtain

$$\bar{U} = B^{-\frac{1}{n}} (V^2 - V_o^2)^{\frac{1}{n}} \quad (55)$$

From equation (54),

$$\frac{dU}{dt} = \frac{\frac{1}{n} (V^2 - V_0^2)^{\frac{1}{n} - 1} 2V \frac{dV}{dt}}{B^{\frac{1}{n}}} \quad (56)$$

upon rearrangement equation (56) becomes

$$\frac{dU}{dt} = \frac{R^{-\frac{1}{n}} (V^2 - V_0^2)^{\frac{1}{n}} 2V \frac{dV}{dt}}{n (V^2 - V_0^2)} \quad (57)$$

therefore,

$$\sqrt{\frac{dU^2}{dt^2}} = \frac{B^{-\frac{1}{n}} (V^2 - V_0^2)^{\frac{1}{n}} 2V \sqrt{\frac{dV^2}{dt^2}}}{n (V^2 - V_0^2)} \quad (58)$$

Since,

$$\sqrt{\frac{dU^2}{dt^2}} = \sqrt{u^2} \quad \text{and} \quad \sqrt{\frac{dV^2}{dt^2}} = \sqrt{v^2} \quad (\text{RMS voltage})$$

equation (58) becomes

$$\sqrt{\frac{u^2}{dt^2}} = \frac{B^{-\frac{1}{n}} (V^2 - V_0^2)^{\frac{1}{n}} 2V \sqrt{v^2}}{n (V^2 - V_0^2)} \quad (59)$$

In order to obtain the relative turbulence intensity, defined by

$$I = \frac{\sqrt{u^2}}{U} \quad (60)$$

equation (59) is divided by equation (55) to yield

$$\frac{\sqrt{\frac{u^2}{dt^2}}}{U} = \frac{2V \sqrt{v^2}}{n (V^2 - V_0^2)}$$

From the anemometer calibrations previously performed it was found that the relationship between velocity and voltage was in agreement with King's law (see Appendix A) and  $n = .5$ ,

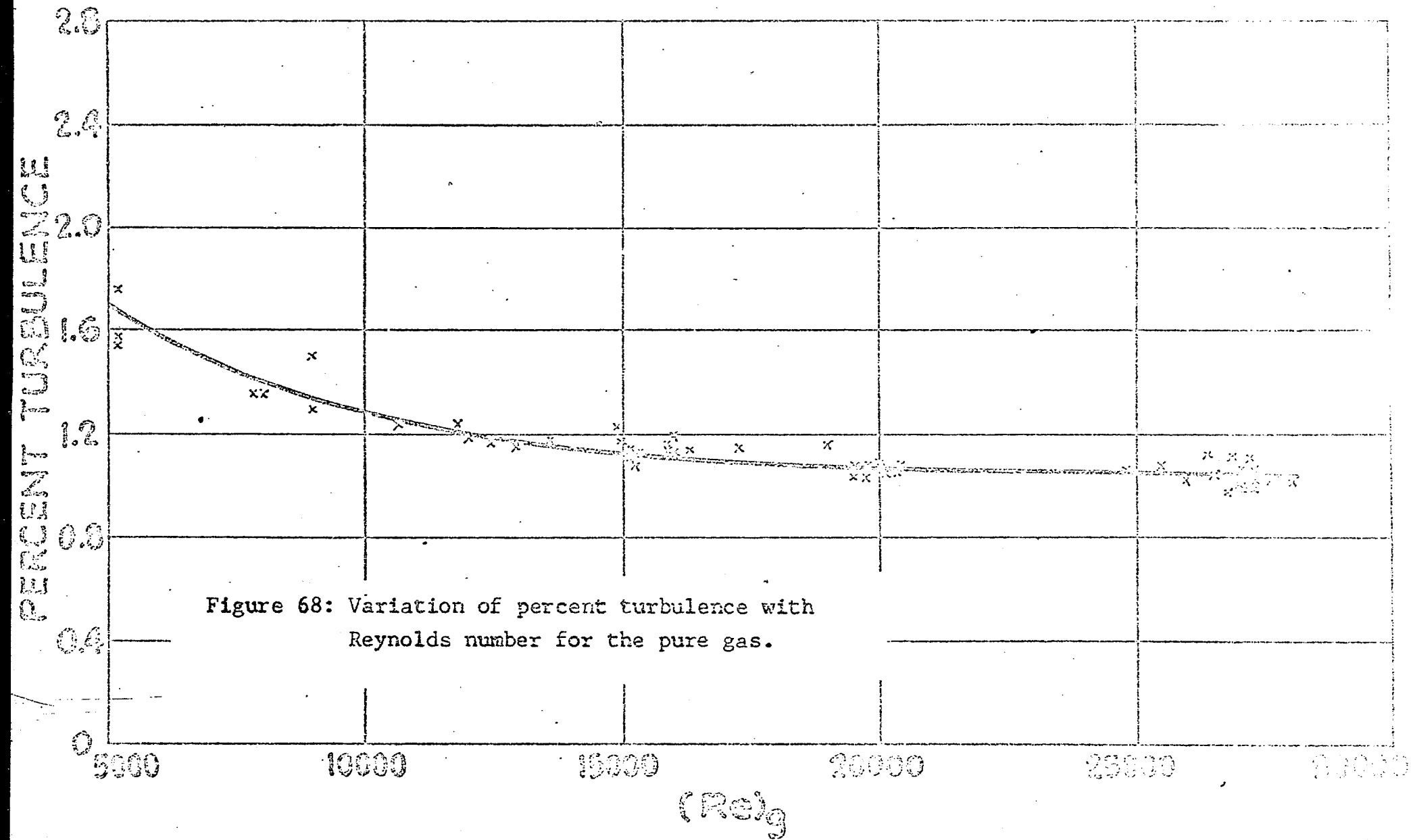
so that

$$I = \frac{\sqrt{\overline{u^2}}}{\bar{U}} = \frac{4\bar{V} \sqrt{\overline{v^2}}}{(\bar{V}^2 - V_0^2)} \quad (61)$$

and the percent turbulence is simply 100 I.

Another method of relating the root mean square and D.C. voltage to the relative intensity of turbulence is by point to point calculations. In this procedure, the calibration curves for each probe at each temperature are used. The RMS voltage is divided by the slope of the curve at the recorded D.C. voltage and yields the RMS fluctuating velocity. This fluctuating velocity is then divided by the value of velocity obtained from the anemometer calibration at the recorded D.C. voltage so as to obtain the relative intensity of turbulence. Values of I obtained using this method were compared with those from equation (61) and agreement to within 5% was found between the two approaches. In this investigation the values of I reported are those obtained using equation (61).

The pure gas turbulence results obtained in the downward vertical leg of the loop with the probe in the centerline position are presented as a function of gas Reynolds number in figure 68. As can be seen from the figure, an increase in Reynolds number results in a decrease in the centerline percent turbulence. This trend is consistent with the results of other investigators with both air (ref. 65) and liquids (ref. 66). The explanation of this phenomenon appears to be that as the Reynolds number is increased the thickness of the



laminar sublayer is decreased and more turbulence occurs in the vicinity of the wall resulting in a lower percent turbulence in the center of the tube. As the velocity decreases the laminar sublayer becomes thicker and the turbulence in the core and at the centerline increases.

The magnitude of the percent turbulence found in this study, however, is substantially lower than that reported in previous investigations. This is apparently due to the fact that the turbulent structure recovery after any obstruction requires a longer length of undisturbed tubing ( $L/D \approx 150$  (ref. 67)) than was available in this investigation. An insufficient length to diameter ratio for turbulence measurements results in lower values for the percent turbulence in the stream. However, since the trend of the data appear to be correct, a reliable estimate of the effect of particles on the relative intensity of turbulence can be obtained by using the ratio of  $I$  with and without particles at any given gas Reynolds number.

Figures 69 - 73 represent plots of the results for the ratio of relative intensity of turbulence with and without particles ( $I_s/I_g$ ) as a function of suspension loading ratio for the five different particle types studied. The data for each particle size are plotted using three different symbols each representing a different Reynolds number range. As can be seen from the figures, no Reynolds number effect is discernable in the Reynolds number range investigated here.

Figure 69: Variation of intensity of turbulence ratio with the loading ratio for 50  $\mu$  Glass Beads at all Reynolds numbers.

KEY

- $(Re)_g = 22375$
- ⊕  $(Re)_g = 16400$
- ⊖  $(Re)_g = 12100$

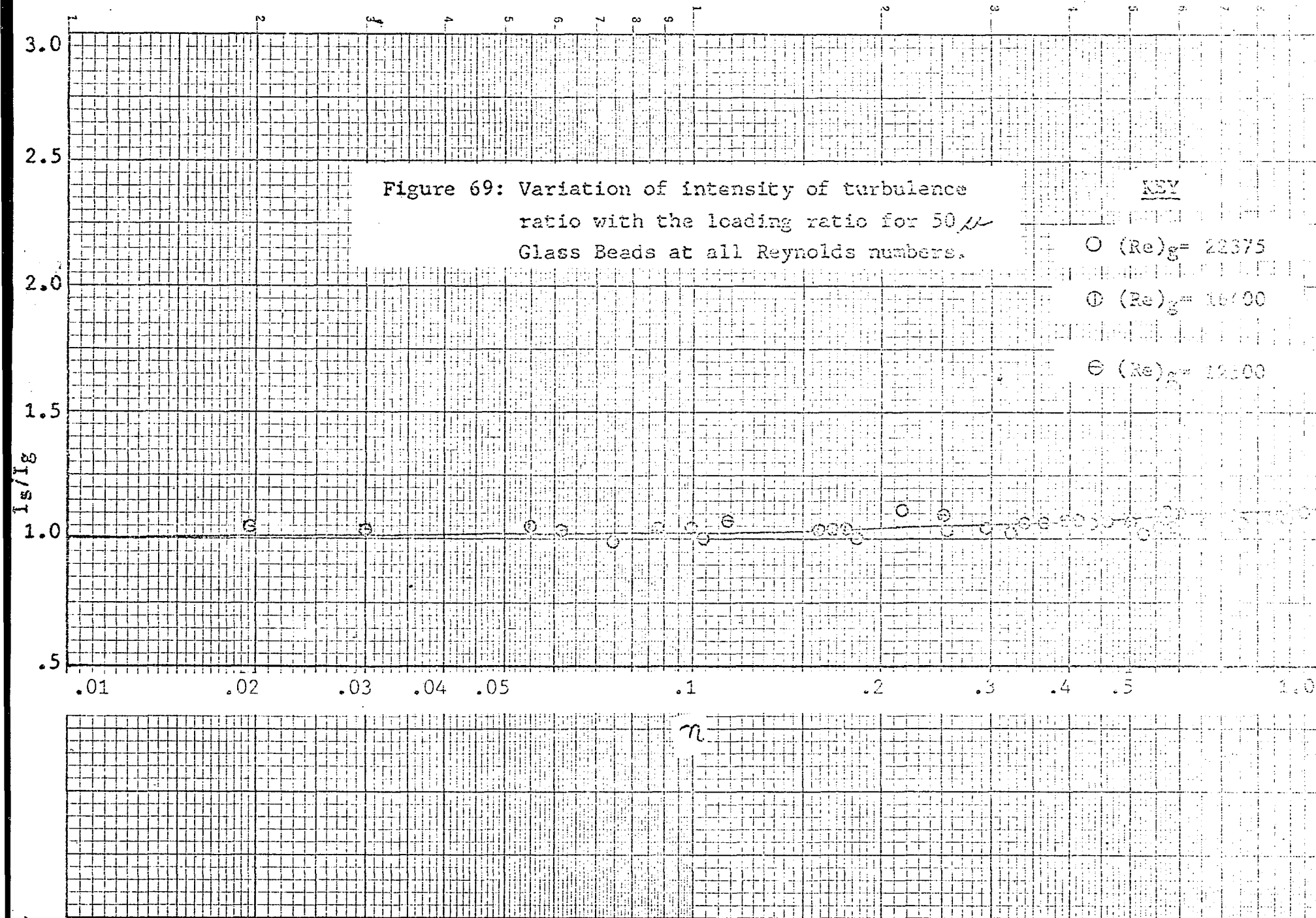
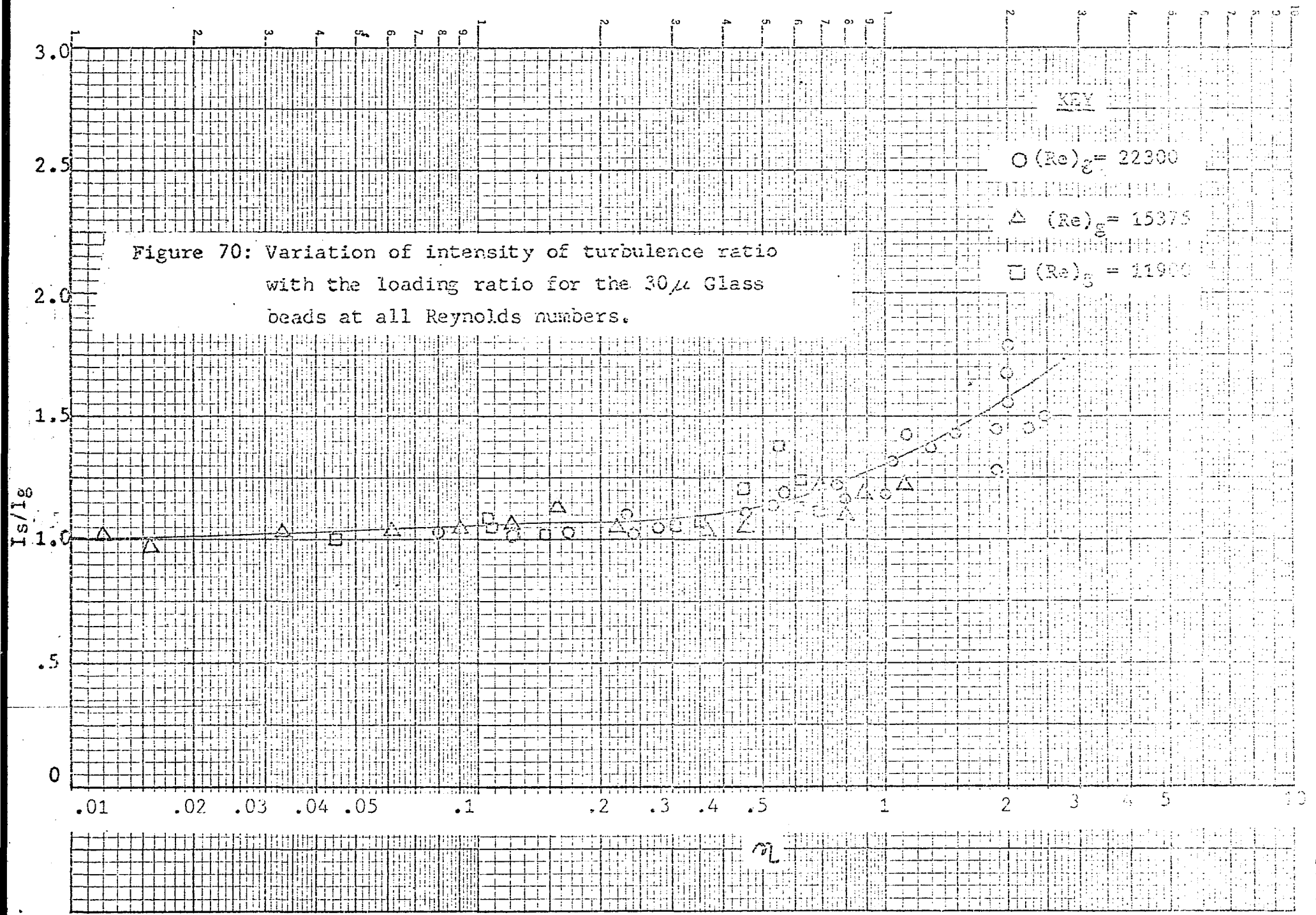


Figure 70: Variation of intensity of turbulence ratio with the loading ratio for the 30 $\mu$  Glass beads at all Reynolds numbers.

KEY  
 O (Re)<sub>g</sub> = 22300  
 Δ (Re)<sub>g</sub> = 15375  
 □ (Re)<sub>g</sub> = 11900



$\mu$

Figure 71: Variation of intensity of turbulence ratio  
 with the loading ratio for the #279 Glass beads  
 at all Reynolds numbers.

○  $(Re)_g = 22600$   
 △  $(Re)_g = 16750$   
 □  $(Re)_g = 13000$

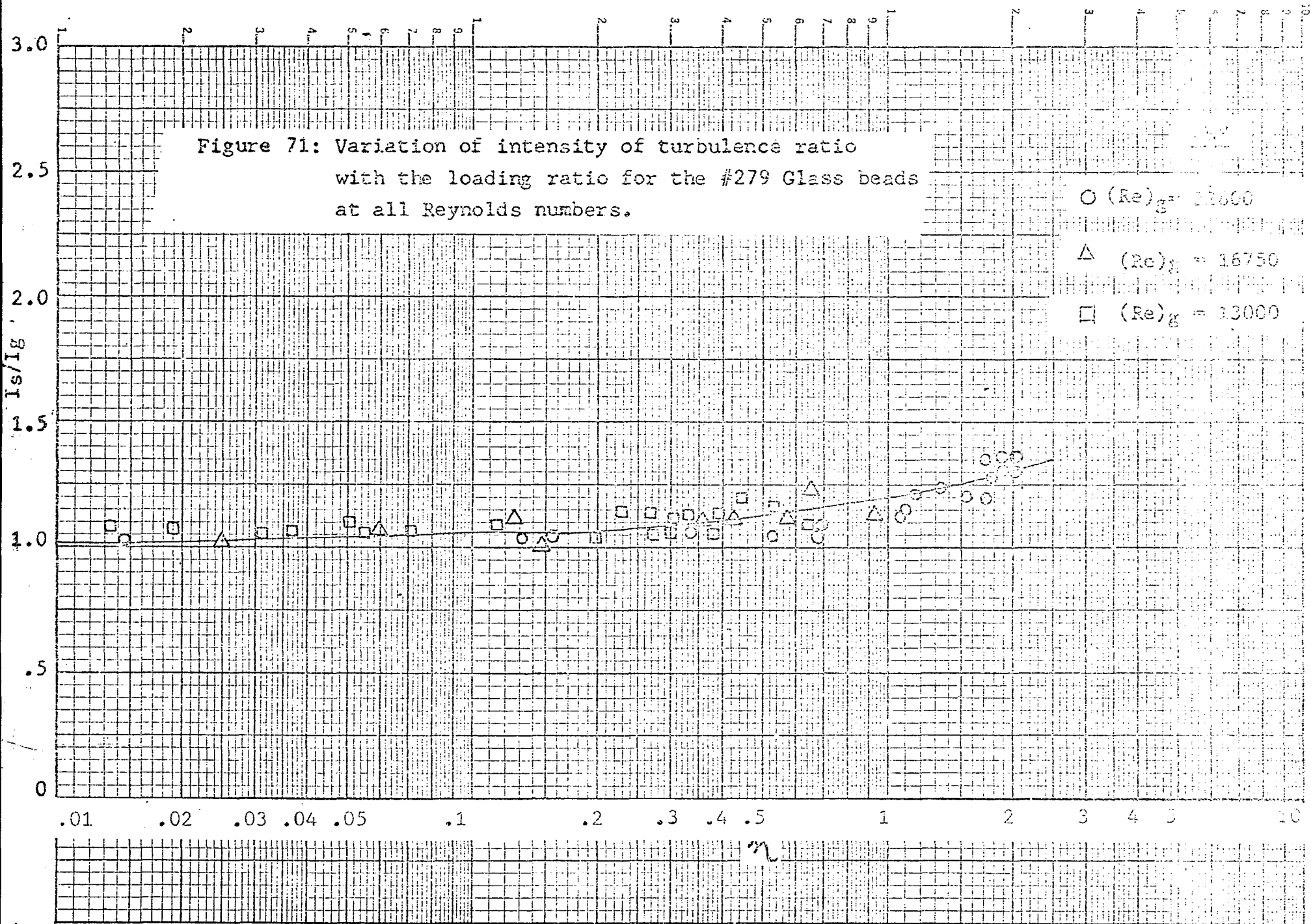
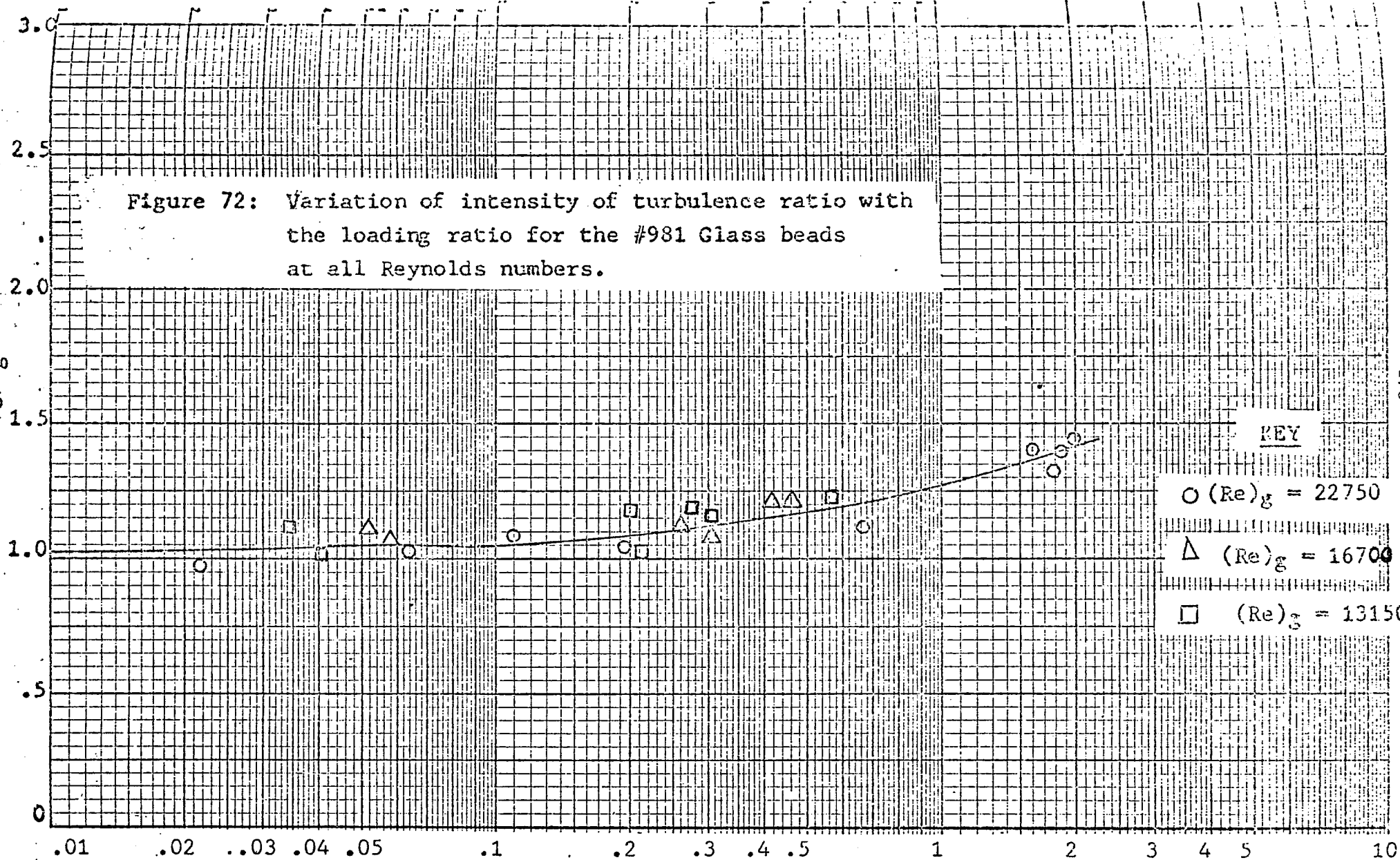


Figure 72: Variation of intensity of turbulence ratio with the loading ratio for the #981 Glass beads at all Reynolds numbers.

$f_s/f_g$



-176-

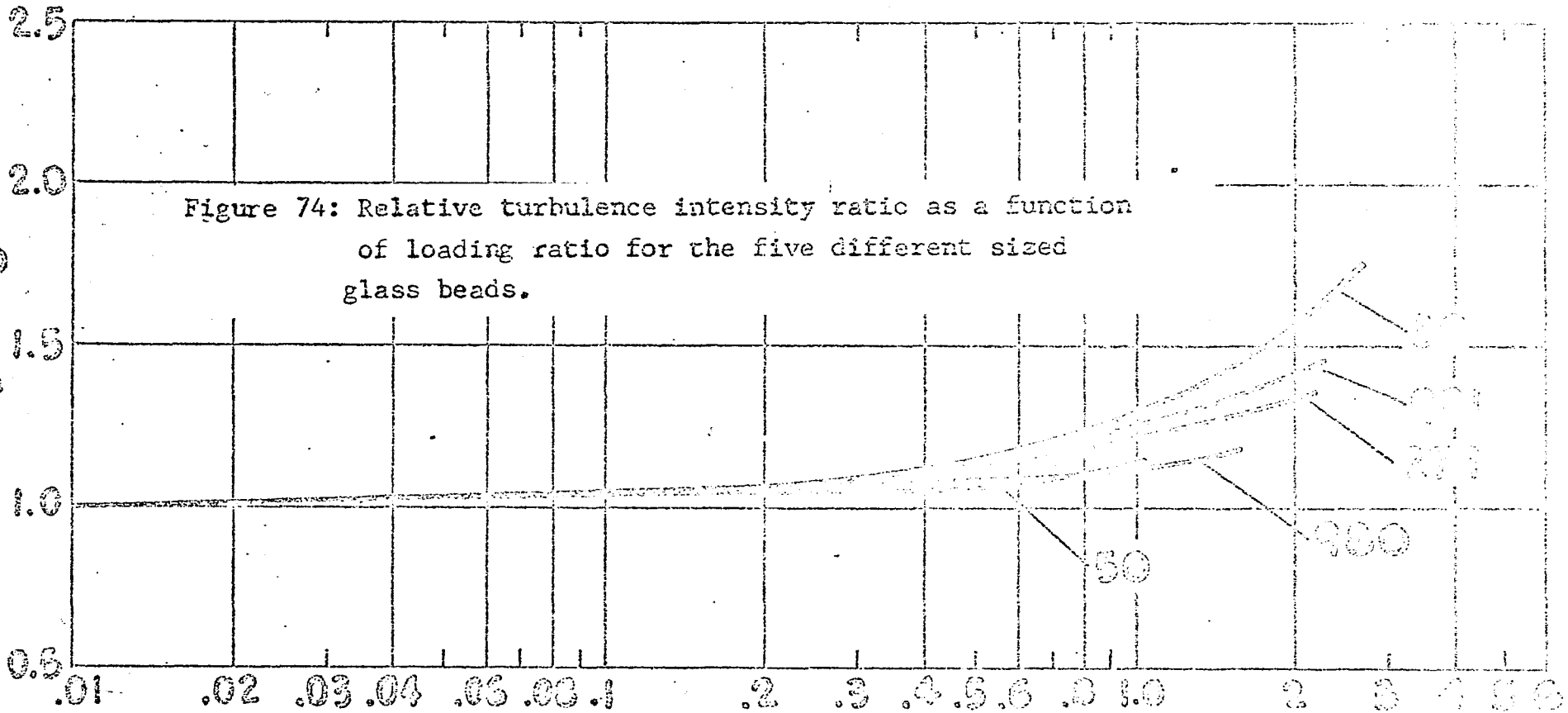
176



Figure 74 is a composite of the curves faired through the data in figures 69 - 73. From this figure it is clear that for all particle sizes the relative intensity of turbulence increases as particles are added to the fluid. This is consistent with the model proposed by Saffman, since removal of energy from the fluid by the particles in the vicinity of the wall would result in a thickening of the laminar sublayer and consequently an increase in the centerline intensity of turbulence.

These trends are also observed for liquid drag reduction and are also attributed to build up of the laminar sublayer (ref. 68). The magnitude of the increase appears to be indicative of the amount of drag reduction obtained for each particle. The figure shows that the greatest increase in turbulence is obtained with the  $30\ \mu$  particles followed by the #981, #279, #980, and  $50\ \mu$  particles. With the exception of the  $50\ \mu$  particles, this was the relative order of the magnitude of drag reduction observed on the vertical test section. The fact that the relative intensity ratio for the  $50\ \mu$  particles is somewhat lower than would be expected on the basis of the friction factor data cannot be explained.

Unfortunately, turbulence measurements could not be made in the horizontal test section as well as in the vertical test section due to a combination of instrumentation, space, and time limitations. Such information would be useful for a clearer understanding of the "drag reduction" phenomena.



*η*

The fact that no Reynolds number effect was discernable for the centerline turbulence results; whereas a Reynolds number effect was clearly evident with the friction factor data appears to be due to the pure gas relations for these results. The friction factor is somewhat dependent on Reynolds number (see equation (34)) even for the pure gas case; whereas, the relative intensity of turbulence at the center of the tube is almost constant for the pure gas in the range of Reynolds number studied (see figure 68). It is therefore not surprising that no Reynolds number effect on the centerline percent turbulence was noticed in the relatively narrow Reynolds number ranges investigated.

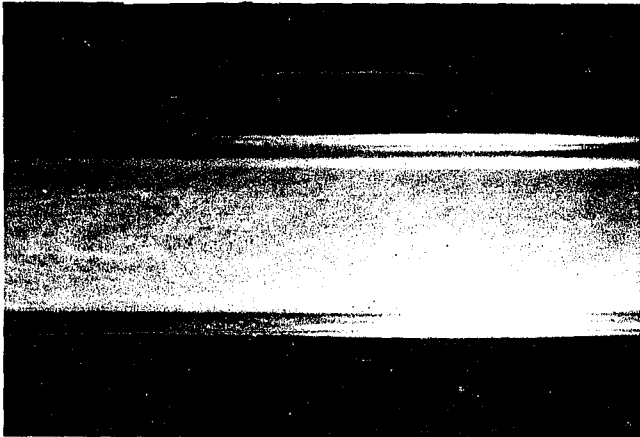
In an effort to obtain additional information on the effect of particles on the flowing gas, gas velocity profiles were taken using the anemometer probe. Velocity profiles could not be made with the downstream pitot static section due to persistent clogging of the impact tube. The shape of the anemometer probe prevented measurements of velocities in the vicinity of the wall so that measurements could only be made between  $0 \leq \frac{r}{r_0} \leq .6$ . In this narrow range the gas velocity profile appeared to be slightly flatter with the suspensions than predicted by the  $\frac{1}{7}$ -th power law for gases. These velocity profile data, however, are considered to be somewhat unreliable due to difficulties experienced in positioning the probe and the length of time required for each traverse which caused a large temperature change during the course of the experiment. These data are therefore not

presented in this dissertation.

Soo et al. (ref. 25), Peskin and Dwyer (ref. 22) and McCarthy and Olson (ref. 28) have reported little or no effect of particles on the gas velocity profile. Their work in addition to the orifice results obtained in this investigation (which were based on an average velocity of  $.8 v_c$ ) seem to indicate that the total velocity profile is relatively unaffected by the presence of particles, although a more intensive investigation of the gas velocity profile in the presence of particles appears to be called for.

Gross flow photography. - Photographs were taken during some closed-loop suspension runs so as to illustrate certain aspects of the flow patterns of the suspensions. These photographs were taken in the horizontal photographic section shown in fig. 6. A relatively large depth of field was used when taking these pictures so that gross flow patterns could be observed. An Edgerton flash with a .5 microsecond duration was placed below and aimed at the photographic section so that the high speed flow patterns could be frozen.

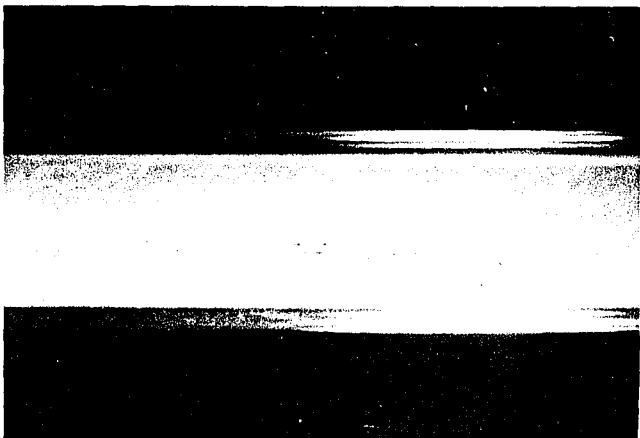
Photographs taken by this procedure of the five different particle sizes under various conditions of flow and loading are shown in figures 75 - 79. For each particle size photographs for both the highest and lowest Reynolds number range investigated are presented. For all particle sizes except the #980 glass beads three different loadings are illustrated by the pictures. Only two different loadings

Figure 75: Gross flow photographs of  $50\ \mu$  particles. $(Re)_g = 25225$  $(Re)_g = 14300$ 

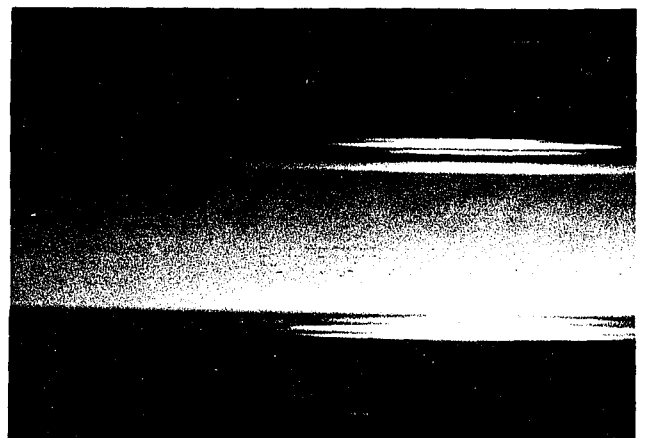
a) Loading ratio = .12



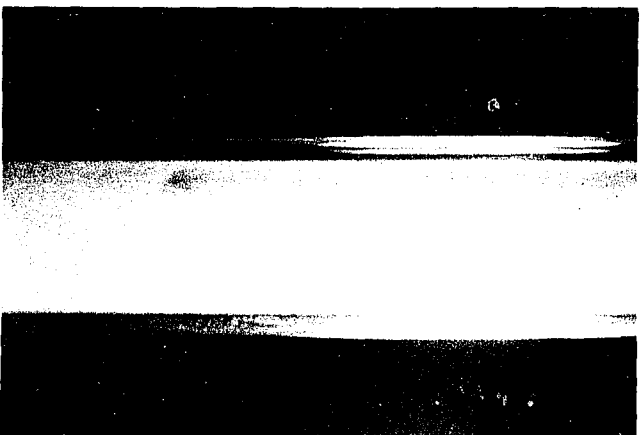
b) Loading ratio = .02



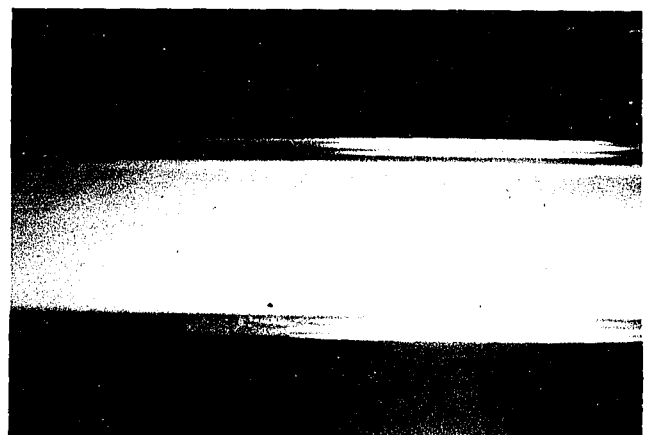
c) Loading ratio = .46



d) Loading ratio = .22



e) Loading ratio = .79



f) Loading ratio = .52

$(Re)_g = 25250$



a) Loading ratio = .12

$(Re)_g = 13675$  183.



b) Loading ratio = .04



c) Loading ratio = .50



d) Loading ratio = .45



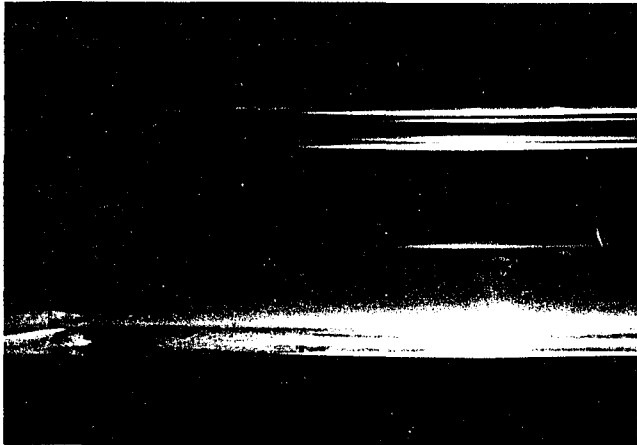
e) Loading ratio = 1.44



f) Loading ratio = .66

Figure 76 : Gross flow photographs of  $30 \mu$  particles.

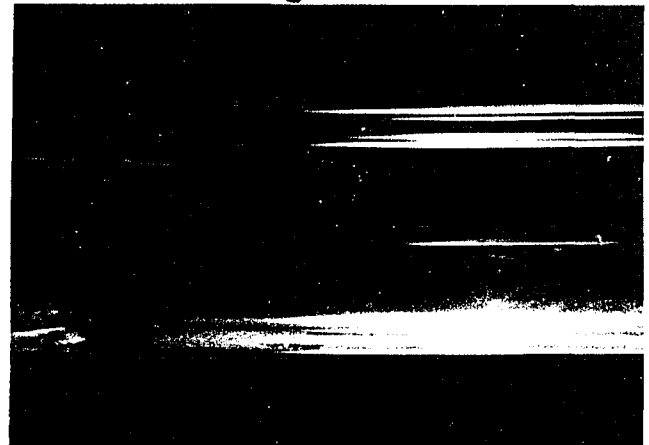
$(Re)_g = 25925$



a) Loading ratio = .16

$(Re)_g = 15000$

185.



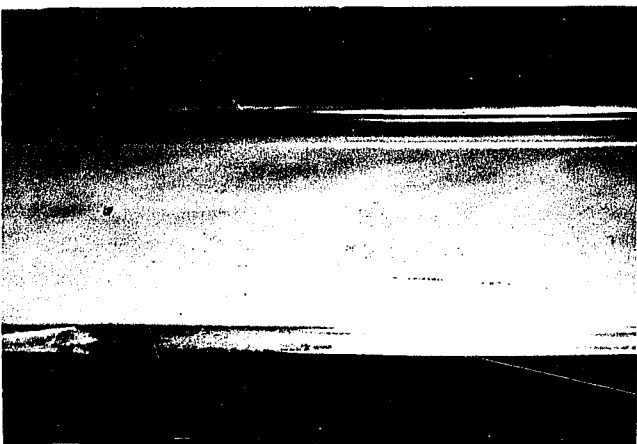
b) Loading ratio = .01



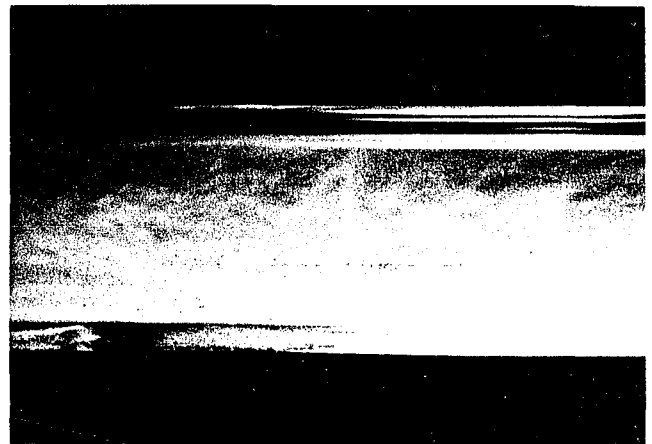
c) Loading ratio = 1.3



d) Loading ratio = .12



e) Loading ratio = 1.82



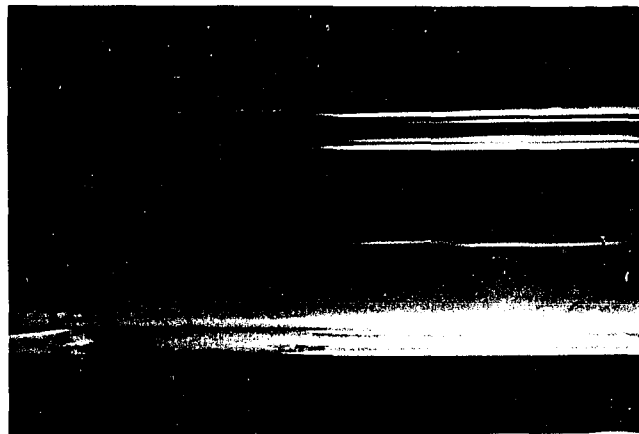
f) Loading ratio = .30

Figure 78: Gross flow photographs of #981 Glass Beads.

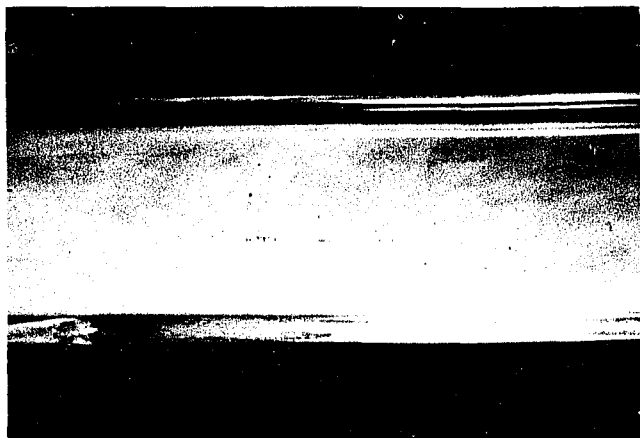
Figure 77: Gross flow photographs of #279 Glass Beads.

 $(Re)_g = 25900$  $(Re)_g = 14400$ 

a) Loading ratio = .14



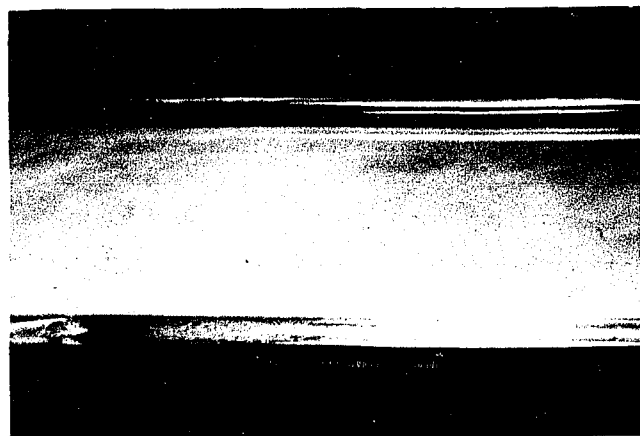
b) Loading ratio = .04



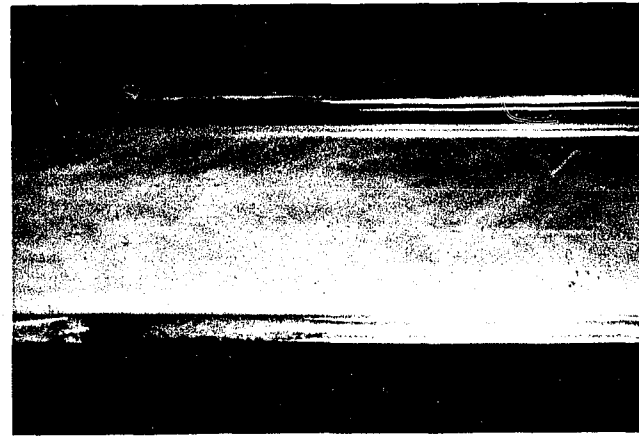
c) Loading ratio = .86



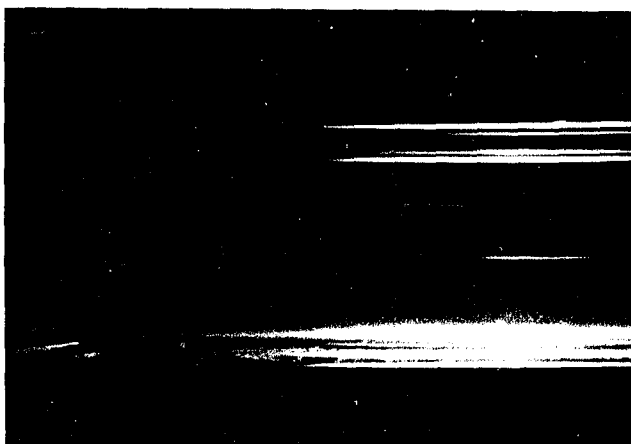
d) Loading ratio = .3



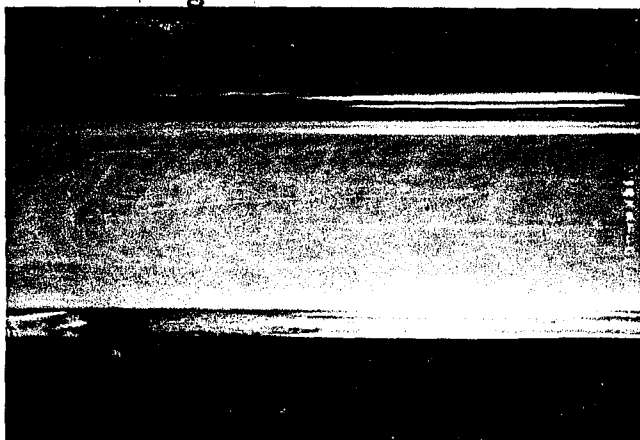
e) Loading ratio = 1.91



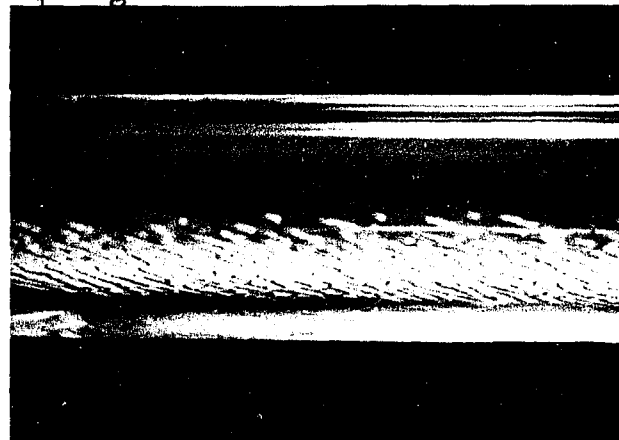
f) Loading ratio = .54



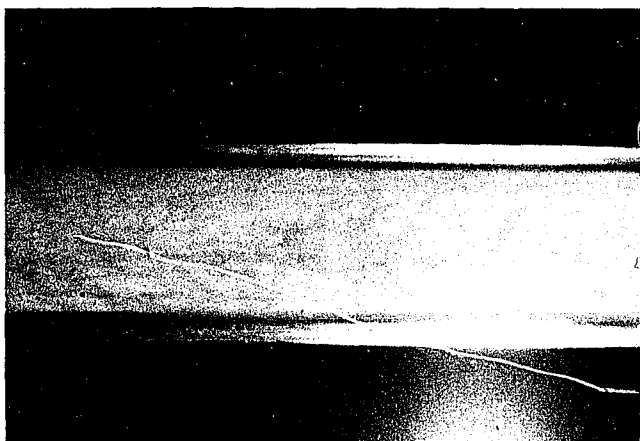
e) Loading ratio = 0.

 $(Re)_g = 27675$ 


a) Loading ratio = .20

 $(Re)_g = 16200$ 


b) Loading ratio = .01



c) Loading ratio = .74



d) Loading ratio = .10

Figure 79: Gross flow photographs of #980 Glass Beads.

conditions at each Reynolds number are shown for the #980 particles. The case of no loading in the loop is shown by figure 79e and can be used for the purpose of comparison.

By comparing the photographs for the  $50\mu$  and  $30\mu$  particles (where drag increase was observed in the horizontal section) to those for the smaller particles, certain flow differences seem evident. Whereas, the  $50\mu$  and  $30\mu$  particles do not appear to be following the turbulent fluctuations of the fluid to any great extent, the smaller particles show wisps of particle eddies indicating that they are more closely following the fluid flow. The #980 glass beads shown in figure 79 appear to have the greatest number of these eddies as well as the smallest size.

The "segregated" flow phenomena is shown by figure 76 for the  $30\mu$  glass beads. In this figure, the uneven distribution of the particles with greater particle density at the bottom than the top of the tube is clearly indicated.

By studying figures 75 - 79 it can be seen that this effect diminishes as the particle size decreases. The photographs for the  $50\mu$  glass beads are somewhat more difficult to analyze due to the fact that the camera was at a slightly greater distance from the photographic test sections when these pictures were taken. Consequently, less detail is evident in the photographs.

The type of coating or accumulation visually observed for the #980 glass beads is shown by figures 79b & d. The fine structure of the coating and tendency to deposit in the

flow direction are also indicated.

The photographic results presented above were all taken through a horizontal test section. Although it would have been desired to take photographs of the flow patterns in a vertical section, this was not feasible due to severe space limitations in the vicinity of the two pyrex vertical sections.

Particle size analysis. - The effect on the particle size and shape of continuous recirculating through the gas-solid circulator and the closed loop was also investigated during the course of this study. Samples of particles which had been continuously recirculated for long periods of time were collected in the sintered tube shown in Figure 6 and particle size distributions were obtained by use of a Coulter counter. In addition to these recirculated samples, particle samples taken before circulation in the loop were also analyzed. The results of these analyses are presented in figures 80 - 84. Each figure has two curves, one representing the initial size distribution of the particles and the other showing the effect of recirculation on this initial distribution.

Figure 80 shows the "before" and "after" distribution of what has been referred to previously as the  $50\mu$ -particles. The analysis indicated that the true average diameter of these particles before recirculation was approximately  $59\mu$ . It should be noted at this point, however, that some difficulties were experienced with this sample when using the same solution for testing as with the other samples. The sample was therefore reexamined by the Coulter counter using

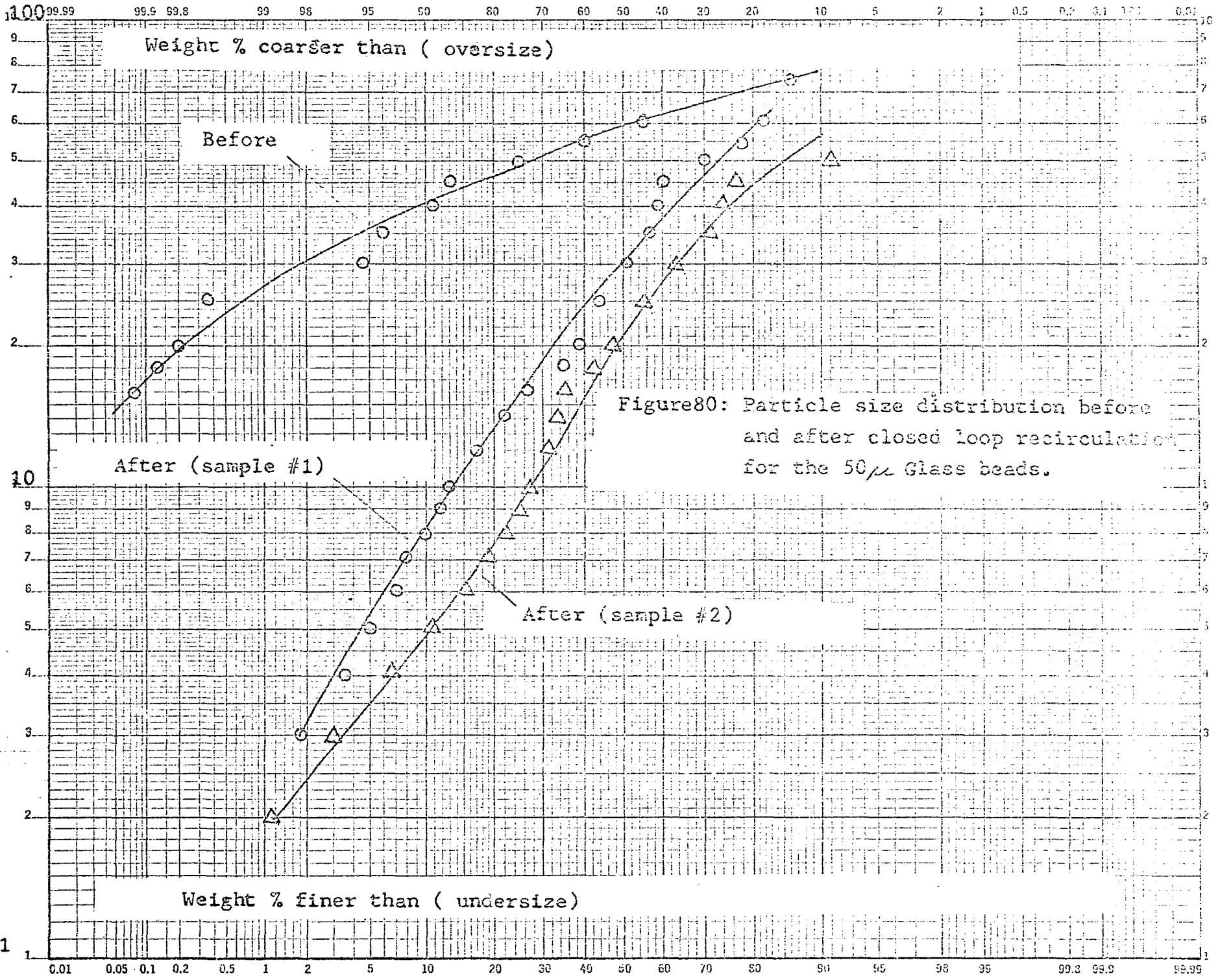


Figure 80: Particle size distribution before and after closed loop recirculation for the 50 $\mu$  Glass beads.

Particle size (microns)

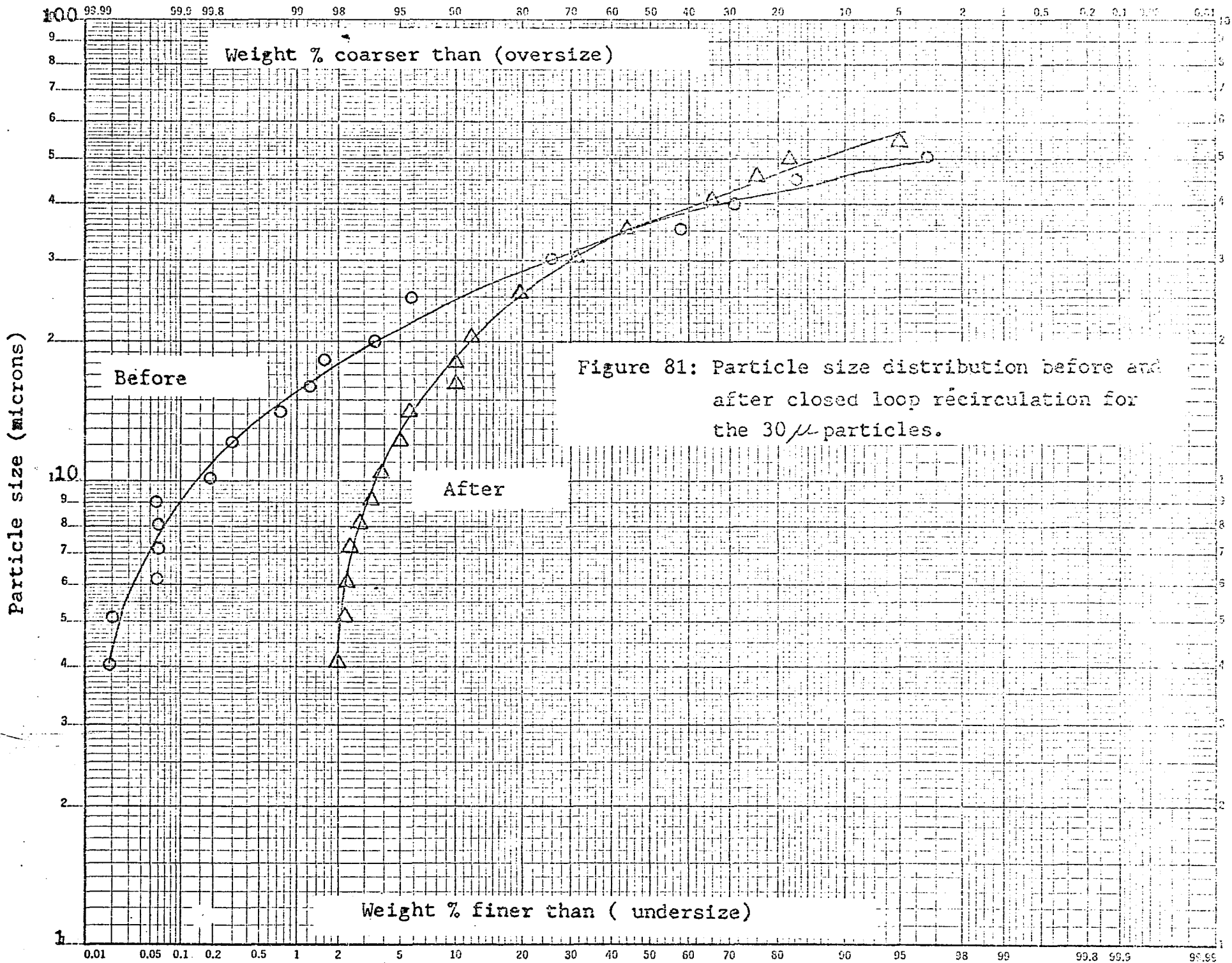
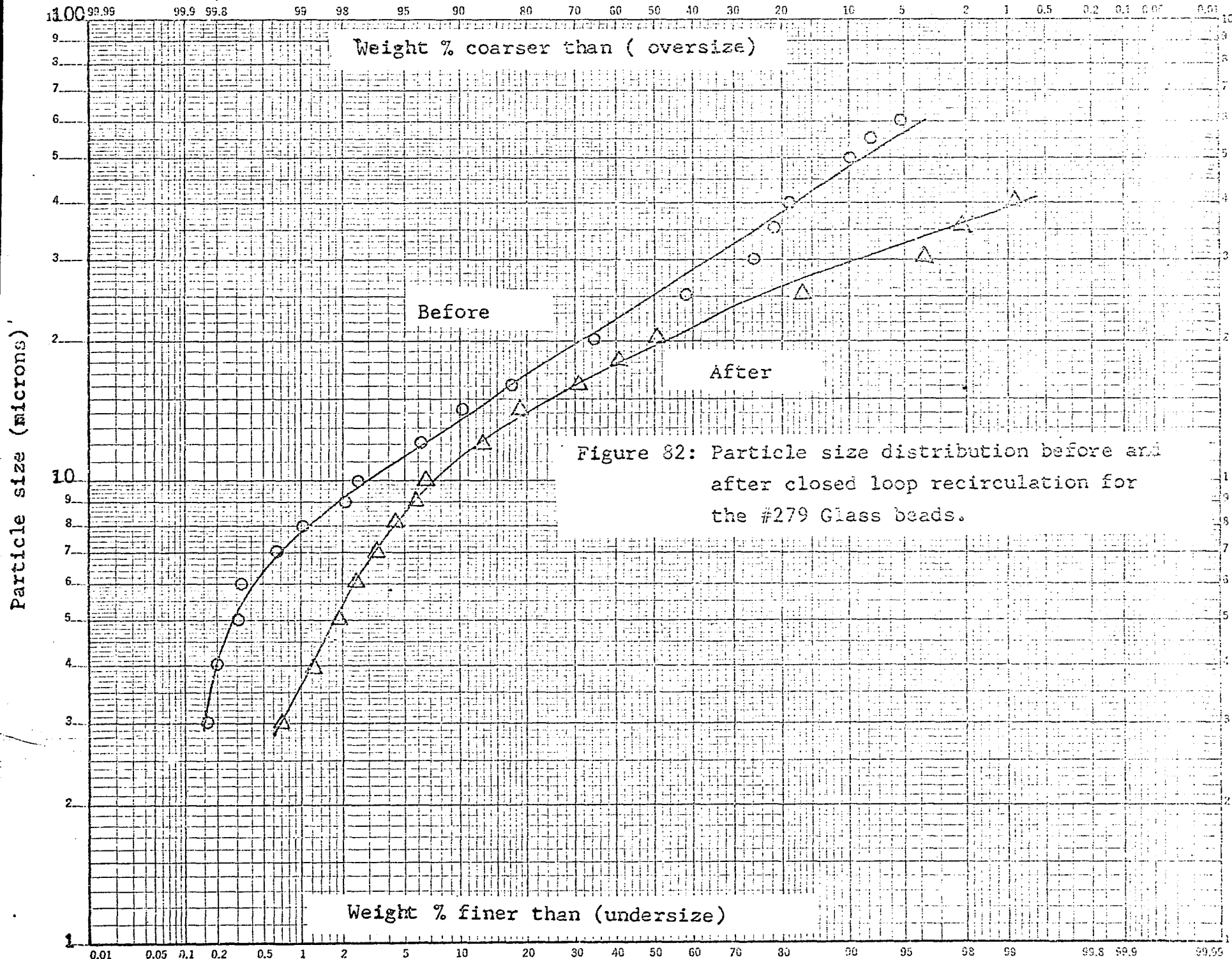


Figure 81: Particle size distribution before and after closed loop recirculation for the 30 $\mu$  particles.



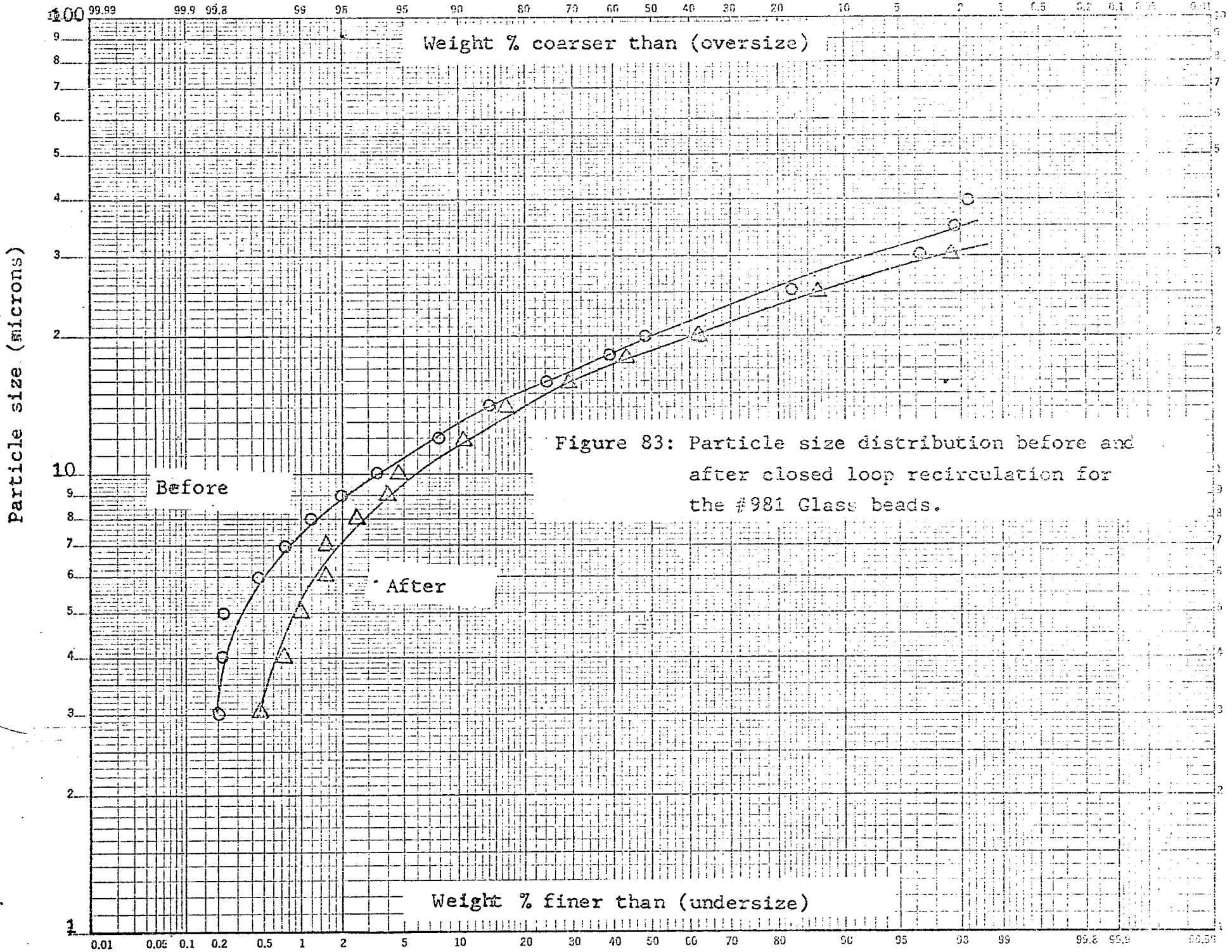


Figure 83: Particle size distribution before and after closed loop recirculation for the #981 Glass beads.

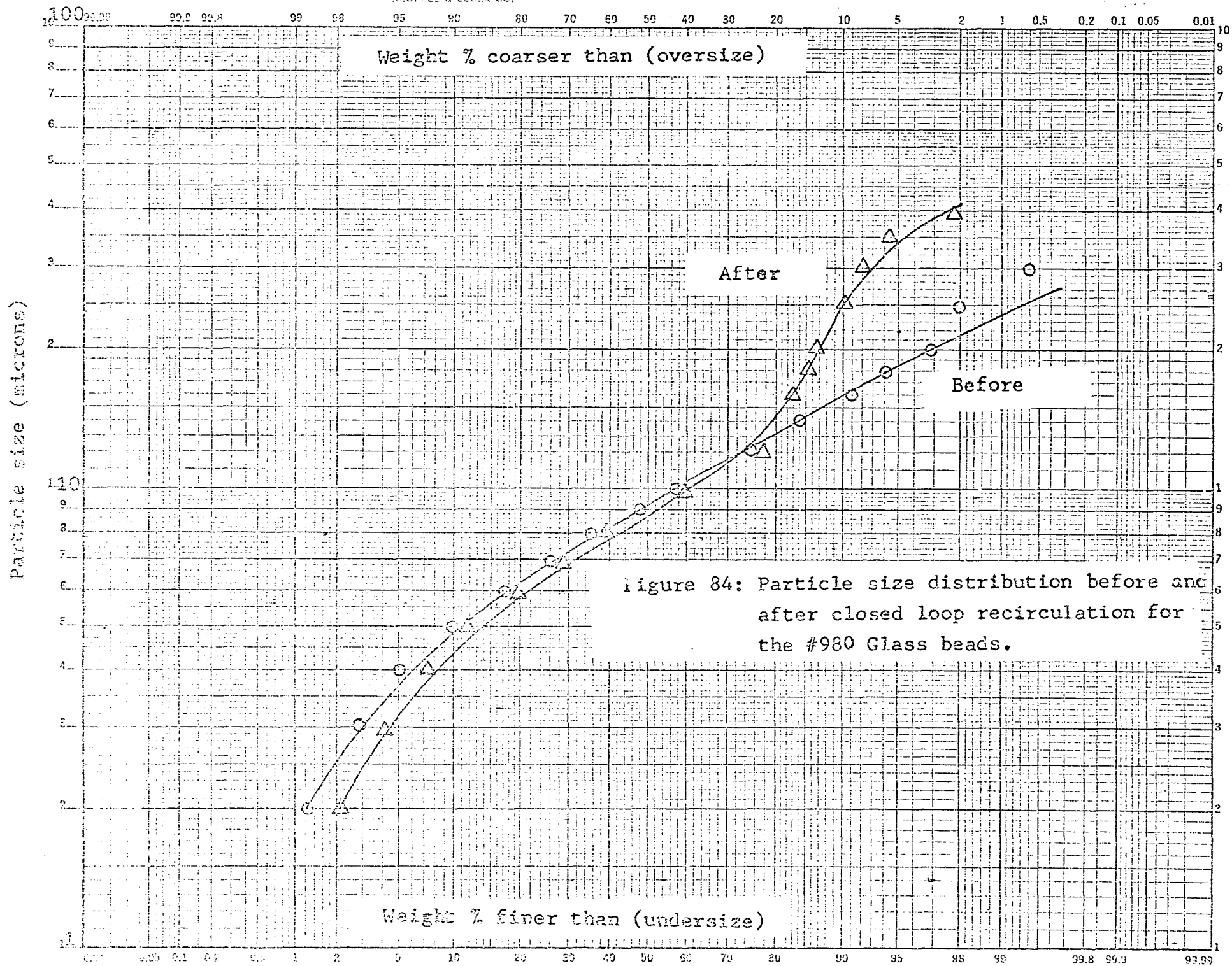


Figure 84: Particle size distribution before and after closed loop recirculation for the #980 Glass beads.

two other solutions. The results showed the same trend for the size distribution but with mean particle diameters of 44- and 46- $\mu$ .

The "after" results for the 50 $\mu$  particles were obtained from two different samples, each recirculated for approximately the same length of time under similar conditions of particle loading. These size distributions as indicated by the two lower curves in figure 80 show mean diameters of 20.5- and 31 $\mu$ , respectively. However, this in itself is quite a deceptive statistic. The results from both samples indicate that the distribution after recirculation has a double node, one at a particle size of approximately 50 $\mu$  and one around 30 $\mu$ . This would appear to indicate that the observed decrease in average particle diameter may not be the result of attrition alone but may also be caused by contaminants picked up during recirculation. Microscopic examination of these samples also revealed the presence of smaller irregular shaped, dark contaminants amongst the larger spherical glass beads. A photograph of one of these samples obtained using a metalograph is shown in figure 12b. Although the photograph seems somewhat unclear, the larger particles and smaller contaminants are visible. The figure also shows that the size of the spherical glass beads are approximately the same as those before recirculation. Due to the irregular shape of the contaminants and their dark color it may be concluded that they are small pieces of the metal loop (probably near the elbows) which have been eroded away and

become part of the recirculating stream.

The effect of recirculation on the  $30\mu$  particles is indicated in figure 81. The figure indicates that the mean particle size before recirculation is approximately  $34\mu$ ; whereas after recirculation the mean diameter is about  $36\mu$ . The fact that the size distributions appear relatively close also seem to show that very little particle attrition occurs for the  $30\mu$  particles. Microscopic examination revealed little or no contamination of the sample. The metalography photographs for the  $30\mu$  particles, shown in figure 13, also indicate that the particle sizes before and after recirculation are roughly the same and show little or no contamination of the used sample.

Figure 82, which shows the effect of recirculation on particle size for the #279 glass beads, reveals that the average particle diameters before and after recirculation are  $25\mu$  and  $20\mu$  respectively. The size distributions also indicate a slightly higher percentage of finer particles after recirculation. This would tend to indicate that there is some particle attrition, although not very much, for these particular samples. The metalography photographs for these particles shown in figure 14 do not indicate appreciable attrition or contamination of the sample.

The size distributions for the #981 glass beads before and after circulation through the loop are indicated in figure 83. A comparison between figures 82 and 83 reveals that the size distributions both before and after recirculation

for the #981 beads are very similar to those for the #279 particles. The only difference appears to be that before recirculation, the #279 beads have a larger percent of coarser material than the #981 particles. The mean diameters of the #981 beads as obtained from the figure are  $20\mu$  and  $18\mu$  before and after recirculation, respectively. The analysis indicates little evidence of particle attrition or contamination of the sample. These observations can also be made of the metalographic photographs of the #981 beads shown in figure 15.

The smallest particles used in this investigation were the #980 glass beads, for which size distribution curves are presented in figure 84. These curves show that the average diameters before and after circulation are  $7\mu$  and  $8.5\mu$ , respectively. The shape of the curves also indicates that little or no particle attrition occurred as a result of recirculating these particles through the loop. There does, however, appear to be some inconsistency between the results at the coarser end of the distribution. The after sample contains a larger percentage of coarse material as well as some large particles. This is probably due to contamination of the sample to a slight degree by recirculating through the system. Metalography photographs of the #980 glass beads both before and after recirculation are shown in figure 16. Although the figures do not indicate any inconsistencies of the sample, such contaminations would be difficult to see in a photograph due to the relatively small number of large contaminants

required to effect the results reported using the Coulter counter.

In conclusion it appears that particle attrition does not occur to any large extent with any of the particles tested, with the possible exception of  $50\mu$  particles. However, the particle size reduction for the  $50\mu$  particles appears to be mainly due to erosion of small pieces of metal from the loop by the particles and their subsequent addition to the fluid stream.

## V. CONCLUSIONS

A closed-loop system capable of continuously recirculating gas-solid suspensions has been built. This system was used to measure pressure drops, gas velocities, turbulence intensities and particle concentrations with the aid of a solid state anemometry unit and a specially designed and calibrated two-phase mass flow meter. Five different sizes of glass beads were studied during the investigation at three different gas Reynolds number ranges for both a vertical and horizontal test section. From the results of this investigation the following conclusions can be reached:

1. "Drag reduction" does occur with gas-solid suspensions for both horizontal and vertical test sections.
2. The results from the horizontal section in the loading ratio range up to 2.5 indicate that the "drag reduction" is greatest for the smallest particles (approximately 20%). Drag increases of as much as 40% were noted when the two largest size particles were circulated.
3. The vertical test section results for the same loading ratios indicate that "drag reduction" is at an optimum for the  $30\mu$  particles (approximately 75%) and that the amount of drag reduction decreases for the larger or smaller particles.
4. Except for the smallest particle size, the friction factor results for the vertical section were always lower than the horizontal section. For the smallest

particles the magnitude of the friction factor ratios in both sections was essentially the same.

5. The friction factor results for the vertical section can be explained by an analytical model proposed by Saffman (ref. 47) which indicates that due to the relaxation time of the particles, energy is extracted from the fluid stream instead of being dissipated at the wall.
6. The horizontal results cannot be explained by this theory because of gravitational effects which cause "bouncing" and "segregated" flow in the section.
7. At any suspension concentration the results from both test sections indicate that the lower the Reynolds number the higher the ratio of suspension to gas friction factor. This Reynolds number trend has been reported in many previous experimental investigations, even with large particles.
8. This investigation is the first reported experimental study in which a thermistor anemometer probe was used for gas velocity determination in a gas-solid suspension.
9. Calibrations of these thermistor probes obey King's law but are quite sensitive to temperature and are therefore required at a number of different temperatures.
10. These probes do not break when placed in the gas-solids stream even for very long periods of time.

Periodic checks on the calibration, and a continual check of the zero flow readings when working with the suspensions, indicate that the probe is essentially unaffected by the particles.

11. Orifice coefficient results based on anemometer velocities for both pure gas and suspensions show no discernible effect of particles. This confirms previous contentions that an orifice plate may be used to meter gas flow in gas-solids suspensions and is further evidence that the anemometer is essentially unaffected by the presence of the particles in the loading ratio range studied.
12. Studies of the flowing suspension concentration as a function of the weight of particles added to the system indicate that the smaller particles are initially more difficult to entrain and settle out at smaller concentrations than the large particles. This agrees with Soo's contention (ref. 45) that the saltation velocity goes through a minimum with a decrease in particle size so that very small particles actually require a higher velocity to keep them in suspension than larger particles.
13. Gross flow photographs of the horizontal test section indicate that the smaller particles are more easily dispersed in the gas and follow more closely the turbulent fluctuations in the fluid velocity.

14. The photographs also illustrate the "segregated" flow phenomena exhibited with large particle flows in the horizontal section.
15. Measurements of the intensity of turbulence taken in the downward vertical section of the loop for the pure gas indicate that over a large Reynolds number range the intensity of turbulence increases as the Reynolds number decreases. The trend is consistent with previous investigations and can be attributed to a build-up of the laminar sub-layer at lower Reynolds numbers.
16. The turbulence results, however, are substantially lower in magnitude than those found in previous investigations. This is attributed to an insufficient length of undisturbed tubing from the orifice to the anemometer probe (see Figure 6).  
The net result of this small L/D ratio is a decrease in the magnitude of the centerline turbulence although the correct trend with Reynolds number is still obtained. Ratios of the relative intensity of turbulence between the pure gas and the suspension should therefore reflect the effect of particles on the turbulence.
17. Results from these intensity ratio data for the five particle sizes investigated indicate that the percent turbulence at the center of the tube increases as particles are added to the system. This is consistent with Saffman's model since extraction of energy from

the fluid by the particles in the vicinity of the wall would result in a thickening of the laminar sub-layer and a consequent increase in the centerline turbulence.

18. The intensity of turbulence results do not show a discernible Reynolds number effect at any loading ratio for any of the particles investigated. This is probably due to the relatively small Reynolds number range studied.
19. The centerline turbulence intensity ratio appears to be an indicator of drag reduction since the highest intensity ratio was observed for the 30 $\mu$  particles where the greatest drag reduction was also observed. With the exception of the 50 $\mu$  glass beads, the higher the relative intensity ratio, the more drag reduction obtained.
20. Particle size analysis reveals little particle attrition with all particles except the 50 micron particles.
21. Particle size analysis of the 50 micron sample after recirculation in the closed loop, reveals that this sample may have been contaminated by metal eroded from the loop.

## VI. RECOMMENDATIONS FOR FUTURE WORK

While a great deal of new information has been obtained from this investigation, there are still many unanswered questions which should be resolved. For example: Will drag reduction still be observed with particles larger than  $50\mu$  in the vertical section? How important are electrostatic effects? Is there any difference between pressure drop measurements taken in test sections of different materials, e.g., glass or metal? What effect does particle size have on the strain gage calibration? What effect does the particle material (composition, density, shape, etc.) have on the pressure drop?

In addition to answering some of these questions it would be very valuable to be able to measure both the gas and particle velocity profiles in the tube. The gas velocity profiles can be readily measured with our present anemometer unit using a modified thermistor probe. Particle velocity profiles have been successfully measured by McCarthy and Olson (ref. 28) and others using special photographic techniques. A knowledge of the slip velocity of the particles at different radial positions in the tube in both the horizontal and vertical test section is necessary to test the particle stabilizing theory of Saffman (ref. 47) as well as to develop a mathematical model to describe the experimental results. It would also be very desirable to have measurements of the intensity of turbulence at different radial positions in the tube especially in the vicinity of the wall.

The effect of the particles on the turbulent energy spectra would be important for the formulation of a model. This information could be obtained by use of a spectrum analyzer in conjunction with the anemometer and the experimental loop. Increasing the length of undisturbed tubing prior to taking turbulence measurements would also give more significance to the turbulence data obtained.

Photographs of the gross flow patterns in the vertical test section as well as turbulence measurements in the horizontal section would also further elucidate the phenomena. Several instrumentation additions would tend to improve the accuracy of the data obtained. A linearizer which would result in straight line anemometer calibrations and allow the percent turbulence to be read directly would shorten data taking and processing time as well as improve the accuracy of the data. In view of difficulties experienced in positioning and moving the anemometer probe when making traverses across the tube, the development of an improved traversing system (preferably automatic) is also necessary.

## VII. LITERATURE CITED

- (1) Zenz, F.A. and Othmer, D.F., "Fluidization and Fluid-Particle Systems", Reinhold Publishing Corp. (1960).
- (2) Hinkle, B.L., "Acceleration of Particles and Pressure Drops Encountered in Pneumatic Conveying" Ph.D. Thesis, Georgia Inst. Tech. (1953).
- (3) Vogt, E.G. and White, R.R., Ind. Eng. Chem., 40, 1731 (1948).
- (4) Gasterstadt, J., Forsh. Arb. Ing. Wes., 265, 1 (1924).
- (5) Belden, D.H. and Kassel, L.S., Ind. Eng. Chem., 41, 1174 (1949).
- (6) Wen, C.Y. and Simons, H.P., A.I.Ch.E. J., 5, 263 (1959).
- (7) Dogin, M.E. and Lebedev, V.P., Int. Chem. Eng., 2, 64 (1962).
- (8) Doig, I.A. and Roper, G.H., I & EC Fund, 6, 247 (1967).
- (9) Doig I.A. and Roper, G.H., Aust. Chem. Eng., 4, 1 (1963).
- (10) Hariu, O.H. and Molstad, M.C., Ind. Eng. Chem., 41, 1148 (1949).
- (11) Clark, R.H., Charles, D.E., Richardson, J.F. and Newitt, D.M., Trans. Inst. Chem. Eng., 30, 209 (1952).
- (12) Helander, R.E., "The Flow Characteristics of Air-Solids Mixtures", Ph.D. Thesis, Northwestern Univ. (1956).
- (13) Mitlin, L. "A Study of Pneumatic Conveying with Special Reference to Particle Velocity and Pressure Drop During Transport", Ph.D. Thesis, Univ. of London (1954).
- (14) Julian, F.M., "A Study of Pressure Drop in Gas-Solid Flow", M.S. Thesis, Univ. of Houston (1964).
- (15) Farbar, L., Ind. Eng. Chem., 41, 1184 (1949).
- (16) Mehta, N.C., Smith, J.M. and Comings, E.W., Ind. Eng. Chem., 49, 986 (1957).
- (17) Pfeffer, R., Rossetti, S.J., and Lieblein, S., NASA TN, D 3603 (1966).
- (18) Anon: Gas-Suspension Coolant Project, Rept. BAW-1159, The Babcock and Wilcox Co. (1959).

Literature Cited cont.

- (19) Anon: Gas-Suspension Task II, Rept. BAW-1181, The Babcock and Wilcox Co. (1959).
- (20) Schluderberg, D.C., Whitelaw, R.L. and Carlson, R.W., Nucleonics, 19, 67 (1961).
- (21) Wachtell, G.P., Waggener, J.P. and Steigelmann, W.H., Rept. NYO-9672, AEC (1961).
- (22) Peskin, R.L. and Dwyer, H.A., Rept. NYO-2930-1 (101-ME-F), AEC 1964.
- (23) Korn, A.H., Chem. Eng., 57, 108 (1950).
- (24) Peskin, R.L., Quarterly Repts. 63-1 and 64-1, Contract No. AT (30-1) 2930, Rutgers Univ. (1963).
- (25) Soo, S.L., Trezek, G.J., Dimick, R.C. and Hohnstreiter, G.F., I & EC Fund., 3, 98 (1964).
- (26) Soo, S.L. and Trezek, G. J., I & EC Fund., 5, 388 (1966).
- (27) Thomas, D.G., A.I. Ch.E. J., 6, 631 (1960).
- (28) McCarthy, H.E. and Olson, J.H., I & EC Fund., 7, 471 (1968).
- (29) Rosenecker, C.N., Coates, N.H. and Lucas, H.G., Report of Investigations 7019, Bureau of Mines (1966).
- (30) Gibson, H.G., Abel, W.T. and Fasching, G.E., Proc. Multi-Phase Flow Symp, ASME, Philadelphia, pp. 49-54 (1963).
- (31) Depew, C.A. "Heat Transfer to Flowing Gas-Solids Mixtures in a Vertical Circular Duct, Ph.D. Thesis, Univ. of Calif. (1960).
- (32) Tien, C.L., J. Heat Transfer, 83, 183 (1961).
- (33) Tien, C.L. and Quan, V., Paper No. 62-HJ-1t, ASME (1962).
- (34) Boothroyd, R.G., Trans. Instn. Chem. Engrs., 44, 306 (1966).
- (35) Boothroyd, R.G., Trans. Instn. Chem. Engrs., 45, 297 (1967).
- (36) Boothroyd, R.G., J. Sci. Instrum., 44, 249 (1967).

Literature Cited cont.

- (37) Taylor, G.I., Proc. Lond. Math. Soc., 20, 196 (1921).
- (38) Soo, S.L., I & EC Fund., 1, 33 (1962)
- (39) Soo, S.L., A.I. Ch.E. Preprint 36E, Dallas (1966).
- (40) Soo, S.L., A.I.Ch.E. J., 7, 384 (1961).
- (41) Soo, S. L. and Tien, C.L., J. Appl. Mechanics, 27E, 5 (1960).
- (42) Soo, S.L. and Regalbuto, J.A., Can. J. Chem., 38, 160 (1960).
- (43) Hirshfelder, J.O., Curtiss, C.F. and Bird, R.G., "Molecular Theory of gases and Liquids", John Wiley and Sons (1954).
- (44) Sproull, W.T. Nature, 190, 976 (1961).
- (45) Soo, S.L. "Fluid Dynamics of Muliphase Systems", Blaisdell Publishing Co. (1967).
- (46) Saffman, P.G., Nature, 193, 463 (1962).
- (47) Saffman, P.G., J. Fluid Mech., 13, 120 (1962).
- (48) Michael, D.H., J. Fluid Mech., 15, 19 (1964).
- (49) Julian, F. M., and Dukler, A.E., A.I.Ch.E. J., 11, 853 (1965).
- (50) Gill, W.N. and Scher. M., A.I.Ch.E. J., 7, 61 (1961).
- (51) Savins, J.G. Soc. Petr. Eng. J., 4, 203 (1964).
- (52) Fabula, A.G., Proc. Fourth Intern. Congr. on Rheology, 455 (1965).
- (53) Ernst, W.D., A.I.Ch.E. J., 12, 581 (1966).
- (54) Hershey, H.C. and Zakin, J.L., I & EC Fund., 6 381 (1967).
- (55) Astarita, G., I & EC Fund., 4, 354 (1965).
- (56) Agoston, G.A., et.al., Ind. Eng. Chem., 46, 1917 (1959).
- (57) Savins, J.G., Preprint 1724, SPE Symp. on Rheologically Complex Fluids, Houston (1966).
- (58) Radin, I., M.S. Thesis, Univ. of Missouri at Rolla (1968).

Literature Cited cont.

- (59) Daily J.W., and Bugliarello, G., Tappi, 44, 497 (1961).
- (60) Bobkowicz, A.J., and Gauvin, W.H., Can. J.Chem. Eng., 43, 87 (1965).
- (61) Vanoni, V.A. and Nomicos, G.N., Trans. ASCE, 125, 1140 (1960).
- (62) Patterson, G.K., Zakin, J.L. and Rodriguez, J.M., Paper in press (1969).
- (63) Foust, A.S., Wenzel, L.A., Clump, C.W., Maus, L. and Anderson, L.B., "Principles of Unit Operations", John Wiley & Sons, Inc. (1960).
- (64) Orr, C., "Particulate Technology, " The Macmillan Company (1966).
- (65) Laufer, J., Nat'l Advisory Comm. Aeronaut. Rept. 1053 (1951).
- (66) Martin, G.Q., and Johanson, L.N., AIChE J., 11, 29 (1965).
- (67) Patterson, G., Personal Communication (1969).
- (68) Patterson, G.K., "Turbulence Measurements in Polymer Solutions Using Hot-Film Anemometry", Ph.D. Thesis, University of Missouri at Rolla (1966).
- (69) Perry, J.H., editor, "Chemical Engineers Handbook, 4th Edition", McGraw-Hill Book Company (1963).

## VII. LIST OF SYMBOLS

<u>Symbols</u>	<u>Definitions</u>	<u>Units</u>
a	constant defined by equation(46)	dimensionless
A	cross sectional area of tube	(L <sup>2</sup> )
A <sub>D</sub>	parameter defined by equation(18)	dimensionless
b	constant defined by equation (46)	"
B	experimentally determined constant in equation(54)	"
B <sub>v</sub>	function of dimensionless group Rep (C <sub>D</sub> ) <sup>2</sup> (see equation (17))	"
C <sub>D</sub>	drag coefficient	"
C <sub>p</sub>	specific heat	(Q/MT)
C <sub>v</sub>	orifice coefficient	dimensionless
D	tube diameter	( L )
D <sub>p</sub>	particle diameter	( L )
f	Fanning friction factor	dimensionless
f <sub>B</sub>	Blasius friction factor = 4 x Fanning friction factor	"
f <sub>g</sub>	pure gas friction factor	"
f <sub>m</sub>	friction factor defined by equation (22)	"
f <sub>p</sub>	particle friction factor	"
f <sub>s</sub>	suspension friction factor based on the suspension density	"
f <sub>s</sub> '	suspension friction factor based on the pure gas density	"
F	force	( F )
F <sub>D</sub>	drag force	( F )
F <sub>G</sub>	function defined by equation (16)	dimensionless
F <sub>r</sub>	Froude number	"

List of Symbols (cont.)

<u>Symbols</u>	<u>Definitions</u>	<u>Units</u>
g	acceleration of gravity	(L/t <sup>2</sup> )
g <sub>c</sub>	gravitational constant	( $\frac{ML}{Ft^2}$ )
G	mass velocity	(M/L <sup>2</sup> t)
h	convective heat transfer coefficient	(Q/L <sup>2</sup> T)
I	relative turbulence intensity	dimensionless
k	Von Karman constant	"
k <sub>1</sub> , k <sub>2</sub>	constants defined by equation (37)	"
k <sub>1</sub> ', k <sub>2</sub> '	constants defined by equation (44)	"
k <sub>1</sub> ", k <sub>2</sub> "	constants defined by equation (46)	"
K	modified Von Karman constant defined by equation (20)	"
l	function of $Re_p(C_D)^{\frac{1}{2}}$ defined by equation (17)	"
L	length of pipe	( L )
m	mass	( M )
n	number of particles per unit volume of mixture	dimensionless
n	experimental constant in equation (54)	"
P	pressure	(F/L <sup>2</sup> )
ΔP	pressure drop	(F/L <sup>2</sup> )
ΔP <sub>a</sub>	acceleration pressure losses	(F/L <sup>2</sup> )
ΔP <sub>h</sub>	gravity pressure head in vertical section	(F/L <sup>2</sup> )
ΔP <sub>m</sub>	measured pressure drop	(F/L <sup>2</sup> )
ΔP <sub>mc</sub>	measured pressure drop corrected for length of manometer leads	(F/L <sup>2</sup> )
R	universal gas constant	

List of Symbols (cont.)

<u>Symbols</u>	<u>Definition</u>	<u>Units</u>
Re	Reynolds number	dimensionless
t	time	( t )
T	temperature	( T )
u	fluctuating velocity	(L/t)
U	point bulk velocity	(L/t)
$\bar{U}$	bulk velocity	(L/t)
v	velocity	(L/t)
$v_{ps}$	terminal settling velocity	(L/t)
V	anemometer D.C. voltage,	(volts)
$V_{rms}$	root mean square voltage,	(volts)
$V_{rms0}$	initial root mean square velocity	(volts)
$V_{ST}$	strain gage readout	(volts)
$V_{ST0}$	strain gage readout for pure gas flow	(volts)
$V_o$	no flow anemometer D.C. voltage	(volts)
W	mass flow rate	(M/t)
$\rho$	density	(M/L <sup>3</sup> )
$\rho'$	bulk density	(M/L <sup>3</sup> )
$\eta$	particle loading ratio	dimensionless
$\delta$	$(C_p)_p / (C_p)_g$ ratio of specific heats	"
$\mu$	microns	( L )

List of Symbols (cont.)Subscripts

s suspension

g gas

p particle

1 initial

2 final

avg average

f fluid

## IX. APPENDIX A

## METHODS OF CALCULATION AND SAMPLE COMPUTATIONS

## 1. Pitot-Static Section Velocity Profiles.

Velocity data using the downstream pitot-static section were obtained across the tube diameter at the following positions:

<u>Position</u>	<u>Distance from top inner tube wall (inches)</u>
1	.031
2	.071
3	.131
4	.201
5	.301
6	.441
7	.581
8	.681
9	.751
10	.801
11	.841

With exception of 1, 11 and 6 these are the positions recommended (ref. 69) for a standard 10 point traverse for obtaining average velocity in circular tubes. Positions 1 and 11 were used instead of those recommended because the size of the impact tube precluded the possibility of measurement closer to the tube wall. Position 6 corresponds to the center of the tube, within the accuracy of the manual traverse used for positioning. Although measurements at the center of the tube are not necessary for the standard 10 point traverse, these measurements were taken so that the resulting velocity profiles could be compared with those predicted by the 1/7th power law using the centerline velocity.

The data necessary to determine each velocity were the pitot static pressure drop and the temperature of the flowing air.

$$v = C_{pt} \sqrt{2g_c \frac{(-\Delta P)}{\rho}} \quad \text{A-1}$$

where

$$\rho = .0808 \left( \frac{492}{460+T} \right) \quad \text{A-2}$$

and  $C_{pt}$ , the pitot tube coefficient, was found to be unity.

A sample computation for obtaining the average velocity from the raw data is presented below. Since the computations at each position along the tube are essentially the same only calculations for one position will be illustrated.

Data from typical run were as follows:

position - 6

$$T = .935 \text{ mv} = 74.25^\circ \text{ F}$$

$$\rho = .0808 \left( \frac{492}{534.3} \right) = .0744 \frac{\text{lb}}{\text{ft}^3}$$

$$v = 8.03 \sqrt{\frac{-\Delta P}{.0744}}$$

$$v = 29.4 \sqrt{-\Delta P}$$

The pressure drop was measured using three instruments:

an R. Feuss micromanometer reading mm of water, a movable leg manometer reading in feet of water, and a hook gage reading in inches of water. It was therefore necessary to convert each reading into  $\text{lb}/\text{ft}^2$ . The instrument readings were:

$$\begin{aligned} \text{a) Micromanometer, } -\Delta P &= 16.75 \text{ mm H}_2\text{O} \\ -\Delta P &= 16.75 \text{ mm H}_2\text{O} \times .003281 \frac{\text{ft}}{\text{mm}} \times 62.2 \frac{\text{lb}}{\text{ft}^3} = 3.425 \frac{\text{lb}}{\text{ft}^2} \end{aligned}$$

$$\text{b) Movable leg manometer, } -\Delta P = .0550 \text{ ft. of H}_2\text{O, } -\Delta P = .0550 \text{ ft.} \times \frac{62.2 \text{ lb}}{\text{ft}^3} = 3.425 \frac{\text{lb}}{\text{ft}^2}$$

$$\text{c) Hook gage, } -\Delta P = .6635 \text{ in. H}_2\text{O, } -\Delta P = .6635 \text{ in.} \times \frac{62.2 \text{ lb}}{\text{ft}^3} \times \frac{1 \text{ ft}}{12 \text{ in}} = 3.44 \frac{\text{lb}}{\text{ft}^2}$$

The velocities obtained were:

$$\text{Micromanometer } - v = 29.4 \sqrt{3.425} = 54.4 \frac{\text{ft}}{\text{sec}}$$

$$\text{Movable Leg } - v = 29.4 \sqrt{3.425} = 54.4 \frac{\text{ft}}{\text{sec}}$$

$$\text{Hook Gage } - v = 29.4 \sqrt{3.44} = 54.6 \frac{\text{ft}}{\text{sec}}$$

Similar calculations were performed at the remaining ten positions in the tube. These velocities were then plotted as a function of tube position on arithmetic graph paper. A curve was faired through the points to represent the velocity profile. Representative values of the velocity were then read from the curve at each radial position (r) where data were obtained. These velocities were then multiplied by r. For the example under consideration, these results were tabularized as follows:

<u>Position</u>	r	v	vr
6	.0035	54.4	.190
7	.1435	51.6	7.40
5	.1365	52.8	7.23
8	.2435	47.8	11.62
4	.2365	49.5	11.70
9	.3135	44.0	13.78
3	.3065	45.7	14.02
10	.3635	39.9	14.50
2	.3665	41.1	15.08
11	.4035	34.2	13.79
1	.4065	33.5	13.62
w	.4375	0	0

An arithmetic plot of  $vr$  as function of  $r$  was then prepared as shown in figure A-1.

The average velocity  $\bar{v}$  is defined by

$$\bar{v} = \frac{2\pi \int_0^{r_0} vr \, dr}{\pi r_0^2} \quad \text{A-3}$$

so that upon substitution of .4375 for  $r_0$ , equation A-3 becomes

$$\bar{v} = 10.45 \int_0^{r_0} vr \, dr$$

The value  $\int_0^{r_0} vr \, dr$  was determined by finding the area under the curve shown in figure A-1 by use of a polar planimeter. for the example under consideration the area was 4.08. So that,

$$\bar{v} = 4.08 (10.45) = 42.7 \frac{\text{ft}}{\text{sec}}$$

and

$$\frac{\bar{v}}{v_c} = \frac{42.7}{54.4} = .788$$

## 2. Anemometer Calibration.

Five thermistor probes were calibrated using the downstream pitot-static section during the course of the investigation. For the sake of brevity a sample calculation for only one probe at one temperature and one velocity will be illustrated below. A typical calculation was performed as follows:

DATA:

Probe #5

RPM = 13200

$T = .95 \text{ mv} = 75^\circ\text{F}$

$\rho_g = .0743$

$\Delta P_{pt} = 6.75 \frac{\text{lb}}{\text{ft}^2}$  (after conversion from mm water)

Figure A 1: Variation of the product  $v_r$  with radial distance  $r$  for a typical run.

15.0

10.0

5.0

0

product  $v_r$ , (ft/sec) in.

.10

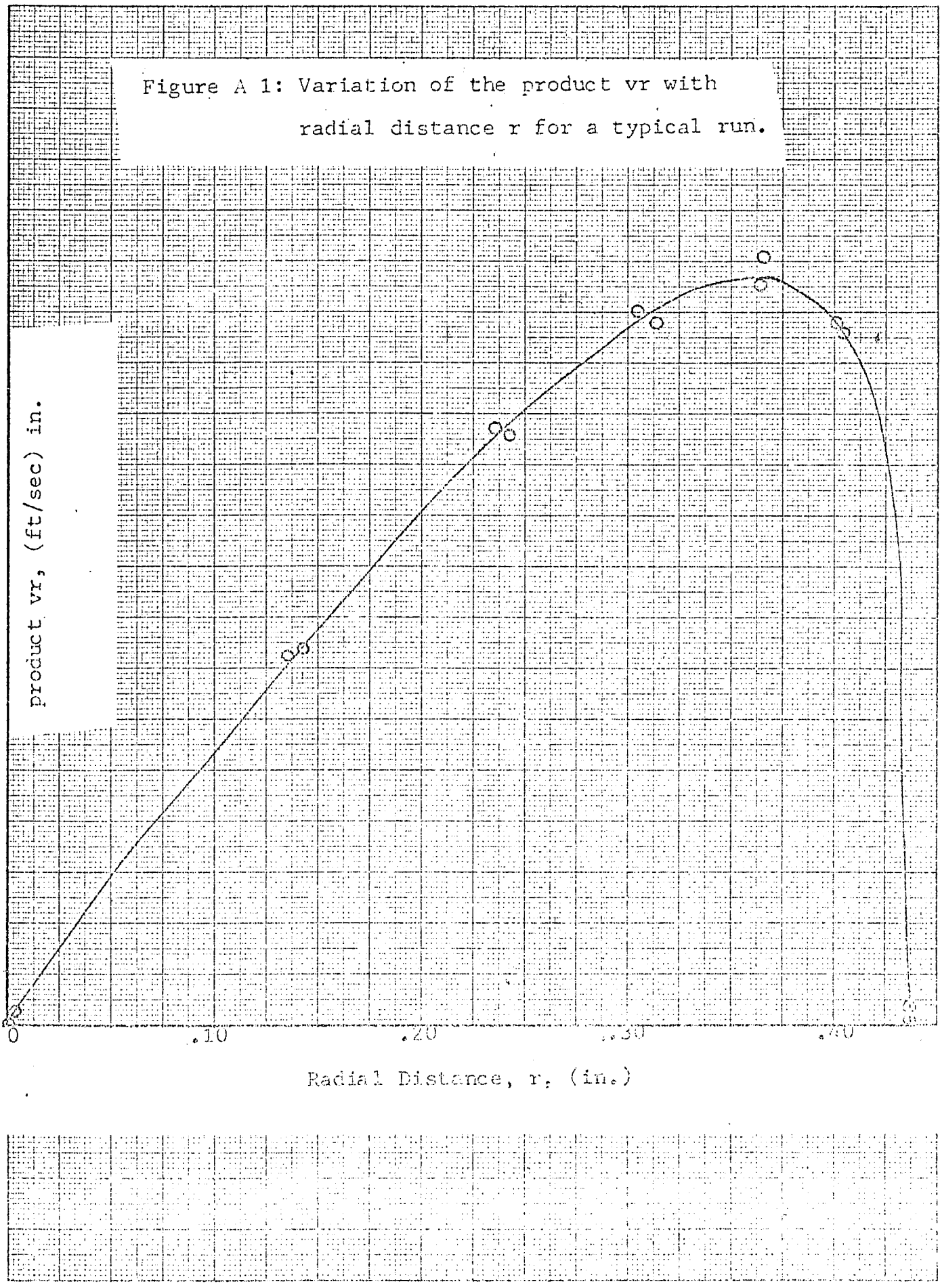
.20

.30

.40

Radial Distance,  $r$ , (in.)

10 X 10 TO THE CENTIMETER 46 1513  
13 X 25 CM.  
KEUFFEL & ESSER CO.



$$v_c = \sqrt{\frac{2g_c \Delta P_{pt}}{\rho_g}}$$

$$v_c = \sqrt{\frac{64.4}{.0743} (6.75)} = 29.4 \sqrt{6.75} = 76.5 \frac{\text{ft}}{\text{sec.}}$$

$$V = 6.065 \text{ volts}$$

$$V_o = 3.745 \text{ volts} \quad \text{RPM} = 0$$

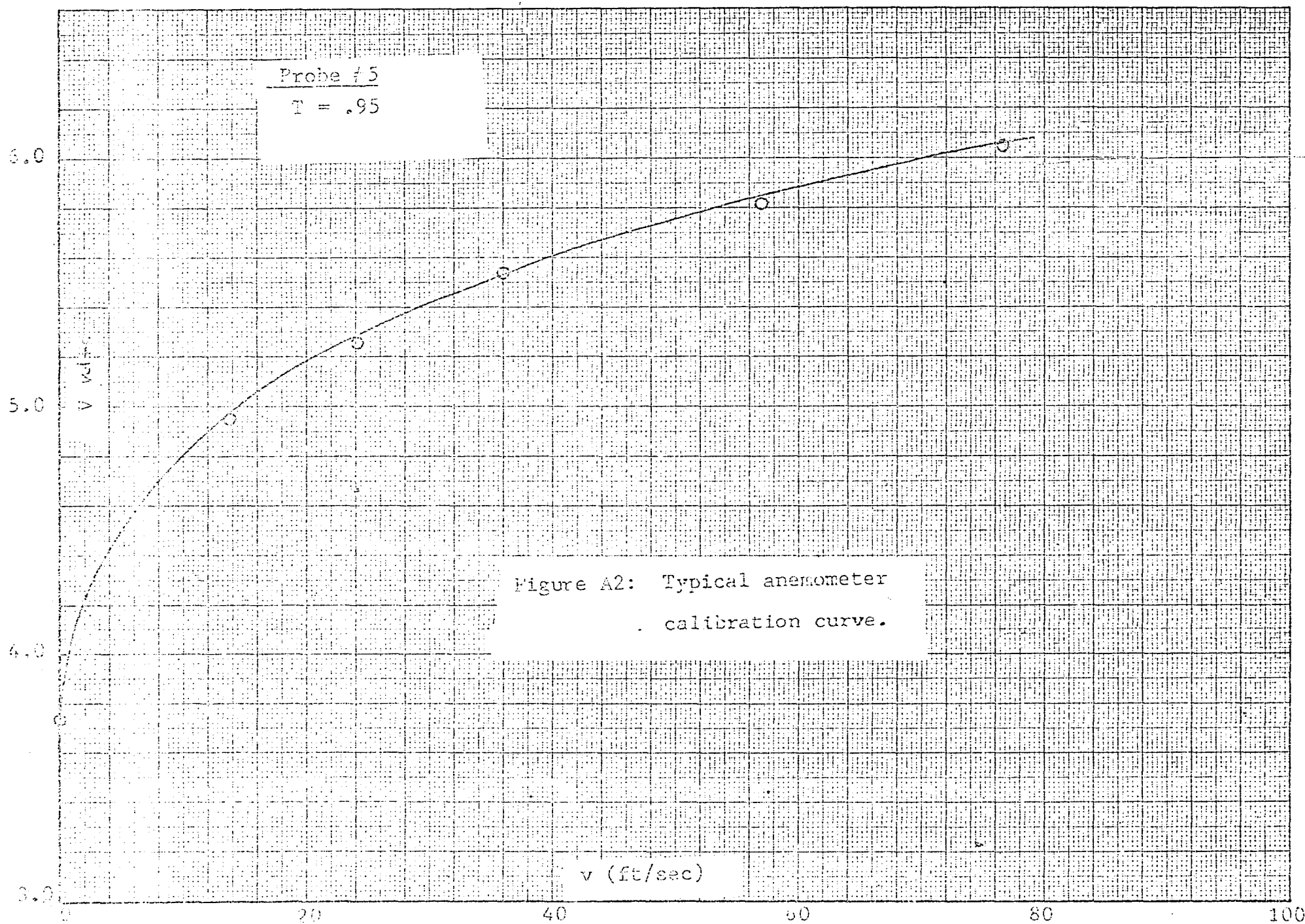
Data were calculated in a similar manner for all velocities at a minimum of 6 temperatures between  $T = .90$  and  $1.20$  mv. A typical curve showing the relation between  $V$  and  $v_c$  at a given temperature is shown in figure A2. A series of these curves for at least six different temperatures was then crossplotted so as to obtain a curve of  $V$  as a function of  $T$  with  $v_c$  as a parameter (see figure 20). King's law for flow around a cylinder would predict that the relation between  $V$  and  $v_c$  would take the following form:

$$V^2 - V_o^2 = Bv_c^n \quad \text{A-4}$$

for the anemometer unit used in this investigation. If this were so, a plot of  $\log (V^2 - V_o^2)$  as a function of  $\log v_c$  would result in a straight line of slope  $n$ . Such a plot is shown in figure A3 for three different temperatures using probe #5. As can be seen, the resultant curves are three straight lines of slope approximately equal to .5 as predicted by King's law.

### 3. Friction Factor and Reynolds Number.

The gas Reynolds number and the Blasius friction factor for the horizontal and vertical test sections were



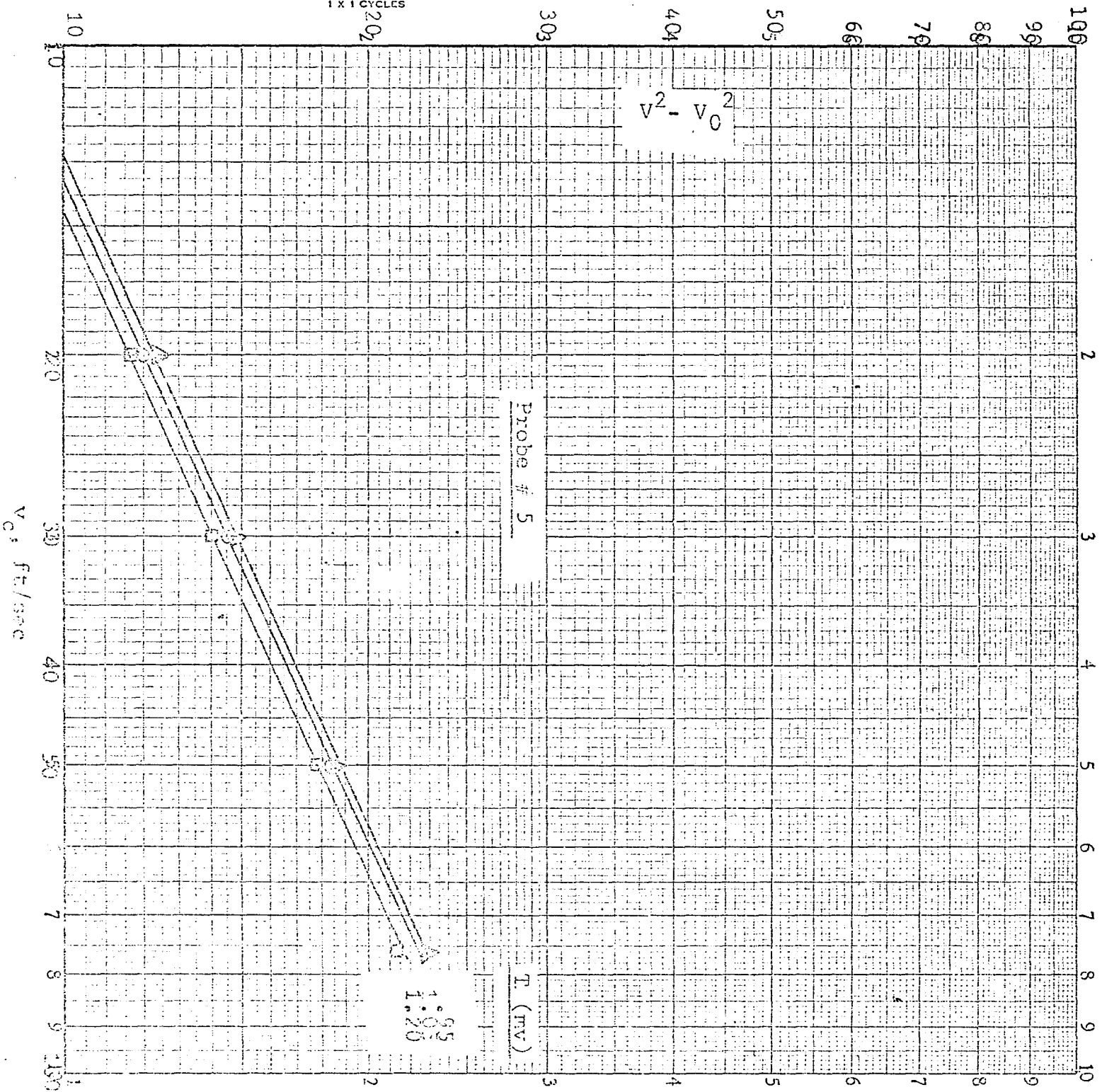


Figure A3: Variation of  $\log(V^2 - V_0^2)$  with  $\log V_c$ .

calculated from the following equations:

$$(\text{Re})_g = \frac{\rho \bar{v} D}{\mu} \quad \text{A-5}$$

$$f_g = \frac{2g_c \Delta \text{PD}}{\rho \bar{v}^2 L} \quad \text{A-6}$$

where  $\rho$  is the average gas density,  $\bar{v}$  is the average velocity through the test section, and  $D$  and  $L$  are the diameter and length of each section respectively. The average velocity was obtained by one of three methods. If a velocity profile was available, the average velocity calculated as outlined in section A-1 was used. If no velocity profile data was available, then a value of  $.8 v_c$  was used. The centerline velocity was obtained either by the anemometer probe in the downward vertical section or the pitot-static section in the lower horizontal portion of the loop. With either method corrections for static pressure difference in the horizontal section and both static pressure and diameter differences in the vertical section had to be made. Since the anemometer probe was calibrated against the downstream pitot-static section which remained at atmospheric pressure throughout the experiment, the static pressure where the velocity measurements were made was assumed to be atmospheric. Sample calculations of a typical run where the centerline velocity was obtained with the anemometer will be presented below. The pressure drops were measured with the R. Feuss micromanometer and have been converted to  $\frac{\text{lb}}{\text{ft}^2}$  in the manner illustrated in section 1.

DATA:

$$\text{RPM} = 13200.$$

$$T = 77^{\circ}\text{F}$$

$$v_c = 77.3 \frac{\text{ft}}{\text{sec}} \quad (\text{as obtained from anemometer calibration curve})$$

$$\mu = (.0169/1488) \sqrt{(537/492)} = 1.188 \times 10^{-5} \frac{\text{lb}}{\text{ft-sec}}$$

$$\rho = .0808 \left(\frac{492}{537}\right) = .0741 \text{ lb/ft}^3$$

Horizontal test section:

$$P_s = 1.5 \text{ in } H_g \text{ gauge}$$

$$\Delta P_m = 4.28 \frac{\text{lb}}{\text{ft}^2}$$

$$\rho = .0808 \left(\frac{492}{537}\right) \left(\frac{31.4}{29.9}\right) = .0777 \frac{\text{lb}}{\text{ft}^3}$$

$$\bar{v} = .8 v_c \left(\frac{.0741}{.0777}\right) = .8 (72.3) (.955) = 58.9 \frac{\text{ft}}{\text{sec}}$$

$$D = .0729 \text{ ft}$$

$$L = 3.33 \text{ ft}$$

$$(Re)_g = \frac{\rho \bar{v} D}{\mu} = \frac{.0777(58.9)(.0729)}{1.188 \times 10^{-5}} = 28126$$

$$f_g = \frac{2g_c \Delta P_m}{\rho \bar{v}^2 L} = \frac{(64.4)(4.28)(.0729)}{(.0777)(58.9)(3.33)} = .0224$$

Vertical test section:

$$P_s = 2.00 \text{ in } H_g \text{ gauge}$$

$$\Delta P_m = 1.737 \frac{\text{lb}}{\text{ft}^2}$$

Since the pressure drop is very small compared to the static pressure and because the loop flow is essentially isothermal, acceleration effects are negligible and  $\Delta P = \Delta P_m$  for both vertical and horizontal test sections.

$$\rho = .0741 \left( \frac{31.9}{29.9} \right) = .0790 \text{ lb/ft}^3$$

$$\bar{v} = .8v_c \left( \frac{\rho_c}{\rho} \right) \left( \frac{A_o}{A} \right)$$

Since the diameter of the anemometer probe section is 7/8" and that of the vertical test section is 1",

$$\frac{A_o}{A} = .765$$

therefore,

$$\bar{v} = .8 (77.3) \left( \frac{.0741}{.0790} \right) (.765) = 44.5 \frac{\text{ft}}{\text{sec}}$$

$$D = .0833 \text{ ft.}$$

$$L = 2.5 \text{ ft.}$$

$$(\text{Re})_g = \frac{\rho \bar{v} D}{\mu} = \frac{.0790 (44.5) (.0833)}{1.188 \times 10^{-5}} = 24650$$

$$f_g = \frac{2g_c \Delta P D}{\rho \bar{v}^2 L} = \frac{(64.4)(1.737)(.0833)}{(.0790)(44.5)^2 (2.5)} = .0239$$

#### 4. Orifice Coefficient.

Calculations of the orifice coefficient were based on a mean velocity determined by using the center line velocity from the anemometer multiplied by .8. The coefficient was determined using the relation

$$C_v = \rho \bar{v} \sqrt{\frac{1 - \beta^4}{2g_c \Delta P \rho}} \quad \text{A-7}$$

where  $\Delta P$  is the pressure drop through the orifice,  $\rho$  is the density of the gas upstream of the orifice,  $\bar{v}$  is the average velocity through the orifice and  $\beta$  is the ratio of the diameter of the orifice to that of the upstream channel. It should be noted that equations recommended for the

calculation of the coefficient of discharge for gas flow generally include an expansion factor,  $Y$ . For incompressible flow this factor is unity. Since the primary interest of the orifice coefficient results is in the effect of the particles on the coefficient, this factor has been assumed to be unity in all orifice coefficient calculations. A sample calculation for a typical experimental condition is given below. The data recorded were as follows:

$$\text{RPM} = 13200$$

$$T = 77^{\circ}\text{F}$$

pressure at upstream orifice top = 1.00 in Hg

pressure drop through the orifice = 16.8 in. of 1.75 SG

gage fluid = 29.4 in. of water =  $152 \frac{\text{lb}}{\text{ft}^2}$

$$v_c = 77.3 \frac{\text{ft}}{\text{sec}}$$

diameter of orifice = .435 in.

$$D = .875 \text{ in}$$

$$\beta = \frac{.435}{.875} = .497$$

$$\rho = .0741 \left( \frac{30.9}{29.9} \right) = .0767 \text{ lb/ft}^3$$

correcting the anemometer velocity for pressure and area differences through the orifice,

$$\bar{v} = .8v_c \left( \frac{.0741}{.0767} \right) \left( \frac{1}{\beta^2} \right)$$

$$\bar{v} = .8(77.3) (.967) (2.01)^2 = 232 \frac{\text{ft}}{\text{sec}}$$

$$(1 - \beta^4) = .939$$

so that,

$$C_v = .0767(232) \sqrt{\frac{.939}{64.4 (152)(.0767)}}$$

$$C_v = (.0767) 232 \sqrt{.00125}$$

$$C_v = .629$$

$$R_{eo} = \frac{\rho \bar{v} D}{\mu} = \frac{(.0767)(232)\left(\frac{.435}{12}\right)}{1.188 \times 10^{-5}} = 56640$$

The fact that the calculated results of orifice coefficient as a function of Reynolds number are in good agreement with those given in reference 59 for circular square edged orifices seems to indicate that the assumption that  $Y=1$  is not unreasonable.

#### 5. Strain Gage Calibration.

The two phase flow meter also required calibration for the pure gas condition. This was done using both open and closed loop configurations. In the open loop configuration velocities were determined by the pressure drop from a calibrated pitot tube located as illustrated in figure 10. In the closed loop studies velocities were determined by anemometry. A sample calculation for an open loop situation is shown below:

$$\text{RPM} = 13500$$

$$V_{ST} = .3000 \text{ mv}$$

$$\Delta P_{PT} = 6.60 \frac{\text{lb}}{\text{ft}^2}$$

$$T = 74^\circ \text{F}$$

$$\rho = .0808 \left(\frac{492}{534}\right) = .0745 \frac{\text{lb}}{\text{ft}^3}$$

$$v_c = 29.5 \quad 6.60 = 75.8 \frac{\text{ft}}{\text{sec}}$$

$$v_c = 5.65 \frac{\text{lb}}{\text{ft}^2 \text{ sec}}$$

For the closed loop configuration no calculation is required.

#### OPEN LOOP CALCULATIONS

Open loop calculations were performed mainly in the calibration of the two phase flow meter with suspension flow. In this procedure the mass flow rate of solids was calculated by dividing the weight of particles collected by the time required for collection. The centerline mass velocity was calculated as outlined in section 5 and the strain gage output was read directly from the recorder. No other calculations were required.

#### CLOSED LOOP CALCULATIONS

1. Mass Flow Ratios. - Mass flow ratios were calculated using the relation:

$$\eta = \left[ \frac{V_{ST}}{.0217(\rho_{vc})^{1.808}} \cdot .590 \right]^{1.238} \quad (48)$$

derived as shown previously.

A sample computation for a typical experimental run is shown below. For this run the data obtained were as follows:

$$\text{RPM} = 9500^\circ \text{F}$$

Weight added : 80.0 gms - #981 GLASS BEADS

$$V_{ST} = .3100 \text{ mv}$$

$$T = 82.1$$

$$\rho_{vc} = 3.82 \frac{\text{lb}}{\text{ft}^2 \text{-sec}} \quad (\text{obtained from anemometry})$$

$$\eta = \left[ \frac{.3100}{.0217 (3.82)^{1.808}} - .590 \right]^{1.238}$$

$$\eta = .62$$

## 2. Friction Factors.

Friction factors for the horizontal section were calculated in the same manner as shown earlier for the pure gas case. This is so because of the definition of  $f_s'$  which is based on gas properties. The vertical test section friction factors when determined with suspensions as the working fluids must be corrected for the head of solids in the vertical section. This is accomplished by defining

$$\Delta P_f = \Delta P_m - \eta (\rho_g L) \quad (53)$$

A sample computation for a typical run is shown below.

For this run the data obtained were as follows,

RPM 9500

Weight added 80.0 grams - #981 glass beads

$V_{ST} = .3100$  mv

$T = 82.1^\circ$  F

$\rho \bar{v}_c = 3.82 \frac{\text{lb}}{\text{ft}^2\text{-sec}}$  (obtained from anemometry)

Vertical section  $\Delta P_m = .8281 \frac{\text{lb}}{\text{ft}^2}$  (converted from mm water)

$P_s = 1.10$  in Hg gauge

The calculations are as follows,

$\eta = .6157$  (as shown in previous section)

$\rho \bar{v} = .8(3.82)$

the average mass velocity in the vertical test section must

be corrected for area difference, so that

$$(\rho \bar{v})_{\text{vert}} = .8(3.82) \left(\frac{49}{64}\right) = 2.34 \frac{\text{lb}}{\text{ft}^2 \text{ sec}}$$

$$\rho_g = .0808 \frac{(492)}{542} \left(\frac{31}{29.9}\right) = .0762 \frac{\text{lb}}{\text{ft}^3}$$

$$\Delta P_f = .8281 - .6157 (.0762) \left(\frac{30}{12}\right)$$

$$\Delta P_f = .8281 - .1170 = .7111 \frac{\text{lb}}{\text{ft}^2}$$

$$f_s' = \frac{\Delta P_f 2g_c D}{(\rho \bar{v})_{\text{vert}} \bar{v}_{\text{vert}} L}$$

so that,

$$f_s' = \frac{(.7111) (61.4) \left(\frac{1}{12}\right)}{(2.34) (30.8) \left(\frac{30}{12}\right)} = .0211$$

The gas Reynolds number calculated using  $(\rho \bar{v})_{\text{vert}}$  is found to be 16380. Using the relation

$$f_g = .0050 + \frac{.50}{(\text{Re})_g^{.32}}$$

which was found to be a good fit for the vertical test section data,

$$f_g = .0280$$

so that

$$\frac{f_s'}{f_g} = \frac{.0211}{.0280} = .754$$

3. Orifice Calculations. - Orifice calculations for the case of suspension flow were made exactly as outlined earlier for the pure gas case.

4. Turbulence Calculations. - Turbulence calculations for both

pure gas and suspension cases were made in the same manner using the relation

$$\% \text{ TURBULENCE} = \frac{400 \bar{V} V_{\text{rms}}}{\bar{V}^2 - V_o^2} \quad (61)$$

A typical calculation was as follows,

$$\text{Wt} = 35 \text{ gms} - \#279 \text{ Glass beads.}$$

$$V = 5.790 \text{ volts}$$

$$(\text{Re})_g = 19796 \text{ (calculated using anemometer calibration)}$$

$$\eta = .0602 \text{ (as illustrated previously)}$$

$$V_o = 3.67 \text{ volts}$$

$$V_{\text{rms}} = .0092 \text{ volts}$$

Probe in centerline position.

So that,

$$\% \text{ Turb.} = \frac{400 (5.79) (.0092)}{(5.79)^2 - (3.67)^2}$$

$$\% \text{ Turb.} = 1.062$$

The ratios  $I_s/I_g$  were calculated using the pure gas turbulence results at a given Reynolds number. For example from figure 68.

$$I_g = .01038$$

so that,

$$\frac{I_s}{I_g} = \frac{.01062}{.01038} = 1.023$$

## X. APPENDIX B

## INSTRUMENTATION READING ERRORS

This section of the dissertation will present the magnitude of the instrumentation errors encountered during this investigation. A more complete error analysis would not yield significant results because the major errors encountered in this study were probably due to the assumptions made for calculation purposes. For example, what is the error involved in assuming that the average velocity is  $.8 v_c$  for suspension flow? What error is involved in the calculation of loading ratio for all size particles using the calibration obtained for the  $30\mu$  glass beads? These are questions which cannot be answered at the present time. So that, until future investigations clarify the errors involved in these assumptions a complete error analysis is really not possible.

An alternative to the preferred error analysis is simply listing the instrumentation reading errors. Thus, if at some future date the inaccuracies involved in the assumptions are determined a more complete error analysis could be undertaken.

The instruments read during the course of this investigation include the Brush recorder (for both temperature and strain gage readout), the R. Feuss micromanometer (for both pressure drop and pitot tube velocity) the digital voltmeter (for anemometric velocity measurement) the RMS voltmeter (for turbulence measurements), U-tube manometers (for static pressure measurements) and an electrical timer and triple

beam balance (for open loop calibration).

For thermocouple readout the Brush recorder was used only with a  $10 \mu\text{V}/\text{div}$  sensitivity. This means that it could be read accurately only to the nearest  $5 \mu\text{V}$ . Five microvolts corresponds to about  $.3^\circ\text{F}$  for chromel-alumel thermocouples in this temperature range. So that an average temperature reading error would be

$$\frac{\delta T}{T} = \frac{.3}{75} = .004 \text{ or } .4\%$$

The two phase flow meter readout on the Brush recorder was measured with the  $10 \frac{\mu\text{V}}{\text{div}}$  sensitivity for readout up to .50 mv and with the  $20 \frac{\mu\text{V}}{\text{div}}$  sensitivity for readout between .50 mv. and 1.00 mv. So that the average reading errors on both scales would be

$$\frac{\delta V_{sr}}{V_{sr}} = \frac{.005}{.25} = .02 = 2\%, \quad 10 \frac{\mu\text{V}}{\text{div}} \text{ sensitivity}$$

and

$$\frac{\delta V_{ST}}{V_{ST}} = \frac{.010}{.75} = .0133 = 1.3\%, \quad 20 \frac{\mu\text{V}}{\text{div}} \text{ sensitivity.}$$

The R. Feuss micromanometer has a reading accuracy of .5% of full scale reading. For an average piece of velocity profile data where

$$\Delta P_{PT} = 167.5 \times .10 \text{ (Scale factor)} = 16.75 \text{ mm H}_2\text{O}$$

$$\delta \Delta P_{PT} = .005 (200) \times .10 = .10 \text{ mm H}_2\text{O}$$

so that the reading error is

$$\frac{\delta (\Delta P_{PT})}{\Delta P_{PT}} = \frac{.10}{16.75} = .00597 = .6\%$$

Whenever possible these micromanometers were read on the most sensitive scale available so that most of the

readings were over 100 divisions using the particular arc factor, and the relative reading error was small as illustrated above. It should also be noted that the pitot tube pressure drop error results in only half the error velocity, due to the relationship between the two (see equation A-1).

For pressure drop the same error is obtained as shown above. For a typical case with pressure drop of a flowing suspension,

$$\Delta P_m = 106.0 \times .2 \text{ (scale factor)} \times .003281 \times 62.2 = 4.28 \frac{1b}{ft}^2$$

$$\Delta P_m = .005 \text{ (200)} \times .2 \times .003281 \times 62.2 = .0404 \frac{1b}{ft}^2$$

so that,

$$\frac{\delta(\Delta P_m)}{\Delta P_m} = \frac{.0404}{4.28} = .00945 = 1\%$$

For every anemometric velocity determination two reading errors resulted from the digital voltmeter, one in the zero reading the other with the flow measurement. Hence, for a typical case, realizing that the instrument can be read to the nearest .002 volts (with the sensitivity of 10 volts full scale),

$$\frac{\delta V_o}{V_o} = \frac{.002}{3.745} = .000533 = .05\%$$

and

$$\frac{\delta V}{V} = \frac{.002}{6.065} = .00033 = .03\%$$

The small values of these errors are misleading, however, in that they are only instrument reading errors and do not include calibration or temperature correction errors which are incurred when converting the recorded voltage to a velocity.

The RMS Voltmeter may be read to the nearest .0002 volts

(using the scale employed throughout this investigation),  
hence for a typical case

$$V_{rms} = .0092$$

$$\delta V_{rms} = .0002$$

and

$$\frac{\delta V_{rms}}{V_{rms}} = \frac{.0002}{.0092} = .0217 = 2.2\%$$

The U-tube manometers may be read to .1 inch of the gage fluid in each leg. For a typical static pressure measurement, where

$$P_s = 1.5 \text{ in. Hg gage}$$

the reading error incurred would be

$$\frac{\delta P_s}{P_s} = \frac{.1}{1.5} = .0667 = 6.67\%$$

However, the  $\delta P_s$  of .2 in. Hg is almost negligible when the static pressure is converted to in. Hg absolute, for example

$$\frac{\delta P_s}{P_s \text{ (absolute)}} = \frac{.2}{31.4} = .006375 = .64\%$$

For the orifice calibration a typical error would be, for the case of  $\Delta P_o = 16.8$  in. of 1.75 SG gage fluid

$$\frac{\delta \Delta P_o}{\Delta P_o} = \frac{.2}{16.8} = .0119 = 1.19\%$$

The open loop calibration required only three significant measurements aside from pitot tube and recorder output. Two weighings (an initial and final weight) and a time of operation. The errors incurred would be as follows for the worst cases of each measurement,

$$\begin{aligned} Wt &= 250.0 \text{ gms} \\ 2 \delta Wt &= .2 \text{ gms} \end{aligned}$$

$$\frac{2 \delta Wt}{Wt} = \frac{.2}{250.0} = .0008 = .08\%$$

and

$$t = 100 \text{ secs.}$$

$$t = .1 \text{ sec}$$

so that

$$\frac{\delta t}{t} = \frac{.1}{100} = .001 = 1\%$$

It should be again emphasized that the errors presented above merely represent instrument reading errors and by no means represent the actual errors incurred during this investigation.

## XI. VITA

Salvatore J. Rossetti received his undergraduate education at the City College of New York and received his Bachelor of Engineering degree in Chemical Engineering in February, 1964.

With the aid of a City University research assistantship, and an NDEA Title IV fellowship he continued graduate studies at the City College. He wrote a thesis entitled "Thermophysical Properties of Gas-Solid Suspensions and the use of such Suspensions as Working Fluids in a Gas Brayton Cycle Power Generation System" in partial fulfillment of the requirements for the degree of Master of Engineering (Chemical Engineering), and received the degree in May, 1966.

The author continued his studies towards a doctorate degree supported by a National Aeronautics and Space Administration grant. After defending his dissertation, the author plans to work for Esso Research and Engineering Company in Linden, New Jersey.